

# Stochastic Dynamics in Sand and Cells

This thesis was reviewed by:

prof.dr. M. E. Cates

prof.dr. D. Frenkel

prof.dr. W. van Saarloos

prof.dr. C. F. Schmidt

dr. R. J. Wijngaarden



VRIJE UNIVERSITEIT

# Stochastic Dynamics in Sand and Cells

ACADEMISCH PROEFSCHRIFT

ter verkrijging van de graad Doctor aan  
de Vrije Universiteit Amsterdam,  
op gezag van de rector magnificus  
prof.dr. T. Sminia,  
in het openbaar te verdedigen  
ten overstaan van de promotiecommissie  
van de faculteit der Exacte Wetenschappen  
op vrijdag 24 maart 2006 om 10.45 uur  
in de aula van de universiteit,  
De Boelelaan 1105

door  
Jeroen Sebastiaan van Zon  
geboren te Haarlem.

promotor: prof.dr. F. C. MacKintosh

copromotor: dr. P. R. ten Wolde

---

This thesis is based on the following publications:

- J.S. van Zon and F.C. MacKintosh,  
*Velocity distributions in dissipative granular gases*,  
Phys. Rev. Lett. **93**, 038001 (2004).
- J.S. van Zon, J. Kreft, D. I. Goldman, D. Miracle, J.B. Swift and H. L. Swinney,  
*Crucial role of sidewalls in velocity distributions in quasi-two-dimensional granular gases*,  
Phys. Rev. E **70**, 040301(R) (2004).
- J.S. van Zon and P.R. ten Wolde,  
*Simulating biochemical networks at the particle level and in time and space: Green's function reaction dynamics*,  
Phys. Rev. Lett. **94**, 128103 (2005).
- J.S. van Zon and F.C. MacKintosh,  
*Velocity distributions in dilute granular systems*,  
Phys. Rev. E **72**, 051301 (2005).
- J.S. van Zon and P.R. ten Wolde,  
*Green's function reaction dynamics: A particle-based approach for simulating biochemical networks in time and space*,  
J. Chem. Phys. **123**, 234910 (2005).
- J.S. van Zon, M. Morelli and P. R. ten Wolde,  
*Diffusion of transcription factors can drastically enhance the noise in gene expression*,  
to be submitted.
- J.S. van Zon, J. Kreft, D. I. Goldman, D. Miracle, J.B. Swift and H. L. Swinney,  
*Time and space independent velocity distributions in an oscillated granular gas*,  
to be submitted.

---

---

# Contents

|  |           |
|--|-----------|
| <b>I Granular Materials</b>                                  | <b>1</b>  |
| <b>1 Introduction</b>  | <b>3</b>  |
| 1.1 An overview . . . . .                                    | 4         |
| 1.2 Granular solids . . . . .                                | 7         |
| 1.3 Jamming and granular solid-liquid transitions . . . . .  | 10        |
| 1.4 Granular liquids . . . . .                               | 13        |
| 1.5 Granular gases . . . . .                                 | 22        |
| <b>2 Velocity distributions: simulations</b>                 | <b>31</b> |
| 2.1 Introduction . . . . .                                   | 32        |
| 2.2 Numerical simulation . . . . .                           | 39        |
| 2.3 Clustering . . . . .                                     | 42        |
| 2.4 Velocity distributions . . . . .                         | 45        |
| 2.5 A model without spatial degrees of freedom . . . . .     | 55        |
| 2.6 Relation to experiments . . . . .                        | 58        |
| 2.7 Conclusions . . . . .                                    | 61        |
| <b>3 Velocity distributions: experiments</b>                 | <b>63</b> |
| 3.1 Introduction . . . . .                                   | 64        |
| 3.2 Experimental setup and simulations . . . . .             | 65        |
| 3.3 Image analysis . . . . .                                 | 68        |
| 3.3.1 Image restoration . . . . .                            | 68        |
| 3.3.2 Locating candidate particles . . . . .                 | 70        |
| 3.3.3 Discarding false positives . . . . .                   | 72        |
| 3.3.4 Determining positions at sub-pixel precision . . . . . | 72        |
| 3.3.5 Linking positions into trajectories . . . . .          | 73        |
| 3.4 Steady state . . . . .                                   | 75        |
| 3.4.1 Horizontal velocity distributions . . . . .            | 78        |

|           |  |            |
|-----------|--|------------|
| 3.4.2     | Vertical velocity distributions and collision statistics . . . . . | 82         |
| 3.5       | Velocity distributions . . . . .                                   | 84         |
| 3.5.1     | Steady-state distributions . . . . .                               | 84         |
| 3.5.2     | Single Particle Dynamics . . . . .                                 | 87         |
| 3.5.3     | Single particle model . . . . .                                    | 88         |
| 3.6       | Discussion and conclusions . . . . .                               | 90         |
| <b>II</b> | <b>Biochemical Networks</b>  | <b>91</b>  |
| <b>4</b>  | <b>Introduction</b>  | <b>93</b>  |
| 4.1       | Introduction . . . . .   | 94         |
| 4.2       | Molecular biology of the bacterium . . . . .                       | 99         |
| 4.2.1     | The lac operon . . . . .   | 100        |
| 4.2.2     | The $\lambda$ switch . . . . .                                     | 102        |
| 4.3       | Biochemical networks . . . . .                                     | 105        |
| 4.3.1     | Statistical properties of biochemical networks . . . . .           | 105        |
| 4.3.2     | Stochastic fluctuations in simple biochemical networks . . . . .   | 109        |
| 4.4       | Models of stochastic gene expression . . . . .                     | 113        |
| 4.5       | Molecular noise as a source of variation . . . . .                 | 116        |
| 4.6       | Noise and robustness in genetic networks . . . . .                 | 118        |
| 4.7       | Spatial fluctuations . . . . .                                     | 122        |
| <b>5</b>  | <b>Green's-function reaction dynamics</b>                          | <b>127</b> |
| 5.1       | Introduction . . . . .   | 128        |
| 5.2       | Overview of the algorithm . . . . .                                | 131        |
| 5.2.1     | Green's functions . . . . .  | 132        |
| 5.2.2     | Two-particle algorithm . . . . .                                   | 136        |
| 5.2.3     | Many-particle algorithm . . . . .                                  | 138        |
| 5.2.4     | Boundary conditions . . . . .                                      | 141        |
| 5.2.5     | Green's function for $U(\mathbf{r}) = 0$ . . . . .                 | 144        |
| 5.2.6     | Drawing random numbers from an arbitrary distribution . . . . .    | 147        |
| 5.3       | Results . . . . .  | 148        |
| 5.3.1     | Bi-molecular reaction . . . . .                                    | 149        |
| 5.3.2     | Simple model of gene expression . . . . .                          | 152        |
| 5.3.3     | Performance . . . . .  | 161        |
| 5.4       | Discussion and conclusions . . . . .                               | 163        |

|  |            |
|--|------------|
| <b>6 Spatial fluctuations of transcription factors</b> | <b>167</b> |
| 6.1 Introduction . . . . .                             | 168        |
| 6.2 Model and simulation . . . . .                     | 169        |
| 6.3 Simulation results: dynamics and noise . . . . .   | 173        |
| 6.4 Simulations results: operator binding . . . . .    | 176        |
| 6.5 Two-step kinetic scheme . . . . .                  | 179        |
| 6.6 Discussion . . . . .                               | 182        |
| 6.7 Conclusion . . . . .                               | 184        |
| <b>Bibliography</b>                                    | <b>185</b> |
| <b>Samenvatting</b>                                    | <b>199</b> |
| <b>Dankwoord</b>                                       | <b>209</b> |
| <b>Curriculum Vitae</b>                                | <b>213</b> |

*Contents*

---



---

**Part I**

**Granular Materials**



---

# Chapter 1

## Introduction

## 1.1 An overview

When R. A. Bagnold (1896-1990), officer in the British Army Royal Engineers, crossed the Libyan Desert in 1930 with only 3 Model A Ford cars, while on leave from his post in Egypt, his expedition was probably the first to explore what is one of the largest deserts in the world – about the size and shape of the Indian subcontinent. He found an alien landscape. Where in more temperate and accessible deserts the landscape is effected by moisture, vegetation and the presence of animals and men, one finds in the interior of the great deserts only wind and sand. In temperate deserts the sand hills are often chaotic and disordered. Instead, in the interior of the Libyan Desert, Bagnold found that [1]:

... the observer never fails to be amazed at a simplicity of form, an exactitude of repetition and geometric order unknown in nature on a scale larger than that of crystalline structure. In places vast accumulations of sand weighing millions of tons move inexorably, in regular formation, over the surface of the country, growing, retaining their shape, even breeding, in a manner which, by its grotesque imitation of life, is vaguely disturbing to an imaginative mind. Elsewhere the dunes are cut to another pattern – lined up in parallel ranges, peak following peak in regular succession like the teeth of a monstrous saw for score, even hundreds of miles, without a break and without a change of direction, over a landscape so flat that their formation cannot be influenced by any local geographical features. Or again we find smaller forms, rare among the coastal sand hills, consisting of rows of coarse-grained ridges even more regular than the dunes. Over large areas of accumulated sand the loose, dry, uncemented grains are so firmly packed that a loaded lorry driven across the surface makes tracks less than an inch in depth. Then, without the slightest visual indication of a change, the substance only a few inches ahead is found to be a dry quicksand through which no vehicle can force his way. At times, especially on a still evening after a windy day, the dunes emit, suddenly, spontaneously, and for many minutes, a low-pitched sound so penetrating that normal speech can be heard only with difficulty.

That the regular patterns of dunes described by Bagnold are not restricted to the Libyan Desert alone, is shown in Fig. 1.1, where satellite images of dune fields in Namibia and even on Mars exhibit similar regular patterns. During his expeditions, many of which were undertaken in his free time or on short leaves, Bagnold became fascinated by the striking symmetry and geometrical regularity of the desert dunes.

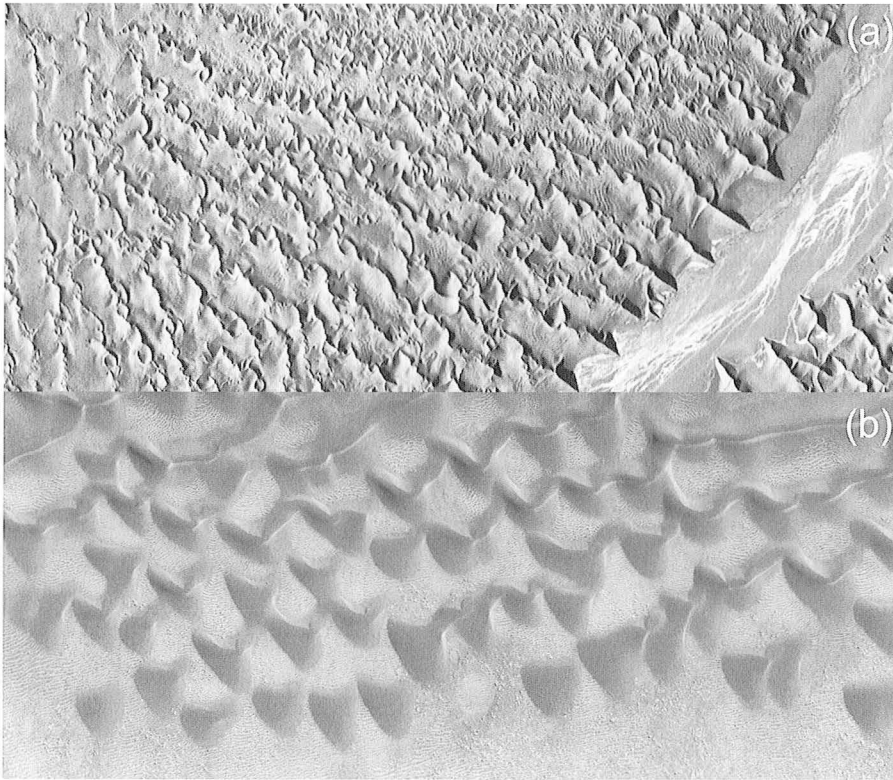


**Figure 1.1:** *Satellite images of dune fields. (a) Sand dunes of Sossusvlei in the Namib desert, Namibia. The image was obtained by Surrey Satellite Technologies. The width of the figure corresponds to around 10 km. (b) Sand dunes at the edge of the Proctor Crater, Mars. Smaller ridges are visible between the dunes as white speckles. The image was obtained by the Mars Global Surveyor Orbiter. The width of the figure corresponds to around 5 km.*

When he retired from the army and returned to England in 1935, he did numerous experiments to understand dune formation, both in the desert and in the laboratory, where he used wind tunnels to understand the interaction between sand and air. The regularity of dune fields had convinced him that dune formation was governed by simple laws. He postulated that once the basic laws of interaction between air and a single grain of sand were understood, application of these laws to wind blowing over a vast expanse of sand would be enough to explain the shape of dunes and the regular arrays of dune fields, without the need to invoke more complicated geological factors. Bagnold remarked that in this sense “... the subject of sand movement lies far more in the realm of physics than of geomorphology.” [1]

Bagnold abandoned his research for military service in the Second World War, during which he used his experience in desert exploration to found the Long Range Desert Group, which was able to penetrate the Libyan Desert and, among other things, managed almost single-handedly to prevent the Italian army in North-Africa from seizing the Suez canal [2]. After the Second World War, Bagnold returned to his research but, for the lack of easily accessible deserts in England, instead turned to the transport of grains not by air but by water, studying sediment transportation in rivers and beaches. Of dune formation, Bagnold apologizes that “. . . the subject is very much a borderline one . . .” in that it involves “. . . a large number of widely different fields of knowledge – geophysics, meteorology, aerodynamics, hydraulics, geology, geomorphology, &c.” [1] It is precisely this area of research – understanding the complex collective behavior of granular particles, arising from simple interactions between individual grains, that is nowadays the focus of the study of granular materials.

The science of granular materials studies grains of sand, powders, nuts or metal beads that are piled up together, avalanched down slopes, carried by air or water, or mixed by shaking them violently. Even though it was pioneered by Bagnold in the context of dune formation, research on granular materials is not restricted to deserts alone. A variety of geophysical processes, such as avalanches, mud slides or quicksand involve large number of macroscopic grains. In the industrial world granular materials are stored in silos and are mixed and transported by the flow of gas and liquids. As we will see below, in each of these applications the collective behavior of the grains can be surprising and often very complicated.

The physics of dune formation is particularly difficult and is still poorly understood, yet it contains many of the ingredients that has attracted the attention of physicists to the area of granular materials. One of the central observations that Bagnold made in the context of dune formation is that sand can behave like the different phases of molecular matter. This is obvious for everybody who has played with sand on the beach. The natural state of sand on a beach is much like a solid: a pile of sand will remain stable once erected. On the other hand, it is possible to pour sand out of one’s hand much like a fluid. Sand can switch from solid to the liquid state and back. When, for instance, the slope of a sandpile becomes too steep, the top layer of the slope will enter a liquid state and flow down the pile as an avalanche. Sand only enters the liquid state when energy is inserted, for instance in the case of an avalanche by the force of gravity. One of the key insights of Bagnold was that also strong wind can fluidize the top layer of desert sands and that it is this fluid-like layer that contributes to the transport of sand and consequently to the formation of dunes.

Physicists have developed a large toolset to describe molecular solids and fluids. One of the main themes in research on granular materials is to what extent this toolset can be used to describe the behavior of large numbers of macroscopic grains in the solid-like and fluid-like states [3]. As I will describe in more detail below, many of the most interesting phenomena – where the deviations from the behavior of molecular matter are largest – occur when the grains can switch from solid-like to liquid-like behavior and back. This is partly why it has remained difficult to understand where avalanches will occur or under what precise conditions a rain-soaked mountain slope will turn into a devastating mud slide.

Another theme is suggested by the fact that granular materials consist of large numbers of approximately identical particles. This invites a description of granular materials using tools from statistical physics. This approach is most often used on the third phase of granular materials, namely *granular gases*: dilute granular fluids, where the grains interact not through rubbing and sliding as in the case of dense granular liquids, but predominantly through two-body collisions. The main potential difficulty in describing granular gases using statistical physics is that a granular gas consists of macroscopic particles that dissipate energy upon collision, in contrast to molecular gases where the collisions are elastic and the system is in thermal equilibrium. As a consequence, it is *a priori* not clear whether the properties of granular gases can be described by tools from equilibrium statistical mechanics. This is the focus of the research in Chapters 2 and 3.

Many of the complicated phenomena observed in the solid and the liquid state of granular materials have parallels in the granular gases. In fact, granular gases are often studied as simple model systems for understanding the properties of granular materials in general. Therefore, I will first give a more detailed overview of the research done on granular solids, granular fluids and granular gases before briefly introducing my research on granular gases at the end of this chapter.

## 1.2 Granular solids

A pile of sand or grains in a silo are examples of what are called granular solids. Surprisingly enough, the behavior of a silo full of grains is strikingly different from that of a silo full of an equivalent mass of a simple molecular solid, such as plastic. This difference is due to two related properties of granular solids: the random packing of the granular particles that constitute the solid and the way the weight of the solid is distributed among them.

When one fills a container with granular particles like ball bearings, and mea-

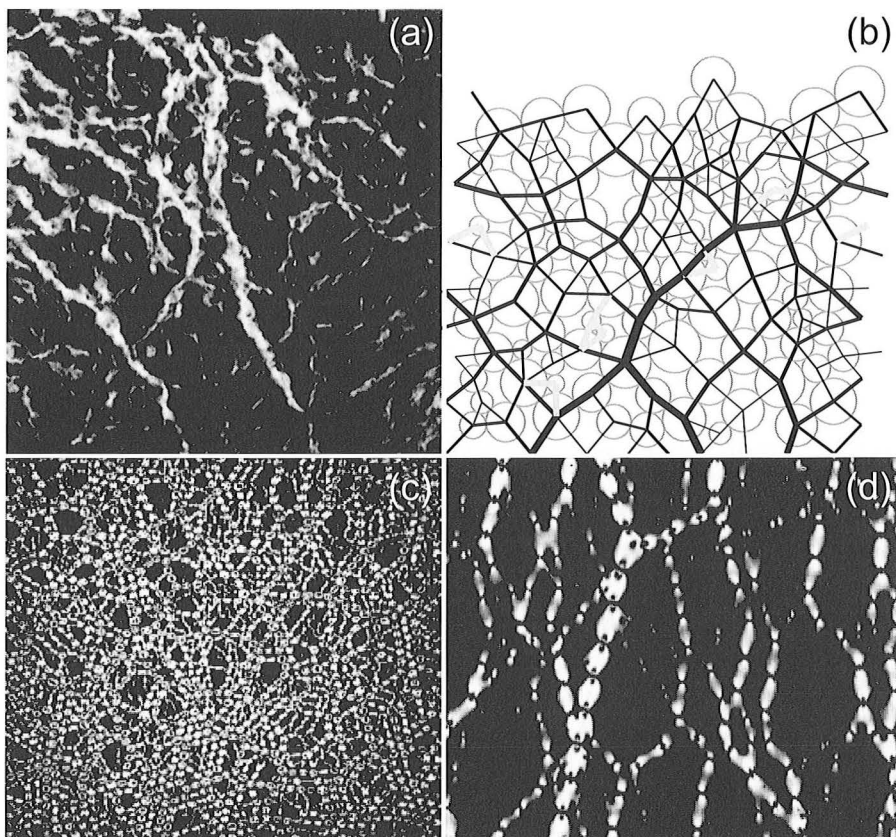


**Figure 1.2:** Force chains in granular materials (a) Force chains in three-dimensional collection of glass beads. Force is exerted by a piston from the top. Stress in the beads induces birefringence, so that beads that carry a load appear bright when imaged through crossed circular polarizers. (b) Force chains in a simulation of a two-dimensional layer of beads. The black lines indicate a force between particles. The thickness of the lines indicates the magnitude of the force. Grey lines indicate particles that do not exert force on each other. Force is exerted from the top. (c) Force chains in a two-dimensional layer of disks. The beads are isotropically compressed and parts of the disks that carry a load appear bright due to stress-induced birefringence. (d) Detail of (c). Fig. (a) is taken from Liu et al. [4], (b) is taken from Head et al. [5] and (c) and (d) are taken from Majmudar et al. [6].

sures the fraction of volume occupied by the ball bearings, one finds a volume fraction of around  $\phi \approx 0.6$ , depending on the procedure of filling. This packing is referred to as *random loose packing*. If one shakes the container, the packing fraction



goes up and the grains will ultimately settle in a denser configuration with volume fraction  $\phi \approx 0.64$ , called *random close packing*. This is considerably less dense than the most efficient packing, *ordered close packing*, with a packing fraction  $\phi = 0.74$ . Ordered close packing corresponds to the way oranges are stacked on the market, with the subsequent layer of oranges placed between the oranges of the previous layer. In contrast, random packings are disordered and one can find voids between the particles almost as large as the particles themselves.

How granular materials are compacted is studied by preparing the granular solid in a random loose packed state and perturbing the system by tapping it. As the system is tapped repeatedly, the grains will compact and the volume fraction will increase towards the random close packed limit. Similar behavior can be found in the kitchen, for instance when filling a jar with rice. When the jar is apparently filled to the top, shaking the jar will often compact the rice considerably, often leaving centimeters for even more rice. Experiments find that granular materials relax to the random close packed state logarithmically slow. Even after thousands of taps, a layer of grains might undergo significant compaction before eventually reaching a steady state. The reason for this is that most of the voids between particles are large, but not quite large enough to fit a particle. As a consequence, many particles have to be displaced in order for a particle to fit into one of the voids. The amount of particles to be displaced increases rapidly with increasing volume fraction so that many more taps are required before such a displacement occurs. These properties of granular solids in the random close packed state are reminiscent of the dynamics of glasses.

The disordered packing is directly responsible for the different way that forces are distributed in granular solids. For a tall block of a normal solid the pressure at the bottom of the block increases with the height of the block. In contrast, when a silo is filled with grains the pressure at the bottom will reach a maximum value independent of the amount of grain in the silo. This is what makes an hour glass filled with sand a better timekeeping device than an hour glass filled with water. In the case of granular particles, the friction between the grains and the sidewalls of the silo support the extra weight. Furthermore, it is found that the forces on the bottom and the walls of a silo are far from uniform. Experiments show that in granular solids a small fraction of the particles often carry most of the weight of the other particles.

The force distributions within a granular material can be visualized by using beads made out of photo-elastic materials. Photo-elastic materials change the circular polarization of light depending on the stress in the material. When the system is imaged through crossed circular polarizers beads under stress appear bright. Examples of typical force distributions for both experiments and simulations are shown in

Fig. 1.2. It is clear that forces are not distributed homogeneously, but are organized along chains of particles. These so-called *force chains*, formed by only a fraction of the particles in the pile, carry the bulk of the load. Some of the other particles hardly carry any weight at all.

The distribution of forces in the pile can be quantified, for instance by placing a piece of carbon paper on the bottom of the pile and measuring the area of the marks left by the beads. As it turns out, this distribution of forces  $f$  is well described by  $P(f) = C \exp(-f/f_0)$ . This means that very large forces can occur more frequently than expected for a Gaussian distribution with the same mean force. Such a force distribution, including force chains, is predicted by a simple two-dimensional model, where each grain distributes its weight randomly over the two grains below it [4]. The occurrence of force chains in granular materials means that locally the force on the walls of the silo can be much larger than anticipated by a conventional continuum description of solids. In the past there have been several cases of silo collapse during unloading of the silos, that might have been due to the existence of force chains.

### 1.3 Jamming and granular solid-liquid transitions

A granular material may flow like a liquid when energy is provided, for instance in the form of gravity when grains of sand flow down the slope of a dune. In striking contrast to ordinary fluids, granular materials exhibit sudden and spontaneous transitions between the fluid and the solid state.

The transition from the solid to the liquid state can be readily observed in a pile of sand. A stable pile of sand retains its slope against the force of gravity, just like an ordinary solid. Yet, if the pile is tilted or vibrated, the slope will become unstable and the upper layer will flow. Such solid-to-liquid transitions in granular materials are better known as *avalanches*. On the other hand, a flowing granular material may suddenly and without apparent reason freeze in its current configuration, a phenomenon known as *jamming*. It is a common observation that salt, when poured from a saltshaker, sometimes suddenly stops flowing. Only after shaking the saltshaker the flow of salt will resume. Similarly, but on a much more dramatic level, jamming can occur in the flow of grains from a silo or in the transport of powder or grains through a conduit. In such cases, the most sophisticated solution currently often consists of pounding the conduits until the jam suddenly disappears.

The nature of these transitions is closely related to the occurrence of force chains within granular materials. In the case of avalanches, the transition is initiated by the break-up of force chains due to changes in the configuration of the grains in

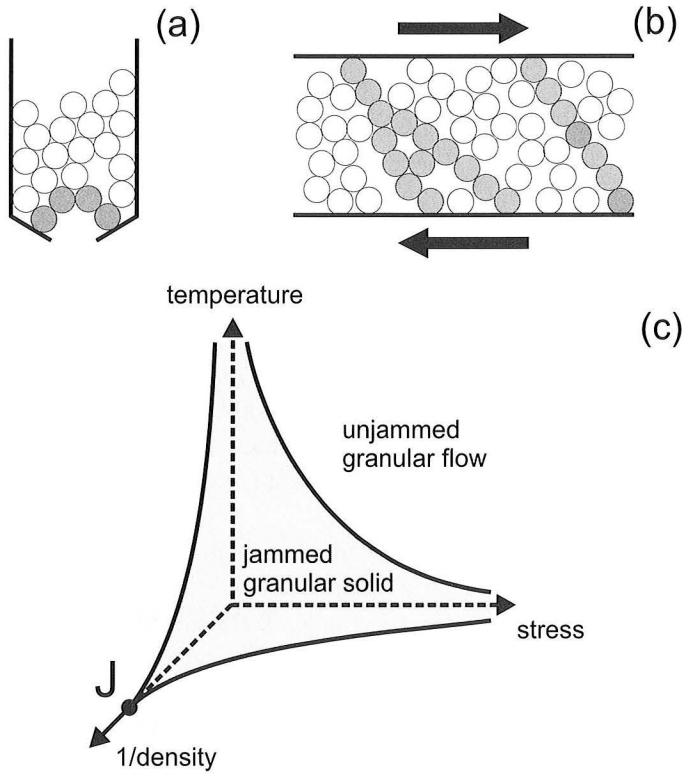


**Figure 1.3:** (a) Arching in granular flow from a hopper. The particles that comprise the arch are shaded and carry most of the load of the grains. (b) Jamming in a sheared granular material. The stress is carried by the force chains indicated by the shaded particles. (c) A speculative jamming phase diagram. Jamming occurs in the shaded area near the origin, for high density and low temperature and stress. The transition between the jammed and the unjammed region at zero temperature and zero stress occurs at point *J*.

the granular solid. In the case of jamming, on the other hand, a stable network of force chains develops suddenly in a freely flowing granular fluid. It was only recently appreciated that jamming is a general phenomenon, the importance of which might extend far beyond granular materials into the physics of colloids, glasses and possibly even traffic jams.

Flowing grains show *dilatancy*, meaning that a flowing layer will expand due to collisions between individual grains. It is because of this property of sand that when walking on the beach the sand around your foot appears dry, whereas everywhere

else it is wet. Normally, the sand on the beach is settled enough to form a densely packed state that doesn't allow water to penetrate. When you push down with your feet into the sand, the movement of the sand beneath your feet causes grains in the vicinity to dilate, leaving enough room between the grains for the water to drain into. As a result a halo of dry sand appears around your foot. This effect also illustrates that, in order to move, flowing grains require a larger volume than grains at rest. When grains flow in a confined geometry, like a silo or a pipe, locally the density can become so high that flow becomes impossible and the system jams.

When jamming occurs in granular flow, the system develops force chains that carry the load. In uniformly flowing grains, such as the grains of salt from the salt-shaker, the force chains often take the shape of arches. An example of *arching* is shown in Fig. 1.3(a). Such a configuration carries the load of the rest of the grain very effectively, just like its architectural counterpart. For a sheared granular fluid the force chains in the jammed state take the shape of linear structures spanning from one boundary to the other along the principal stress axis, as is shown schematically in Fig. 1.3(b).

Such a linear force chain is very successful in supporting a large load along its own axis, but cannot support even a small load along another axis. As a consequence, jammed granular materials are *fragile*, in the sense that they can support the shear stresses in the current jammed state, but are very sensitive to minor disturbances in that state [7]. Even a small difference in the configuration of the grains or shear in a slightly different direction cannot be sustained by the force chains and will cause the grains to flow and reorganize until it jams again. Consequently, introducing some random motions to the grains in the jammed state, for instance by shaking it, can bring the system to the unjammed state.

It has been speculated that the jamming-unjamming transition can be described like a conventional phase transition, such as the transition between the solid and the liquid phase [8]. A tentative phase diagram is shown in Fig. 1.3(c) and depends on the density, the temperature and the stress. For low density the system will consist of loose grains that will only interact by infrequent collisions and no jamming will occur. For a critical density the grains will have such difficulty moving past each other that force chains develop that span the entire sample and the system will jam. When the granular flow is arrested it can either be unjammed by imposing some random motions to the grains by shaking them, analogous to thermal fluctuations, or by increasing the shear on the system.

Granular materials consist of macroscopic grains that dissipate energy when they collide with or rub against each other and energy must be supplied to keep the system flowing. Such systems are far from thermal equilibrium and, consequently, it is not at all obvious whether jamming can be described as a phase transition. Sur-

prisingly, recent simulations suggest that this is indeed the case for the jamming transition at zero temperature and zero applied stress [9]. In this study, it is determined for different densities  $\phi$  if the sample is jammed, by measuring whether it can support a load or a shear. They find that all configurations of grains have a transition from the jammed to the unjammed state at some critical densities  $\phi_c$ . In all cases, the pressure  $p$  and the static shear modulus  $G$  vanish at the jamming transition as:

$$p(\phi), G(\phi) \sim (\phi - \phi_c)^{\alpha_p, \alpha_G}, \quad (1.1)$$

but with different exponents  $\alpha_p$  and  $\alpha_G$ . Such *critical* behavior is indicative of a second order phase transformation and suggests that the system has a critical point at the critical density  $\phi_c$ . The jamming transition is reminiscent of geometric phase transitions such as the percolation transition. There is a surprising connection between random close packing and the critical point at  $\phi_c$ . For small systems, every initial configuration jams at a different density  $\phi_c$ . However, when the number of particles is increased, the critical density converges towards the value for random close packing,  $\phi_c \approx 0.64$ , even though random close packing itself remains a controversial concept due to the lack of a proper definition.

It is an open question to what extent the jamming transition for granular materials in the presence of random motions or shear stress also behaves like a proper phase transition. At the same time, it is known that a large variety of systems, such as foams, colloidal suspensions and glasses show sudden transitions from a fluid-like to a solid-like state, just like the jamming transition in granular flow. It has been proposed that all these transitions could be described by the phase diagram shown in Fig. 1.3(c) [8]. A recent experiment on a suspension of attractive colloidal particles supports this idea [10]. In this case, the axes of the phase diagram become  $1/\phi$ , the inverse particle density,  $k_B T/U$ , the temperature normalized by the inter-particle attractive energy  $U$  and  $\sigma$ , the applied stress. Remarkably, at the transition all relevant parameters show critical behavior of the form in Eq. 1.1 and the system is well described by a phase diagram like Fig. 1.3(c). All these observations point to a fundamental link between such diverse phenomena as jamming in granular materials, the glass transition in molecular fluids and gelation in colloidal suspensions, which is particularly interesting as the glass transition itself is poorly understood.

## 1.4 Granular liquids

When enough energy is supplied, for instance in the form of shaking, by gravity or by air currents, a pile of grains will lose stability and will start to flow. It is tempting to think of such granular liquids as ordinary liquids whose molecules are macroscopic

grains. In particular, one could wonder to what extent a granular liquid can be described in a coarse-grained way by a set of hydrodynamical equations, similar to the Navier-Stokes equations for incompressible molecular fluids. It seems that this is unlikely to work. One reason is that the interactions between macroscopic grains are complicated and dominated by friction. As a consequence, granular flow is dissipative and energy is not conserved. Another reason is that, in contrast to molecular liquids, there is no clear separation in length scales, as the size of the particles is often comparable to the scale of the dynamics of the granular fluid. These differences can lead to behavior that is very different from ordinary liquids. For simple shear flow, for instance, most of the flow is restricted to a layer of 5-10 grains wide called a *shear band* [11]. Likewise, in an avalanche only a top layer of a few particles thick participates in the flow [3]. It is not clear how such behavior could be successfully incorporated in a hydrodynamic theory.

Does this mean that a granular liquid is not at all like a molecular liquid? Surprisingly, experiments suggest rather the opposite. In many cases, the behavior of fluidized grains shows striking similarities to that of normal liquids, even though the underlying dynamics are often completely different. Below, I will discuss two typical examples, namely the granular analogs of Rayleigh-Bénard convection and the Faraday instability. However, the fluid-like behavior observed in granular liquids is usually more complicated than that of normal liquids. Often, granular liquids show behavior that has not been observed for molecular fluids. Examples such as size segregation due to convection rolls and soliton structures in the case of the Faraday instability I will discuss below as well.

A related question is to what extent the random motion of driven grains is analogous to thermal fluctuations and can be described by an effective *granular temperature*. This was done, for instance, for the jamming phase diagram in Fig. 1.3. Molecular temperature is only properly defined in thermal equilibrium. Since driven granular systems dissipate energy, it is not clear whether granular temperature, defined as the mean kinetic energy per particle, is a useful quantity. Surprisingly, Rayleigh-Bénard convection in granular fluids shows a dependence on the granular temperature that is very similar to that seen in molecular liquids, as I will discuss below. The general question whether in driven granular materials the granular temperature is a meaningful analog of molecular temperature is especially important when describing granular gases and is one of the main subjects of the research in Chapters 2 and 3.

Convection rolls in granular fluids were first observed in the study of the so-called *Brazil-nut effect* [13]. When a container with mixed nuts is shaken, the largest nuts in the mix (which, apparently, is often the Brazil nut) tend to rise to the surface. Such size segregation occurs readily when granular materials are shaken. For

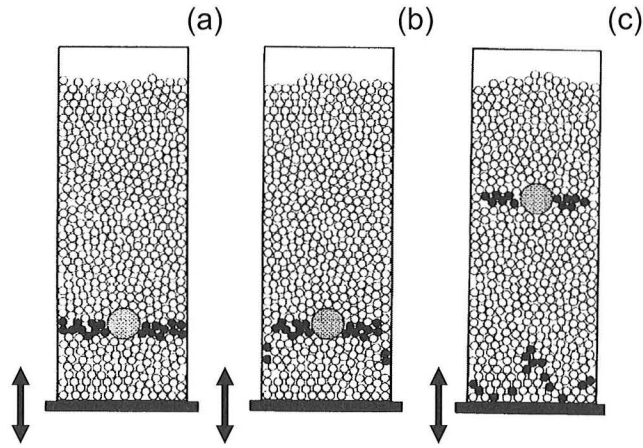


**Figure 1.4:** Schematic diagram of size segregation by convection rolls. (a) Initial configuration before tapping. A large bead is inserted in a container filled with smaller beads. The beads in the same layer as the large bead are colored to allow their motion to be followed. (b) After a few taps the colored beads at the wall have moved to the bottom. (c) After more taps, the colored beads in the center have moved to the surface, together with the large bead. At the same time, the color beads at the wall have moved further to the bottom. When at the bottom, the colored particles move inwards and start to rise again, tracing the outline of the convection roll. The real experiment is performed in a cylindrical container. The figure is adapted from Ref. [12].

instance, in the industrial processing of powders, shaking is often used to mix different types of powders. It has long been known that, counterintuitively, such shaking could actually lead to segregation depending on parameters like particle size and weight ratio. Originally, it was proposed that segregation occurs as a vibrated granular layer expands, allowing the smaller particles to fall under a large particle [14]. In a somewhat related way, it is speculated that large boulders can rise up through the soil in cold areas due to prolonged freeze-thaw cycles, sometimes leading to intricate spatial patterns [15].

Experiments, however, showed that this picture is at least incomplete [12]. When a cylinder filled with glass beads of a fixed size is subjected to a series of single vertical shakes, it was found that the beads in the center of the cylinder rise up, while those close to the wall move downwards. Beads reaching the bottom of the container move inwards and begin to move up in the central region of the tube. Beads that reach the surface move towards the wall and then descend towards the bottom. The resulting collective motion of the beads is very much like convection in a molecular fluid.



How this convective flow leads to size segregation is shown schematically in Fig. 1.4. In this figure a large bead is inserted at the bottom in the container and the trajectories of the large particle and the smaller beads that are initially in the same layer are followed as the system is shaken. Because of the convective motion, both the large particle and the smaller beads in its direct vicinity rise up and the beads closest to the outer wall move down. Crucially, the downwards movement of the beads is found to be restricted to a very narrow layer close to the outer wall, as is clear from Fig. 1.4(b). Size segregation now occurs because the large bead, once having risen to the surface with the smaller beads, is not able to follow the convective flow down the narrow outer region and remains trapped at the surface. More complicated behavior is also observed. For instance, in the *reverse Brazil-nut effect*, only large and heavy particles move to the surface, while equally large but light particles migrate to the bottom [16].

In the above experiments, convection is directly related to friction between the beads and the sidewalls, as the downward motions of beads near the boundaries is only observed to occur when the walls are rough. An obvious question is then whether granular convection is an artifact of friction with the boundary and only superficially similar to normal convection or whether the parallels run deeper. In molecular liquids, thermal convection occurs when a sufficiently large difference in temperature exists between the bottom and the top of the liquid. For small temperature differences, the liquid that is heated at the bottom experiences an upward force due to buoyancy. This force is balanced by the viscosity of the liquid, resisting upward motion, and by thermal diffusion, leveling the temperature gradient. In this case no convection occurs and all heat transport occurs by thermal conduction. Only for temperature differences higher than a critical value does convective motion set in. For large temperature gradients, the flow eventually becomes turbulent.

When a container with a granular material is shaken vigorously, particles acquire kinetic energy by collisions with the bottom. As these particles collide with other particles, some energy is dissipated due to friction between the particles. As a consequence, the average amount of kinetic energy per particle decreases towards the top surface. When, in analogy to molecular liquids, the mean kinetic energy per particle is seen as a temperature, this means that due to the dissipative collisions, a shaken granular liquid will develop a temperature gradient. This difference in granular temperature becomes larger if the amount of dissipation per collision is increased. It was shown that such a system indeed has a transition to a convective regime as the amount of dissipation is increased beyond a critical value [17]. Here, the system was enclosed in a container with elastic walls, so that any effect of friction with the walls is eliminated. Particles received a random kick when they hit the bottom of the box, simulating vibrations of the container. Examples of typical single



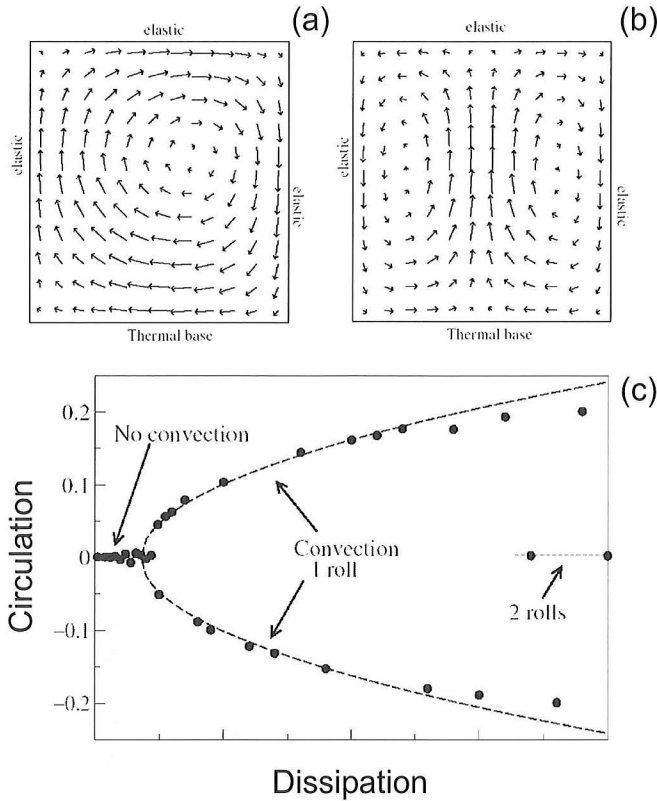


**Figure 1.5:** Thermal convection in a granular fluid driven at the bottom. (a) A single convection roll. Size and direction of the mean particle velocities are indicated by arrows. (b) A double convection roll. (c) The circulation in the container as a function of the amount of dissipation. For small dissipation, no circulation occurs. Above a critical amount of dissipation, convection sets in and circulation due to a single convection roll is apparent. For higher dissipation, double convection rolls are observed. The circulation grows as the square root of the amount of dissipation, indicated by the dashed lines. Figure adapted from Ref. [17].

and a double convection rolls are shown in Fig. 1.5(a) and (b).

The transition from the conductive to the convective regime can be quantified by measuring the amount of mass circulation around the center of the container. It is shown in Fig. 1.5(c) that for small dissipation, the system has no circulation as convection rolls are absent. Above a critical amount of dissipation, the circulation is either positive, corresponding to a clockwise convection roll, or negative,

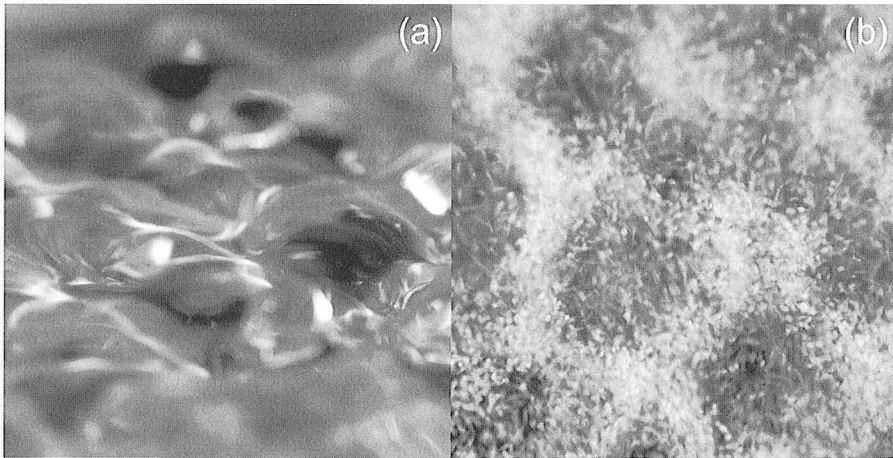


**Figure 1.6:** Faraday waves obtained by the author with a primitive setup that shakes a container in the vertical direction. (a) Faraday waves in water. The standing waves organize in a square pattern. (b) Faraday waves in ordinary sand. Also here a square pattern is visible. For sand, both square and hexagonal patterns are seen in the container. In both cases, the waves are viewed from the side at an inclined angle and shaking occurs at a frequency of around 100 Hz. Photographs by R. Koops.

corresponding to a counter-clockwise convection roll, depending on the initial conditions. For higher dissipation, it is also possible to find both a clockwise and a counter-clockwise convection roll in the container, leading to zero net circulation. Similar convection roles also occur with periodic boundaries in the horizontal direction, eliminating the role of sidewalls altogether. This indicates that there is indeed a fundamental link between granular convection and thermal convection in liquids and that the granular temperature plays a role similar to the molecular temperature in this system. For very large dissipation, however, the system does not become turbulent but separates into a dense layer floating on a dilute gas-like layer. This is a granular analog of the Leidenfrost effect, where water droplets float on their own vapor if water is poured on a hot surface.

In 1831, Faraday reported that when a fluid layer is oscillated in the vertical direction, in his case by drawing a violin bow down the side of square plate covered by various liquids, the liquid surface develops a pattern of standing waves, nowadays called *Faraday waves* [18]. In general, when a liquid is vibrated in an open container with a frequency  $f$  and amplitude  $A$ , the surface will remain flat when the amplitude stays below a critical value  $A_C$ . If the amplitude is increased beyond this value,

the flat surface becomes unstable and a pattern of standing waves will appear. An example of such a pattern is shown in Fig. 1.6(a). For simple fluids, the standing waves usually show a square pattern. For more viscous fluids or fluids that are driven in a more complicated way these patterns can consist of lines, hexagons or even quasiperiodic structures. The form of these patterns do not depend on the shape of the container. Most often, Faraday waves oscillate with frequency  $f/2$ , half the frequency of the driving cycle, so that hills in one driving cycle become valleys in the next.

Surprisingly, a vertically shaken layer of small grains shows patterns similar to Faraday waves, as can be seen in Fig. 1.6(b) and Fig. 1.7. This similarity is all the more remarkable when one realizes that the underlying mechanism is very different in the two cases. For molecular liquids, Faraday waves are a surface effect and can be described in terms of interacting non-linear waves. The granular system, on the other hand, consists of individual grains that can be found quite far above the bulk of the layer, making it impossible to define a proper surface. This also means that in the granular fluid surface tension is absent, whereas in the molecular liquid it needs to be taken into account. Also, for molecular liquids all the dynamics is restricted to the surface alone and the liquid layer stays in contact with the container throughout the driving cycle. In contrast, in granular fluids the Faraday instability only occurs when the entire layer loses contact and later collides with the container, as I will explain now.

As the driving frequency and amplitude are varied, the system shows a rich variety of different standing wave patterns [19]. Some, such as square patterns, striped patterns (shown in Fig. 1.7(a)) or hexagonal patterns (shown in Fig. 1.7(b)) are similar to the  $f/2$  patterns observed in molecular liquids. Other patterns are not easily found in normal liquids, like kinks, where the layer shows no surface pattern but one part of the container oscillates at the opposite phase of the other part. For larger amplitude there are several patterns that oscillate at a frequency  $f/4$ , a quarter of the driving frequency, and ultimately the system enters a disordered state (shown in Fig. 1.7(c)).

The occurrence of these patterns can be explained in a quantitative way by a wonderfully simple model [19]. In this model, the entire layer is treated as a single particle on top of an oscillating plate. Because of the many inelastic collisions within the layer, one assumes that collisions between layer and the plate are completely inelastic, meaning all kinetic energy of the layer is dissipated at the instant that it hits the plate. On the other hand, the layer will lose contact with the plate when the plate is above its equilibrium position and moving with an acceleration larger than  $g$ , the acceleration due to gravity.

When we keep the driving frequency  $f$  fixed, but increase the amplitude  $A$  slowly,

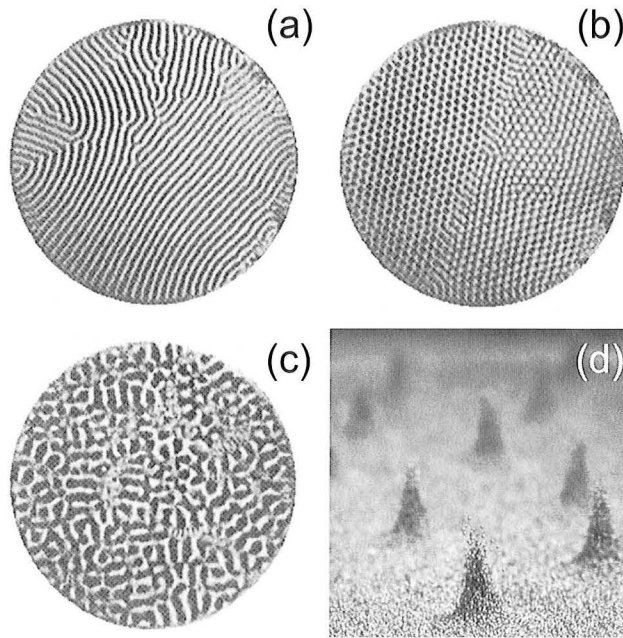


**Figure 1.7:** Faraday waves in a layer of 0.15-0.18 mm bronze spheres. The layer is shaken in the vertical direction with a frequency of  $f = 67$  Hz. Typical patterns are shown for increasing amplitude  $A$ . (a)  $f/2$  stripes. (b)  $f/2$  hexagons. (c) disordered pattern. The system is viewed from above and illuminated in such a way that particles at the top appear bright while particles at the bottom appear dark. (d) For some values of  $f$  and  $A$  oscillons appear, localized excitations that behave as independent ‘particles’. Here, the system is viewed from the side. Figures are adapted from Refs. [19] and [20].

initially the layer will never detach from the plate. When the amplitude is increased beyond a critical value, the layer will detach from the plate for a part of the driving cycle. As the amplitude is increased further, something surprising occurs: the oscillation undergoes period-doubling. The layer is no longer detached for a fixed time for each driving cycle, but alternates between a short time and a long time. This happens because now the layer not only collides with the plate when it is below the equilibrium position and moving up, but also briefly when it is above the equilibrium position and moving down. Up to this amplitude, the layer in the experiment remains flat and one can recognize whether the system is in the period-doubled state by hearing the peculiar rattling of the layer against the plate.

When the amplitude is increased even further, there is a transition back to a

state with only a single period, but now the layer is detached from the plate for more than one driving cycle, leading to an oscillation with frequency  $f/2$ . When this happens, it is in principle possible for parts of the layer to oscillate at a different phase with respect to each other. Even though initially the system will oscillate as a single layer, parts of the layer will move out of phase due to the random nature of the collisions of the grains. When this occurs, the layer organizes in squares or lines. If the amplitude is increased more, the layer continues to oscillate with a frequency  $f/2$ , but undergoes again a period doubling-bifurcation similar to the one above. In this case, a hexagonal pattern develops. In comparison, molecular fluids develop hexagonal patterns of Faraday waves when forced with two, slightly different frequencies. In a similar fashion, the simple one-particle model can also quantitatively explain for what frequency and amplitude kinks and  $f/4$  patterns occur.

A spectacular phenomenon observed at the boundary between the flat layer and the Faraday waves are *oscillons*, stable localized excitations that are peaks at one driving cycle and craters at the next [20]. Several oscillons are visible as peaks in Fig. 1.7(d). These excitations do not arise spontaneously, but appear when the surface layer is perturbed or as remnants of a standing wave pattern. Oscillons are reminiscent of *solitons*, which are stable localized solutions to non-linear equations that retain their shape and size upon interaction with each other. Interestingly, solitons are almost never found in dissipative systems, whereas oscillons are a direct consequence of the dissipative collisions between individual grains. Very similar excitations are found in highly dissipative molecular liquids, most notably in colloidal suspensions [21].

As an amusing aside, soliton-like structures also occur elsewhere in granular materials, in a way that Bagnold would certainly have enjoyed. Many dune fields consist of Barchan sand dunes: dunes that consist of a gentle rise leading to a steep, crescent shaped slope. Barchan sand dunes can be seen in Fig. 1.1(b). When the direction of the wind is constant, these dunes retain their shape and move in the downwind direction with speeds between 5-50 meter per year. Small dunes move much faster than large dunes. This difference between dunes of different size was apparently known to Saharan people [22]. They would use dunes as a storage space for valuables, burying the goods at the front side and retrieving them after a while at the back end. Depending on the size of the dune, goods could be stored this way for any period between 5 months and 25 years, depending on the dune size. Recently, model calculations have shown that Barchan dunes might behave like solitons [23]: in the model, small fast-moving Barchans can pass through larger slow-moving ones, while retaining their shape in the process. Due to the slow movement of dunes it is difficult to measure this behavior directly. However, small Barchans are often

observed at the downwind side of large ones, suggesting that small Barchans can overtake larger ones in one way or another.

The strong parallels between the behavior of granular liquids and molecular liquids can sometimes be unexpected and quite striking. For instance, when I was working in the group of Prof. Harry Swinney on the research presented in Chapter 3, others were testing a setup that consisted of a two-dimensional packing of cylinders confined between glass plates. In order to create a very loose packing of the cylinders, a strong air current was injected at the bottom of the layer. Such *fluidized beds* are often used in industry for the processing of powders and show immensely complicated behavior. The air doesn't rise up uniformly through the layer of cylinders but in large air bubbles, that are much larger than the diameter of the particles. As a consequence, fluidized beds give the impression of a 'boiling' granular liquid. These bubbles arise even though granular fluids have no surface tension.

Normally, bubbles form irregularly throughout the bottom layer. However, when a large cylinder was inserted at the bottom, the bubbles appeared in a very regular fashion at the surface of the large cylinder, perhaps because its presence disrupts the packing of surrounding small cylinders. Overall, the resulting bubbles look surprisingly similar to those rising up in a glass of beer. There exist many more examples of such unexpected similarities between the granular and molecular liquids than I have room here to discuss. At the same time, a universal hydrodynamic theory underlying the behavior of granular fluids is still lacking and, consequently, a separate explanation has to be formulated for each individual case. This makes the study of the fundamental properties of granular liquids very interesting for physicists.

## 1.5 Granular gases

Dilute granular liquids are often called *granular gases*. Whereas in dense granular liquids, grains can rub against or rest on one another, leading to such complicated behavior as jamming, for granular gases most interactions occur through collisions only. Because of this and because the mean free path of the grains in the gas is much longer than in the dense liquid, granular gases are relatively simple. This makes granular gases the ideal system to study another fundamental question, namely to what extent the behavior of granular materials can be correctly modeled by the tools of equilibrium statistical physics that are so successful in describing molecular matter.

For molecular matter in thermal equilibrium the dynamics of a system is completely determined by its Hamiltonian and its temperature  $T$ . Specifically, the prob-

ability to find the system in a state  $s$  is proportional to:

$$P_s \sim e^{-E_s/k_B T}, \quad (1.2)$$

where  $E_s$  is the energy of the system in state  $s$  [24]. For dilute molecular gases, the Hamiltonian is often simple enough to use Eq. 1.2 directly, without many approximations. A different approach to understand the behavior of molecular gases is by *kinetic theory* [24]. Here, one studies analytically the behavior of large assemblies of particles as they interact with each other by collisions.

An example of a granular gas is shown in Fig. 3.2, where a layer of small metal beads is constrained between two vertical plates and shaken in the vertical direction. It is tempting to think of the grains in the granular gas as similar to molecules in a normal gas. In particular, one could interpret the random spread in velocity of the grains as something like a temperature and define, in analogy to molecular gases, a *granular temperature*  $\sigma^2$  as:

$$\sigma^2 = \langle v^2 \rangle - \langle v \rangle^2, \quad (1.3)$$

where all particles in the gas have unit mass,  $v$  is the velocity of the particles and the brackets indicate an ensemble average over all particles. One major difference, however, between molecular and granular gases is that the latter are dissipative; because the grains in the granular gas are macroscopic particles, they dissipate kinetic energy upon collision. The importance of this can be easily seen from the following example. When a single macroscopic particle, such as a single M&M, is dropped on a table it will bounce around several times before finally coming to rest. A bag of M&Ms, on the other hand, will not bounce on a table like a single M&M but will instead directly come to rest. This is due to the inelastic collisions between the M&Ms in the bag, dissipating all the kinetic energy in a very short time upon collision with the table <sup>1</sup>.

As a consequence of these inelastic collisions, a granular gas will quickly come to rest when left alone. In order to keep the grains in motion energy has to be supplied to the system by some kind of external driving. This means that a granular gas is a system that is *far from equilibrium* and it is not clear in advance whether the tools from equilibrium statistical mechanics can be applied in such a case. Far-from-equilibrium systems in general are poorly understood and by trying to understand granular gases we will perhaps learn things that can be applied to the general case.

<sup>1</sup>The importance of M&Ms in the science of granular materials should not be underestimated. Apart from great demonstration material as described above, research on M&Ms first showed that random close packing occurs at a density dramatically higher for ellipsoids than for spheres [25]. In fact, the random close packing density  $\phi = 0.64$  obtained for spheres appears to be an lower limit. For M&Ms a density of  $\phi = 0.68$  is reported.



Below, I will give a brief overview of the research performed in recent years on granular gases. First, I will discuss the dynamics of freely cooling gases, where the dynamics is governed only by the dissipative collisions. Then, I will discuss driven gases, where energy is supplied to keep the gas in steady state. In all cases, large deviations from the behavior of molecular gases are found, due to the absence of equipartition and the occurrence of spontaneous clustering. Sometimes, however, granular gases unexpectedly behave like a gas in thermal equilibrium, for instance obeying the fluctuation-dissipation theorem as described below. Finally, I will briefly introduce my work on velocity distributions in granular gases. A more thorough introduction, however, will be postponed until Chapter 2.

When grains in a granular gas collide, they dissipate kinetic energy. Inelastic collisions are usually modeled by a coefficient of restitution  $\eta$  in the following way; if two particles  $i$  and  $j$  with one-dimensional velocities  $v_i$  and  $v_j$  collide, their velocities change as:

$$v'_i = \frac{1 - \eta}{2}v_i + \frac{1 + \eta}{2}v_j, \quad (1.4)$$

$$v'_j = \frac{1 + \eta}{2}v_i + \frac{1 - \eta}{2}v_j. \quad (1.5)$$

In such a collision, momentum is conserved but energy is not. For  $\eta = 1$ , the collision is elastic and Eqs. 1.4 and 1.5 reduce to the collision rules for elastic collisions. For  $\eta = 0$ , the collisions are completely inelastic and all relative velocity between the particles is dissipated. Steel particles, for instance, have  $\eta \approx 0.9$ .

When a large number of grains is distributed uniformly over a container and when they are given some random initial velocity, the particles will lose energy by collisions and, consequently, the gas will cool, as quantified by a decreasing granular temperature. Such a *freely cooling gas* does not remain uniform like a molecular gas, but instead forms dense clusters of particles [26, 27]. Examples of such clusters are shown in Fig. 1.8. The velocity of the particles in the clusters is very small – they have almost zero granular temperature.

Inelastic collisions cause cluster formation in the following way: when in a small region of the container the density increases because of random fluctuations, the number of collisions increases. As the number of collisions increases, more energy is dissipated, leading to a lower local granular temperature. As a consequence, the particles in that region will move less than in the surrounding area, meaning that effectively the local pressure is lower than the surrounding pressure. This in turn will lead to a further influx of particles, increasing the density even more. Cluster formation occurs more readily when the collisions between particles become more



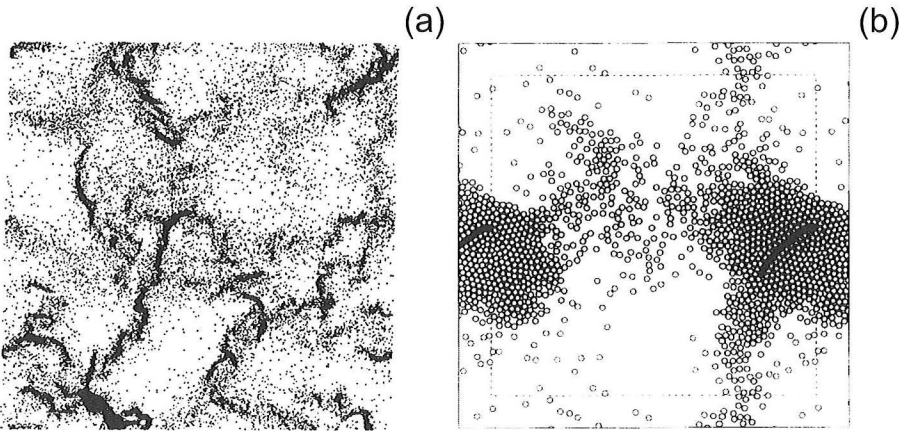


**Figure 1.8:** Clusters in freely cooling granular gases. (a) The positions of 40000 particles after each particle experienced 500 collisions on average. The particles are organized in string-like clusters that have very low granular temperature. The coefficient of restitution is  $\eta = 0.6$ . For nearly elastic collisions no clusters form. Figure taken from Ref. [26]. (b) The positions of 1024 particles as inelastic collapse occurs. The line of particles indicated in black experience a rapidly increasing number of collisions among each other and are in the process of inelastic collapse. Figure taken from Ref. [27].

inelastic. As the resulting string-like clusters show structures that are surprisingly similar to those of the distribution of galaxies in the universe, it has even been suggested that the evolution of the universe might have parallels to that of a freely cooling granular gas [3].

Simulations of cluster formation often show *inelastic collapse*, where small numbers of particles collide infinitely often within a finite time, dissipating all their relative velocity in the process [27]. In Fig. 1.8(b), a line of particles that are about to undergo inelastic collapse is indicated. Such singular behavior is similar to that of a particle bouncing on a table. Every time the particle collides with the table, it loses a fraction of its velocity due to dissipation. As a consequence, it will take less time for the particle before it bounces on the table again. This leads to a sequence of faster and faster collisions, until after a finite time the particle comes to rest on the surface on the table. In this example, the particle is attracted towards the table by gravity, but in cooling granular gases inelastic collapse happens solely due to the dynamics of the particles. Surprisingly, it has been shown that inelastic collapse does not require a large cluster of particles to occur. Rather, in two-dimensions a minimum of three particles can be sufficient [28].

It has been argued that inelastic collapse is an artifact of the assumption that par-

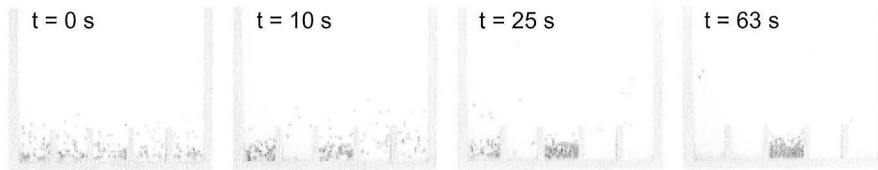


**Figure 1.9:** Clustering in a gas of 195 steel beads of radius 1.5 mm. At  $t = 0$  the beads are uniformly distributed over five compartments. The container is shaken at 21 Hz and with an amplitude of 3.0 mm and the particles quickly collect themselves in one of the five containers. In the less dense containers particles on average have more kinetic energy, which can be seen from the fact that they jump higher. The pictures are taken from Ref. [33].

ticles are perfect hard spheres. More realistic models of inelastic collisions assume that collisions occurring in rapid succession are completely elastic [29] or assume that the coefficient of restitution is velocity dependent [30], approaching  $\eta = 1$  for very small velocities. In a replication of the experiment described above, it has been shown that for a steel ball bouncing on a plate, the coefficient of restitution indeed behaves in such a way, but with a very large spread in  $\eta$  [31]. When using such collision models, the process of inelastic collapse ceases to be singular, but nevertheless still shows lines of particles colliding very often, dissipating almost all of their relative velocity in a short time.

Clustering also occurs in driven granular gases, where energy dissipation in collisions is compensated by some form of energy injection. For instance, cluster formation was observed in a simulation of a one-dimensional granular gas confined between an elastic boundary and a driving boundary [32]. When a particle collides with the driving boundary, its velocity is replaced with one drawn from a Gaussian distribution, compensating for the loss of kinetic energy due to the inelastic collisions within the gas. Instead of evolving towards a spatially homogeneous state, the majority of the particles collapse into a dense, slow moving cluster close to the elastic wall while a few particles travel between the driving wall and the cluster at much higher velocities. This occurs even for nearly elastic particles with  $\eta = 0.95$ .

An experiment showing a striking example of cluster formation in a driven granular gas is shown in Fig. 1.9 [34]. Here, a container is subdivided into smaller compartments by walls and metal beads are initially distributed homogeneously over the compartments. Surprisingly, as the container is vibrated all the beads will cluster in one of the compartments. Such cluster formation is similar to that in freely cooling gases, as described above. If, by a fluctuation, one of the compartments has a slightly higher density the mean kinetic energy of the particles will be lower.

As a consequence, particles in the dense compartment are much less likely to have enough velocity to jump over the wall into another compartment. This results in an influx of particles from neighboring compartments, which amplifies the effect further.

Even when evident clustering does not take place in a granular gas, more subtle effects might still be observed. For instance, an ideal gas is spatially featureless. This can be quantified by measuring the pair correlation function  $g(r)$ , the density of particles at a distance  $r$  from a randomly selected particle, which for a ideal gas of non-interacting particles is constant. However, in a simulation where inelastic particles are heated uniformly by continuously adding a random amount of velocity to all of the particles, it is found that  $g(r)$  is peaked for  $r$  close to the particle radius [35]. This means that particles are on average closer to each other than in the case of an ideal gas. This happens because the relative velocity between particles is reduced in inelastic collisions. Similarly, experiments on particles rolling on an inclined surface, show that velocities of particles are highly correlated, with closer particles having much more aligned velocities than in an ideal gas [36]. In both cases, the correlations occur over distances of many particle diameters.

The above results might suggest that granular gases are very different from molecular gases and that insights gained from equilibrium statistical physics cannot be directly applied to granular gases. Unexpectedly, however, a recent experiment showed that this seems not the case for the fluctuation-dissipation theorem [37]. The fluctuation-dissipation theorem is one of the major results of modern statistical physics and relates the spontaneous fluctuations around thermal equilibrium to the response of this system when it is perturbed slightly away from equilibrium.

If, for instance, a torsion oscillator is immersed in a molecular gas at some temperature  $T$ , the torsion oscillator will feel a small random torque, due to collisions between the molecules in the gas and the torsion oscillator. By measuring the fluctuations in the angular deflection  $\theta(t)$  of the torsion oscillator, one can construct the power spectrum  $S(\omega)$  of the fluctuations. At the same time, the torsion oscillator can be forced to rotate by applying some kind of oscillatory torque  $C(\omega)$ . If the amplitude of the oscillation is small enough, the system will respond in a linear way like  $\theta(\omega) = \chi(\omega)C(\omega)$ . The susceptibility  $\chi(\omega)$  then depends on some kind of friction parameter, in this case the viscosity  $\alpha$  of the surrounding gas. The fluctuation-dissipation theorem now relates the fluctuations  $S(\omega)$  to the response  $\chi(\omega)$  as  $4k_B T \chi''(\omega) = \omega S(\omega)$ , where  $\chi''(\omega)$  is the loss modulus of the response function  $\chi(\omega) = \chi'(\omega) - i\chi''(\omega)$ . As the only external parameters in this equation are the temperature  $T$  and the viscosity  $\alpha$ , this result means that macroscopic properties such as viscosity are completely determined by microscopic fluctuations, quantified only by the temperature  $T$ .

One can perform a similar experiment in a granular gas of glass beads rather than a molecular gas [37]. In this case, the particles are driven by shaking the container by a white noise with frequencies between 300-900 Hz and with an average amplitude  $A$ . A torsion oscillator, consisting of a cone with a layer of beads glued to its surface, is inserted in the gas and will rotate randomly due to collisions with the beads in the gas. An external torque can also be applied to the cone and the response of the gas to this rotation can be measured just like in the case of a molecular gas. Surprisingly, for large enough amplitude  $A$  the power spectrum and the response obey the fluctuation-dissipation very well, even though the granular gas is far from thermal equilibrium. In contrast, for colloidal suspensions or glasses there is often much less agreement. This result suggests that the granular gas has a well-defined granular temperature  $T$  and viscosity  $\alpha$ . The viscosity is found to be inversely proportional to the shaking amplitude  $A$ : the granular gas flows more easily when the shaking is more vigorous.

Does this mean that granular temperature as a quantity is as well defined as molecular temperature? This is still an open question. On the one hand, simulations have shown that the temperature obtained from the fluctuation-dissipation relation agrees with that by measuring the mean kinetic energy in the gas according to Eq. 1.3, a first requirement for the granular temperature to be a useful quantity [38]. On the other hand, it was shown by experiment that in binary mixtures of different types of grains, both species have a different granular temperature [39]. Interestingly, it was shown in a simulation that even though the temperatures are different, a fluctuation-dissipation relation holds for each species separately [40].

The work presented in this part of my thesis is related to the above questions. We studied both by simulation and experiment the velocity distribution  $P(v)$  of the particles in a granular gas. For a molecular gas, the velocity distribution of the particles is given by the well-known Maxwell-Boltzmann distribution [24]. In contrast, in a granular gas the velocity distribution is not a Gaussian but often rather a *stretched-Gaussian* distribution of the form:

$$P_\alpha(v) = A \exp(-B |v/\sigma|^\alpha), \quad (1.6)$$

where  $A$ ,  $B$  and  $\alpha$  are fitting parameters and  $\sigma^2$  is the granular temperature as defined in Eq. 1.3. In molecular gases, the velocity distribution has an exponent  $\alpha = 2$ . In experiments where monolayers of metal beads are confined between vertical walls and shaken in the vertical direction, an universal velocity distribution with  $\alpha = 1.5$  was found that was insensitive to the details of the driving mechanism [41]. However, different experimental setups often find other exponents. A few

important questions have remained unanswered. First, is there a universal velocity distribution for granular gases? If so, what is its precise functional form? If not, how does it change as function of external parameters such as the amount of dissipation or the precise way of driving the system? Finally, why is the velocity distribution in granular gases non-Gaussian in the first place?

In Chapter 2, we study these questions by simulation. We find no evidence for a universal velocity distribution for granular gases, as was proposed by Ref. [41]. Instead, we observe a family of distributions as we change parameters such as number of particles, density, inelasticity and the mechanism of heating. Surprisingly, we can describe all these distributions by just two parameters, the coefficient of restitution  $\eta$  and a new parameter  $q$ , that indicates how often particles collide and dissipate energy in comparison to how often they get heated by the driving mechanism. The parameter  $q$  depends sensitively on the details of the experimental setup and we propose that it is the variation in this parameter that can explain the different velocity distributions obtained in recent experiments.

In Chapter 3, I present results on experiments performed on granular gases in the Center for Nonlinear Dynamics at the University of Texas in Austin. We measure the dynamics of individual beads in an experimental setup often used to characterize the velocity distribution in granular gases. Our setup allows us to measure the density, the granular temperature and the velocity distribution as a function of the position in the box and the phase of the driving cycle. We find no evidence that non-Gaussian velocity distributions arise by averaging over regions with different density or granular temperature, as was suggested in Ref. [42]. Instead, we see that the velocity distribution is remarkably insensitive to such variations. Importantly, we find that the velocity distribution is not determined by the intrinsic dynamics of the gas, but rather by friction between the beads and the sidewalls. This means that previous experimental results obtained by several other groups will have to be reconsidered.



---

## **Chapter 2**

# **Velocity distributions: simulations**

J.S. van Zon and F.C. MacKintosh,  
*Phys. Rev. Lett.* 93, 038001 (2004)

J.S. van Zon and F.C. MacKintosh  
*Phys. Rev. E* 72, 051301 (2005)

## 2.1 Introduction

Dilute granular systems, or *granular gases*, have been extensively studied both experimentally and theoretically, in large part as simple model systems exhibiting non-equilibrium and dissipative behavior. These systems are intrinsically dissipative and out of equilibrium. Since the collisions in such a gas are inelastic, a gas-like state is achieved only with a constant *drive*, or input of energy. Otherwise, all motion ceases after only a finite time [32, 43]. If the system is driven, then the gas reaches a steady state in which the energy dissipated in the inelastic collisions is balanced by the energy injected in to the gas by the driving mechanism.

In experiments, one usually drives a granular gas by shaking or vibrating the walls of the container [36, 41, 44–50]. The most common experimental setups are shown schematically in Fig. 2.1. This type of heating is often referred to as *boundary heating*. Because energy is inserted into the system in a spatially inhomogeneous way, granular gas often develop gradients in density and mean kinetic energy. I will discuss this below in more detail. Because these gradients complicate the analysis of the dynamics of granular gases, it is useful to drive the gas in a spatially homogeneous way. Often, this is implemented by subjecting each particle individually to a stochastic driving force. This type of heating is referred to as *uniform heating* [35] and is used in simulations [42, 51–53] and analytical theory [54, 55]. In this case, the dynamics of individual particles in the absence of collisions is given by the following stochastic equation of motion:

$$\frac{d^2 \mathbf{x}_i}{dt^2} = \boldsymbol{\xi}_i(t), \quad (2.1)$$

where the particle has unit mass,  $\mathbf{x}_i$  is the position of particle  $i$  and  $\boldsymbol{\xi}_i(t)$  is a random acceleration due to stochastic forcing. The stochastic forcing is often assumed to be *white noise forcing* and uncorrelated for different particles  $i$  and  $j$ , so that:

$$\langle \xi_{i\alpha}(t) \rangle = 0, \quad (2.2)$$

$$\langle \xi_{i\alpha}(t) \xi_{j\beta}(t') \rangle = \xi_0^2 \delta_{ij} \delta_{\alpha\beta} \delta(t - t'), \quad (2.3)$$

where  $\alpha$  and  $\beta$  label the different components of the forcing and  $\xi_0$  is the strength



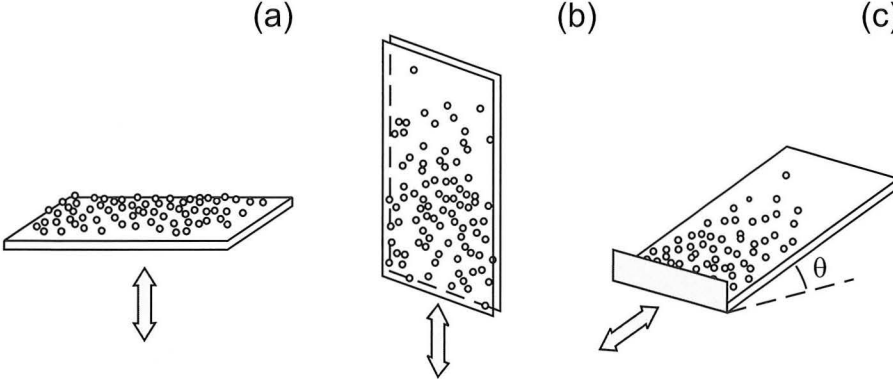


**Figure 2.1:** Different experimental setups for studying two-dimensional granular gases. (a) Particles driven by vertical vibration of a horizontal plate [46–50]. For low shaking amplitude, particles cannot hop over one another and the motion is effectively two-dimensional. (b) Particles confined to move between two vertical walls and vibrated in the vertical direction [41]. The gap between the walls is slightly bigger than a particle diameter, so that the gas is two-dimensional. (c) Particles rolling on an inclined slope, tilted by an angle  $\theta$  [36, 44, 45]. Driving occurs through a vibrating wall at the bottom (indicated in gray).

of the forcing. For uniform heating, the system reaches a steady state where the energy dissipated in inelastic collisions is balanced by energy injected by the stochastic forcing. Uniform heating is assumed to give a good description of granular gases far away from the driving boundaries and when the gradients are small on the scale of the mean free path of the particles.

One of the most fundamental aspects of molecular gases is the Maxwell-Boltzmann velocity distribution [24]. A very general and striking feature of driven dissipative gases, however, is the apparently strong deviation from this classical behavior. Often, in granular gases the velocity distribution is a *stretched Gaussian* of the form:

$$P(v) = A \exp(-B |v/\sigma|^\alpha), \quad (2.4)$$

where  $A$  and  $B$  are fitting parameters and  $\sigma^2 = \langle v^2 \rangle$  is often called the *granular temperature*, in analogy with equilibrium gases. For classical elastic gases, the velocity distribution is a Gaussian distribution with exponent  $\alpha = 2$ . For granular gases, however, a wide variety of distributions is found, from Gaussian with  $\alpha = 2$  [49, 50] to exponential with  $\alpha = 1$  [42, 46, 55]. Often, an intermediate distribution with exponent  $\alpha = 3/2$  is found [41, 53, 54, 56]. In some cases, the exponent is found to vary between  $1 < \alpha < 2$  as one changes parameters such as shaking amplitude [48] or number of particles [57]. In many cases, it is found that the velocity distribution

cannot be described by a single exponent  $\alpha$  for all velocities, but instead shows two distinct regimes as a function of  $v$ , each with a distinct exponent  $\alpha$ , for the same external parameters, such as  $\eta$ ,  $\phi$  and  $N$ . In such case, a *crossover* from one exponent  $\alpha \approx 2$  for small velocities to an exponent  $1 < \alpha < 2$  for high velocities is often observed [36, 45, 47, 51, 52, 58–60]. The nature of these crossovers often depends strongly on experimental parameters.

This multitude of velocity distributions observed for granular gases raises several fundamental questions. First, is there a universal velocity distribution for granular gases, just like the Maxwell-Boltzmann velocity distribution for molecular gases? And if so, what is the exact shape of the distribution? Second, why is such a variety of velocity distributions observed, both in experiment and in simulation and analytical theory? Finally, why do the velocity distributions observed in granular gases deviate strongly from Gaussian distributions in the first place? Before formulating possible answers to these questions, I will first briefly discuss the recent literature.

Olafsen and Urbach studied the velocity distributions of a monolayer of steel balls on a vertically shaken horizontal plate, indicated schematically in Fig. 2.1(a) [46, 48–50]. When the shaking amplitude is small enough, the particles cannot jump over one another and the motion is effectively two-dimensional. The energy injected into the vertical direction by the plate is converted into horizontal motion by collisions with other particles. Also, rotational motion is converted in horizontal motion by friction between the particles and the plate. Because the energy injection occurs in a spatially homogeneous way, no large scale density gradients occur. However, in this experiment the energy injection is not stochastic forcing as defined in Eq. 2.1. Because all the particles are vibrated by the same plate, the forcing is highly correlated between different particle. The motion of the particles in the horizontal plane is measured for different shaking amplitudes and shaking frequencies.

For low shaking amplitude, the velocity distribution  $P(v)$  for the two horizontal components is found to be exponential with  $\alpha = 1$ , insensitive to variation of other parameters and the exact mechanism of shaking [46]. When the velocities are scaled by  $\sigma$ , where  $\sigma^2$  is the granular temperature, all velocity distributions collapse on the same curve. This feature is reminiscent of the behavior of molecular temperature in classical gases and is often observed for granular gases. However, as the shaking amplitude is increased the velocity distributions become Gaussian with  $\alpha = 2$  [48]. For such high amplitudes, the particles are able to jump over one another and the gas ceases to be two-dimensional. If a lid is placed on top of the gas, so that the motion of the particles is forced to remain two-dimensional even for high amplitudes, the resulting velocity distribution has an exponent  $\alpha = 1.5$ . That the exact mechanism of driving is important in determining the shape of the velocity distribution is shown

when the experiment is repeated for a rough plate, by glueing particles to its surface [49]. Now, collisions with the plate inject energy directly in the horizontal direction, as the particles collide with the balls glued to the horizontal plate. In this case, the velocity distribution is Gaussian for a wide range of shaking amplitudes. Similar behavior is also seen when a layer of light particles is placed on top of a horizontal monolayer of heavy particles and again shaken in the vertical direction [50]. In this case, the top layer of light particles have a Gaussian velocity distribution even though the bottom layer shows non-Gaussian behavior. In a similar experiment on a horizontal monolayer of particles, Losert *et al.* found a horizontal velocity distribution with exponent  $\alpha = 1.5$  for high shaking amplitudes, in the absence of a lid [47].

A related type of experiment was performed by Aranson and Olafsen with electrostatically driven granular gases [56]. Here, large number of very small bronze beads is driven by an alternating electrical field between two capacitor plates. If the frequency of the alternating field is large enough, the particles form a two-dimensional horizontal layer suspended between the two plates. Energy is converted from the vertical direction to the horizontal direction by collisions between particles. In this case, the velocity distribution has an exponent  $\alpha = 1.5$  for a range of frequencies.

Rouyer and Menon studied the velocity distributions of a vertical monolayer of particles, confined to move in the vertical plane and shaken in the vertical direction [41]. Their setup is indicated schematically in Fig. 2.1(b). The system is vibrated at high frequency and amplitude, so that particles gain energy by collisions with both the top and the bottom of the container. As a consequence, the density distribution of particles as function of the height is approximately symmetrical with a maximum in the middle of the container. Due to the collisions occurring at the driving boundaries, the density of the gas varies strongly at the top and bottom of the container, both in space and as a function of the phase of the driving cycle. In the center of the container, however, the density is stationary and homogeneous in space. The dynamics of the granular gas are measured in this region, so that the results are not distorted by averaging over dynamics that varies in time and space. In this region, the velocity distribution  $P(v_z)$  of the vertical velocity  $v_z$  is asymmetrical due to gravity. The horizontal velocity distribution  $P(v_x)$  is symmetrical and has a universal exponent  $\alpha = 1.5$  over a wide range of shaking frequencies and amplitudes and within the stationary regions is independent of position in the container or the phase of the driving cycle.

A velocity distribution with exponent  $\alpha = 3/2$  is found often in granular gases and has a special significance because it is predicted by kinetic theories of granular gases [54]. This exponent is found for the asymptotic high-velocity tail of the

velocity distribution by solving the Boltzmann equation for the velocity distribution function  $f(\mathbf{v}, t)$ :

$$\frac{\partial}{\partial t} f(\mathbf{v}, t) = I(f, f) + \frac{\xi_0^2}{2} \left( \frac{\partial}{\partial \mathbf{v}} \right)^2 f(\mathbf{v}, t). \quad (2.5)$$

Here,  $I(f, f)$  is the collision integral and describes the time evolution due to the inelastic collisions. The last term is similar to a diffusion term in the velocity and describes the spreading of the velocity due to uniform heating. In steady state, Eq. 2.5 predicts a high-velocity tail of the form in Eq. 2.4 but with prefactor  $\beta = (1 - \eta^2)^{-1/2}$ , where  $\eta$  is the coefficient of restitution, and  $\alpha = 3/2$ . However, because of the dependence on the coefficient of restitution, this function cannot describe the entire velocity distribution but only the asymptotic high-velocity tail. The universal distribution of exponent  $\alpha = 1.5$  in the experiment of Rouyer and Menon, on the other hand, is observed over the entire range of velocities. In addition, with a simplified version of the Boltzmann equation, called the inelastic Maxwell model, a different exponent  $\alpha = 1$  was obtained for a uniformly heated gas.

Blair and Kudrolli studied the velocity distributions of particles rolling on an inclined plane, indicated schematically in Fig. 2.1(c) [36, 45]. The particles are driven by an oscillating wall at the lower boundary. When two rolling particles collide, they slide a short distance until their rotational motion has adapted to the new direction of the translational velocity. As sliding friction is much stronger than rolling friction, rolling particles dissipate more energy in collisions. This is reflected in the observed coefficient of restitution, which is  $\eta \approx 0.5$  for particles rolling on the inclined plane rather than  $\eta = 0.93$  for steel particles in the other setups. This makes it possible to study the velocity distribution outside of the range  $\eta \approx 1$ .

It is found that in this case the velocity distribution  $P(v_x)$  of the velocity perpendicular to the motion of the oscillating wall cannot be described by a single exponent  $\alpha$  for the entire range of velocities [45]. Instead, the velocity distribution shows a crossover from a Gaussian distribution with  $\alpha = 2$  for low velocities to a non-Gaussian distribution with  $1 < \alpha < 2$ , independent of the driving frequency. The velocity distribution is most strongly non-Gaussian for a slight tilt angle  $\theta = 0.1$ . As the tilt angle is increased to  $\theta = 6.7$ , the crossover disappears and the velocity distribution becomes close to a Gaussian over the entire range of velocities. For large tilt angles, the particles experience a large acceleration due to gravity and thus return to the driving wall more rapidly, effectively increasing the heating rate. The shape of the distribution is also observed to depend on the number of particles [36]. For a large number of particles  $N = 1000$  the velocity distribution is strongly-non Gaussian and shows a crossover in the exponent  $\alpha$ . If the number of particles is decreased, however, the crossover becomes weaker and eventually disappears in the

dilute limit  $N = 100$ , where the velocity distribution is well fitted by an exponent  $\alpha = 1.5$  for the entire velocity range. The crossovers in the velocity distribution observed here are also seen in simulations, but not necessarily at low coefficient of restitution [51, 52, 57, 59, 60].

Several suggestions have been put forward to explain the non-Gaussian features of the velocity distribution and the variety of velocity distributions observed in experiments, analytical theory and simulations. Puglisi *et al.* have suggested that clustering and density fluctuations could be responsible for non-Gaussian velocity distributions [42]. Cluster formation is often seen in driven granular gases. Olafsen and Urbach observed a clustering transition as the shaking amplitude was decreased. In this clustered state, the granular gas separates into dense solid-like clusters surrounded by particles that remain in the gas-like state [46]. The clusters exhibit a hexagonal close-packed order and the particles remain in constant contact with each other and the plate. Similarly, Kudrolli *et al.* found that particles rolling on an inclined plane form large dense clusters for low shaking amplitude [44]. These clusters are found far from the moving boundary for low tilt  $\theta \approx 0$ , but are close to the oscillating wall for larger inclination. In all these clusters, particles have a very high collision rate and very low relative velocities. However, even away from clustering transition, where the granular gas on average appears spatially uniform, significant density fluctuations occur: small transient clusters are continuously formed and subsequently dissolved by collisions with the surrounding high-velocity particles [46]. Puglisi *et al.* showed theoretically that such density fluctuations could lead to non-Gaussian velocity distributions when small regions with constant local density have a Gaussian velocity distribution but with a different granular temperature  $\sigma^2$  that depends on the local density [42]. Indeed, averaging Gaussian distributions with different widths leads to stretched Gaussians of the form in Eq. 2.4. Furthermore, the granular temperature is expected to decrease in regions of high density, because of the large collision rate.

Unfortunately, this idea is not supported by experiment. Olafsen and Urbach studied the dependence of the local granular temperature  $\sigma^2$  on the local density [48]. They find that the granular temperature does decrease with density in the strongly clustering state for low shaking amplitude. However, outside the clustering state the granular temperature is independent of the local density, even though significant density fluctuations still occur. Both Olafsen and Urbach and Rouyer and Menon find that for small regions of constant local density the local velocity distribution is still non-Gaussian. In fact, the local velocity distribution was the same velocity distribution as observed for the entire gas, when normalized by the granular temperature [41, 48].

Non-Gaussian velocity distributions could originate in a more subtle way by spa-

tial correlations. Even in the absence of significant density fluctuations, granular gases often show spatial correlations in density [35, 36, 45, 46] and in velocity [36, 49]. Density correlations are measured by the radial distribution function  $g(r)$ , measuring the average density of particles at a distance  $r$  from a given particle. For dilute granular gases, the radial distribution is not constant, as it would be for a dilute molecular gas, but is peaked close to particle contact at  $r = R$ , where  $R$  is the radius of the particles [35, 45]. For dense granular gases, the radial distribution function  $g(r)$  is often oscillatory with a period of a particle diameter [45, 46]. This is indicative of liquid-like rather than gas-like order. Velocity correlations are often measured by the longitudinal velocity correlations  $C_{\parallel}$ , defined by:

$$C_{\parallel}(r) = \frac{1}{N_r} \sum_{i \neq j}^{N_r} v_i^{\parallel} v_j^{\parallel}, \quad (2.6)$$

where the sum is over the  $N_r$  pairs of particles that are separated by a distance  $r$ . The parallel velocity  $v_{\parallel}$  is the component of the velocity parallel to the vector separating the centers of particles  $i$  and  $j$  and is affected most strongly by the inelastic collisions. Blair and Kudrolli find in their setup that the granular gas exhibits significant longitudinal velocity correlations that become more long-ranged for increasing density [36]. These correlations probably arise because the velocities are parallelized in inelastic collisions. Prevost *et al.* find that the longitudinal velocities are strongly anti-correlated when the gas is driven by a smooth plate and strongly correlated when driven by a rough plate [49]. In all cases, density and velocity correlations have a range of several particle diameters.

Strong spatial correlations might lead to non-Gaussian velocity distribution as they indicate the absence of *molecular chaos*, which is a crucial approximation for finding a Gaussian velocity distribution from the Boltzmann equation. However, the influence of spatial density correlations on the shape of the velocity distribution is not clear. Experiments that show liquid-like density correlations often have strongly non-Gaussian velocity distributions [36, 46]. On the other hand, non-Gaussian velocity distributions are also observed for weak density correlations [45] and in the complete absence of density correlations apart from excluded volume [56]. Strong positive spatial velocity correlations are accompanied by non-Gaussian velocity distributions in the setup of Blair and Kudrolli [36]. On the horizontal plate, on the other hand, non-Gaussian velocity distributions occur for negative velocity correlations, whereas Gaussian distributions are recovered for positive velocity correlations [49]. As a consequence, the influence of spatial correlations on the shape of the velocity distribution remains unclear.

A possible origin for non-Gaussian velocity distributions might be found in the

details of the heating mechanism. Even though velocity distributions are insensitive to changes in parameters such as the shaking frequency and amplitude, they seem to be sensitive to other parameters. For instance, Prevost *et al.* observe a more Gaussian velocity distribution when the granular gas is driven by a rough plate, directly injecting energy into the horizontal degrees of freedom [49]. A similar trend is seen in the experiment of Baxter and Olafsen, where a top layer of light particles is driven indirectly by a bottom layer of vibrated particles. In this case the observed velocity distribution is Gaussian [50]. These results cast some doubt on the validity of using uniform heating as an approximation of the driving mechanism as is done in theoretical calculations [54, 55] and some numerical simulations [51, 52]. If some of the characteristics of the driving mechanism are indeed important in determining the velocity distribution, it is possible that relevant results can only be obtained using a more realistic model of boundary heating. However, non-Gaussian velocity distributions have been observed both in simulations using uniform heating [51, 52] and boundary heating [57–60].

In this Chapter, we study the velocity distributions of two-dimensional granular gases by numerical simulation, both for uniform and boundary heating. We show that rather than a universal distribution with  $\alpha = 3/2$ , a family of distributions with apparent exponents covering a wide range of values  $\alpha < 2$  is expected, depending on both material and experimental conditions. Furthermore, we show that the velocity distribution is governed primarily by the relative importance of collisions to heating, i. e. the way in which energy flows through the system of particles. Specifically, we introduce a new parameter  $q = N_H/N_C$ , which measures the ratio between numbers of heating events and collisions experienced on average by a typical particle. These theoretical observations can explain both the observed non-Gaussian behavior, as well as the ambiguities in the experimental and theoretical literature on dissipative gases to date. We also show that the behavior of the velocity distributions seems to be captured quantitatively by a simple model that takes only  $\eta$  and  $q$  into account, with no spatial degrees of freedom. We also review the evidence of the role of  $q$  in recent experiments.

## 2.2 Numerical simulation

We use an event-driven algorithm to simulate  $N$  particles of radius  $a$  moving in a two-dimensional box. In an event-driven algorithm, the systems is propagated from collision to collision: for each pair of particles is determined when in the future they will collide. The system is propagated until the moment of the first collision. At the moment of collision, the velocities of the colliding particles are update according to



the collision rule and the procedure is repeated. An event-driven simulation scheme is very efficient as in dilute gases particles move by rectilinear motion most of the time and experience collisions only infrequently.

Particles gain energy by heating and lose energy through inelastic collisions. For a two-dimensional granular gas, we implement inelastic collisions in the following way: we assume that during an inelastic collision of particles  $i$  and  $j$  only  $\mathbf{v}_{\parallel,i}$ , the component of the velocity  $\mathbf{v}_i$  parallel to the inter-particle vector  $\mathbf{r}_{ij} = \mathbf{r}_i - \mathbf{r}_j$  changes. This means that we assume that any tangential friction between the particles is absent and the particles always have zero angular momentum. We can decompose the velocity  $\mathbf{v}_i$  in normal and tangential components  $\mathbf{v}_{\parallel,i}$  and  $\mathbf{v}_{\perp,i}$  as follows:

$$\mathbf{v}_{\parallel,i} = (\mathbf{v}_i \cdot \hat{\mathbf{r}}_{ij})\hat{\mathbf{r}}_{ij}, \quad (2.7)$$

$$\mathbf{v}_{\perp,i} = \mathbf{v}_i - \mathbf{v}_{\parallel,i}, \quad (2.8)$$

where  $\hat{\mathbf{r}}_{ij}$  is the unit vector in the direction of  $\mathbf{r}_{ij}$ . At the moment of collision, we change the normal component  $\mathbf{v}_{\parallel,i}$  according to the one-dimensional collision rule for inelastic collisions in Eq. 2.11. Then, for the normal component  $\mathbf{v}'_{\parallel,i}$  of the velocity of particle  $i$  after collision with particle  $j$ , one has:

$$\mathbf{v}'_{\parallel,i} = \frac{1-\eta}{2}\mathbf{v}_{\parallel,i} + \frac{1+\eta}{2}\mathbf{v}_{\parallel,j}, \quad (2.9)$$

where  $\eta$  is the coefficient of restitution. The new velocity  $\mathbf{v}'_i$  for particle  $i$  after the collision with particle  $j$  is:

$$\mathbf{v}'_i = \mathbf{v}_i - \mathbf{v}_{\parallel,i} + \mathbf{v}'_{\parallel,i}. \quad (2.10)$$

Inserting Eqs. 2.7 and 2.9 into Eq. 2.10 yields the two-dimensional inelastic collision rule for the velocity of particle  $i$  after collision with another particle  $j$ :

$$\mathbf{v}'_i = \mathbf{v}_i - \frac{1+\eta}{2}(\mathbf{v}_i \cdot \hat{\mathbf{r}}_{ij} - \mathbf{v}_j \cdot \hat{\mathbf{r}}_{ij})\hat{\mathbf{r}}_{ij}. \quad (2.11)$$

where  $0 \leq \eta < 1$  is the coefficient of restitution and  $\hat{\mathbf{r}}_{ij}$  is the unit vector connecting the centers of particles  $i$  and  $j$ . We prevent inelastic collapse using the TC model of Luding and mcNamara, setting the coefficient of restitution to unity if the particle is involved in another collision within a very short time of the previous one [29].

We perform simulations with both uniform and boundary heating. For uniform heating we adapted an one-dimensional algorithm described in Ref. [35]. When heating uniformly, each individual particle is heated by adding a random contribution to the velocity of each particle during a time step  $\Delta t$ :



$$\mathbf{v}_i(t + \Delta t) = \mathbf{v}_i + \sqrt{h\Delta t}\mathbf{f}(t), \quad (2.12)$$

where  $\mathbf{f}(t)$  is a random vector whose components are uniformly distributed between  $-\frac{1}{2}$  and  $\frac{1}{2}$  and  $h$  is proportional to the heating rate. The dependence on the time step is chosen so that the energy input does not depend on the size of the time step. The kinetic energy of the system after heating is:

$$K = \frac{1}{2} \sum_i \mathbf{v}_i \cdot \mathbf{v}_i + \sqrt{h\Delta t} \sum_i \mathbf{v}_i \cdot \mathbf{f}(t) + \frac{1}{2} h\Delta t \sum_i \mathbf{f}(t) \cdot \mathbf{f}(t) \quad (2.13)$$

Because the term linear in  $\mathbf{f}(t)$  vanishes on average, the average energy input per unit time per particle is  $\frac{1}{2}h\langle \mathbf{f} \cdot \mathbf{f} \rangle$ , independent of the size of the time step  $\Delta t$ .

After heating the system is transferred to the center-of-mass frame, to prevent the build-up of large center-of-mass velocities as a consequence of the inelastic collisions. Particles move in a box with periodic boundary conditions to simulate bulk behavior. The time step  $\Delta t$  is chosen in such a way that on average the number of collisions per time step is less than one.

In boundary heating, particles gain velocity upon collision with the boundary. For simplicity, we assume that the collision with the boundary is elastic. In that case, a collision occurs by reflecting  $\mathbf{v}_\perp$ , the component of the velocity perpendicular to the boundary. Heating occurs by adding a random amount of velocity to  $\mathbf{v}_\perp$ . Then after collision with the boundary one has:

$$\mathbf{v}'_i = \mathbf{v} - 2\mathbf{v}_\perp + \sqrt{h}\mathbf{f}(t). \quad (2.14)$$

Particles move in a circular box. A symmetrical container has the advantage that it allows us to examine density and granular temperature gradients along a single coordinate  $r$ , the distance from the center of the box, as in the one-dimensional case [32]. This method of heating at the boundary is analogous to the technique described in Ref. [58].

We start the simulation by distributing the particles uniformly over the box. When using boundary heating, we give each particle a small, uniformly distributed velocity to enable particles to reach the boundary. Then particles are heated and we allow the system to reach a steady state before taking data. For both uniform heating and boundary heating, data is collected periodically every time step  $\Delta t$ . For uniform heating, data is taken when the particles are heated, so  $\Delta t$  equals the time between heating events. In our simulations, we vary the coefficient of restitution  $\eta$ , the areal density  $\phi$  and the number of particles  $N$ . The radius  $R$  of the particles depends on  $\phi$  and  $N$  as  $\phi = N\pi R^2/A$ , where  $A$  is the area of the container.

## 2.3 Clustering

Dense clusters of particles occur for a wide range of parameters when heating through the boundary, but are absent for uniform heating. This occurs as particles are compressed in the center of the box by the pressure of particles moving in from the boundary. As the cluster grows in size, it can no longer be destroyed by the impact of high velocity particles and the cluster remains stable. Examples for increasing amounts of dissipation are shown in Fig. 2.2. As energy dissipation is increased, either by decreasing  $\eta$  or increasing the number of collisions, the gas develops a liquid-like cluster surrounded by a hot gas. For higher dissipation, the cluster grows in size and ultimately shows crystalline order, including defects and disclinations. The smaller clusters are highly dynamic and assemble and disassemble as they move around the container. The formation of a cluster in time is shown in Fig. 2.3.

For measurements of the velocity distribution, the gas has to be in the homogeneous gas state. To avoid values of  $\phi$  and  $\eta$  corresponding to the formation of clusters in our simulation, we constructed a phase diagram. We did this by counting for every particle the average number  $N_{6R}$  of neighbors with their center within a distance smaller than or equal to  $6R$  from its center, where  $R$  is the radius of the particles. When the gas is in a hexagonal close packed state  $N_{6R} = 36$ . We obtained the distribution  $P(N_{6R})$  for different values of  $\phi$  and  $\eta$ . An example for  $N = 350$  and  $\phi = 0.1$  is shown in Fig. 2.4.

For  $\eta = 0.9$  the distribution corresponds to a state with the particles uniformly distributed over the box and the peak of the distribution at the mean value  $\overline{N}_{6R} = 3.6$ . For  $\eta = 0.7$  the distribution becomes bimodal, with a broad peak at high  $N_{6R}$  corresponding to the densely-packed cluster and a peak at  $N_{6R} = 1$  corresponding to the surrounding dilute gas. The distribution shows a continuous variation for  $\eta$  in between, which makes it hard to pinpoint an exact value of  $\eta$  for which clusters first form. Still, by looking at the shape of the distributions, it can be argued that the transition occurs somewhere between  $\eta = 0.75$  and  $\eta = 0.85$ . This was repeated for different values of  $\phi$ , which allowed us to determine a sort of phase or state diagram. Specifically, we determined the limit of a pure gas-like phase, and all results presented below were obtained in this state. Unfortunately, as the transition from the homogeneous gas state to the cluster state is very gradual, we are unable to present here an accurate phase diagram.

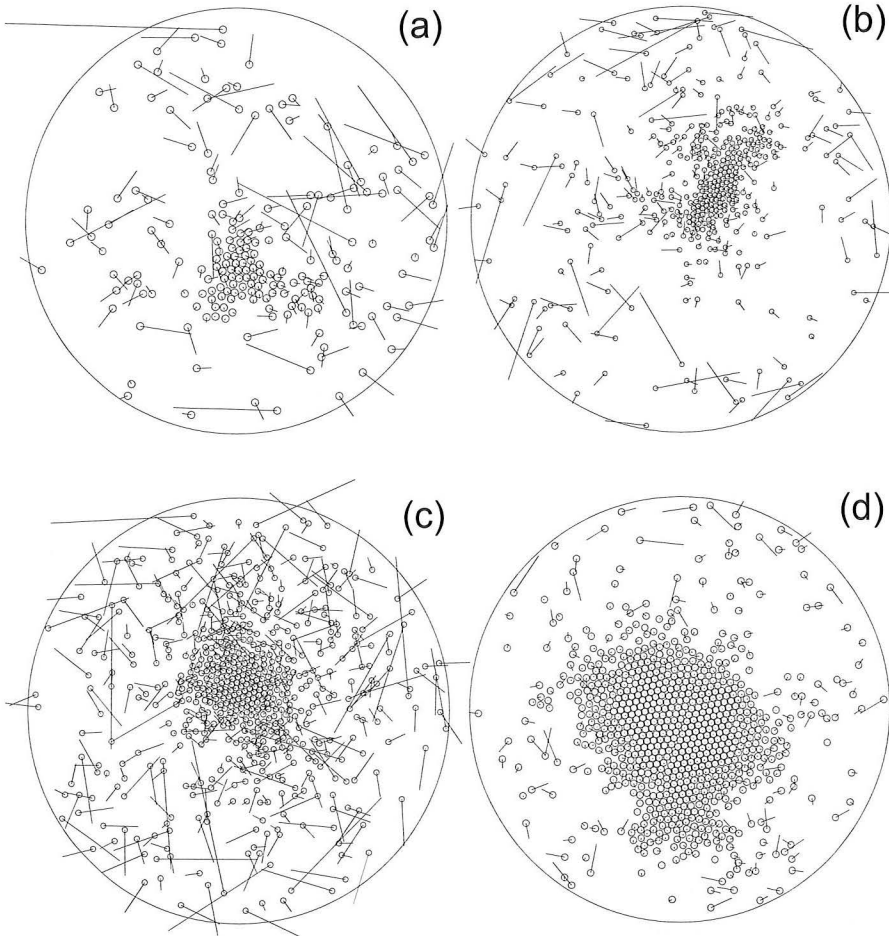


**Figure 2.2:** Snapshots of the clustered state for (a)  $N = 200$ ,  $\phi = 0.06$  and  $\eta = 0.5$ , (b)  $N = 400$ ,  $\phi = 0.05$  and  $\eta = 0.6$ , (c)  $N = 600$ ,  $\phi = 0.1$  and  $\eta = 0.8$  and (d)  $N = 800$ ,  $\phi = 0.2$  and  $\eta = 0.7$ . The circles indicate the current positions of the particles, while the lines show the direction and magnitude of the velocity. The smaller clusters show more liquid-like order, whereas in the bigger clusters the order is crystalline. In the latter case, the hexagonal ordering of the clusters sometimes shows defects. In (d), for instance, the cluster appears to exhibit distinct crystal-like domains.

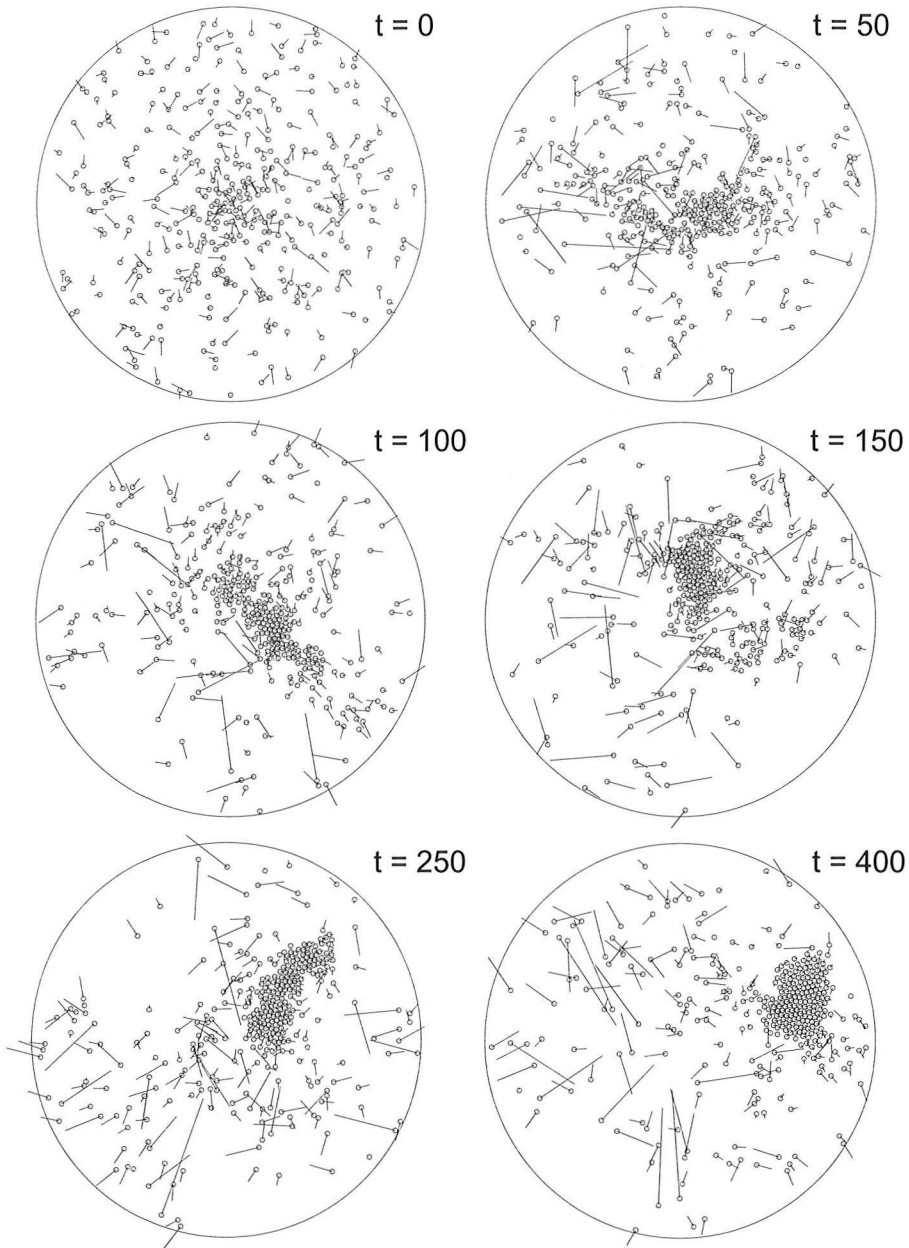


**Figure 2.3:** Formation of a cluster for  $N = 350$ ,  $\phi = 0.05$  and  $\eta = 0.6$ . Lines indicate direction and magnitude of the velocities of the particles. At  $t = 0$ , the system starts with the initial conditions described in Section 2.2. At  $t = 100$  a cluster has formed. The cluster travels around the box and is about to hit the wall at  $t = 400$ .

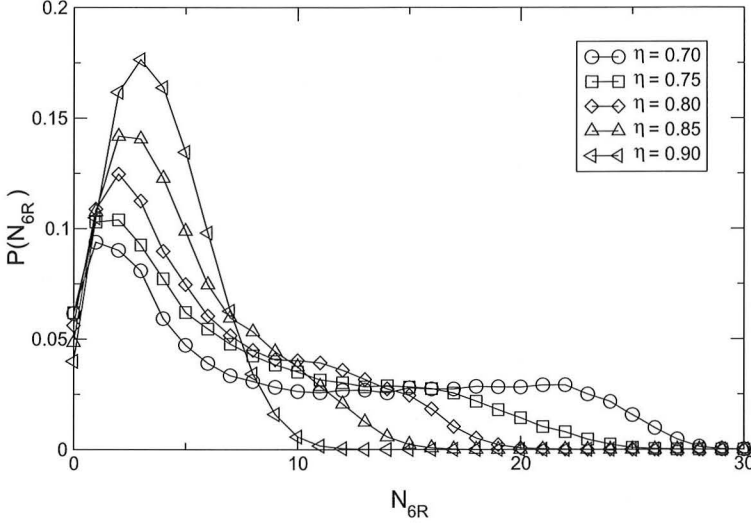


**Figure 2.4:** Number of neighbors within a distance  $6R$  of a given particle for  $N = 350$ ,  $\phi = 0.1$  and  $\eta = 0.7(\circ)$ ,  $0.75(\square)$ ,  $0.8(\diamond)$ ,  $0.85(\triangle)$  and  $0.9(\nabla)$ . On average  $N_{6R} = 3.6$  for  $\phi = 0.1$ .

## 2.4 Velocity distributions

For a velocity distribution of the form in Eq. 2.4, it is more convenient to plot the double logarithm of the velocity distribution  $P(v)$  against the logarithm of the velocity  $v$ . Specifically, we know that:

$$-\ln[P(v)/P(0)] = B(v/\sigma)^\alpha, \quad (2.15)$$

$$-\ln\{-\ln[P(v)/P(0)]\} = \ln B - \alpha \ln(v/\sigma). \quad (2.16)$$

Thus, when we plot the double logarithm of the velocity distribution against the logarithm of the velocity as in Eq. 2.16, the local slope yields the local exponent of the velocity distribution. In particular, when plotted this way a Gaussian velocity distribution is a straight line with slope  $-2$ . In the case of a velocity distribution that has two regimes with different exponents  $\alpha$ , in this representation the velocity distribution will have different slopes for the two regimes. We will use this representation throughout this chapter and in Chapter 3 when studying the exponent  $\alpha$ .

The velocity distributions  $P(v_x)$  for uniform heating are shown in Figs. 2.5 and 2.6. The velocity component  $v_x$  is scaled by  $\sigma_x = \langle v_x^2 \rangle^{1/2}$  and the maximum of the distribution  $P(v_x/\sigma_x)$  is scaled to be unity. For a broad range of the parameters  $\phi$  and  $\eta$  the velocity distributions are very close to Gaussian. For  $\eta = 0.8$  the velocity

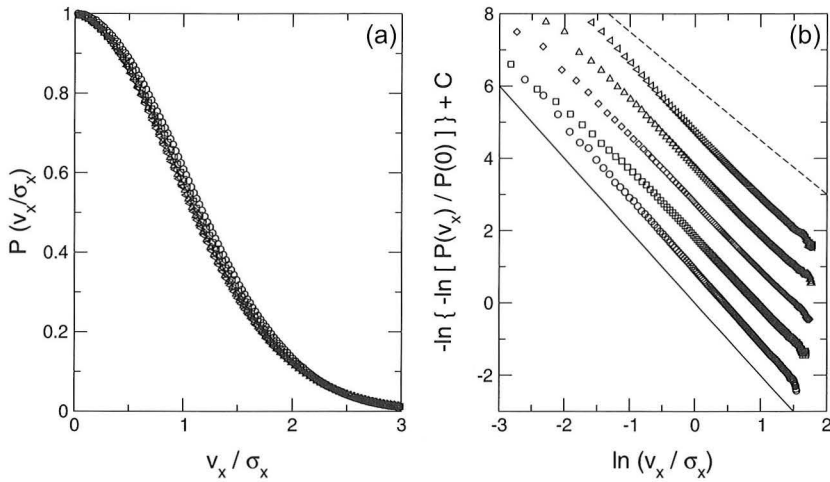


**Figure 2.5:** Uniform heating. (a)  $P(v_x/\sigma_x)$ . (b)  $-\ln\{-\ln[P(v_x/\sigma_x)]\}$  versus  $\ln(v_x/\sigma_x)$ . Data for both figures is taken for  $N = 350$  and for  $\phi = 0.02$  and  $\eta = 0.8(\circ)$ ,  $0.6(\square)$ ,  $0.4(\diamond)$ ,  $0.2(\triangle)$ ,  $0.1(\triangleleft)$ . A Gaussian is shown as a solid line with slope  $-2$  and the distribution obtained by Rouyer and Menon is shown as the dashed line with slope  $-1.5$ . The velocity distributions are shifted by a constant amount  $C$  for clarity.

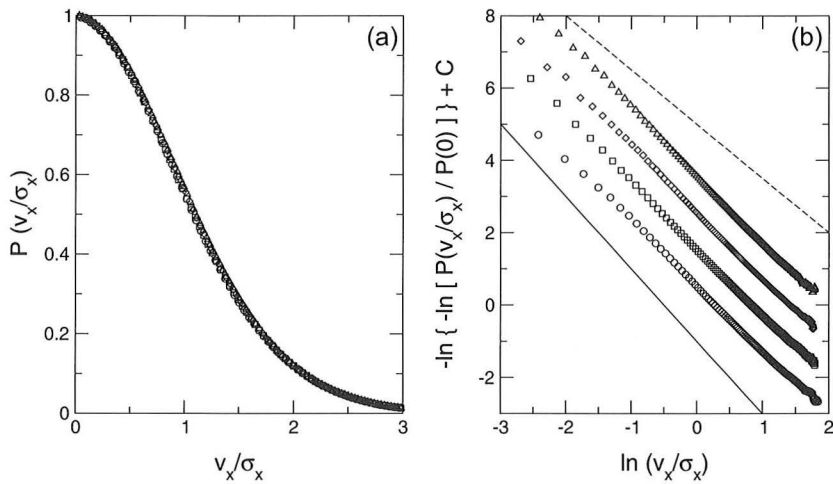


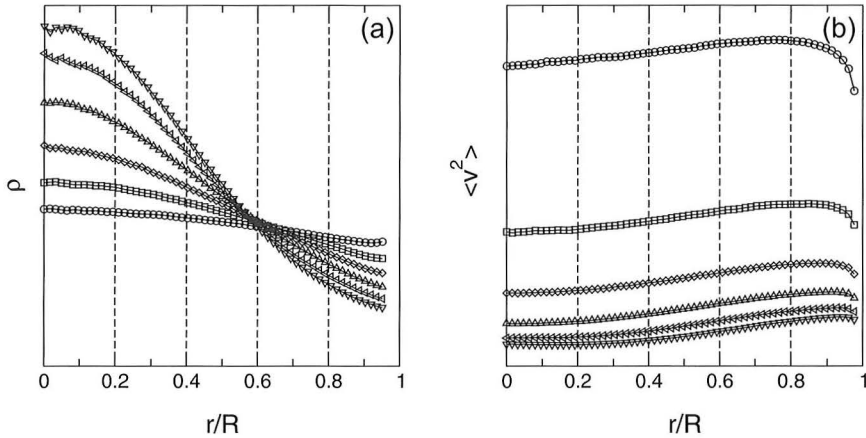
**Figure 2.6:** Uniform heating. (a)  $P(v_x/\sigma_x)$ . (b)  $-\ln\{-\ln[P(v_x/\sigma_x)]\}$  versus  $\ln(v_x/\sigma_x)$ . The dashed lines have slope  $-2$  and  $-1.5$ . Data for both figures is taken for  $N = 350$  and for  $\eta = 0.2$  and  $\phi = 0.1(\circ)$ ,  $0.05(\square)$ ,  $0.02(\diamond)$ ,  $0.01(\triangle)$ .

distributions can be fitted by a distribution with  $\alpha = 2.0$ . This decreases only slightly for  $\eta = 0.1$ , which can be fitted by a distribution with  $\alpha = 1.9$ . Values of  $\alpha$  are found to be independent of  $\phi$ . These exponents are constant over the entire observed range of velocities and we find no evidence of a velocity distribution with  $\alpha = 1.5$  for the range of  $\phi$  and  $\eta$  we examined. This agrees with observations made before in Ref. [53].

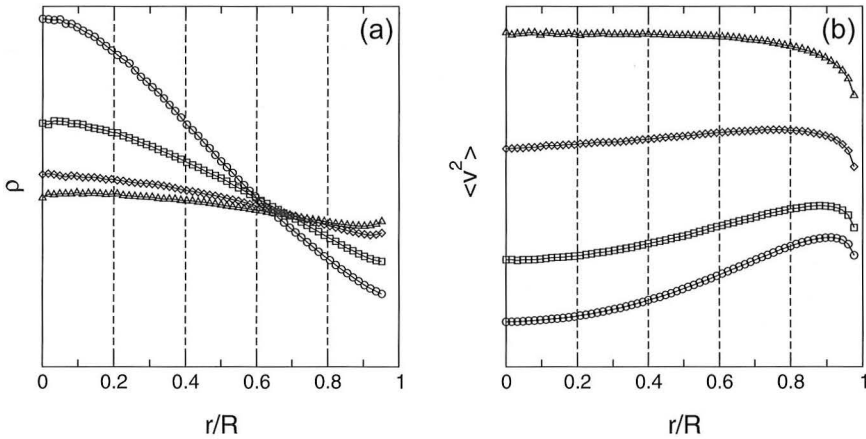
For boundary heating the gas develops a gradient in both density and mean kinetic energy as shown in Fig. 2.7 and 2.8. Ideally, we want to measure velocity distributions in a region where the gradient is small. To this end we divided the box in five rings of width 0.2. These rings are indicated in Fig. 2.7 and 2.8. Only for values of  $\phi$  and  $\eta$  close to the clustering state, does the density within a ring vary by more than 10%. The velocity distributions  $P(v_x)$  for particles within the different rings are shown in Fig. 2.9. Figure 2.9(a) shows  $P(v_x)$  with the velocity component  $v_x$  scaled by  $\sigma_x = \langle v_x^2 \rangle^{\frac{1}{2}}$  and the maximum of the distribution scaled to be unity. When normalized by  $\sigma_x$  the velocity distributions for different rings in the container have largely the same shape for smaller velocities, even though density and mean kinetic energy vary considerably between these rings. This is a feature that is observed for all values of  $\phi$  and  $\eta$ , even close to the cluster state. Similar observations have been made in Ref. [58].

Fig. 2.9(b) shows the behavior of the exponent  $\alpha$ . This behavior is very different from the case of uniform heating. For uniform heating  $\alpha$  has the same value over the entire observed range of velocities. For boundary heating, on the other hand,  $\alpha$  has a constant value  $\alpha_1$  over the low-velocity range but crosses over to different value  $\alpha_2$  when above a critical velocity  $v_c$ . For all rings the distribution for smaller velocities is close to Gaussian with  $\alpha_1 \approx 1.8$ . For the inner three rings the distribution for velocities higher than  $v_c$  is well described by a single exponent  $\alpha_2 < 1.5$ . For the outer rings this behavior is more complicated.

In Fig. 2.10 we show the effect of a change in  $\phi$  and  $\eta$  on the shape of the velocity distributions. Here we focus on the velocity distribution as measured in the ring with  $0.4 < r \leq 0.6$ . This has the advantage of good statistics, but for values of  $\phi$  and  $\eta$  close to a cluster, we might see effects due to the density gradient in the gas. As shown in Fig. 2.10(a) the exponent  $\alpha_1 = 1.8$  except for  $\eta = 0.4$ , where  $\alpha_1 = 1.6$ . For  $\eta = 0.9$  there is no crossover in the observed range of velocities. In the other distributions one does observe a crossover and the point where it occurs shifts down to lower velocities as  $\eta$  is decreased. It is clear that the distribution for velocities above the crossover cannot be described by a single exponent. For low enough  $\eta$ , the distribution seems to approach a constant exponent for high velocities. This exponent decreases from  $\alpha_2 = 1.3$  for  $\eta = 0.7$  to  $\alpha_2 = 1.0$  for  $\eta = 0.4$ . Velocity distributions with a similar dependence on  $\eta$  have been observed before in Refs.



**Figure 2.7:** Boundary heating. (a) The average number density  $\rho$  as a function of distance  $r$  to the center of the box. The container has radius  $R$ . Data taken for  $N = 350$ ,  $\phi = 0.02$  and  $\eta = 0.9(\circ)$ ,  $0.8(\square)$ ,  $0.7(\diamond)$ ,  $0.6(\triangle)$ ,  $0.5(\nabla)$  and  $0.4(\triangleright)$ . (b) The mean kinetic energy  $\langle v^2 \rangle$  per particle as a function of  $r$ , for the same values of  $\phi$  and  $\eta$ . The dashed lines indicate the concentric rings, within which the velocity distributions were separately calculated.



**Figure 2.8:** Boundary heating. (a) The average number density  $\rho$  as a function of distance  $r$  to the center of the box. Data taken for  $N = 350$ ,  $\eta = 0.9$  and  $\phi = 0.1(\circ)$ ,  $0.05(\square)$ ,  $0.02(\diamond)$  and  $0.01(\triangle)$ . (b) The mean kinetic energy  $\langle v^2 \rangle$  per particle as a function of  $r$ , for the same values of  $\phi$  and  $\eta$ . Note that even for the dilute case  $\phi = 0.01$  the mean kinetic energy profile is not constant, but drops at the boundary of the box. The profile only becomes constant after a certain distance into the container; that corresponds to the mean free path of particles leaving the boundary. This feature, together with the rise in density we observe close to the boundary, has been described also in Ref. [60]



[52] and [60].

In Fig. 2.10(b) we examine the behavior of the velocity distributions as the area density is varied. Again, we find that for smallest velocities the distribution is close to Gaussian with  $\alpha_1 \approx 1.8$  for all  $\phi$ . A crossover in exponent  $\alpha$  is observed for every  $\phi$  and the velocity at which the crossover occurs hardly shifts as  $\phi$  is varied. The distributions approach a constant exponent for high velocities. This exponent goes down from  $\alpha_2 = 1.5$  for  $\phi = 0.01$  to  $\alpha_2 = 1.0$  for  $\phi = 0.05$ . In general, the deviations from Gaussian become more pronounced as dissipation increases, i.e. as  $\phi$  increases or as  $\eta$  decreases. When  $\alpha_2$  decreases it is increasingly difficult to describe the distribution with a single exponent  $\alpha_2$  for the highest velocities. It may well be that this regime, corresponding to the highest velocities in both our simulations and the recent experiments, is different from the *asymptotic* high-velocity tail predicted by kinetic theories [54].

In Fig. 2.11 we summarize the differences in velocity distributions obtained for uniform and boundary heating. For uniform heating the velocity distribution is close to Gaussian for a large range of  $\eta$ . In contrast, for boundary heating the distribution is only Gaussian in the nearly elastic case  $\eta = 0.9$ . As the coefficient of restitution is lowered, a crossover develops where the exponent changes from  $\alpha_1 \approx 2$  to a lower value  $\alpha_2$ . The exponent  $\alpha_2$  becomes smaller as dissipation is increased (for smaller  $\eta$  or higher  $\phi$ ) and we find any value in the range  $0.7 \lesssim \alpha_2 < 2$ . The crossover in exponent is observed in boundary heating for all values of  $\phi$  and  $N$ .

We also find for a certain range of parameters an exponent  $\alpha_2 = 1.5$  for the high velocity tail. For their experiments Rouyer and Menon used  $N$  particles with  $\eta \approx 0.9$ , where  $100 < N < 500$  and  $0.05 < \phi < 0.25$  [41]. In Fig. 2.12 we plotted the velocity distribution for  $\eta = 0.9$ ,  $\phi = 0.05$  and several values of  $N$ . We also show the fit with  $\alpha = 1.52$  as made in Ref. [41]. This line clearly coincides with the velocity distribution found by the present simulation for velocities beyond the crossover. This suggests that instead of a universal distribution with  $\alpha = 1.5$ , they might have observed a part of a more complex velocity distribution, with more than one apparent exponent.

To test whether the velocity distributions we find here are only observed for this specific driving mechanism of heating through a circular boundary, we constructed different systems that drive through boundaries in a different way. For instance, we constructed a box with periodic boundary conditions that includes a small circular region around the center. Within this circular region particles are uniformly driven but outside of the region they are not heated at all. For particles within the circular region we observe velocity distributions that are Gaussian. On the other hand, for particles outside of the circular region we observe the same non-Gaussian velocity distributions as seen in the case of a circular boundary.

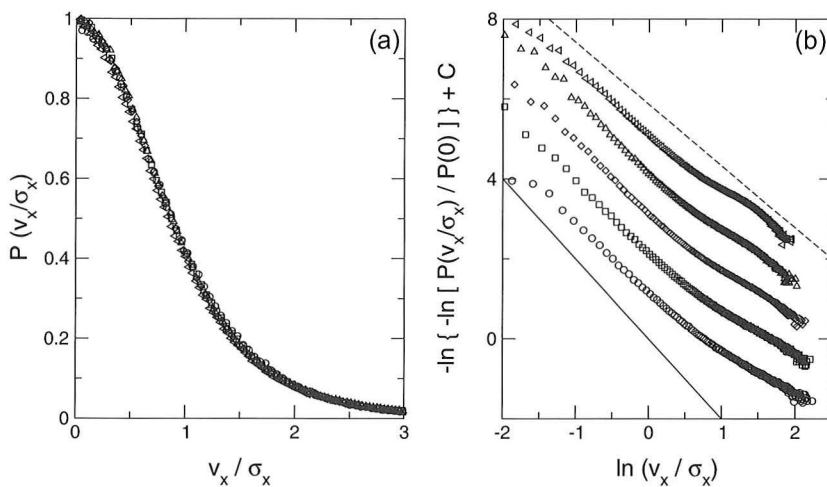


**Figure 2.9:** Velocity distributions for boundary heating calculated separately within the concentric rings shown in Figs. 2.7 and 2.8, i.e., for  $0 < r \leq 0.2$  ( $\circ$ ),  $0.2 < r \leq 0.4$  ( $\square$ ),  $0.4 < r \leq 0.6$  ( $\diamond$ ),  $0.6 < r \leq 0.8$  ( $\triangle$ ) and  $0.8 < r \leq 1$  ( $\triangleleft$ ), where  $r$  is distance to the center. Data were taken for  $N = 350$ ,  $\phi = 0.05$  and  $\eta = 0.8$ . (a)  $P(v/\sigma_x)$ . (b)  $-\ln\{-\ln[P(v_x/\sigma_x)/P(0)]\}$  versus  $\ln(v_x/\sigma_x)$ . The local slope corresponds directly to the local exponent  $\alpha$ .

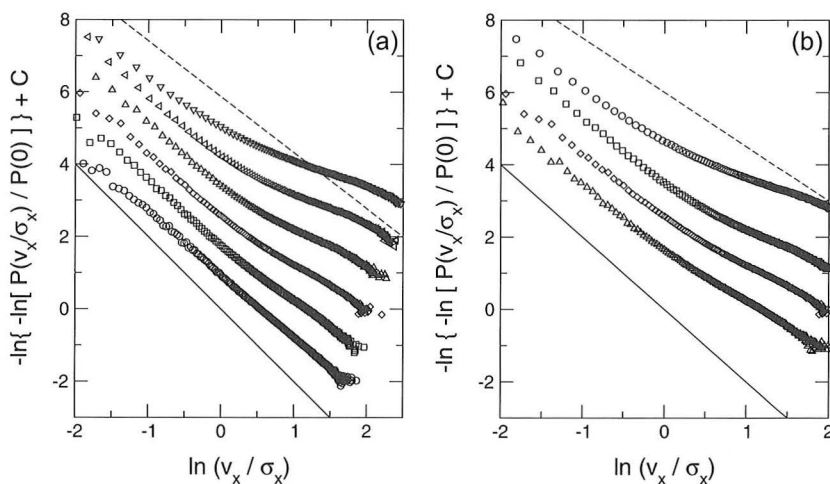


**Figure 2.10:** Boundary heating. (a)  $-\ln\{-\ln[P(v_x/\sigma_x)/P(0)]\}$  versus  $\ln(v_x/\sigma_x)$  for  $N = 350$ ,  $\phi = 0.02$  and  $\eta = 0.9$  ( $\circ$ ),  $0.8$  ( $\square$ ),  $0.7$  ( $\diamond$ ),  $0.6$  ( $\triangle$ ),  $0.5$  ( $\triangleleft$ ) and  $0.4$  ( $\nabla$ ). (b)  $-\ln\{-\ln[P(v_x/\sigma_x)/P(0)]\}$  versus  $\ln(v_x/\sigma_x)$  for  $N = 350$ ,  $\eta = 0.7$  and  $\phi = 0.01$  ( $\circ$ ),  $0.02$  ( $\square$ ),  $0.03$  ( $\diamond$ ) and  $0.05$  ( $\triangle$ ).

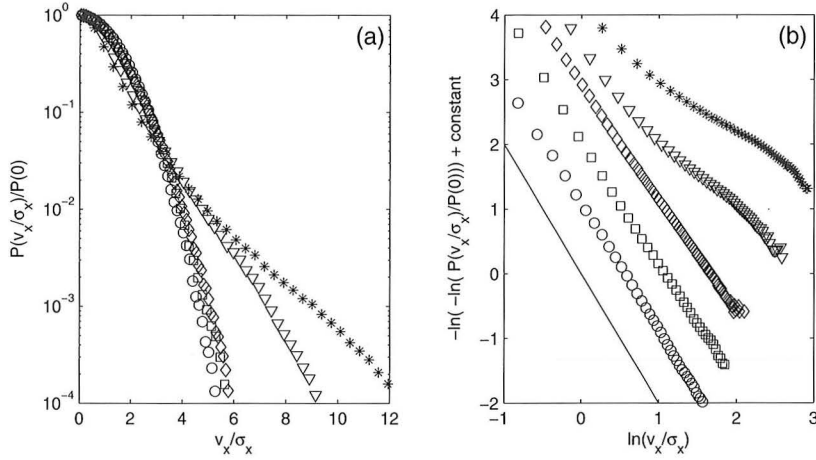


**Figure 2.11:** Velocity distributions for  $N = 350$  and  $\phi = 0.02$ . Shown are both results for uniform heating with  $\eta = 0.8$  ( $\circ$ ),  $\eta = 0.1$  ( $\square$ ) and results for boundary heating with  $\eta = 0.9$  ( $\diamond$ ),  $\eta = 0.6$  ( $\nabla$ ) and  $\eta = 0.4$  ( $*$ ). (a)  $P(v_x/\sigma_x)$  (b)  $-\ln\{-\ln[P(v_x/\sigma_x)]\}$  versus  $\ln(v_x/\sigma_x)$ . A Gaussian is shown as a solid line.

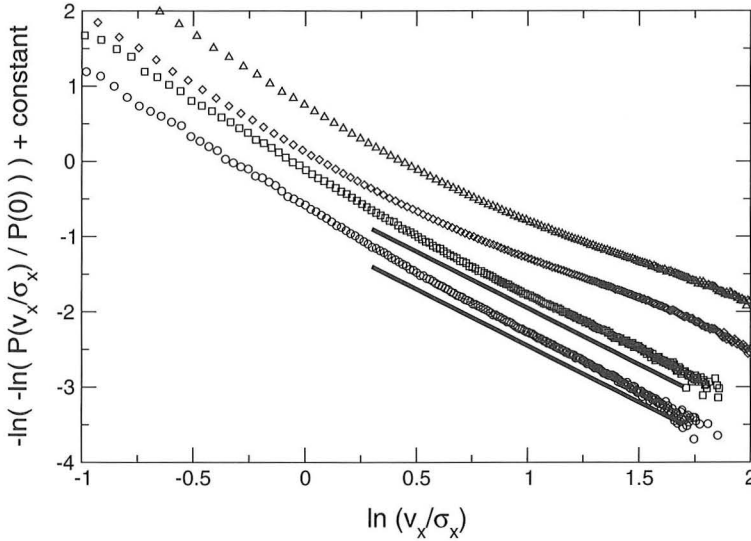


**Figure 2.12:** (a)  $-\ln\{-\ln[P(v_x/\sigma_x)]\}$  versus  $\ln(v_x/\sigma_x)$  for  $N = 350$ ,  $\phi = 0.05$  and  $\eta = 0.9$  ( $\circ$ ),  $N = 500$ ,  $\phi = 0.05$  and  $\eta = 0.9$  ( $\square$ ),  $N = 350$ ,  $\phi = 0.05$  and  $\eta = 0.8$  ( $\diamond$ ),  $N = 350$ ,  $\phi = 0.25$  and  $\eta = 0.9$  ( $\triangle$ ). The solid lines correspond to the fit as made by Rouyer and Menon and has an exponent  $\alpha = 1.52$ . The range of the solid lines corresponds to half the range used by Rouyer and Menon in their fit, but contains about 80% of their data points.

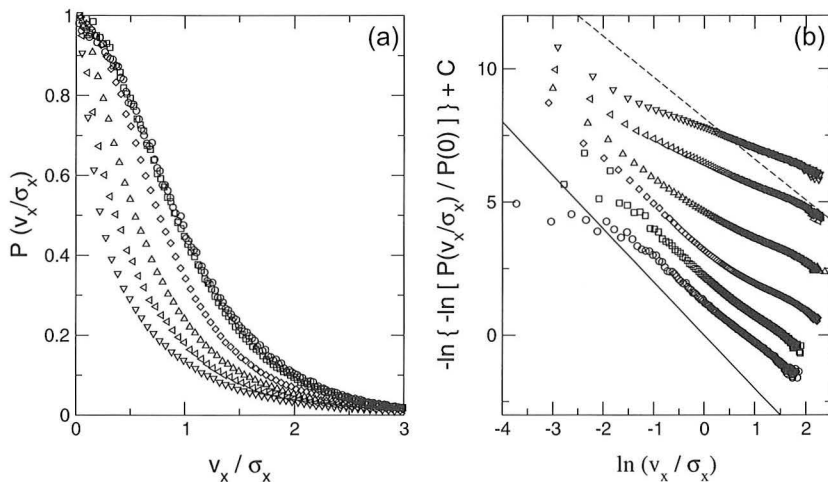


**Figure 2.13:** Boundary heating. (a)  $P(v_x/\sigma_x)$  for different values of  $N$ . (b)  $-\ln\{-\ln[P(v_x/\sigma_x)]\}$  versus  $\ln(v_x/\sigma_x)$ . Data is taken for  $\phi = 0.05$ ,  $\eta = 0.8$  and  $N = 50(\circ)$ ,  $100(\square)$ ,  $200(\diamond)$ ,  $500(\triangle)$ ,  $700(\triangleleft)$  and  $1000(\nabla)$ .

To test whether velocity distributions are sensitive to the precise way of heating at the boundary, we changed our heating algorithm so that when a particle hits the boundary, the angle of reflection is random and the magnitude of the new velocity is drawn from a Gaussian distribution. This has a minor effect on the distribution for the highest velocities, but leaves all major differences between uniform and boundary heating intact.

Finally, we studied the behavior of the velocity distribution for different particle numbers  $N$ . Figure 2.13(a) shows that, as  $N$  increases, the velocity distributions become more narrow for smaller velocities, but fall off less rapidly in high velocity regime. This is shown more clearly in Fig. 2.13(b). We find that the distribution for velocities larger than the crossover velocity is well described by a single exponent that decreases from  $\alpha_2 = 1.7$  for  $N = 50$  to  $\alpha = 0.7$  for  $N = 1000$ . The crossover shifts to lower velocity and becomes sharper as  $N$  is increased. Instead of approaching a limiting velocity distribution as  $N$  is increased, we find that the shape of the velocity distribution depends not only on  $\eta$  and  $\phi$ , but also on  $N$  for all values of  $N$  we examined. This indicates that for boundary heating there is no thermodynamic limit. For uniform heating, on the other hand, the velocity distribution is largely insensitive to changes in  $N$ .

The main difference between uniform and boundary heating is that in the first case heating takes place homogeneously throughout the box, whereas in the latter

case energy is injected inhomogeneously at the boundaries. This is not the direct cause for the difference in velocity distributions. As we will show below, when heating homogeneously one can go from a Gaussian distribution to one with a crossover by increasing the time step  $\Delta t$  between heatings. In this case the number of particles heated per unit time becomes smaller than the average number of collisions, dissipating energy. The reverse is also true. When heating inhomogeneously through a boundary, one finds Gaussian distributions in very dilute systems, when the particles on average collide more often with the boundary than with other particles. This suggests that in our system the shape of the velocity distribution is not a function of all parameters  $\eta$ ,  $\phi$ ,  $N$  and the details of the energy injection, but only of  $\eta$  and  $q = N_H/N_C$ , the ratio between the average number of heatings  $N_H$  and the average number of collisions  $N_C$ .

This idea can easily be tested in boundary heating. When increasing the number of particles  $N$  or the area fraction  $\phi$ , the average number of collisions increases. One can show in a mean field approximation that  $q \sim (N\phi)^{-1/2}$ . The average distance a particle travels between collisions is given by  $l_{coll} \sim 1/\phi$ . For a box of area  $A$  the average distance between boundaries is given by  $l_{heat} \sim A^{1/2} \sim (N/\phi)^{1/2}$ . Finally, we know  $N_H/N_C \sim l_{coll}/l_{heat}$ . Our simulation obeys this approximation very well. In Fig. 2.14 we show velocity distributions for  $\eta = 0.8$  and different combinations of  $N$  and  $\phi$ . We measure the heating-dissipation ratio  $q$  in the simulation and show velocity distributions with the same  $q$  on top of each other. For  $q = 1.3$  and  $q = 0.13$  we find excellent collapse for different  $N$  and  $\phi$ , even when we scale the system by a factor 8. For  $q = 0.013$ , where spatial correlations become very strong, we still find reasonable collapse. As we increase  $q$  we observe the usual pattern, where a crossover appears in a distribution that was initially close to a Gaussian.

To test that whether non-Gaussian velocity distributions can occur when heating homogeneously, we use a different heating mechanisms that is spatially homogeneous and where the ratio  $q$  can be adjusted. With this heating mechanism, described in Ref. [51], we can reproduce the entire family of distributions as observed for boundary heating. In this case, every time step  $\Delta t$ , we select at random two particles and add to these particles a random but opposite velocity to conserve the total momentum. On average heating is spatially homogeneous and in the limit of small  $\Delta t$  this heating mechanism approaches uniform heating. When  $\Delta t$  is small, many heatings occur for every collision whereas for large  $\Delta t$ , particles collide many times before being heated. By increasing  $\Delta t$ , the parameter  $q$  is decreased.

The effect of changing  $\Delta t$  is shown in Fig. 2.15. Here, we show the velocity distribution for  $N = 350$ ,  $\phi = 0.02$  and  $\eta = 0.4$ . The gas is heated using the two-point heating algorithm described above, while we vary the time between heatings,  $\Delta t$ . For  $\Delta t = 0.01$  the distribution has a exponent  $\alpha = 1.7$  that is approximately

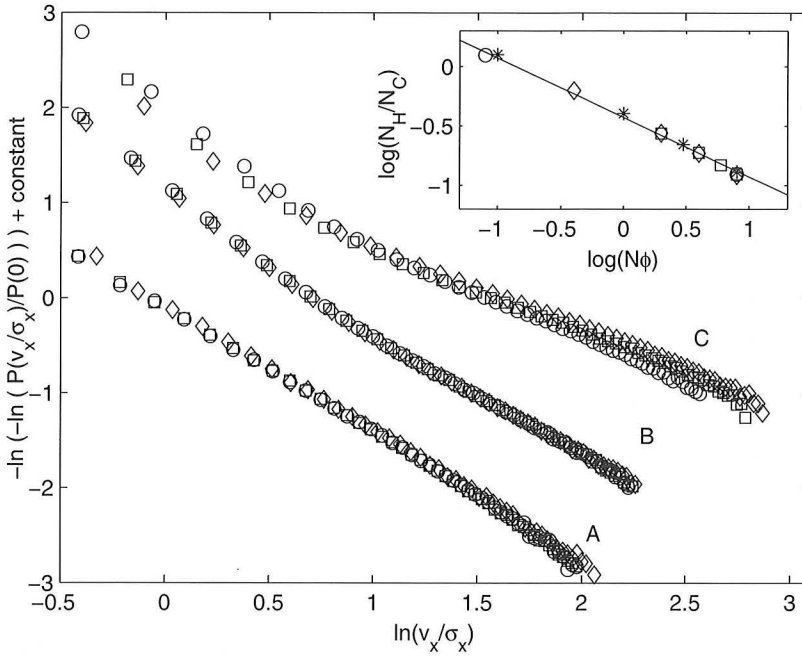


**Figure 2.14:** Velocity distributions for different values of the heating-dissipation rate  $q$ , heating through the boundary. Distributions with the same  $q$  are shown on top of each other. (A)  $q = 1.3$  and we show  $N = 100$  and  $\phi = 1 \cdot 10^{-3}$  ( $\circ$ ),  $N = 200$  and  $\phi = 5 \cdot 10^{-4}$  ( $\square$ ),  $N = 800$  and  $\phi = 1.25 \cdot 10^{-4}$  ( $\diamond$ ). (B)  $q = 0.13$  and we show  $N = 100$  and  $\phi = 0.08$  ( $\circ$ ),  $N = 200$  and  $\phi = 0.04$  ( $\square$ ),  $N = 400$  and  $\phi = 0.02$  ( $\diamond$ ). (C)  $q = 0.013$  and we show  $N = 100$  and  $\phi = 0.4$  ( $\circ$ ),  $N = 200$  and  $\phi = 0.2$  ( $\square$ ),  $N = 400$  and  $\phi = 0.1$  ( $\diamond$ ). Inset: Heating-dissipation ratio  $q$  for  $N = 800$  ( $\circ$ ),  $N = 400$  ( $\square$ ),  $N = 200$  ( $\diamond$ ) and  $N = 100$  ( $*$ ) for several values of  $\phi$ . The line is a fit of the form  $(N\phi)^{1/2}$ .

constant over the observed range. When  $\Delta t$  is reduced a clear crossover develops. The behavior of the velocity distribution for velocities higher than the crossover velocity is more complicated than in boundary heating. There is also a sharp kink at the high-velocity end that we have been unable to explain so far. For small  $\Delta t$ , the velocity distribution is Gaussian over the entire range of velocities. For larger  $\Delta t$ , the resulting velocity distribution is reminiscent of the distributions seen for boundary heating, where a crossover in the exponent occurred for similar values of  $\eta$ . This confirms the idea that uniform heating and boundary heating describe different limits of the same granular gas, for  $q \gg 1$  and  $q \sim 1$ , respectively.

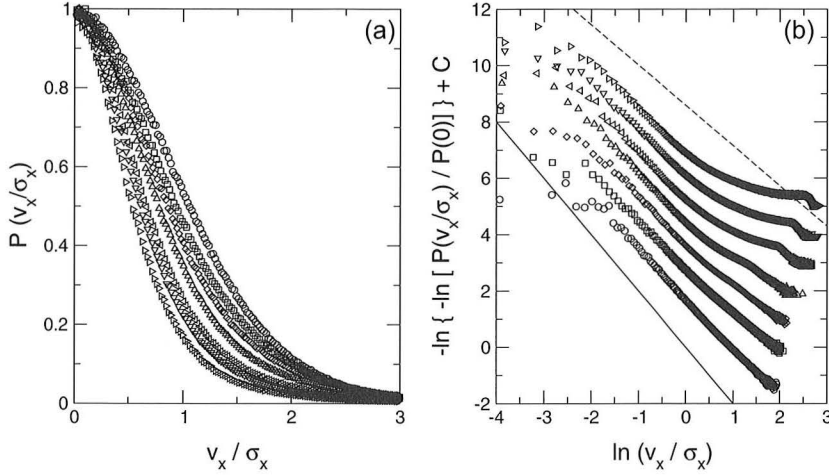


**Figure 2.15:** Two-point heating. (a)  $P(v_x/\sigma_x)$  for different values of  $\Delta t$ . (b)  $-\ln\{-\ln[P(v_x/\sigma_x)/P(0)]\} + C$  versus  $\ln(v_x/\sigma_x)$ . Data is taken for  $N = 350$ ,  $\phi = 0.02$ ,  $\eta = 0.4$  and  $\Delta t = 0.01(\circ)$ ,  $0.03(\square)$ ,  $0.05(\diamond)$ ,  $0.10(\triangle)$ ,  $0.30(\triangleleft)$ ,  $0.50(\nabla)$  and  $1.00(\triangleright)$ .

## 2.5 A model without spatial degrees of freedom

It has been speculated that the non-Gaussian distributions are caused by spatial correlations in the gas [42]. However, we can qualitatively reproduce the different distributions we observe in simulation with a simple model (based on Ref. [61], but including dissipation) of a two-dimensional inelastic gas of  $N$  particles without spatial degrees of freedom.

In our model, every time step we select at random  $C$  pairs of particles  $i$  and  $j$  and let them collide. At the same time we randomly select  $H$  particles  $k$  and heat those by adding a random amount to their velocity. Collisions in our model occur by selecting at random particles  $i$  and  $j$  and an uniformly distributed impact parameter  $-2a < b < 2a$ , where  $a$  is the radius of the particles. In order to apply the inelastic collision rule in Eq. 2.11 we need to know the inter-particle vector  $\mathbf{r}_{ij}$  as a function of the impact parameter. The unit vector  $\hat{\mathbf{r}}_{ij}$  is given by:

$$\hat{\mathbf{r}}_{ij} = \begin{pmatrix} \cos \theta \\ \sin \theta \end{pmatrix}, \quad (2.17)$$

with  $\theta = \arcsin(b/2R) + \arccos(\mathbf{v} \cdot \hat{\mathbf{s}}/v)$ , where  $\mathbf{v} = (\mathbf{v}_j - \mathbf{v}_i)/2$  is the velocity in the center-of-mass frame and  $\hat{\mathbf{s}}$  is a unit vector along a reference axis. Combining Eq. 2.17 with the collision rule in Eq. 2.11 yields:

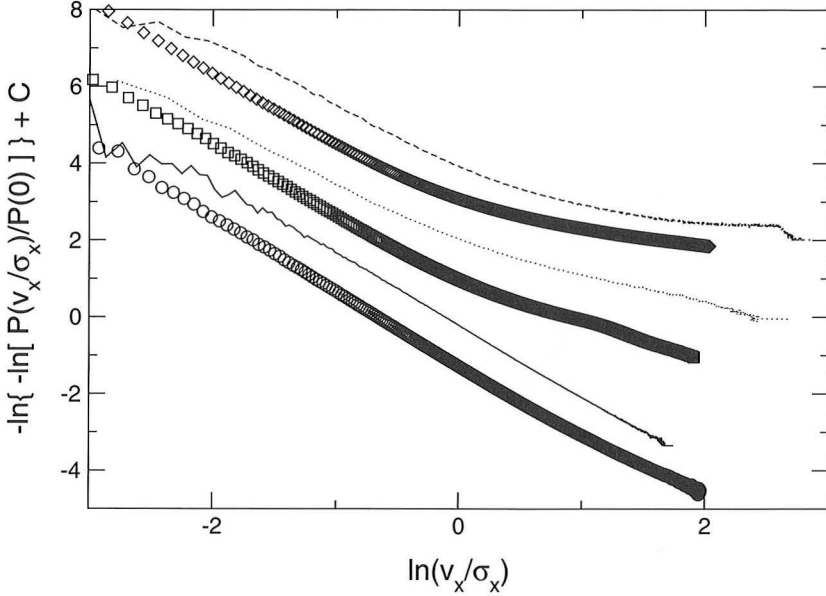


**Figure 2.16:**  $-\ln\{-\ln[P(v_x/\sigma_x)/P(0)]\} + C$  versus  $\ln(v_x/\sigma_x)$ . The symbols shown are velocity distributions acquired by simulation for  $q = 120$  (uniform heating,  $\circ$ ),  $0.08$  (boundary heating,  $\square$ ),  $0.012$  (homogeneous two-point heating [51],  $\diamond$ ). The lines show the velocity distributions found in the model for the same values of  $q$  (solid, dotted, dashed).

$$\mathbf{v}'_i = \mathbf{v}_i - \frac{1 + \eta}{2} \begin{pmatrix} \cos^2 \theta & \sin \theta \cos \theta \\ \sin \theta \cos \theta & \sin^2 \theta \end{pmatrix} (\mathbf{v}_i - \mathbf{v}_j), \quad (2.18)$$

where  $\mathbf{v}_i$  and  $\mathbf{v}_j$  are the velocities of particles  $i$  and  $j$ ,  $\eta$  is the coefficient of restitution and  $\theta$  is the angle between the separation vector  $\mathbf{r}_{ij}$  and a reference axis  $\hat{\mathbf{s}}$ . We discard values of  $\theta$  corresponding to  $(\mathbf{v}_j - \mathbf{v}_i) \cdot \mathbf{r}_{ij} < 0$  as these represent unphysical collisions. We heat the particles  $k$  by adding a random amount of velocity according to Eq. 2.12. To prevent the velocities from running away, we subtract the center-of-mass velocity after heating. In a single time step,  $N_H = H$  particles are heated and  $N_C = 2C$  particles collide. As a consequence,  $q = H/(2C)$ . This model is similar to the inelastic Maxwell model with white noise forcing [55], but here, in addition we can explicitly adjust the heating and collision independently, allowing us to study the behavior as a function of  $q$ . As such it is based upon the work of Ulam[61], but including dissipation. We can measure the heating-dissipation ratio  $q$  in simulations of uniform and boundary heating and in Fig. 2.16 we compare velocity distributions from the model and simulations for different values of  $q$ . We find good qualitative



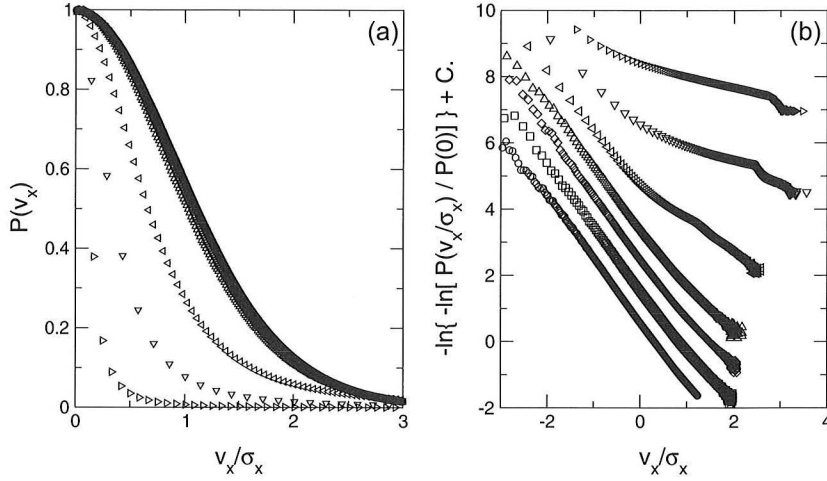


**Figure 2.17:** Velocity distribution for the simple model with  $N = 500$  and  $\eta = 0.4$ . (a)  $P(v_x/\sigma_x)$ . (b)  $-\ln\{-\ln[P(v_x/\sigma_x)/P(0)]\} + C$ . Data is for different values of  $q = \frac{H}{2C}$ :  $q = 50$  ( $\circ$ ),  $q = 5$  ( $\square$ ),  $q = 1$  ( $\diamond$ ),  $q = 0.5$  ( $\triangle$ ),  $q = 0.05$  ( $\triangleleft$ ),  $q = 5 \cdot 10^{-3}$  ( $\nabla$ ) and  $q = 5 \cdot 10^{-4}$  ( $\triangleright$ ).

agreement between simulation and model, even though it has no spatial degrees of freedom. This implies that spatial correlations play a minor role, if any, in  $P(v)$ . Even though kinetic theories have established that certain specific non-Gaussian velocity tail arise in the absence of spatial correlations [54, 55, 62], it has remained an open question whether the entire family of non-Gaussian velocity distributions observed in experiments can be explained without spatial correlations [42].

We study the properties of the model in more detail in Fig. 2.17, where we plot velocity distributions obtained with the simple model for an inelastic gas with  $\eta = 0.4$ . We varied the number of heatings and the number of collisions in a single time step from  $H = 100$  and  $C = 1$  to  $H = 1$  and  $C = 1000$ . As  $q$  is lowered, the velocity distributions develop a crossover and for  $q \ll 1$  the distributions are strongly non-Gaussian, similar to the velocity distributions obtained for  $\Delta t \gg 1$  in two-point heating. In Fig. 2.18 we keep  $q = 0.025$  fixed and vary  $\eta$ . We see that the crossover point shifts to lower velocities as  $\eta$  is lowered.

Not only does the model yield velocity distributions comparable to uniform and boundary heating for similar values of  $q$ , it also qualitatively reproduces the family of distributions observed for the simulations. The transition in Fig. 2.17 as  $q$  is increased compares well to the same transition in Fig. 2.15, where  $\Delta t$  is decreased. Also, the crossover that develops in Fig. 2.10 as  $\eta$  is increased is similar to those

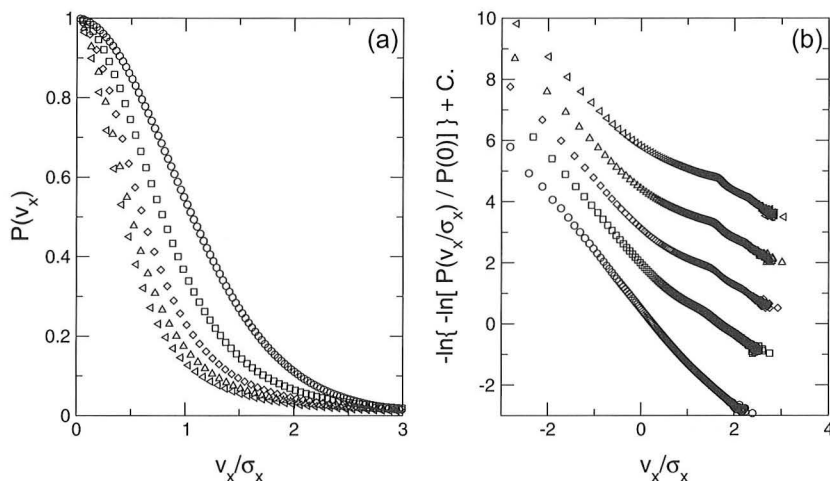


**Figure 2.18:** Velocity distribution for the simple model with  $N = 500$  and  $q = 0.025$ . (a)  $P(v_x/\sigma_x)$ . (b)  $-\ln\{-\ln[P(v_x/\sigma_x)/P(0)]\} + C$ . Data is for  $\eta = 0.9$  ( $\circ$ ),  $0.7$  ( $\square$ ),  $0.5$  ( $\diamond$ ),  $0.3$  ( $\triangle$ ) and  $0.1$  ( $\triangleleft$ ).

seen in Fig. 2.18. This confirms that the velocity distributions are non-Gaussian not because of spatial correlations. Rather, it is the flow of energy through the system, mediated by the inelastic collisions, that determines the shape of the velocity distribution.

## 2.6 Relation to experiments

Unfortunately, experimental results for velocity distributions have remained ambiguous. Different setups and driving mechanisms usually give different velocity distributions. The distribution with a universal exponent of  $\alpha = 1.5$  was obtained by Rouyer and Menon for a setup where particles were confined between two vertical plates and driven in the vertical direction. However, for a different setup, where particles on a horizontal plate were driven in the vertical direction, Olafsen and Urbach found crossovers from exponential to Gaussian distributions when changing the driving of the particles [46, 48, 49]. Blair and Kudrolli used a setup where particles move along an inclined plane [36, 45]. Friction with the plane during collisions reduced the coefficient of restitution to  $\eta \approx 0.5$ , much lower than the coefficients of restitution usually reached in other setups. They found the distribution with exponent  $\alpha = 1.5$  only in the very dilute case. Otherwise, the distributions deviated strongly from both Gaussian and the distribution obtained by Rouyer and Menon.

This different behavior of the velocity distribution from experiment to experiment has yet remained unexplained.

Because of the absence of gravity and friction in our simulations, it is not possible to do a direct comparison between our simulation and experiments. In the experiment of Rouyer and Menon the driving is through the boundary, but there are some significant differences between their heating mechanism and the one we use in simulations with boundary heating. Due to gravity and the geometry of the setup the injection of energy in the experiment of Rouyer and Menon is mainly in the vertical direction. This energy is transferred into the horizontal direction by collisions between particles. Another difference is that in the experiment the frequency of driving is relatively low. Because of this the dynamics of the gas close to the driving boundary is strongly dependent on the phase of the driving cycle. In fact, it has been shown in simulation that for a system similar to the experiment by Rouyer and Menon, a shockwave propagates up through the gas [63]. At a certain distance from the boundary the time dependence has decayed away and the gas enters a steady state. It is in this steady state that the velocity distributions are measured.

It is not yet established how this time dependence and the occurrence of a shock wave influences the velocity distributions in the steady state. A priori it is not clear if it is possible to compare velocity distributions in systems with a strong time-dependence, like the experiments, with those that have no time dependence, as is the case in our simulations. There are, however, reasons to assume this is possible. The velocity distributions in the experiment of Rouyer and Menon are measured only in the direction orthogonal to the driving direction. Simulations show that the effect of the shock in the direction orthogonal to the shock is usually relatively weak and decay rapidly in height [63]. In the steady state, influence of the shock is absent in the orthogonal direction, even while it still may be apparent in the direction perpendicular to the driving direction. So, if we only look at velocity distributions in the orthogonal direction and in the steady state, a comparison between the experiment and our simulations is be valid.

It is also not clear how in this experiment the dynamics of the gas shape the velocity distribution and whether it is controlled by the parameter  $q$ . We speculate that in the steady state the system behaves in fact like a one-dimensional inelastic gas. Fast upward moving particles inject energy in the orthogonal direction when colliding with particles in the steady state, effectively functioning as a heat source. In this picture the mean number of collisions between fast upwards moving particles and particles in the steady state would be  $N_H$ , the average number of heatings, and collisions between the particles in the steady state mutually would be  $N_C$ , the average number of collisions. One way of changing the shape of the velocity distribution would be changing the fraction of particles in the steady state. More particles in

the steady state would lower  $N_H$  and increase  $N_C$  leading to more non-Gaussian velocity distributions.

The above considerations not only apply to the experiment of Rouyer and Menon but to most of the other experiments as well. In the experiments of Blair and Kudrolli and those of Olafsen and Urbach velocity distributions are measured orthogonal to the driving direction. In both cases it is not so much the collisions with the bottom plate that drive the gas in the orthogonal directions, but mainly off-angle collisions between fast upward moving particles with particles that have low velocities in the orthogonal directions. It is in these experiments rather than those of Rouyer and Menon that we find a similar dependence on  $\eta$  and  $q$  as we describe in this article.

In the setup of Olafsen and Urbach velocity distributions go from non-Gaussian to Gaussian when a rough plate is used instead of a flat plate [48]. On a flat plate, energy is injected only in the in-plane directions by off-angle collisions between neighboring particles. With a rough plate, energy is injected directly into the directions parallel to the plate every time a particle collides with the plate, effectively increasing the number of heatings over collisions. Baxter and Olafsen observe the same behavior in a system where a layer of heavy particles is inserted between the other layer of particles and a flat bottom plate [50]. Particles from the upper layer have off-angle collisions with the layer of heavy particles, injecting energy in the in-plane directions every cycle. Particles in the upper layer show Gaussian velocity distributions, whereas particles in the lower layer have non-Gaussian velocity distributions.

The clearest sign of a potential role of  $q$  is seen in an experiment by Blair and Kudrolli [36, 45]. Here the number of collisions is increased by adding more particles. As a result, their velocity distributions develop the same crossover we see both in our simulations and model. The reason why these transitions are not visible in the experiment by Rouyer and Menon as they increase number of particles, is likely that in the first case the effective coefficient of restitution is much lower,  $\eta \approx 0.5$ , due to friction with the inclined plane. These observations have recently been reproduced in simulation [59].

Again, one of the main problems considering the velocity distributions in granular gases is that different setups and experiments usually find different velocity distributions. As we have shown in this section, this variation in velocity distributions could be accounted for largely by changes in the parameter  $q$  among the different setups and experimental conditions. In this way, our finding of the controlling parameter  $q$  could ultimately explain these seemingly inconsistent results.

## 2.7 Conclusions

We compared the velocity distributions of a granular gas that was driven by uniform heating and by heating through the boundary. Both in theory and simulation studies, it is often implicitly assumed that far from the boundary the dynamics of granular gases is well described by uniform heating. Here, we find that there are clear qualitative differences. When driven through the boundary, for instance, the gas can form coexisting “cool” liquid-like clusters surrounded by a “hot” gaseous state for certain values of  $\phi$  and  $\eta$ . Such clusters do not occur in our simulations with uniform heating. For increasing dissipation, these clusters grow in size and ultimately exhibit crystalline order.

The difference between uniform heating and boundary heating also extends to the velocity distributions. In both cases, we studied the dynamics of the granular gases while systematically varying all relevant parameters. For uniform heating, we confirmed that the distribution was close to Gaussian for a wide range of the coefficient of restitution  $\eta$ , area fraction  $\phi$  and particle number  $N$ . When heating through the boundary, we found that the granular gas developed spatial gradients in density and mean kinetic energy, with density peaking in the center and mean kinetic energy at the boundary. Surprisingly, the velocity distributions are relatively insensitive to the precise position in these gradients. When normalized by the mean kinetic energy, the velocity distributions collapse on each other, consistent with previously reported results [41, 58]. For boundary heating, the velocity distribution is often non-Gaussian, with the precise shape depending sensitively on  $\eta$ ,  $\phi$  and  $N$ . Only for dilute systems of almost elastic particles do we find the Gaussian distribution that is always observed for uniform heating. Furthermore, we show that there is no evidence for a universal velocity distribution with a constant exponent  $\alpha = 1.5$ . Instead, for boundary heating, we find that velocity distributions cross over from one exponent to another for high velocities. For this regime we observe a wide range of exponents and we find  $\alpha = 1.5$  only for specific values of  $\phi$  and  $\eta$ . These qualitative differences between the velocity distributions for uniform and boundary heating demonstrate that the form of the distributions is not simply a function of material parameters (e.g.,  $\eta$ ).

Instead, we show that the distribution of velocities for dissipative gases, while not universal in form, seems to depend only on two parameters: the coefficient of restitution  $\eta$  (a material parameter) and  $q = N_H/N_C$ , the average ratio of heatings and collisions in the gas (a function of experimental conditions). We find that velocity distributions range from Gaussian for  $q \gg 1$ , where heating dominates dissipation, to strongly non-Gaussian for  $q \ll 1$ , where the dynamics of the gas is dominated by the dissipative collisions between particles.

Finally, a simple model of a driven, inelastic gas without spatial degrees of freedom reproduces the entire family of velocity distributions we find in simulation, as we vary  $\eta$  and  $q$ . This means that the velocity distributions are non-Gaussian not because of spatial correlations. Rather, it is the cascade of energy from a few high-energy particles to the slow-moving bulk of the gas that is the key determinant of the non-Gaussian velocity distributions. These observations should aid in the construction of a kinetic theory of dissipative gases and help explain the sometimes confusing results of recent experiments.

---

## **Chapter 3**

# **Velocity distributions: experiments**

J.S. van Zon, J. Kreft, Daniel I. Goldman,  
D. Miracle, J.B. Swift and Harry L. Swinney  
*Phys. Rev. E* 70, 040301(R) (2004)  
J.S. van Zon, J. Kreft, Daniel I. Goldman,  
D. Miracle, J.B. Swift and Harry L. Swinney  
*to be submitted*

### 3.1 Introduction

In this chapter, we study how the dynamics of granular gases can be studied experimentally. In Chapter 2, we focused on understanding how the dissipative dynamics of inelastic gases leads to non-Gaussian velocity distributions. Here, we study by experiment how the velocity distributions are determined by the friction between granular particles and the sidewalls of the container. We also investigate the influence of the complicated dynamics of granular gases both in space and time on the shape of the velocity distribution, as obtained experimentally.

The velocity distributions of granular gases are often studied in confined monolayers of grains, including vertical [41], inclined [36, 45] and horizontal layers [46, 50]. In most experiments the granular gas is driven inhomogeneously by an oscillating boundary [36, 41, 45]. As a consequence, properties of granular gases like the density or granular temperature often depend on time and on position in the container. In the vertically oscillated gas the behavior of the grains varies significantly both in time and space as a shock wave travels upwards through the gas [63, 64]. Consequently, local properties, like the areal density  $\rho$  and the granular temperature  $T$  of the gas, vary between different heights in the gas and different phases of the driving cycle.

Velocity distributions are usually obtained by averaging over regions with different local properties. Several authors have addressed the influence of this averaging process on the velocity distributions [41, 45, 46]. For instance, it has been suggested that non-Gaussian velocity distributions might arise by averaging over regions of different granular temperature and density that do have a Gaussian velocity distribution locally [42]. However, there is experimental evidence that such averaging is not responsible for non-Gaussian velocity distributions in granular gases [45, 46]. Furthermore, non-Gaussian velocity distributions are still observed in the steady state of the gas, where density no longer fluctuates with the phase of the driving cycle [41]. Yet, even when the density is constant in time, spatial gradients in density and granular temperature might still occur and it is not clear what the effect is of averaging the velocity distribution over this region. Exactly how local properties like



density and granular temperature vary with height in the container and phase of the driving cycle has been studied by simulation [63, 64], but has not been measured experimentally in great detail [41].

In our experiments on a vertically oscillating monolayers of spheres, we are able to resolve the dynamics of the areal density  $\rho$ , the horizontal granular temperature  $T_x$  and the vertical granular temperature  $T_z$  and the corresponding velocity distributions  $P(v_x)$  and  $P(v_z)$  as a function of the height in the box  $z$  and the phase of the driving cycle  $\phi$ . This allows us to experimentally address these questions regarding averaging, as we can monitor the local properties inside and outside of the steady state and study the effect of the local fluctuations on the resulting velocity distribution. Furthermore, most experiments are carried out in containers that are not evacuated. Potentially, the presence of air can influence the behavior of the gas, including the velocity distributions, either through increased friction with the air or through electrostatic interactions between particles and the wall. In our setup, we can evacuate the container to study the effect of air on the dynamics of the granular gas. Surprisingly, we find that the velocity distribution depends only weakly on the position in the container or on the phase of the driving cycle, even outside of the steady state region and close to the bottom of the container. We also find that the velocity distribution is not changed upon evacuation of the container.

Many experiments have been conducted on monolayers of particles because limiting the motion in one dimension allows the use of a video camera to record the entire velocity field [36, 41, 44–49]. Since velocities in the suppressed direction can never be fully eliminated, these systems are quasi-two-dimensional (2D), not strictly 2D. In such confined geometries, particles can make as many or more collisions with the wall as with other grains during one driving cycle. Collisions with walls may then influence the shape of the velocity distribution function. We find that the confining sidewalls play a major role in determining the velocity distribution function, which we obtain from experiments and simulations on a vertically oscillating monolayer of particles whose motion is suppressed in one horizontal direction.

## 3.2 Experimental setup and simulations

Our setup is similar to the one used by Rouyer and Menon [41] and consists of 130 steel or brass beads of diameter  $d = 1.6$  mm, confined between two vertical Plexiglas plates. These plates are separated by a gap of  $1.15d$  and we use sidewalls of Plexiglas to confine the particles to a region of  $48d$  in the horizontal direction by  $32d$  in the vertical direction. The container is airtight and can be evacuated. The steel particles have a coefficient of restitution  $\eta \approx 0.9$  and the brass particles have  $\eta \approx 0.8$ . We

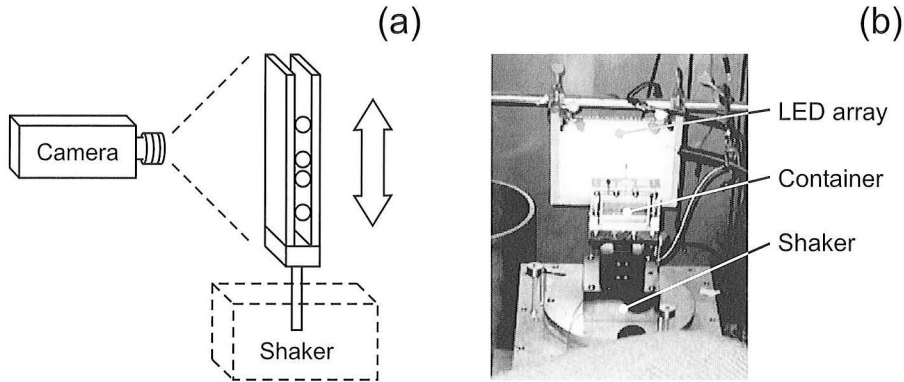


**Figure 3.1:** (a) Schematic setup of the experiment. A monolayer of metal beads confined between two vertical sidewalls is shaken in the vertical direction by an electromechanical shaker. A high-speed digital camera records the motion of the particles. (b) The actual setup. The shaker is in a heavy metal base to suppress motions in the horizontal direction. The container is made of Plexiglas and airtight. On top of the container the nozzle used to evacuate the container is visible. The container is lit from behind by an LED array.

use an electromechanical shaker (VTS 100, Vibration Test Systems) to shake the container sinusoidally in the vertical direction and an airbearing to constrain any horizontal motion. A schematic representation of the setup is shown in Fig. 3.1. The driving frequency was  $f = 50\text{Hz}$  and the peak acceleration  $\Gamma = 4\pi^2 f_2 A/g = 20$ . This corresponds to an amplitude  $A = 1.25d$ . The peak acceleration we use is much smaller than the values used for  $\Gamma$  by Rouyer and Menon. As a consequence, our gas is only heated by the bottom of the container and the density profile is not symmetric around the center of mass. Particle motions are recorded by a high-speed digital camera (Phantom V4, Vision Research) at a frame rate of 1000 per second and 512x512 pixels. We use backlight illumination by an LED-array to light the container. As a consequence, the beads appear as black disks against a bright background. Images of the granular gas as obtained by the camera are shown in Fig. 3.2.

We compare our experimental observations with simulations of the same experimental setup. For this an event-driven algorithm described in Ref. [65] was used, which was conducted for the same  $\Gamma$ ,  $f$ , and sidewall separation as the experiment. The parameters characterizing ball-ball interactions were the minimum coefficient of restitution  $\eta = 0.7$ , the coefficient of sliding friction  $\mu_b = 0.5$ , and the rotational coefficient of restitution  $\beta = 0.35$ . The coefficient of restitution varies with relative normal velocity ( $v_n$ ) as described in Ref. [65]: the coefficient of restitution is the

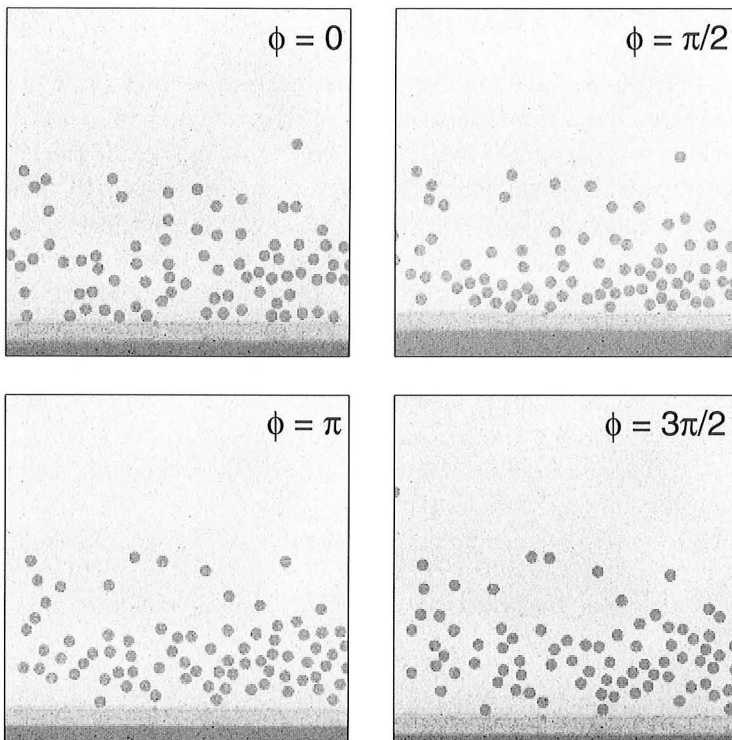


**Figure 3.2:** A  $27d$  by  $27d$  portion of the box as seen through the camera for different phases of the driving cycle. At  $\phi = 0$ , the bottom plate is in the equilibrium position and moving upwards. At this peak acceleration, the gas is only heated at the bottom of the container.

maximum of  $\eta$  and  $1 - (1 - \eta)(v_n/\sqrt{gd})^{3/4}$ . The TC model of Luding and McNamara was also used to prevent inelastic collapse by setting the coefficient of restitution to unity if a particle was involved in another collision within  $3.7 \times 10^{-4}$  seconds of the previous one [29]. For interactions between balls and the container (both the sidewalls and bottom), we used the same values for  $e$  and  $\beta$ , but we varied the coefficient of sliding friction with the wall from  $\mu_w = 0$  (no sidewall or bottom friction) to  $\mu_w = 1$ . To reproduce the experiment,  $N = 130$  particles were simulated in a box of height  $200d$ , width  $48d$ , and plate separation  $1.1d$ . The entire box was oscillated vertically so the particles collided with moving sidewalls, in addition to the bottom, as in the experiment.

### 3.3 Image analysis

In order to study the dynamics of the granular gas, we need to extract the trajectories  $\mathbf{r}_i(t)$  of the particles from the sequence of images obtained by the camera. All particle tracking was performed in IDL (Research Systems Inc). To track the particle positions in time at sub-pixel accuracy we use techniques originally developed for tracking colloidal particles [66]. However, tracking granular particles in our setup comes with difficulties that are different from those encountered when tracking colloidal particles. Colloidal particles have Gaussian intensity profiles when imaged under the microscope, whereas in our setup particles appear as black disks against a bright background. Furthermore, whereas for colloidal particles the background is simple and changes little during measurements, the background in our images has complicated features and oscillates vertically in time, as can be seen in Fig. 3.2. In this section I will give a brief overview of the particle tracking algorithm and how we adapted it for tracking granular particles.

The particle tracking algorithm progresses through five separate steps:

- Individual images are corrected for the background and other imperfections.
- Candidate particle positions are located in each image at pixel precision.
- *False positives*, features on the image that were mistakenly identified as particles, are discarded.
- Positions are refined to sub-pixel precision.
- The time-resolved particle positions are linked into trajectories.

I will discuss these different steps in more detail below.

#### 3.3.1 Image restoration

The particle tracking algorithm we adapted requires particles to be bright objects. Therefore, we first invert all images, so that now particles appear as bright disks on a dark background. The original algorithm in Ref. [66] was designed to handle spatially uniform backgrounds superimposed with long-wavelength modulations in background brightness and short-wavelength noise due to digitization noise in the CCD camera and other hardware. In our case, however, the background has distinct features, such as small scratches and the boundary between the lid and the container. These features could be mistaken as particles at a later stage and it is of great benefit to filter them out already at an early stage.

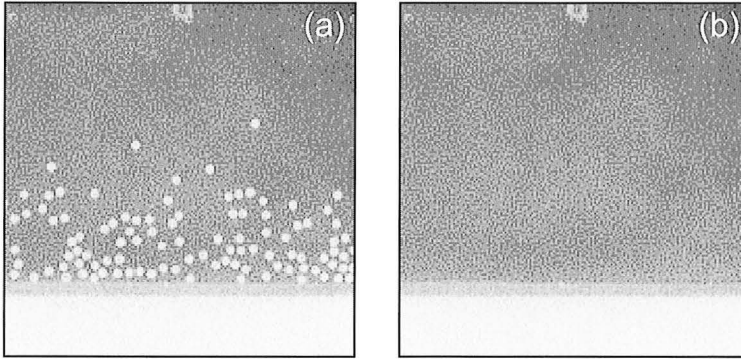


**Figure 3.3:** Background subtraction. (a) A single frame of the container for phase  $\phi = \pi/2$ . (b) Reconstructed background. The background is reconstructed by averaging every pixel over all frames with the same phase  $\phi$ , provided that the current pixel is not occupied by a particle.

We do this by subtracting the background. Because the background is always partly obscured by the particles in the container, we first need to reconstruct the background. Because the container oscillates at a frequency of 50 Hz, we need to reconstruct 20 background images, one at every phase  $\phi$  we record. We do this by averaging every pixel in the background over all frames in a single run with the same  $\phi$ , provided that in this frames in the pixel is not occupied by a particle. We can clearly distinguish between a pixel occupied by a particle and one that is part of the background, because the particles are significantly brighter than the background. An example of a reconstructed background is shown in Fig. 3.3 together with one of the images it is reconstructed from. When the background is subtracted, the particles appear as bright discs on a black background.

In order to correct for short-range noise due to digitization we convolute the image  $A(x, y)$  with a Gaussian kernel [66]:

$$A'(x, y) = \frac{1}{B} \sum_{i, j=-w}^w K_\lambda(i, j) A(x + i, y + j), \quad (3.1)$$

with  $w$  the range of the convolution,  $B = \sum_{i, j} K_\lambda(i, j)$  and the convolution kernel:

$$K_\lambda(i, j) = \exp\left(-\frac{i^2 + j^2}{4\lambda_n^2}\right). \quad (3.2)$$

Digitization noise is often purely random with a correlation length of 1 pixel. Such a convolution with  $\lambda_n \approx 1$  pixel strongly suppresses such noise, without unnecessarily blurring the image.

### 3.3.2 Locating candidate particles

The particle tracking algorithm we adapt assumes that images of particles are strongly peaked around the center of the particle, as is the case for the Gaussian intensity profile obtained for colloidal particles by light scattering. Candidate particles are then identified by finding the brightest pixel within a certain radius. In our case, however, particles are discs of approximately uniform intensity. A convenient approach is to convolve the background subtracted image  $A'(x, y)$  with the image of circle of the same radius  $R$  as the discs in the image:

$$A''(x, y) = \sum_{i, j=-w}^w K_R(i, j)A'(x + i, y + j), \quad (3.3)$$

where  $R$  is the radius of the particle in pixels and the convolution kernel  $K_R(i, j)$  is:

$$K_R(i, j) = \begin{cases} 1 & i^2 + j^2 \leq R^2 \\ 0 & \text{otherwise} \end{cases} \quad (3.4)$$

For odd  $R$ , for instance, the kernel  $K_R(i, j)$  represents the image of a disc of radius  $R$  centered at  $i, j = 0$ . In the continuum case, the convolution of a disc with radius  $R$  with itself is approximately a cone of radius  $2R$ . This is more easily seen in one dimension: in this case a particle of radius  $R$ , centered around  $x = x_0$ , is represented by the particle profile:

$$S(x) = \begin{cases} 1 & x_0 - R \leq x \leq x_0 + R, \\ 0 & \text{otherwise,} \end{cases} \quad (3.5)$$

indicated in Fig. 3.4(a). The convolution of this function with itself is:

$$S'(x) = \int_{-\infty}^{\infty} S(x')S(x + x')dx' \quad (3.6)$$

and is a triangle with radius  $2R$  centered around  $x_0$ , as indicated in Fig. 3.4(b). The convolution in Eq. 3.6 measures the area of overlap between the particle profiles  $S(x')$  and  $S(x + x')$  for each  $x$ . If  $x = x_0 \pm 2R$ , the two profiles are just touching. For  $x = x_0$  the two profiles completely overlap and the convolution has its maximum. The same convolution, but now for the discrete case, is also shown in Fig. 3.4(a) and (b). In two dimensions, the corresponding convolution in Eq. 3.3 with discs imaged by the camera yields a cone with a unique maximum at the pixel in the center of the disc, as long as the kernel  $K_R(i, j)$  has an equal or larger radius  $R$  than expected for the discs in the experiment.

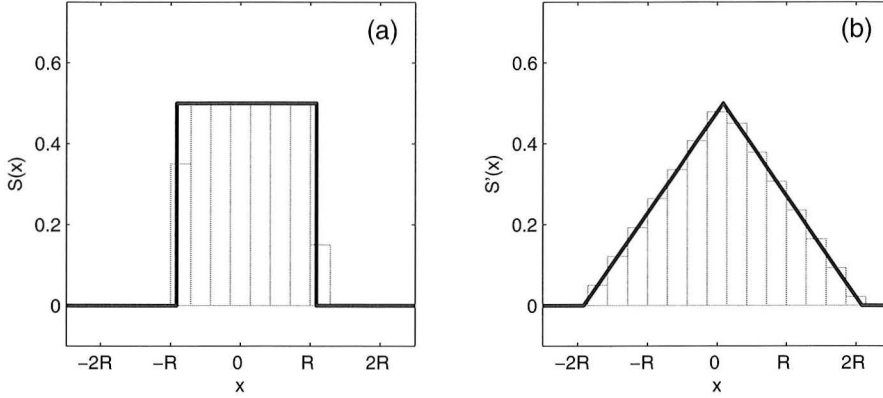


**Figure 3.4:** Finding the center of a particle in one dimension. (a) The particle profile  $S(x)$  (black line) for a particle of radius  $R$  and centered around  $x_0 = 0.3R/7$ . The profile is also shown in the discrete case (gray bars) for pixel size  $\Delta r = R/7$ . Because of the sub-pixel displacement  $x_0 = 0.3\Delta r$ , the discrete profile is asymmetric around the origin. (b) The convolution in Eq. 3.6 of the particle profile  $S(x)$  with itself (black line). The convolution is a triangle with radius  $2R$  centered around  $x_0$ . In the discrete case (gray bars) the convolution yields a similar shape, but is asymmetric around the origin. This asymmetry contains all the information on the sub-pixel displacement  $x_0$ .

After this convolution, each particle within the frame of view can be identified by its local brightness maximum in the convoluted image  $A''(x, y)$ . Using the convolution with the kernel  $K_R(i, j)$  in Eq. 3.4 has an additional advantage. The convolution in Eq. 3.3 is effectively a procedure for comparing the brightness distribution at each pixel in the image with that expected for a disc of radius  $R$ . The brightness maximum in the convoluted image  $A''(x, y)$  reaches its maximum value when the surrounding brightness distribution equals that of a disc. If, on the other hand, the local brightness distribution is that of a false positive with a different shape than that of a disc of radius  $R$ , the brightness maximum is significantly smaller. This makes it much easier to recognize the false positives in subsequent steps. Finally, the centroid, or the position of the particle at pixel precision, is found by gray scale dilation. Gray scale dilation is an elementary morphological operation which sets the value at  $A''(x, y)$  to the maximum value found within a distance  $w$  of the position  $(x, y)$ . A pixel in the original image  $A''(x, y)$  that has the same value in the dilated image is then considered a tentative particle with its center at that location.

### 3.3.3 Discarding false positives

False positives are recognized by studying for each tentative particle the zeroth moment  $m_0$  and second moment  $m_2$  of its brightness distribution, defined as:

$$m_0 = \sum_{i^2+j^2 \leq w^2} A''(x+i, y+j), \quad (3.7)$$

$$m_2 = \frac{1}{m_0} \sum_{i^2+j^2 \leq w^2} A''(x+i, y+j), \quad (3.8)$$

where  $A''(x, y)$  is the image convolved with a disc of radius  $R$  and  $(x, y)$  is the location of the particle's centroid. The zeroth moment  $m_0$  is a measure for the amplitude of the convolution of the particle, or, indirectly, a measure to what extent the intensity profile of the candidate particle looks like that of a disc with radius  $R$ . The second moment  $m_2$  is a measure for the spatial extension of the candidate particle. A candidate particle that is very bright, but is smaller than a disc with radius  $R$  cannot be distinguished from a real particle based on  $m_0$ , but will have a significantly different value of  $m_2$ . When the distribution of moments of the candidate particles is plotted in the  $(m_0, m_2)$  plane, all the granular particles cluster together. False positives can be discriminated from real particles by their moments  $m_0$  and  $m_2$  as they fall outside of this cluster in the  $(m_0, m_2)$  plane. By discarding all candidate particles that lie outside of this range, false positives can be filtered out in a very reliable way. The exact cut-off values for  $m_0$  and  $m_2$  are easily determined by hand.

### 3.3.4 Determining positions at sub-pixel precision

So far we have determined the positions of the particles at pixel accuracy. The actual positions at sub-pixel accuracy are given by  $\mathbf{x} = (x + \epsilon_x, y + \epsilon_y)$ , where the sub-pixel offsets  $\epsilon_x$  and  $\epsilon_y$  are calculated by the first moments:

$$\begin{pmatrix} \epsilon_x \\ \epsilon_y \end{pmatrix} = \frac{1}{m_0} \sum_{i^2+j^2 \leq w^2} \begin{pmatrix} i \\ j \end{pmatrix} A''(x+i, y+j), \quad (3.9)$$

where  $m_0$  is the zeroth moment in Eq. 3.7 and  $A''(x, y)$  is the convolved image. In principle, this procedure gives the exact sub-pixel offset. For instance, calculating the first moment of the discretized intensity distribution in Fig. 3.4(b) correctly reproduces the offset  $\epsilon_x = 0.3\Delta r$ . In practice, the accuracy of determining the sub-pixel offset is limited by experimental noise.



### 3.3.5 Linking positions into trajectories

Particle positions are linked into trajectories by assuming that the probability of a certain displacement between consecutive frames decreases with the size of the displacement. The most likely assignment of particle labels from one frame to the other is the one that maximizes the total probability. Because the algorithm was developed in the context of colloids, the probability distribution of displacements is the Gaussian distribution expected for diffusion. We find that this distribution also gives satisfactory results in our case, provided that the displacement between two frames is never more than a particle diameter. The algorithm allows for the deletion and creation of particle labels as particles move out of the field of view.

Figure 3.5 shows the application of the particle tracking algorithm on a frame from an experimental run. After background subtraction, the particles appear as bright disks on a black background and a considerable amount of noise is visible on the intensity distribution of the particles. After convolution, isolated particles appear as cones with the brightest pixel at the center of the disc. When particles are in close proximity, the convolved image is more complicated as the region between the particles receives contributions from both particles. The particle positions at sub-pixel position are shown overlayed over the original inverted image. The velocities of the particles are calculated by the displacement between subsequent frames divided by the time between frames.

We tested the algorithm by generating a fake data set from simulation data. From the positions of the particles obtained by simulation we generated high-resolution images of particles in the container. We then sampled these figures down to a resolution comparable to the resolution of the images obtained experimentally. At this resolution particles have a radius of  $R = 13$  pixels. The velocities of the particles and time resolution between consecutive frames were comparable to those in the experiment. We superimposed different levels of random noise on top of the images to probe the sensitivity of the particle tracking algorithm to experimental noise. In Fig. 3.6 we compare the velocity distribution measured directly in the simulation with those calculated from the particle trajectories obtained by the particle tracking algorithm. This figure shows excellent overlap for levels of noise comparable to those observed in the experiment, indicating that we should be able to reliably generate velocity distributions from images obtained experimentally.

We estimated the accuracy with which we measure the particle positions by monitoring the horizontal velocity of particles in the granular gas. Because gravity operates in the vertical direction, the particles undergo rectilinear motion in the horizontal direction. By measuring the variations in velocity obtained for such trajectories, we can estimate the positional accuracy. These measurements indicate that we can

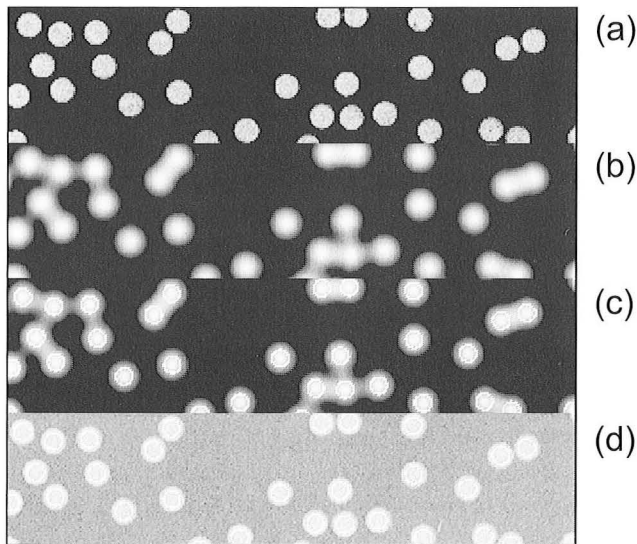


**Figure 3.5:** Different steps of the particle tracking algorithm. (a) After background subtraction. (b) After convolution with the image of a disk of radius  $R$ . (c) After finding the brightest pixel and discarding false positives. (d) Particle positions at sub-pixel position overlaid over the original inverted image.

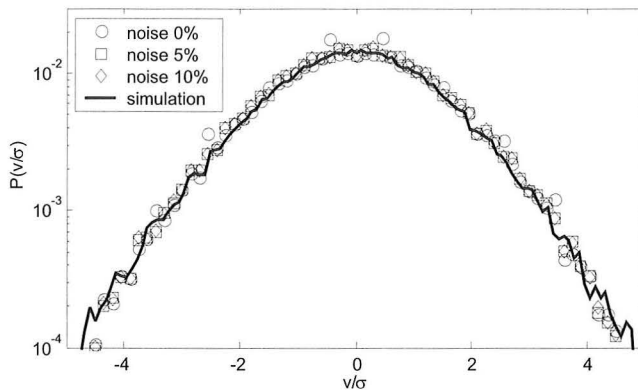


**Figure 3.6:** Accuracy of particle tracking. Velocity distributions obtained directly from the simulation (black line) and obtained by the particle tracking algorithm without noise (circles), with 5% noise (squares) and with 10% noise (diamonds). The velocity distribution without noise has peaks superimposed at  $\pm 3n/2(v/\sigma)$  with  $n = 0, 1, \dots$ . These peaks are due to an artifact in the fake data generation and disappear when noise is present.

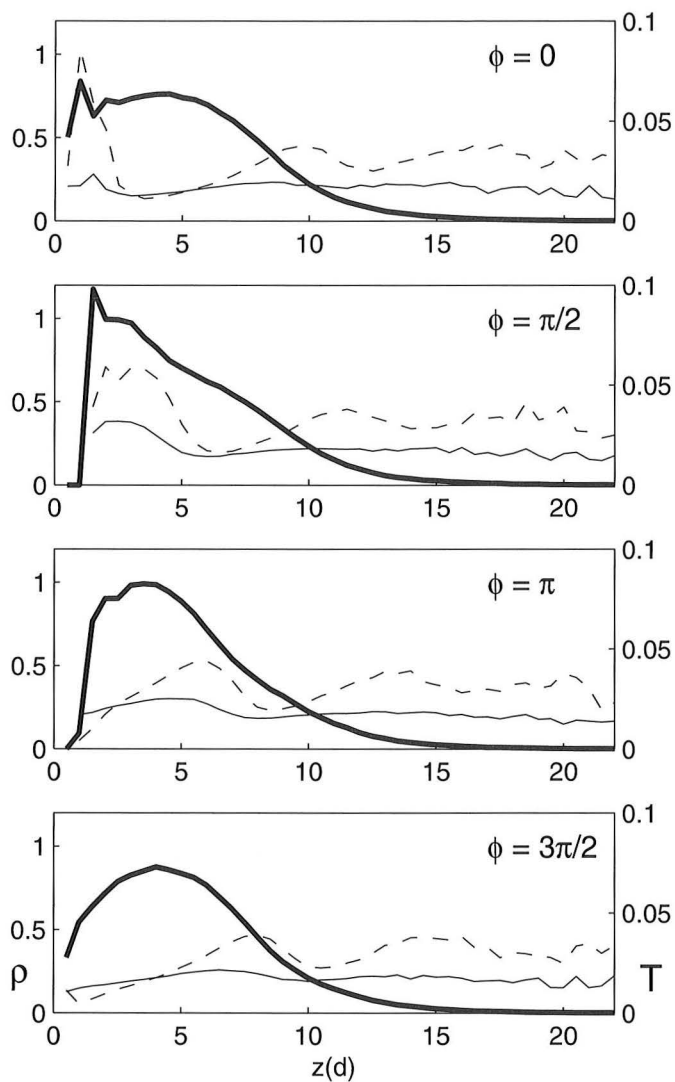
resolve particle displacements up to an accuracy of 0.004mm (or  $0.0025d$ ).

To analyze the gas, we divide the container into horizontal slices of height  $d$ , as the system should be invariant in the horizontal direction, and record the density and temperature of the gas in these slices. To resolve the dynamics in time, each cycle was divided into 20 bins. The aerial density  $\rho$  is defined as the total area of the particles in the slice divided by the area of the slice. The granular temperatures are defined as  $T_x = \langle (v_x - \langle v_x \rangle)^2 \rangle$  and  $T_z = \langle (v_z - \langle v_z \rangle)^2 \rangle$ , where  $x$  is the horizontal direction,  $z$  is the vertical direction and  $\langle \rangle$  denotes an average taken over all particles in the same slice and at the same phase in the cycle. For each run, the peak acceleration was ramped up to the desired value in 20 driving cycles, after which data was taken for 102 cycles. Statistical properties are obtained by averaging over 7650 driving cycles.

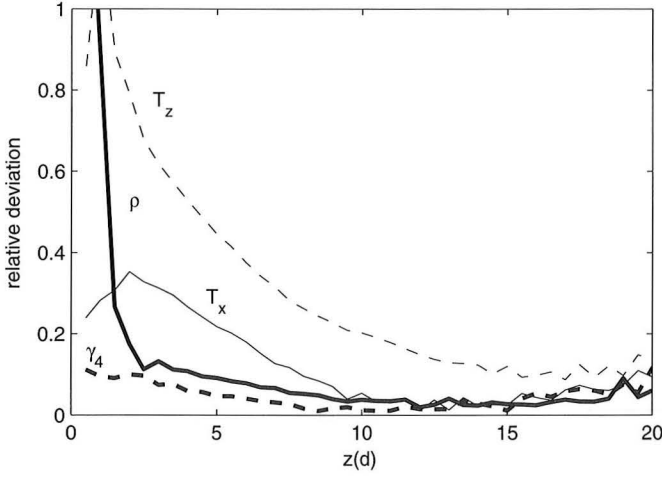
### 3.4 Steady state

Figure 3.7 shows the dependence of  $\rho$ ,  $T_x$  and  $T_z$  on the height in the box and phase of the driving cycle as the container is shaken with  $N = 130$  steel beads,  $f = 50\text{Hz}$  and  $\Gamma = 20$ . At  $\phi = 0$  the bottom plate is in the equilibrium position and moving upwards. It is around this phase in the cycle that the gas collides most strongly with bottom of the container and a strong peak in  $T_z$  develops here as particles get excited in the vertical direction. At  $\phi = \pi/2$  the container is at its maximum height. A strong peak in  $\rho$  near the bottom plate results as particles are pushed up by the plate, along with a second peak higher in the box corresponding to particles still falling towards the plate. Through collisions in the gas energy is transferred from the vertical to the horizontal direction, causing a peak in  $T_x$ . These disturbances in density and temperature travel upwards in the box during the rest of the cycle. For  $\rho$  and  $T_x$  the amplitude of the disturbance decays rapidly with height and above the certain height the gas forms a steady state for these parameters.  $T_z$ , on the contrary, remains oscillatory up until much higher: a wave of high  $T_z$  can still be seen traveling through the gas as a new one is being excited at the bottom of the container.

The existence of a steady state for  $\rho$  and  $T_x$  is made more explicit in Fig. 3.8. Here we show for every height the relative deviation in time of the aerial density  $\rho$ , the granular temperatures  $T_x$  and  $T_z$  and the kurtosis  $\gamma_4$  of the horizontal velocity distribution  $P(v_x)$ . Here, the relative deviation is defined as the standard deviation of the quantity divided by the mean as it varies with the phase of the driving cycle. The kurtosis  $\gamma_4$  of the velocity distribution  $P(v_x)$  is defined as  $\gamma_4 = \langle v_x^4 \rangle / \langle v_x^2 \rangle^2$  and is a measure of the peakedness of the distribution. For a Gaussian distribution  $\gamma_4 = 3$



**Figure 3.7:** Aerial density  $\rho$  (solid thick line) and the granular temperatures  $T_x$  and  $T_z$  (solid thin line and dashed line) shown as a function of the height in the box for  $N = 130$ ,  $f = 50\text{Hz}$  and  $\Gamma = 20$ . Consecutive images represent different phases  $\phi$  in the driving cycle.



**Figure 3.8:** The relative deviation in time of the aerial density  $\rho$  (thick solid line), the kurtosis  $\gamma_4$  (thick dashed line) and the granular temperatures  $T_x$  (thin solid line) and  $T_z$  (thin dashed line) as function of the height in the box. The deviation of the kurtosis was multiplied by a factor 5 for clarity. Above a certain height  $\rho$ ,  $T_x$  and  $\gamma_4$  become stationary, but the deviation of  $T_z$  remains large in this region. Higher in the box, all relative deviations are dominated by noise.

and deviations from this value have been used before to characterize non-Gaussian distributions.

As can be seen in Fig. 3.8 the kurtosis  $\gamma_4$  becomes stationary above a height of  $z = 8d$ . This suggests that above this height the corresponding velocity distribution  $P(v_x)$  is independent of the phase of the driving cycle. A little higher in the box, at  $z = 10d$ ,  $\rho$  and  $T_x$  become constant in time. The reason that the relative deviation of  $\rho$  in this region is bigger than that of  $T_x$  is because the number of particles here becomes very small and the deviation is largely dominated by statistical fluctuations. Fig. 3.8 also shows that  $T_z$  fluctuates much more strongly than  $T_x$  throughout the box and is nowhere stationary. In the upper part of the box the relative deviation in time of all quantities becomes large because of statistical noise. Measurements done at the same  $f$  and  $\Gamma$  but in air or with brass beads instead of steel beads show the same dynamics of  $\rho$ ,  $T_x$  and  $T_z$  in time and space and produce a similar steady state. Furthermore, the space and time dependence of  $\rho$ ,  $T_x$  and  $T_z$  seen in Figs. 3.7 and 3.8 agrees well with results from previous simulations [64].

### 3.4.1 Horizontal velocity distributions

Here, we focus on the dependence of the velocity distributions on the height in the container and the phase of the driving cycle. We study the non-Gaussian features of the velocity distribution in Section 3.5. In Fig. 3.9 we show the velocity distribution  $P(v_x/\sigma_x)$  obtained for  $N = 130$ ,  $f = 50\text{Hz}$  and  $\Gamma = 20$  as a function of the height  $z$  in the container. The distributions are averaged over the driving cycle and normalized by  $\sigma_x^2 = \langle v_x^2 \rangle$ . The velocity distributions are not exactly symmetric around  $v_x = 0$  due to a slight tilt in the container as we show in Section 3.5. The amount of asymmetry varies with the height in the container. A remarkable feature of the velocity distributions observed here is a sharply peaked maximum, which results from friction between the particles and the sidewalls as we will show in Section 3.5. We find that the functional form of the velocity distributions is relatively insensitive to the position in the container. The largest deviation from the distributions observed in the steady state is found close to the bottom of the container, where the fluctuations in density and granular temperature are maximal. In Fig. 3.9, we also show that these velocity distributions are clearly different from both Gaussian distributions and the distribution observed by Rouyer and Menon with  $\alpha = 1.5$ [41]. Next, we examine the dependence of the velocity distribution on the phase of the driving cycle. In Fig. 3.10 we plot  $P(v_x)$  for  $\phi = 0, \pi/2, \pi$  and  $3\pi/2$  and for different heights in the container,  $z = 5d$  and  $z = 10d$ . In both cases, the velocity distributions show little variation when results for different  $\phi$  are plotted on top of each other, even though the gas is in steady state only for  $z \geq 10d$ .

A different representation of the velocity distribution  $P(v_x)$  is shown in Fig. 3.11. Here, we plot the fraction of the particles found in the container at height  $z$  and with vertical velocity  $v_z$ , for successive phases of the driving cycle. Again, at  $\phi = 0$  the container is in the equilibrium position and moving upwards. As the gas is compressed, the velocity distribution widens considerably close to the bottom of the container, corresponding to the peak in  $T_x$  observed in Fig. 3.2. This disturbance decays away as it travels upwards in the container. It is apparent that at  $z = 5d$  the velocity distribution still shows a strong phase dependence, even though when normalized by  $\sigma_x$  this dependence disappears, as shown in Fig. 3.10.

In Fig. 3.12 we focus on the dependence of the high velocity tails of the distributions on the location in the container. When velocity distributions taken from different heights  $z$  are averaged over the driving cycle, we find that in all cases the high velocity tail can be fitted with distribution  $P_\alpha(v)$  with  $\alpha \approx 1.7$ . We find a similar picture when we examine the high velocity tails for different phases of the driving cycle (not shown here). In both cases, we see that the tails are very similar in all cases and that deviations only occur for small velocities in a way that depends on

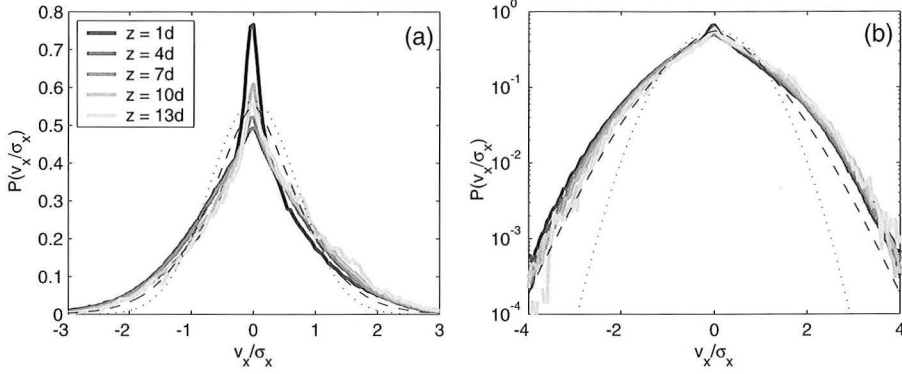


**Figure 3.9:** The horizontal velocity distribution  $P(v_x/\sigma_x)$  for  $N = 130$ ,  $f = 50\text{Hz}$  and  $\Gamma = 20$ , measured for different heights in the box and averaged over the driving cycle. The velocity distributions are shown in (a) linear and (b) logarithmic scales. Also shown is a Gaussian distribution (dotted line) with exponent  $\alpha = 2$  and the velocity distribution found by Rouyer and Menon (dashed line) with exponent  $\alpha = 1.5$ .

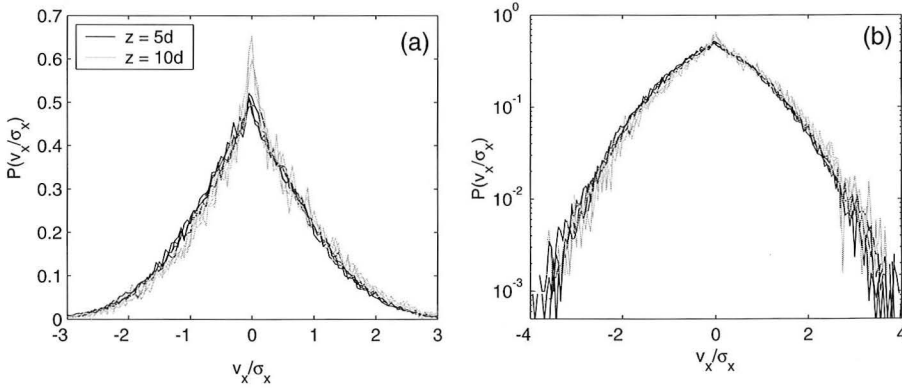


**Figure 3.10:** The horizontal velocity distribution  $P(v_x/\sigma_x)$  for different phases of the driving cycle. Velocity distributions are plotted for  $\phi = 0, \pi/2, \pi$  and  $3\pi/2$  at heights  $z = 5d$  (black lines) and  $z = 10d$  (gray lines) in (a) linear scale and (b) logarithmic scale.

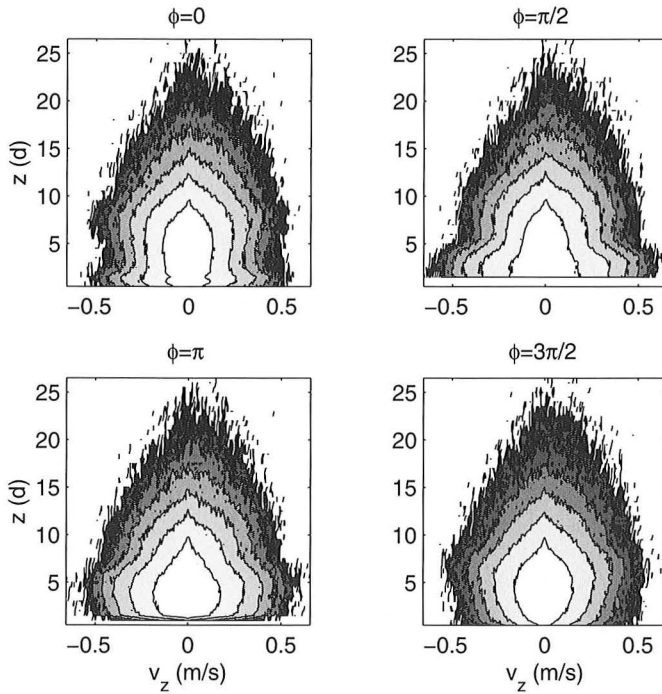


**Figure 3.11:** The fraction of particles  $P(v_x, z)$  found for each value of horizontal velocity  $v_x$  and height in the box  $z$ . The gray scale corresponds to the fraction of particles, running from  $1 \cdot 10^{-6}$  (black) to  $3 \cdot 10^{-4}$  (white) on a logarithmic scale. Different pictures correspond to different phases in the driving cycle.

position and phase. This suggests that the deviations in the kurtosis shown in Fig. 3.8 outside of the steady state area are mainly due to time dependence of the velocity distribution for small velocities.

In Fig. 3.13, we show  $P(v_x)$  both in vacuum and in air and with brass beads instead of steel beads. Fig. 3.13 shows that in all cases the high-velocity tails are well described by a stretched Gaussian with  $\alpha = 1.7$ . These results show that the high velocity tails are insensitive to the presence of air. In the experiment by Rouyer and Menon [41] used a container that was not evacuated. Also, brass beads have a lower coefficient of restitution than steel beads and should dissipate more energy upon collision. This means that the velocity distribution is unaffected by an increase in dissipation, in contrast to Kudrolli and Henry, who report that their velocity distributions become more non-Gaussian as the dissipation is increased [45]. This might be due to the fact that for particles rolling on a slope  $\eta \approx 0.5$ , much lower than



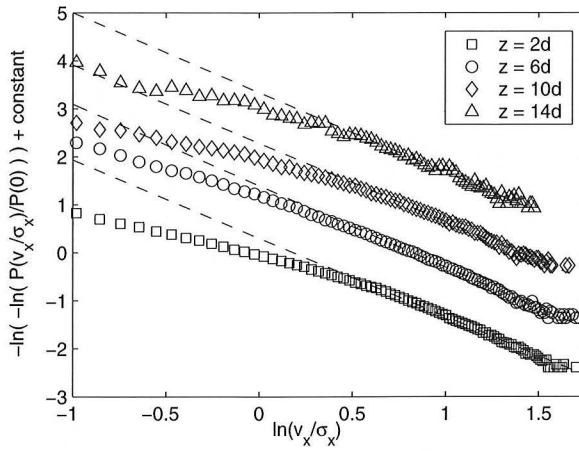


**Figure 3.12:** The double logarithm of the distributions  $P(v_x/\sigma_x)$  as a function of the logarithm of  $v_x/\sigma_x$  for  $N = 130$ ,  $f = 50\text{Hz}$  and  $\Gamma = 20$ . Plotted this way, the slope  $-\alpha$  of the distribution corresponds to the exponent  $\alpha$  of  $P_\alpha(v_x/\sigma_x)$ . Velocity distributions are shown for different heights  $z = 2d, 6d, 10d$  and  $14d$ . Dashed lines shown fits to the high velocity tail by a distribution  $P_\alpha(v)$  with  $\alpha \approx 1.6$  in all cases.

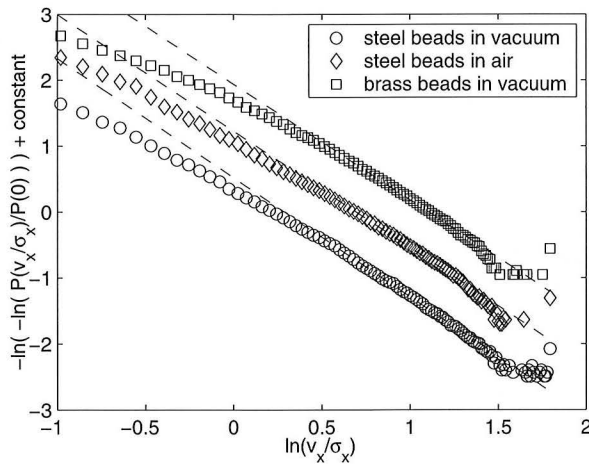


**Figure 3.13:** High velocity tails shown for steel beads in vacuum (circles), steel beads in air (diamonds) and brass beads in vacuum (squares). The distributions are averaged over the steady state region  $8d < z < 25d$  and over the driving cycle. The dashed lines show linear fits through the high-velocity tails of the distributions of  $P_\alpha(v)$  with  $\alpha \approx 1.6$ .

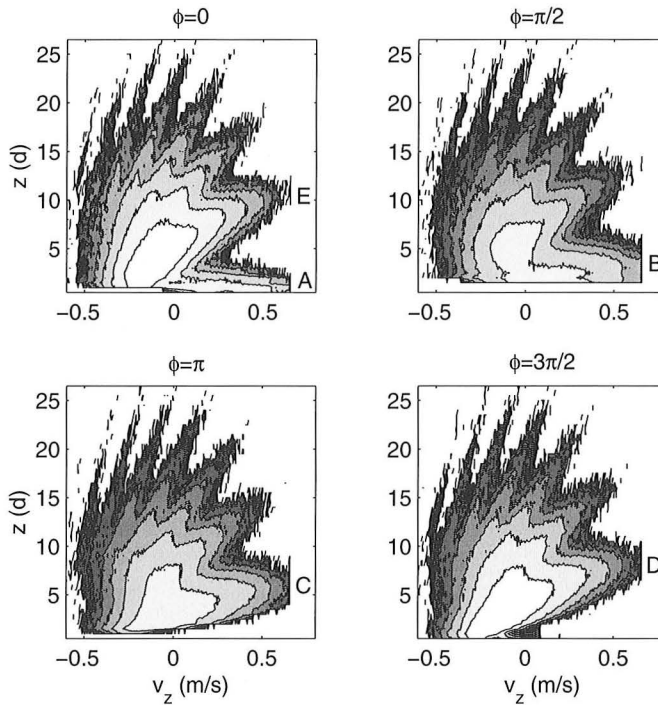


**Figure 3.14:** The fraction of particles  $P(v_z, z)$  found for each value of vertical velocity  $v_z$  and height in the box  $z$ . The gray scale corresponds to the fraction of particles, running from  $1 \cdot 10^{-6}$  (black) to  $3 \cdot 10^{-4}$  (white) on a logarithmic scale. Different pictures correspond to different phases in the driving cycle. For high  $v_z$  or  $z$ , the velocity distribution is organized into discrete bands. The letters A, B, C, D and E identify one of these bands as it evolves through a driving cycle.

$\eta = 0.8$  for brass particles.

### 3.4.2 Vertical velocity distributions and collision statistics

The vertical velocity distribution  $P(v_z)$  has been studied before and is in general an irregular distribution and asymmetric around  $v_z = 0$  [45]. In our case, it proves more insightful to plot  $P(v_z)$  as in Fig. 3.14. When plotted this way, the velocity distribution shows a surprising structure. At high  $v_z$  and  $z$ , the particles are organized in discrete bands of the form  $z = A + Bv_z$  and these bands move through the box in time, as is shown in Fig. 3.14 where we indicate the position of one such band during one driving cycle. The origin of this structure is easily explained. At  $\phi = 0$  the container collides with the gas and excites a wide range of positive vertical velocities

at the bottom of the container. At  $\phi = \pi/2$  the gas leaves the plate. For simplicity we assume that all particles excited by the plate, leave the plate at  $z = 0$  and with some positive velocity  $v$ . If the gas was sufficiently dilute that collisions can be ignored, then each particle would evolve from  $(v = v, z = 0)$  to  $(v - gt, vt - gt^2/2)$  after some time  $t$ . For a band of particles, all excited at  $t = 0$  and  $z = 0$  with a range of vertical velocities  $v_z$ , this gives rise to relation  $z = gt^2/2 + v_z t$  between the height in the box  $z$  and velocity  $v_z$ . So each band observed in Fig. 3.14 corresponds to a collection of particles that was excited by the plate a time  $t$  ago and have been traveling through the box without collisions. At least seven of these bands are clearly visible in Fig. 3.14, meaning that at any moment one can find in the gas the remnants of up to seven cycles ago.

Next, we focus our attention on the collisions occurring in the gas. We extract this data from the particle tracks, by monitoring the relative parallel velocity for each pair of particles that are within a distance  $1.1d$  of each other. The relative parallel velocity is defined as  $(\mathbf{v}_i - \mathbf{v}_j) \cdot \mathbf{r}_{ij}$ , where  $i$  and  $j$  label the particles and  $\mathbf{r}_{ij}$  is the normal vector connecting the particle centers. This velocity is positive when the two particles are approaching and negative when they are moving away from each other. When the sign of the relative parallel velocity changes from positive to negative we assume a collision has happened. For each collision we record at what height in the box and at what phase of the driving cycle it occurred and average over 612 cycles.

In Fig. 3.15 we show the number of collisions per cycle in the gas as a function of height  $z$  in the box and for different phases in the driving cycle. Between  $\phi = 0$  and  $\phi = \pi/2$ , when the collision between the plate and the gas is strongest, the number of collisions increases dramatically near the plate. This peak travels upward with the shockwave, but decays as the density decreases and the motion of the particles become more aligned through the collisions. Above a certain height the number of collisions becomes very small and in the steady state region  $z > 8d$  the number of collisions per particle per cycle becomes as small as 0.1. High in the container we find that the density profile decreases as  $\rho(z) \sim \exp(-az)$ . Such exponential decay has been seen before in experiment [67].

Fig. 3.14 and Fig. 3.15 together explain how in the steady state  $T_x$  is constant, while in the same region  $T_z$  still varies considerably with the phase of the driving cycle. As the gas collides with the plate, then at some height in the steady state region, the vertical velocity distribution  $P(v_z)$  is dominated by particles with negative vertical velocities. When the band of particles excited at the plate travels through the gas as shown in Fig. 3.14, it will at some point reach this region and the velocity distribution will broaden as it now includes many particles with large positive  $v_z$ . This is reflected by a sudden increase in  $T_z$  and the peak in  $T_z$  moves upward in

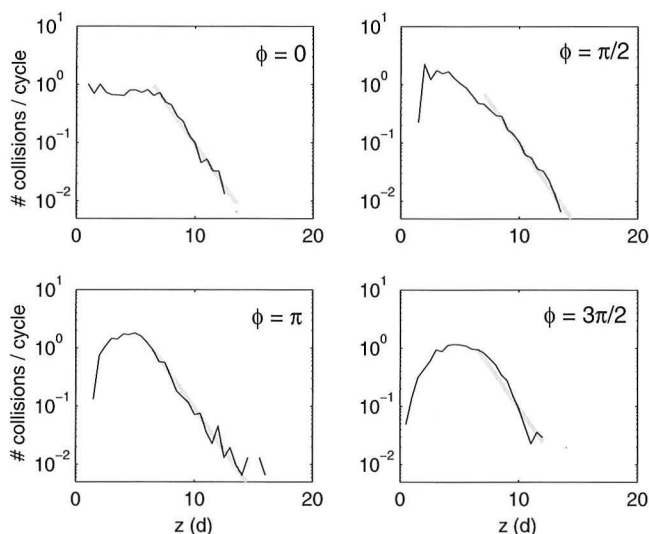


**Figure 3.15:** The number of collisions  $C(z)$  per cycle as a function of height in the box for  $N = 130$  brass beads,  $f = 50\text{Hz}$  and  $\Gamma = 20$ . The different figures correspond to different phases of the driving cycle. The collisions were recorded over 612 cycles. The gray lines show fits of the form  $\rho(z) \sim \exp(-az)$ .

the gas as the bands in Fig. 3.14 do. Above a certain height, as shown in Fig. 3.15, these particles collide only rarely and here the behavior of  $T_z$  is largely dominated by freely moving particles. The only way to transfer energy from the vertical to the horizontal is by collisions, so even though  $T_z$  still fluctuates, these fluctuations no longer can influence  $T_x$  and  $P(v_x)$  above this height.

## 3.5 Velocity distributions

### 3.5.1 Steady-state distributions

Collisions of particles with the bottom plate inject energy mainly into vertical motion. Energy is transferred into the horizontal direction directly through particle-particle collisions and through collisions of rotating particles with the bottom. Close to the bottom plate the areal density  $\rho$  and the probability distributions for the horizontal and vertical components of velocity ( $v_x$  and  $v_z$ ) vary considerably during each oscillation of the plate. However, far above the plate the density and velocity

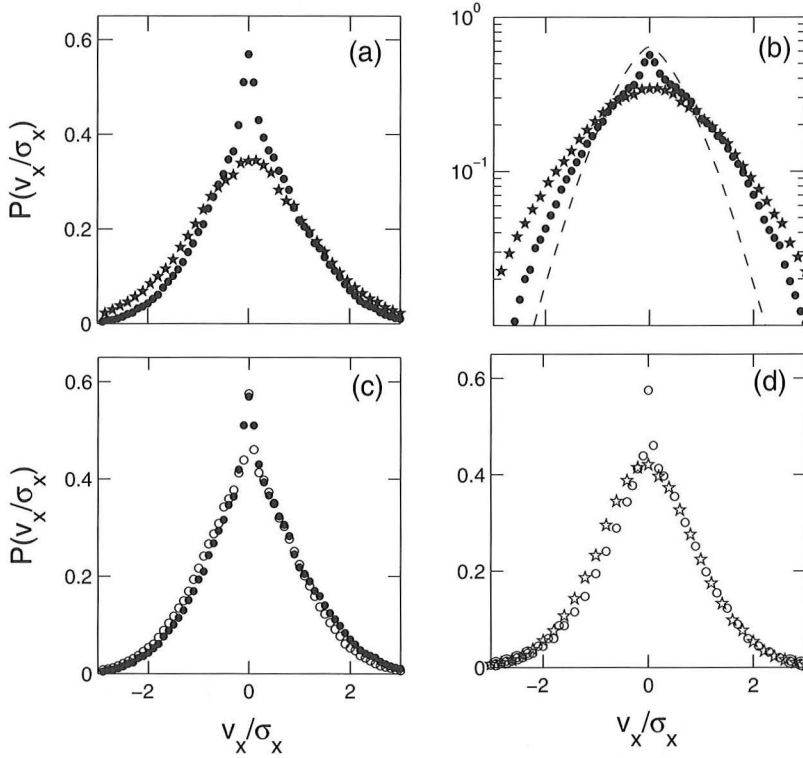


**Figure 3.16:** (a) Linear and (b) logarithmic plots of the velocity distribution  $P(v_x/\sigma_x)$  measured in the steady state region for a system with  $N = 130$ ,  $f = 50\text{Hz}$  and  $\Gamma = 20$ . Distributions are shown for clean particles ( $\bullet$ ) and particles with a small amount of added graphite ( $\star$ ). Also shown is the non-Gaussian result (Eq. 1, dashed line) from the experiment in [41], with  $\alpha = 1.51$  and  $B = 0.8$ . (c) Comparison between experiment ( $\bullet$ ) with particles and simulation ( $\circ$ ) with  $\mu_w = 0.075$ . (d) Comparison of simulations with ball-ball friction  $\mu_b = 0.5$  and with ball-wall friction  $\mu_w = 0.075$  ( $\circ$ ) and  $\mu_w = 0$  ( $\star$ ). The experimental distributions are not precisely symmetric about  $v_x = 0$  due to the container tilting slightly when shaking. To match the asymmetry in the experiment, gravity in the simulation was tilted 1.9 degrees with respect to the normal to the top of the container. This does not affect the functional form of the distributions when compared to simulations without the tilt.

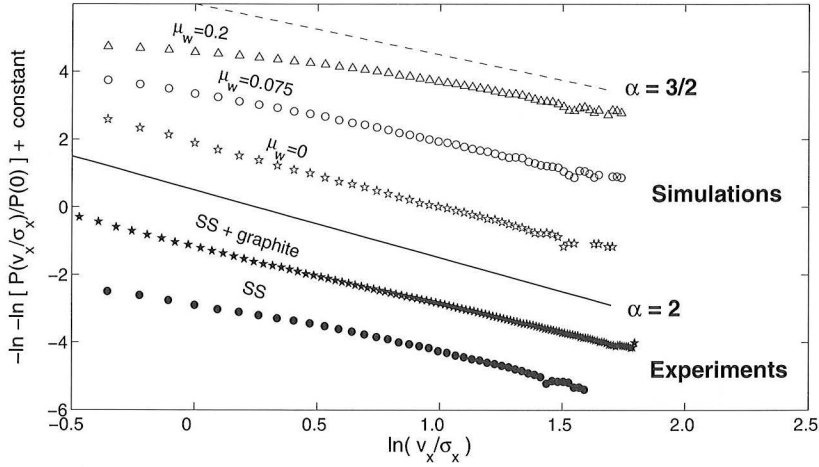


**Figure 3.17:** Double log plot of the velocity distribution functions.  $P_\alpha(v)$  has slope  $-\alpha$ ; to guide the eye, slope  $\alpha = 3/2$  is shown by a dashed line and  $\alpha = 2$  (a Gaussian) by a solid line. Experimental results are shown for clean stainless steel (SS) particles ( $\bullet$ ) and SS particles with graphite added ( $\star$ ). Simulation results are shown for three different values of ball-wall friction  $\mu_w$  with the ball-ball friction held fixed,  $\mu_b = 0.5$ . The data sets have been offset for clarity.

distributions become time independent, as has been shown by Moon *et al.* [64]. Here we examine distribution functions for  $11d < z < 12d$ , which is in the steady state region – the density and horizontal velocity distribution functions change by less than 5% during each cycle.

Our measured and simulated distributions are shown in Fig. 3.16. For clean particles in the experiment and non-zero wall friction in the simulation, the velocity distributions have an unusual characteristic: a sharply peaked maximum, a feature that has been observed before [45, 46] but has not been fully explored. (For  $z < 11d$ , the shape of the distribution changes slightly with height in the box and phase of the driving cycle, but the sharp peak is always present.) We find that the peak disappears when we add approximately 0.0002 kg of graphite powder (a lubricant) to the 0.1 kg of steel spheres [68]. The distributions observed with and without graphite both differ from those in Ref. [41] (cf. Fig. 3.16(b)).

Experiment and simulation are compared in Fig. 3.16(c). For  $\mu_w = 0.075$ , the simulation results agree well with the experiment. The peak of the velocity distribution in the simulation decreases as  $\mu_w$  is decreased, and the peak disappears completely for  $\mu_w = 0$ , as Fig. 3.16(d) shows.

The distributions obtained from experiments on stainless steel particles with

graphite and simulations with  $\mu_w = 0$  are described by a straight line on graphs like those in Fig. 3.17. The slope of such a graph yields the magnitude of the exponent  $\alpha$  in  $P_\alpha(v)$ . In simulations without sidewall friction,  $\mu_w = 0$ , the exponent obtained is 1.8. An exponent of 1.7 is found for the velocity distribution of stainless steel particles with graphite. The peaked distributions are not described by a single value of  $\alpha$ , but we can compare estimates of a local value of  $\alpha$  in the range  $1.0 \lesssim \ln(v_x/\sigma_x) \lesssim 1.6$ : we obtain 1.8 for clean stainless steel particles, while in the simulation,  $\alpha$  increases from 1.3 with sidewall friction  $\mu_w = 0.2$  to  $\alpha = 1.8$  with  $\mu_w = 0.1$ .

### 3.5.2 Single Particle Dynamics

We have shown that interactions with sidewalls strongly affect the functional form of the velocity distribution. This result is supported by our observations in simulations that in the steady state region, a ball collides with the wall typically three times as often as it collides with another ball. To isolate the effects of ball-wall collisions, we have conducted experiments and MD simulations on a single particle in an oscillating container (Fig. 3.18). Because there are no collisions with other particles, the particle's motion is determined only by collisions with the bottom plate and the sidewalls. Figure 3.18(a) shows the time evolution of the horizontal velocity  $v_x$  for a particle in a simulation with  $\mu_w = 0.4$  and  $e = 0.7$ . Each time a particle bounces on the bottom plate, some of the angular momentum of the particle can be transferred into linear momentum in the horizontal direction. These collisions would produce the only changes in  $v_x$  if there were no interaction with the sidewalls, but Fig. 3.18(a) reveals more frequent smaller changes, which correspond to collisions with the sidewall. The staircase-like decrease in velocity (see inset) corresponds to a particle's rattling between the sidewalls, losing energy at every collision. Thus the effect of the sidewalls is to damp the horizontal velocity. The ultimate fate of a single particle, regardless of its initial  $v_x$ , is to bounce vertically on the bottom plate with  $v_x = 0$ .

The horizontal velocity  $v_x$  measured for a single particle in the experiment is shown in Fig. 3.18(b). Collisions with the bottom plate, determined to be when the vertical component of velocity  $v_z$  changes sign, are indicated by the dotted vertical lines. If there were no influence of the sidewalls, the horizontal velocity  $v_x$  would remain constant between these lines. The behavior of the particle between collisions with the bottom plate is more complicated than in the simulation, but it is still clear that the horizontal velocity is damped by collisions with the walls. The damping of the horizontal motion of a single particle illustrated by Fig. 3.18 explains why the velocity distribution for a gas of particles has a peak at  $v_x = 0$  (Fig. 3.16). The over-

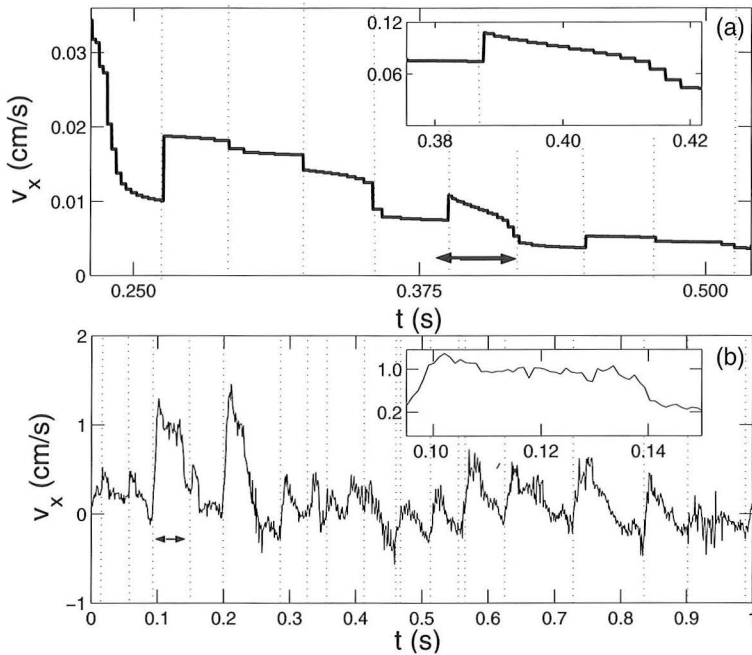


**Figure 3.18:** Horizontal velocity of a single ball on a vertically oscillating plate in (a) simulation ( $\mu_w = 0.4$  and  $\mu_b = 0.5$ ) and (b) experiment. The larger, less frequent jumps are the result of collisions with the bottom plate; these collisions are indicated by the dotted vertical lines. The more frequent smaller changes are the result of collisions with the sidewalls; these changes are clearer in the enlarged scale of the insets. The regions depicted in the insets are indicated by arrows.

populated high energy tails arise because for a distribution with a given variance, the increase in the central peak must be balanced by an increase for  $v > \sigma$ .

### 3.5.3 Single particle model

Features of the velocity distributions obtained from experiment and simulation are well described by a discrete map model with a damped driven single particle. The particle's velocity is initially drawn from a Gaussian distribution of variance unity. The velocity at iteration  $n+1$  is given by  $v_{n+1} = v_n e^{-\gamma}$ . For one percent of the iterations, randomly selected, we replace the velocity  $v_{n+1}$  with a velocity drawn from a Gaussian distribution with variance unity. The velocity probability distribution is constructed from  $n = 10^9$  iterations. The exponential decay of the particle velocity



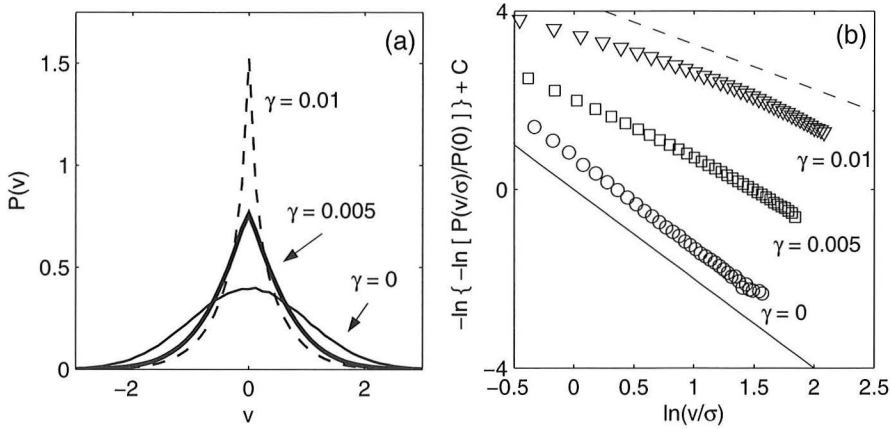


**Figure 3.19:** Velocity distribution  $P(v/\sigma)$  for a model of a damped driven particle. The distributions are shown for increasing damping  $\gamma$ : 0, 0.005, and 0.010. The inset compares the tails of the distributions for the model with a Gaussian distribution (solid line,  $\alpha = 2$ ) and a distribution with  $\alpha = 1.5$  (dashed line). The data sets are offset for clarity.

between iteration steps corresponds to the numerous sidewall collisions that occur between excitations by the plate, and the random replacements of the particle's velocity mimic plate collisions that transfer horizontal momentum to the particle.

This model captures the qualitative behavior of the velocity distributions found in both experiment and simulations, as Fig. 3.19 illustrates. For finite damping,  $\gamma > 0$ , the distribution is strongly peaked at  $v = 0$ , while in the absence of damping,  $\gamma = 0$ , the distribution is Gaussian. Further, damping affects the tails of the distribution: as damping is decreased to zero, double logarithmic plots of the distribution become less curved and the slope increases from 1.3 to 2, just as in the MD simulation (Fig. 3.17). Similar behavior is seen when the damping  $\gamma$  remains fixed, but the heating rate is increased.

The single particle model is similar to a model by Puglisi *et al.* that includes damping of the particle velocities [42]. Increasing the damping in their model also led to non-Gaussian velocity distributions, but a strong peak around  $v = 0$  was not reported. This peak might be absent in their model because particles were driven not by discrete heating events but by continuous white noise, which for strong damping led to Gaussian behavior around  $v = 0$  in their model.

### 3.6 Discussion and conclusions

We studied the behavior of the density  $\rho$ , the granular temperatures  $T_x$  and  $T_z$  and the velocity distributions  $P(v_x)$  and  $P(v_z)$  in a vertically oscillated granular gas, both as function of the height in the box  $z$  and phase of the driving cycle  $\phi$ . These quantities are oscillatory in time close to the bottom of the container, but above a certain height the gas reaches a steady state where  $\rho$ ,  $T_x$  and  $P(v_x)$  are constant in time. In this steady state, both  $T_z$  and  $P(v_z)$  still show strong oscillatory behavior. The velocity distribution  $P(v_x)$  in the steady state is sharply peaked around  $v_x = 0$  and has high velocity tails of the form  $P(v) = A \exp(-B|v/\sigma|^\alpha)$  with  $\alpha = 1.7$ . We find that the high-velocity tails of  $P(v_x)$  depend only very weakly on the position in the container and the phase of the driving cycle, even outside of the steady state region and close to the bottom of the container. The same distribution was found for steel beads as well as for brass beads and both in vacuum and in air, suggesting that it is independent of material properties. Furthermore, we find that the steady state of the granular gas consists mainly of particles that suffer no collision in that region of the container. This explains why the considerable fluctuations of  $T_z$  in the steady state have no influence on either  $T_x$  or  $P(v_x)$ .

The kinetic theory of granular gases is often studied in experiments on confined monolayers of grains because the behavior of all grains for all times can be recorded. However, we have found that the ball-wall friction associated with the confinement should be included in interpreting experiments on monolayers in quasi-2D geometries, including vertical [41], inclined [45], and horizontal layers [46, 50]. Indeed, in an experiment with the last geometry the velocity distribution was peaked for a smooth plate [46], but the peak disappeared when the smooth plate was replaced with a rough plate, which drove horizontal as well as vertical motion [49]. In the model presented in Section 3.5.3 this would correspond to an increase in the heating rate, leading to more Gaussian distributions. Similarly, a recent experiment with a layer of light particles on top of a layer of heavy particles yielded a non-Gaussian distribution for the heavier particles, but Gaussian statistics were found for the lighter particles [50]. The interactions between the particles and the container in these quasi-2D systems may have been principal determinants of the shape of velocity distributions and therefore should be taken into consideration.

---

**Part II**

**Biochemical Networks**



---

## **Chapter 4**

# **Introduction**

## 4.1 Introduction

When one watches bacteria, such as the intestinal bacterium *Escherichia coli*, under the microscope, one gets the distinct impression of watching living beings showing individual behavior. Examples of *E. coli* are shown in Fig. 4.1. If food is plentiful, most of the bacteria swim around rapidly, covering several body lengths in a second. Yet, all bacteria will swim in different directions and some of them will stop swimming every once in a while, tumble around for a bit and then swim off in another direction. At the same time, some bacteria stick to the bottom and form slowly growing colonies. This variation in behavior occurs even when the bacteria are identical twins, having grown from a single initial cell, and when they live in exactly the same environment. On the other hand, their behavior is not completely random but shows a clear purpose. Bacteria continuously take up nutrients from the environment and use them to grow and divide. Even though they swim around seemingly erratically, bacteria will swim towards a food source and, less obviously to the naked eye, will adapt easily to different environmental conditions.

Because of this characteristic behavior under the microscope, bacteria were categorized as living creatures immediately upon their discovery. In a letter to the Royal Society on October 9th 1676 containing the first ever observation of bacteria, Antoni van Leeuwenhoek describes them as [69]:

animals . . . unbelievably small, yes so small, to my eye, that I judged, that a hundred of these small animals, when placed next to each other, would not reach the size of a grain of sand <sup>1</sup>.

Initially, the discovery of bacteria caused quite a stir [70]. Van Leeuwenhoek, a cloth salesman with no formal education in the sciences, would over the years receive a steady stream of aristocrats and royalty to peer through his microscope. At the same time, he produced an equally steady stream of observations of microscopic animals. He found bacteria almost everywhere: in rain water, in the intestines of flies, even in his excrement and his dental plaque. Of the latter, for instance, he remarks that [71]:

I have mixed it several times with pure rain water . . . and often have seen with much amazement that it contained very many extremely small living animals, that moved it vigorously . . . Importantly, I judged that less people live in the united Netherlands, than I carry living animals in my

<sup>1</sup>diertgens . . . ongelooflijk kleijn, ja soo kleijn, in mijn gesicht, dat ik oordeelde, dat bij aldien 100. van dese seer kleinje diertgens, nevens den anderen lagen gestrekt, dat deselvege de lengte, van een grof santie niet soude kunnen bereiken.

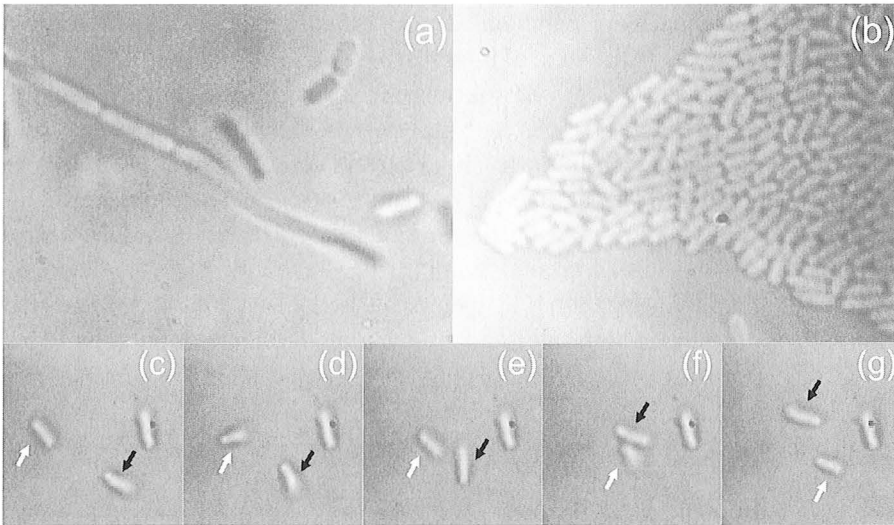


**Figure 4.1:** *E. coli* bacteria under the microscope. (a) A long filamentous cell of *E. coli* surrounded by normal sized cells. (b) A dense colony of *E. coli* bacteria at the interface between water and air. (c)-(g) Freely swimming bacteria. The cells indicated by the black and the white arrow swim in opposite directions. The length of the cells is around  $1 \mu\text{m}$  and the time between (c) and (g) is 0.5 s. Images were obtained by S. Verbrugge and B. van den Broek.

mouth today . . . I thought I saw more than a thousand living animals in a quantity of matter not larger than a hundredth part of a sand grain <sup>2</sup>.

However, the scientific interest in microorganisms quickly dwindled after Van Leeuwenhoek [70]. Scientists generally considered bacteria as a kind of novelty, amusing to look at but not worthy of serious study. Already by the early 1690s, Robert Hooke complained that the general consensus on the use of the microscope was that “the subjects to be enquired into are exhausted, and no more is to be done.” [72] As a consequence, little research was conducted on microorganisms until the nineteenth century when Pasteur and Koch discovered that bacteria do not arise spontaneously from inanimate matter, as was often assumed before, and that bacteria are the cause of many diseases.

<sup>2</sup>ik heb dan het selvige verscheijde malen met suiijver regenwater vermengt . . . en meest doorgaans met groote verwondering gesien, dat in de geseijde materie waren veel seer kleijne levende dierkens, dier haar seer aerdig beweegden . . . wat my belangt ik oordeel van myn selven . . . datten soveel menschen niet leven in onse vereenigde Nederlanden, als ik heden levende dieren in myn mont draag . . . ik imagineerde wel 1000 levende dierkens te sien in een quantiteyt materie die niet groter was als een honderdste part van een santgroote.

One of the reasons why research on bacteria came to a halt for the better part of two centuries was that, at the time of their discovery, the idea of very small animals, even though initially surprising, was not considered very profound. Few would have been amazed if better microscopes had shown that even smaller animals existed. Not before the late nineteenth and early twentieth century, when it became clear that all matter is build from atoms, did one have a true measure of the smallness of bacteria. Now we know that bacteria are actually extremely small. A typical bacterium has dimensions of around  $1\ \mu\text{m}$ . If one takes the distance between an oxygen atom and a hydrogen atom in a water molecule as a measure of the 'size' of an atom, then only around ten thousand atoms fit along the length of a bacterium.

In fact, it turns out that bacteria set the lower limit to the size of living organisms. Currently, the smallest known organism to show independent reproduction is the parasitic bacterium *Mycoplasma genitalium*, having a diameter between  $0.2\text{--}0.3\ \mu\text{m}$ . Viruses are often smaller, but they need larger organisms, like bacteria, to reproduce. The smallness of bacteria has raised the hope that it might be possible to understand how bacteria, and life in general, function on the level of atoms and molecules. A vocal advocate of this view was Erwin Schrödinger, who in his book *What is Life?* speculated that life could be understood by physical laws, in particular based on statistical physics and quantum mechanics [73]. Among other things, he proposed that hereditary information was stored in the chromosomes in the form of an 'aperiodic crystal', little less than ten years before the structure of DNA was finally elucidated by Watson and Crick in 1953.

Since then, biology has made a large leap in this direction. Already in the late 1950s the first structure of a protein, in this case myoglobin, was determined at atomic resolution by X-ray crystallography. Only slightly later was it worked out how the information stored in the DNA is translated into proteins and how the production of proteins can be regulated in response to external cues. In 1977, the first complete sequence of the 5375 base pairs that made up the DNA of the virus  $\phi\text{-X174}$  was determined. Many genome sequences have since followed. For instance, the 4.6 million base pairs that form the genome of *E. coli* were sequenced in 1997 and the 3 billion base pair genome of *Homo sapiens* in 2000. Moreover, the structure of many proteins is now known and their functioning can be understood in atomic detail. All this knowledge makes it possible nowadays to manipulate DNA on a molecular scale, for instance by inserting genes from one organism into the genome of another. As an example, insulin for diabetics is no longer obtained from slaughtered pigs, but instead produced by bacteria that have the gene for human insulin inserted into their DNA.

Even though molecular biology has been tremendously successful in describing the fundamental processes in the cell in molecular detail, it has been much less effec-



tive in explaining how the interactions between all the molecules in the cell give rise to the complicated, purposeful behavior we associate with living organisms. This is partly because, traditionally, molecular biology has taken a reductionist approach, trying to explain biological functions by the behavior of single molecules. Sometimes one will indeed find cases where a specific function is performed by a single protein. Oxygen transport in the bloodstream, as an example, is done by individual myoglobin and hemoglobin proteins. However, most biological functions arise from the interactions between many different proteins. The signal transduction system that allows *E. coli* to swim towards a food source, for instance, consists of a dozen different proteins that are all equally important for proper food location. The desire to study the properties of living cells on the level of an entire system of interacting proteins, rather than on the level of individual proteins is relatively new and this field is often referred to as *systems biology*.

Does this mean that the functioning of living organisms can only be understood by considering all the interactions between the thousands of different types of molecules present in the cell? Fortunately, it seems that life is simpler than that. Many proteins are found to be organized in *modules*, networks of interacting proteins that function relatively autonomously from the rest of the cell [74]. Evidence of the existence of such modules is that processes such as protein synthesis or DNA replication can be reconstituted outside the cell, in a test tube. Moreover, it is found that small networks of interacting proteins can behave like feedback loops, amplifiers, filters or switches. These networks get their input from other proteins that function as sensors, for instance measuring the concentration of a specific molecule within the environment. It is tempting to draw parallels between these *biochemical networks* and electrical circuits.

Most of the early work on elucidating the biochemistry of bacteria consisted of bulk measurements performed in test tubes containing very large numbers of bacteria. In this way, only the average response of bacteria could be measured. Due to recent advances in microscopy it has become possible to study the behavior of these biochemical networks in single cells. This has opened a completely new window in studying bacteria, making it possible to study the dynamics of biochemical networks in much more detail. One of the most important findings is that these networks are often influenced and sometimes dominated by stochastic fluctuations on the molecular level [75]. Experiments find that biochemical networks indeed function like analog electrical circuits, but like circuits operating with just a handful of electrons rather than the  $10^{23}$  found in macroscopic wires. This is because the components in biochemical networks are molecules that often occur in a small number of copies within the cell, sometimes as few as 10-1000 per cell. Below I will show that this leads to stochastic behavior that is never observed in conventional electrical circuits.

It is a natural question to ask how cells can still perform reliably in the presence of random fluctuations in the dynamics of its proteins. For instance, if a cell switches its internal state when the concentration of a signaling molecule increases above a critical concentration, it might switch at the wrong moment if the concentration of the signaling molecules shows large random fluctuations. Nevertheless, cells in the human embryo switch to different cell types in response to external molecular signals in an extremely reliable way over and over again. In general, it is clear that biochemical networks have been adapted over the course of evolution to become relatively insensitive to the presence of these fluctuations. A clear sign of this is that synthetic networks, constructed by cutting and pasting DNA together from different organisms to perform a specific function, often perform much less reliably than their naturally occurring counterparts.

Perhaps surprisingly, the tools for understanding the properties of biochemical networks have come partly from physics. Even simple biochemical networks are often so complicated that for proper understanding mathematical modeling or simulations are necessary. For instance, physicists use techniques from non-linear dynamics to explain the collective properties of networks of interacting proteins. The effects of the random fluctuations that affect the behavior of the cell are often described by statistical mechanics. However, biological systems are usually much more complicated than the systems physicists are used to. They consist of a much more diverse set of building blocks and are shaped in an often haphazard way by evolution. Because of this, the description of biochemical networks still remains a great challenge. The involvement of physicists is not restricted to the theoretical side only. Amusingly, many of the current experiments on biochemical networks are not performed by molecular biologists, but by researchers with a background in physics.

In the rest of this Chapter I will proceed as follows: first, I will give a brief overview of the molecular biology involved in this part of my thesis. Then I will continue to explain how cells can make decisions based upon molecular signals by describing two canonical examples of biochemical networks: the *Lac* operon and the  $\lambda$  switch. Then I will explain the origin of stochastic fluctuations and how they affect the functioning of biochemical networks. I will discuss how cells use these fluctuations as a source of variation and how cells protect themselves against fluctuations, mainly in the context of genetic switches. Finally, I will turn to the role of spatial fluctuations due to diffusion of molecules. I will also briefly introduce the research presented in Chapters 5 and 6.

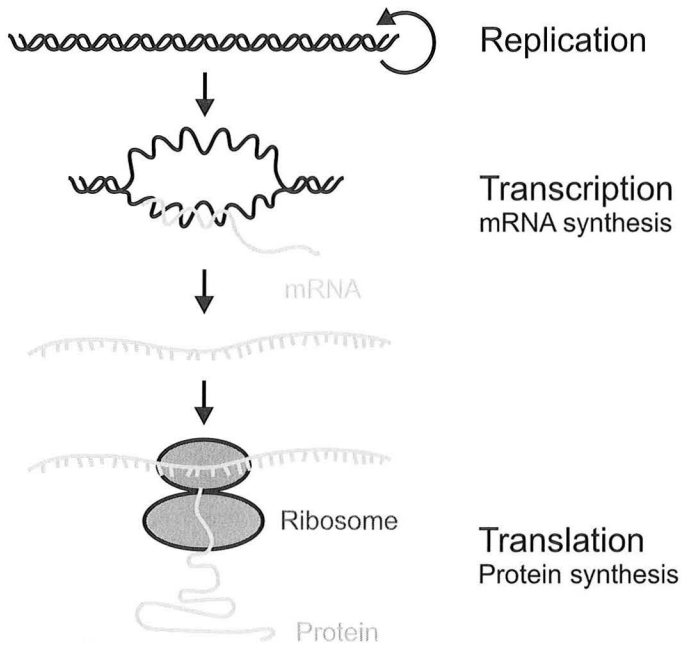


**Figure 4.2:** Schematic representation of the relation between DNA, RNA and proteins. DNA directs its own replication. At the same time, DNA is being transcribed into mRNA by RNA polymerase (RNAP). In turn, mRNA is translated into proteins by ribosomes. Several proteins are translated from a single mRNA. For the proteins to become enzymatically active, the random coil of amino acids first has to fold into its proper configuration.

## 4.2 Molecular biology of the bacterium

Most research on biochemical networks is performed on bacteria because they are simple. All living organisms can be divided in prokaryotes, lacking a proper nucleus, and eukaryotes. Bacteria are an example of the first category, whereas all higher organisms belong to the latter. In both classes, genetic information is stored in the form of deoxyribonucleic acid (DNA). In eukaryotes, all the DNA is contained within the nucleus, a separate compartment within the cell. Such a separation does not occur in prokaryotes, where proteins and DNA are all contained within the same rigid cell wall. In general, eukaryotic cells are much more complicated than prokaryotic cells. Because of this, much of the knowledge in this and the following two sections was originally gained from bacteria and viruses and only later confirmed to be similar in eukaryotes.

All genetic information is stored within the DNA in the form of a sequence of the

nucleotide bases adenine (A), thymine (T), guanine (G) and cytosine (C). DNA is found in the cell in the form of the famous double helix, where each base forms a pair with its complementary base, A with T and G with C. The relation between DNA, ribonucleic acid (RNA) and proteins was elucidated in the 1950s and 1960s and is often summarized in what is called the *central dogma of molecular biology* [76], indicated schematically in Fig. 4.2. DNA directs its own replication, using its two strands as templates for the two new copies. Parts of the DNA are also transcribed into short strands of messenger RNA (mRNA), by a protein called RNA polymerase (RNAP). In turn, mRNA is translated into proteins by ribosomes. Proteins are linear strings of amino acids and ribosomes translate RNA into proteins by incorporating one out of twenty possible amino acids for each codon on the DNA. Codons are sequences of three base pairs and each amino acid is coded for by one or more specific codons. In most cases, the string of amino acids has to fold into the proper three dimensional configuration before the protein becomes active. Although cellular enzymes usually consist only of protein, RNA can also sometimes catalyze reactions. Ribosomes, for example, partly consist of RNA.

Not all parts of the DNA are transcribed equally. For instance, prokaryotes can respond to environmental changes by inducing the production of the appropriate proteins. Such *gene regulation* often occurs by the binding of specific proteins, called transcription factors, to the DNA, thereby inhibiting the production of mRNA. I will now describe in some detail two examples of transcriptional regulation: the lac operon and the  $\lambda$  switch.

### 4.2.1 The lac operon

The bacterium *E. coli* is able to digest lactose, but prefers to feed upon glucose, a more efficient energy source. As a consequence, the proteins responsible for lactose digestion are only produced when *E. coli* has completely exhausted its supply of glucose and when lactose is present in the environment. How the bacterium makes this decision is understood in great detail and is an instructive example of how cells can regulate gene expression [77].

The genes responsible for breaking down lactose are organized in the so-called lac operon, shown schematically in Fig. 4.3(a). The lac operon consists of genes for three proteins: *lacZ*<sup>3</sup>, coding for an enzyme responsible for cleaving the lactose into a form that can be digested by the bacterium, *lacY*, coding for a permease that transports lactose into the cell and *lacA*, coding for an enzyme that helps to break down other lactose-like sugars.

<sup>3</sup>By convention, names of genes are written in italic, with initial letter lowercase. Names of proteins are written non-italic, with first letter uppercase.

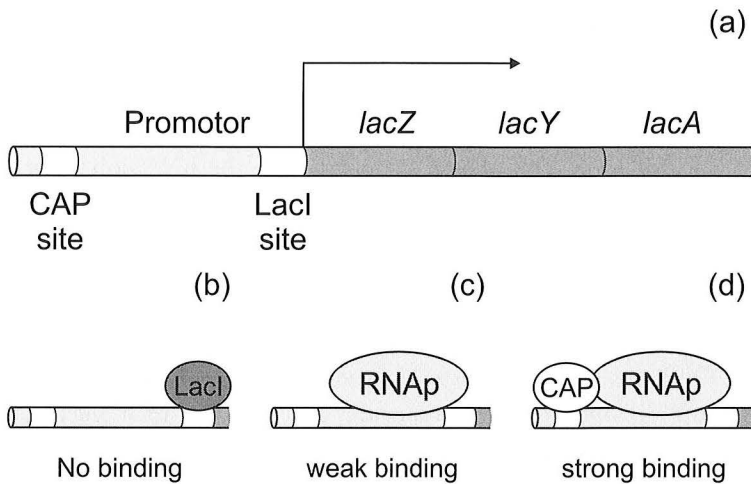


**Figure 4.3:** The *lac* operon. (a) Overview of the *lac* operon. The genes coding for LacZ, LacY and LacA are indicated in dark gray and are transcribed as a single strand of mRNA. The black arrow indicates the start and direction of transcription. The binding sites for CAP and the lac repressor (LacI) are indicated in white and are around 20 bp each. The RNAP binds to the promoter region. The binding site for the lac repressor lies within the promoter and the CAP site lies just upstream of the promoter. (b) In the absence of lactose in the cell, the lac repressor binds to its binding site and prevents the RNAP from binding to the promoter. (c) In the presence of lactose the lac repressor is inactivated and the RNAP binds weakly. The lac genes are transcribed at a low, basal level. (d) In the presence of lactose and the absence of glucose, the CAP protein binds to the DNA and stabilizes binding of the RNAP to the promoter. The expression of the lac genes is fully induced. In reality, the *lac* operon is more complicated, as there are two additional binding sites for the lac repressor that help in repressing the lac genes.

The region in front of the three genes does not code for proteins, but forms a regulatory region, called the promoter region. It has a binding site for the RNA polymerase. If the RNA polymerase binds here, it can start the transcription of the *lac* genes. There are also binding sites for two different proteins. One protein, the lac repressor, only binds to its site in the absence of lactose. The other protein, called CAP, only binds to its site in the absence of glucose.

If lactose is absent in the cell, the lac repressor has a high affinity to its binding site on the DNA. The binding site of the lac repressor overlaps with that of the RNA polymerase, so that a bound lac repressor physically prevents RNA polymerase from binding and consequently prevents the expression of the *lac* genes. On the other hand, when lactose is present it binds to the lac repressor. In response to the binding of lactose, the conformation of the lac repressor changes and the lac

repressor loses its affinity for the binding site on the DNA. This is an example of an *allosteric* interaction, where the binding of a molecule to one part of a protein changes the properties of the protein at a different site.

When the lac repressor is inactivated by the presence of lactose, the *lac* genes are expressed at a low level. The reason for this is that the RNA polymerase binds to the promoter site only weakly, often dissociating before transcription can start. This changes when CAP is bound. The binding site for CAP is just before the promoter region. CAP interacts with RNA polymerase and in this way helps the RNA polymerase to bind to the promoter site. This, in turn, increases the likelihood that transcription of the *lac* genes will be initiated, increasing the expression levels by a factor of 40. Hence, CAP functions as an activator. However, CAP only activates gene expression when it is bound by another small molecule, cyclic AMP. This molecule, in turn, is only produced when glucose is absent. Thus, the *lac* genes are only expressed when lactose is present and glucose is absent, as is summarized in Fig. 4.3(b), (c) and (d).

This example shows how interactions between proteins and DNA can function in detecting and processing signals, such as the concentration of glucose and lactose within the cell. For proper functioning it is essential that the interaction between the binding sites on the DNA and the transcription factors CAP and the lac repressor is very specific. Actually, which genes are regulated by a specific transcription factor is largely determined by the binding site alone: for instance, many genes can be brought under the control of the lac repressor if the binding site for the lac repressor is inserted in the promoter regions.

### 4.2.2 The $\lambda$ switch

When the  $\lambda$  phage, a small virus, invades its host bacterium *E. coli*, it usually integrates its DNA into the chromosome of the bacterium and remains there in a dormant state. In this so-called *lysogenic* state, the viral DNA is duplicated along with that of the bacterium. However, if the bacterium is irradiated with UV light, causing substantial damage to the DNA of the bacterium, the virus wakes up from the dormant state and enters the *lytic* state: the  $\lambda$  DNA is extensively replicated and virus particles are synthesized. After less than an hour the bacterium is destroyed and around a hundred progeny phages are released. In this way, the phage is able to escape when its host dies as a result of UV damage. A similar response happens with the more familiar human *Herpes simplex* virus, that resides in a similar dormant state in neurons around the mouth. When one experiences either physical and emotional stress or too much UV radiation, the virus enters a similar lytic state and abandons the sinking ship in the form of the highly contagious cold sores [78, 79].

The decision of whether to remain lysogenic or become lytic is an example of

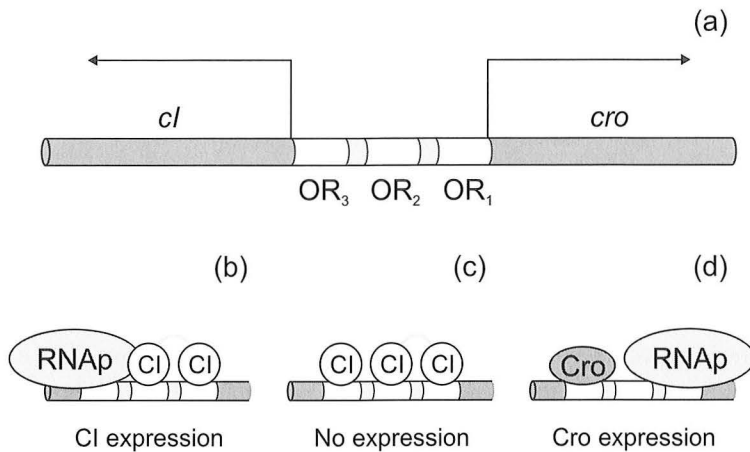


**Figure 4.4:** The  $\lambda$  switch. (a) Overview of the *cI* and *cro* genes. The regions of the DNA coding for CI and Cro are indicated in dark gray. The arrows indicate the starting point and direction of gene transcription. The *cI* and *cro* genes are transcribed in opposing directions. The promoter region for both genes is in between the two genes. The binding sites  $OR_1$ ,  $OR_2$  and  $OR_3$  for CI and Cro are indicated in white and are within the promoter region. (b) At intermediate concentration, CI is bound cooperatively to  $OR_1$  and  $OR_2$ . The cooperative interaction is indicated by the grey lines. CI bound to  $OR_2$  helps the binding of RNAP to the CI promoter, stimulating production of CI. (c) At high concentration, CI also binds to  $OR_3$ , switching off CI production. (d) In the absence of CI, Cro binds to  $OR_3$ , switching off the production of CI. As  $OR_1$  is free of CI, the *cro* gene is transcribed. At high concentrations, Cro also binds to  $OR_1$  and  $OR_2$ .

a genetic switch [77, 80]. The switch is formed by two proteins, Cro and CI, that reside next to each other on the  $\lambda$  chromosome, as is indicated schematically in Fig. 4.4. The genes coding for Cro and CI are transcribed in opposing directions and in between the two genes lies the promoter where RNA polymerase binds. In the promoter region there are three binding sites, called  $OR_1$ ,  $OR_2$  and  $OR_3$ , that bind Cro and CI.

The CI proteins can bind to all three binding sites, but with different affinities. CI has the highest affinity for binding to  $OR_1$  and a much lower affinity for the other two binding sites. As a consequence, for low concentrations of CI only  $OR_1$  will bind CI. However, the binding of CI to  $OR_1$  and  $OR_2$  is *cooperative*, meaning that CI can bind much more easily to  $OR_2$  when another CI is already bound to  $OR_1$ . The binding of CI to  $OR_3$  is independent from the occupancy of the other two binding sites. Cro, on the other hand, binds non-cooperatively and most strongly to  $OR_3$ .

In the lysogenic state CI is the only protein produced by the  $\lambda$  chromosome. In

the lytic state, instead, only Cro is present. The lysogenic state is actively maintained in the following way: when CI is present in the cell it will bind to the binding sites  $OR_1$  and  $OR_2$ . As these binding sites are just upstream of the *cro* gene, they prevent the expression of the Cro protein. On the other hand, the CI protein at the  $OR_2$  binding site helps RNA polymerase bind to the DNA and hence stimulates transcription of the *ci* gene. This situation is indicated in Fig. 4.4(b). Thus, CI functions as a repressor for Cro but as an activator for its own production.

When the concentration of CI becomes very high, the protein will also bind to the third binding site,  $OR_3$ . As  $OR_3$  is located just upstream of the *ci* gene, binding of the CI here prevents binding of RNA polymerase and switches off CI expression. This situation is indicated in Fig. 4.4(c). In this way, the third binding site functions like a thermostat: it ensures that more CI is produced when the concentration is too low, but that no CI is produced if the concentration is high enough. This keeps the concentration at an optimal level, while preventing wastage of the cell's resources.

In the lytic state, Cro binds to  $OR_3$  and blocks the transcription of the *ci* gene. Because CI is absent, the binding sites  $OR_1$  and  $OR_2$  are unbound. This state is depicted in Fig. 4.4(d). RNA polymerase binds strongly to the Cro promoter, so that in this state the Cro gene is fully expressed. So, Cro represses the *ci* gene and thereby indirectly stimulates its own production.

The  $\lambda$  switch is *bistable*, meaning that in steady state the phage could be either in the lysogenic or the lytic state, depending on the initial concentrations of CI and Cro. These steady states are insensitive to small perturbations in the concentrations of CI and Cro. The switch is flipped from the lysogenic to the lytic state by an external cue. When the bacterium is irradiated with UV light, it activates the expression of a number of genes that help the bacterium survive the resulting damage. This response is known as the SOS response. The SOS genes are repressed by a protein called LexA. Following UV damage this protein is inactivated by another protein called RecA. CI is very similar to LexA and is also broken down by RecA as a result of UV damage. When CI is inactivated, Cro is expressed. Cro, in turn, switches off CI production and activates the rest of the genes needed for the lytic state. In this way, the  $\lambda$  chromosome eavesdrops on the internal signals of the bacterium to find out when it is necessary to find another host.

The  $\lambda$  switch is an example of a system involving different types of *feedback*, where the output of the system is fed back into the input. The stimulation by CI of its own production is a case of *positive feedback*, which is often used to amplify signals. The inhibition by CI of Cro and CI production and the inhibition by Cro of CI production are examples of *negative feedback*. By combining different feedback loops, the resulting network can exhibit complicated, non-linear behavior.



## 4.3 Biochemical networks

Nowadays, high-throughput data-collection techniques have made it possible to collect qualitative data on the interactions between the molecules in the cell on an unprecedented level. With microarrays, for instance, one can determine the approximate levels of gene expression for many genes simultaneously. Moreover, technologies such as protein chips or so-called yeast two-hybrid screens make it possible to construct large maps of protein-protein interactions for entire organisms. Currently, however, quantitative data such as binding energies or reaction rates cannot be collected on such large scales and have to be obtained by time-consuming manual labor. This lack of quantitative data means that it is still very difficult to understand and predict the behavior of the large biochemical networks found in the cell.

This situation is currently dealt with in two different ways. One approach is to first try to fully understand the behavior of the simplest biochemical networks found in the cell and only move to more complex networks as our knowledge increases. The other approach is not to focus on the detailed dynamics of the components of the network, but rather to study global organization of biochemical networks. In this way, one can make use of the large amounts of high throughput data available. It turns out that one can already learn a great deal from such an approach. Biochemical networks show very distinct topological features, largely independent of the precise function of their components. I will discuss some of these results below, before turning to the study of simple networks in the rest of this Chapter.

### 4.3.1 Statistical properties of biochemical networks

When studying the architectural properties of large biochemical networks [81], the networks are often reduced to nodes, representing the molecules, connected together by links, representing interactions between the molecules. In the case of networks of protein-protein interactions the nodes are proteins and they are connected by links if they bind to each other. A lot of quantitative data is available for *metabolic networks*, the networks of chemical reactions that process nutrients into fuel and building blocks for the cell. When studying metabolic networks, the nodes are food molecules and they are linked if an enzymatic reaction converts one molecule into another. Most important for our purposes are *transcriptional networks*, where the nodes are genes and they are linked if the product of one gene is a transcription factor for another. The latter two networks are directed: a reaction between one node and another is not necessarily accompanied by a reverse reaction.

The topological properties of networks have been intensively studied as a branch

of mathematics. Traditionally, mathematicians have modeled complex networks either as regular, such as a square lattice, or as completely random, with every node being connected at random to another node. One way to characterize a network is to measure the connectivity  $k$ , the number of links from a node, for the nodes in the network. For a random network, some nodes will have a larger number of nodes than others. In fact, the connectivity distribution  $P(k)$  for random networks has a Poissonian tail [82]:

$$P(k) \sim e^{-k}. \quad (4.1)$$

However, most networks within the cell show a strikingly different connectivity distribution of the form:

$$P(k) \sim k^{-\gamma}, \quad (4.2)$$

where usually  $2 < \gamma < 3$ . Such power-law distributions are called scale-free distributions, because of the lack of a typical node. The variance of the connectivity, for instance, diverges if Eq. 4.2 holds with  $\gamma < 3$  for all  $k$ . These networks are characterized by having a few nodes with a very high connectivity, called *hubs*, and a majority of nodes with only a few connections. In the cell, for instance, ATP is a hub as it helps catalyzing very many reactions. A common feature of scale-free networks is that the nodes form a *small world* [83]: by virtue of the existence of hubs each node is connected to any other node by only a few connections. In this way, changes in one part of the network can propagate to the rest of the network very quickly. Surprisingly, many unrelated networks, such as food webs, networks of neurons or the Internet share these scale-free properties.

The topological features of scale-free networks make them very robust against accidental failure, but leaves them vulnerable to a targeted attack. Due to the presence of hubs, any two nodes in the network remain connected even when up to 80% of the links are removed at random: the many sparsely connected nodes in the network have a minor effect on the networks integrity. In *E. coli* and the yeast *Saccharomyces cerevisiae*, for instance, less than 20% of the protein deletions is lethal [81]. At the same time, removal of a few hubs can separate the network into many small, non-communicating islands. This is reflected by the fact that more than 60% of the proteins in *S. cerevisiae* with more than 15 links are lethal when deleted. Such well connected proteins also tend to be more evolutionarily conserved [81].

Biochemical networks show a large degree of clustering: if node A interacts with node B and node B with node C, it is likely that node A also interacts with node C. The degree of clustering is described by the clustering coefficient  $C(k) = 2n/k(k-1)$ , where  $k$  is the number of neighbors,  $n$  is the average number of links connecting the

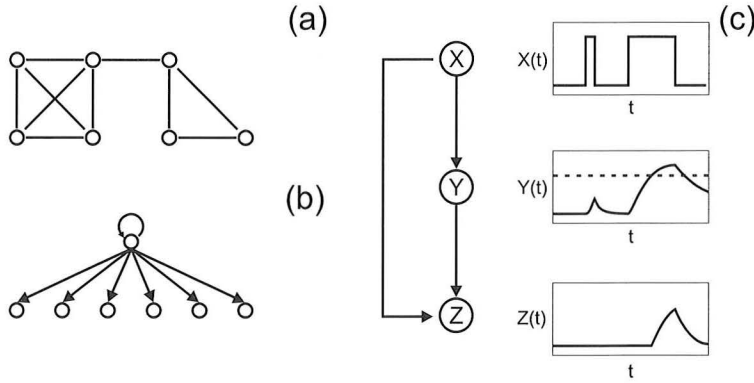


**Figure 4.5:** Examples of modules and network motifs. (a) A highly modular network. The network can be separated into one module consisting of the leftmost four nodes and one module consisting of the rightmost three nodes. Both modules are connected by a single link. (b) Single input module. A single transcription factor regulates the expression of a set of output genes. In *E. coli*, the transcription factors controlling single input motifs often regulate their own expression. (c) The feedforward loop. A transcription factor  $X$  positively regulates a second transcription factor  $Y$  and both  $X$  and  $Y$  positively regulate a gene  $Z$ . The expression of  $Y$  and  $Z$  as a function of input  $X$  is shown in black lines. Only for a sustained activation of  $X$  does  $Y$  reach the activation level for  $Z$  (indicated by the dashed line) and expression of  $Z$  is activated.

neighbors and  $k(k-1)/2$  is the maximum number of links possible between  $k$  neighbors. For biochemical networks,  $C(k) \sim k^{-1}$ . This is an indication of a *hierarchical network*: the majority of the nodes are organized into highly interconnected clusters, while a minority of unclustered hubs allows for connection between the clusters. These clusters likely represent modules of proteins that collectively perform a certain function.

It is also possible to quantify the degree of modularity in networks. The degree of modularity is obtained by finding a division of the nodes into  $K$  modules that maximizes the modularity  $Q$ , defined as [84, 85]:

$$Q = \sum_{s=1}^K \left[ \frac{l_s}{L} - \left( \frac{d_s}{2L} \right)^2 \right], \quad (4.3)$$

where  $L$  is the total number of links in the network,  $l_s$  is the number of links *between* the nodes in module  $s$  and  $d_s$  is the *total* number of out-going links of the nodes in module  $s$ . A highly modular network, such as depicted in Fig. 4.5(a), has a large fraction of the links between nodes in the modules, indicated by  $l_s/L$ . However, if we only try to obtain a division in modules that maximizes the fraction  $l_s/L$ , the

optimal solution is a single module consisting of all nodes in the network. To avoid this trivial solution, one subtracts the expected value of within-module links for a module with the same distribution of links per node but with random connections between the nodes: the fraction of links that are connected to nodes in the module  $s$  is given by  $d_s/2L$  so that for randomly connected nodes, the fraction of links that connect two nodes in module  $s$  is given by  $(d_s/2L)^2$ . Hence, if all nodes divided into modules at random or if all nodes are placed into a single module,  $Q = 0$ .

It is useful to define the normalized modularity  $Q_m$  [85]:

$$Q_m = \frac{Q - Q_{\text{rand}}}{Q_{\text{max}} - Q_{\text{rand}}}, \quad (4.4)$$

where  $Q$  is the modularity obtained according to Eq. 4.3,  $Q_{\text{rand}}$  is the average  $Q$  obtained for networks with the same distribution of links per node but with randomly connected links and  $Q_{\text{max}}$  is defined as the maximal value of  $Q$  for a network with the same distribution of links per node. Biological networks show a high degree of modularity [85]. For instance, the transcriptional network of *E. coli* has  $Q_m = 0.54$ .

Another way to study these clusters is by studying *network motifs* [86, 87]: patterns of connectivity between nodes that occur very often in biochemical networks. These motifs can be found by comparing biochemical networks with randomized networks, where all nodes are rewired at random, but the connectivity distribution is preserved. Counting how often all the possible subnetworks connecting  $n$  nodes occur <sup>4</sup>, one finds that some of these subnetworks occur much more often in biochemical networks than in random networks.

A  $n = 3$  motif frequently encountered in the transcriptional regulation network of *E. coli* is the *feed forward loop*, where gene X regulates gene Y and gene X and Y both regulate gene Z [86, 87]. An example of a feed forward loop is shown in Fig. 4.5(a). Such networks have the interesting property that they can filter out short pulse-like signals. For instance, if X activates Y and Z is only activated when X and Y are present, a high concentration in X will only lead to activation of Z if it remains high for a longer time. This is because it takes some time before X fully induces the expression of Y. If the concentration of X shows a pulse-like increase, then before X has fully induced Y, the concentration of X is already back at the original level. If, on the other hand, X remains high for a long time, then Y is fully induced and expression of Z will also be induced.

Another motif frequently encountered in *E. coli* is the *single input module* [86]. As shown in Fig. 4.5(b), in this type of network motif a single gene controls the expression of a large array of output genes. The output genes often code for a large protein assembly or a metabolic pathway. An example of such a motif is the

<sup>4</sup>For a directed network, such as transcriptional regulation, there are 13 ways to connect  $n = 3$  nodes.

SOS response described in Section 4.2.2, where LexA represses all the SOS response genes.

Even though biochemical networks share many properties with other unrelated networks, it seems that this is not the case for motifs [87]. The network motifs encountered in food webs, electronic circuits and the Internet often show a different topological structure and may reflect the different function of these networks. Feed forward loops are not seen in food webs or in the Internet, but do occur often in networks of neurons. Both in transcriptional and neuronal networks, information coming from the environment is processed to perform the appropriate actions.

### 4.3.2 Stochastic fluctuations in simple biochemical networks

One way to study the dynamics of simple biochemical networks is by studying networks that occur naturally in the cell. However, these networks are often relatively complicated and well adapted to the environment within the cell. More can be learned about what is required for a network to function properly in the cell by studying so-called *synthetic networks*, constructed from components that in the cell usually do not interact with each other. One of the first synthetic networks to have been studied is the *repressilator* [88], shown schematically in Fig. 4.6(a). The repressilator consists of three repressors: LacI, the lac repressor from *E. coli*, TetR, a repressor involved in antibiotic resistance in *E. coli* and CI, from the lambda phage. The network is constructed in such a way that each gene represses another one in a cyclic way: LacI represses production of TetR, which in turn represses CI. Finally, CI represses production of LacI. Models predict that such a network of three negative feedback loops can lead to temporal oscillations in the concentrations of the three repressors involved.

In the experiment, the genes are incorporated into a plasmid, a small circular piece of DNA that occurs naturally in bacteria. A second plasmid is also inserted that carries a gene coding for the green fluorescent protein (GFP) [89] together with a promoter that is repressed by TetR. As a consequence, the amount of GFP in the cell is directly related to the concentration of TetR in the cell and can be directly visualized by measuring the amount of GFP fluorescence. The time evolution of fluorescence is shown in Fig. 4.6(b) and clearly shows oscillatory behavior. Figure 4.6(c) plots the total amount of fluorescence from a single bacterium.

A major difference between the oscillations predicted by the models and those observed in the experiment is that the latter show a large variation in the period and amplitude of oscillation. This variability is most likely due to the stochastic fluctuations in the chemical reactions that occur in the cell [88]. One of the main consequences of this stochastic behavior is that there is a finite correlation time for

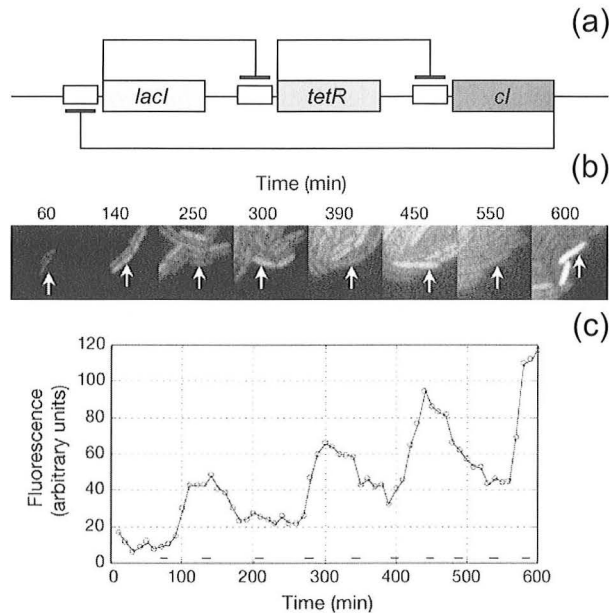


**Figure 4.6:** The repressilator. (a) Schematic overview of the repressilator. The genes are indicated in gray and the promoters in white. The genes *lacI*, *tetR*, *cl* and their specific binding sites are taken from different systems and organisms. Apart from this synthetic network, these genes never control each other. The black lines indicate which gene represses another by binding to the promoter site upstream of the target gene. (b) Time course of fluorescence in individual bacteria. The bacteria are visible as rods. The bacterium indicated by the white arrow shows a temporal oscillation in the amount of fluorescence. (c) Time plot of total fluorescence from the bacterium in (b). Horizontal bars at the bottom indicate cell divisions. The oscillations are accompanied by an overall increase in fluorescence due to the long life time of GFP proteins. Figure adapted from Ref. [88].

the phase of the oscillation: it is seen in the experiments that sibling cells that are all descended from a single parent acquire random differences in the phase over several generations. Most of the phase difference actually occurs at the moment of cell division. This is because at cell division most of the contents of the cell, including the transcription factors of the repressilator, are divided randomly between the two daughter cells. For the repressilator, the correlation time between offspring is around 100 min, or two periods. However, this is still longer than the average cell division time of 50-70 min. This means that, despite the presence of strong fluctuations, the oscillations in the different progeny cells are still correlated after one or two cell divisions.

The stochastic fluctuations in biochemical networks are often referred to as *noise*, in analogy with noise in signal processing networks. If  $P(t)$  is the fluctuating concentration of proteins within the cell, the protein noise  $\eta_P(t)$  is defined as the standard deviation of the protein concentration divided by the mean, or

$$\eta_P^2(t) = \frac{\langle P(t)^2 \rangle - \langle P(t) \rangle^2}{\langle P(t) \rangle^2}, \quad (4.5)$$

where the brackets denote an ensemble average over different cells.

Noise in gene expression can be separated into two different contributions. On the one hand, biochemical processes such as transcription and translation are inherently noisy, as reactions between molecules in the cell are of a probabilistic nature and the molecules themselves move through the cell by diffusion. This source of noise is called *intrinsic noise*. On the other hand, fluctuations in the concentrations of the other molecules in the cell can lead indirectly to a contribution to the total noise. For instance, the concentrations of molecules involved in transcription and translation, such as RNA polymerase and ribosomes, also fluctuate in the cell. This source of noise is called *extrinsic noise*. If the intrinsic noise is considerable, it means that there will be strong fluctuations in gene expression, even when the concentrations of such molecules as RNA polymerase and ribosomes are regulated by the cell to high precision.

It is possible to differentiate between intrinsic and extrinsic noise in the cell experimentally, using the synthetic network shown in Fig. 4.7(a) [90]. Here, the genes for yellow fluorescent protein (YFP) and cyan fluorescent protein (CFP) are integrated symmetrically on the same plasmid. On average, both genes are transcribed equally by RNA polymerase. If the intrinsic noise is very small, the concentration of YFP at any instant of time will be almost equal to the concentration of CFP, but the total concentration of CFP and YFP will show fluctuations due to extrinsic noise. Thus, in the experiment the total level of fluorescence will fluctuate, but all cells will have the same color, i. e. equal levels of CFP and YFP fluorescence. If the intrinsic noise cannot be neglected, YFP will sometimes be expressed at a different level than CFP, for instance because by chance RNA polymerase binds more often to one promoter than to the other. In the experiment, this will produce cells that show both different brightness and different colors.

In Fig. 4.7(b) it is clearly visible that there is a large difference in YFP and CFP expression among different bacteria. This difference changes in time within individual cells. It is also instructive to look at the distribution of YFP and CFP fluorescence intensities, as shown in Fig. 4.7(c). This distribution takes the form of an ellipse with principle axes indicated as A and B. The width of the distribution along the axis where the YFP intensity equals the CFP intensity is a measure of the extrinsic

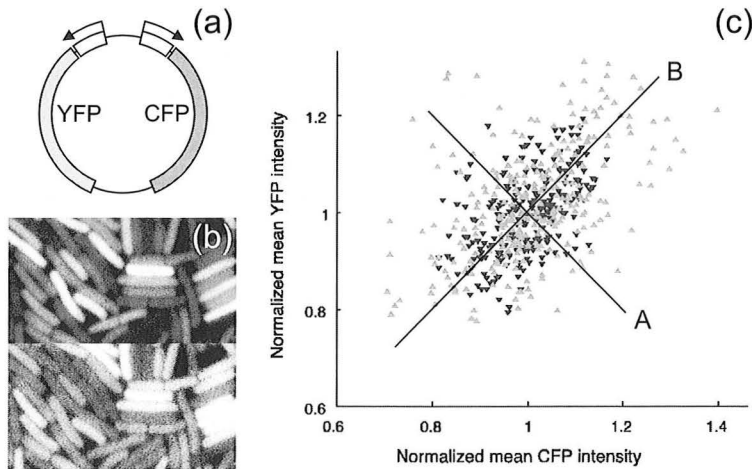


**Figure 4.7:** Intrinsic and extrinsic noise. (a) The construct used to quantify the different noise contributions. The genes for YFP and CFP are indicated in gray. The promoter regions are indicated in white. The genes are arranged symmetrically on the plasmid and have the same promoter to ensure that both genes are transcribed at the same rate on average. (b) Examples of YFP expression (upper panel) and CFP expression (lower panel) in *E. coli*. Cells show variation both in total fluorescence intensity and in the ratio between YFP and CFP fluorescence, leading to bacteria of different colors. (c) Distribution of YFP and CFP fluorescence. Because intrinsic and extrinsic noise are uncorrelated, the distribution has the shape of an ellipse with principal axes A and B. The width of the distribution along axis A is a measure for the intrinsic noise and that along axis B is a measure of extrinsic noise. Figure adapted from Ref. [90].

noise. The width along the other axis is a measure for the intrinsic noise. The extrinsic noise is on average twice as large as the intrinsic noise. Nevertheless, intrinsic noise forms a substantial contribution to the total noise.

Gene regulation by transcription factors is also affected by molecular noise. The relationship between expression rate  $f$  and the repressor concentration  $R$  is often given by a *Hill function* of the form  $f(R) = \beta/[1 + (R/K_d)^n]$ , where  $\beta$  is the expression rate in the absence of repressor,  $K_d$  is the concentration of repressor yielding half the maximal expression rate and  $n$  is the Hill coefficient. If the repressor binds cooperatively, then  $n > 1$  and the rate of gene expression depends very sensitively on the concentration of repressor.

The Hill function can be measured experimentally in single cells by the regulator dilution method [91]. Here, a gene coding for YFP is controlled by the CI repressor from the  $\lambda$  phage. If the production of CI is switched off by a second repressor, the concentration of CI is halved every time the cell divides. By measuring the YFP



fluorescence between division, the expression rate of YFP for different repressor concentrations can be determined. On average, the expression rate is well described by a Hill function, but individual cells can show very large deviations, up to 55% of the mean. These fluctuations vary on the scale of the cell cycle time and are mostly due to extrinsic noise.

More complicated behavior is seen in networks of interacting genes. In a linear cascade of three genes, where each gene represses the next gene in the cascade, it was shown that noise in one gene affects fluctuations in the expression of its downstream genes [92]. In these cascades, noise propagates from one gene to another in a nonintuitive manner and is sometimes amplified in the process. As a result, genes functioning in a cascade can show large fluctuations, even if each individual gene in the cascade has very low intrinsic noise.

## 4.4 Models of stochastic gene expression

Because the causes and effects of molecular noise in biochemical networks are often complicated and counterintuitive, mathematical models are often used to gain more understanding. A rudimentary model of the expression of a protein  $P$  is the linear *birth-and-death process*, given by the following reaction:



Here, a protein  $P$  is produced with rate  $k_p$  and decays with rate  $k_d$ . There are two different ways to incorporate the effect of fluctuations into the rate of protein production and decay. One way is to use a chemical Langevin equation, where noise terms are added explicitly. In this case, the time evolution of the protein concentration is given by

$$\frac{dP(t)}{dt} = k_f - k_d P(t) + \xi(t), \quad (4.7)$$

where  $\xi(t)$  is the noise term. In the absence of fluctuations, when  $\xi(t) = 0$ , Eq. 4.7 reduces to the macroscopic rate equation. This approximation is well defined when the mean protein concentration is large compared to the noise term. For gene expression this is not always valid: the number of transcription factors in the cell can often be very small, sometimes as low as 10-100 copies per cell, so that the discrete nature of the molecules becomes important. In this case, a better approach is to write down the chemical master equation, which describes the time evolution of the probability  $p(n, t)$  of  $n$  proteins being present in the cell at time  $t$  [93]. For the reaction in Eq. 4.6, the master equation is given by:

$$\frac{dp(n,t)}{dt} = k_f p(n-1,t) + k_d(n+1)p(n+1,t) - (k_f + k_d n)p(n,t). \quad (4.8)$$

In steady state, the mean protein number  $\langle n \rangle$  and the variance  $\langle n^2 \rangle$  can be calculated explicitly from the steady state distribution  $p(n) = p(n, t \rightarrow \infty)$  by the use of moment generating functions [93]:

$$\langle n \rangle = \frac{\sum_n n p(n)}{\sum_n p(n)} = k_f / k_d, \quad (4.9)$$

$$\langle n^2 \rangle = \frac{\sum_n n^2 p(n)}{\sum_n p(n)} = k_f^2 / k_d^2 + k_f / k_d, \quad (4.10)$$

so that for the reaction in Eq. 4.6, the noise in protein number  $\eta_P$  is given by:

$$\eta_P^2 = \frac{\langle n^2 \rangle - \langle n \rangle^2}{\langle n \rangle^2} = \frac{1}{\langle n \rangle}. \quad (4.11)$$

This shows that the noise is largest for small protein numbers, where the addition of a single extra protein constitutes a large fluctuation. The noise vanishes for large protein number, as should be expected. Such a dependence of the noise on the mean number of proteins is typical for a Poisson process. For more complicated reaction networks, it is usually not possible to obtain these results analytically. In that case, the master equation can be solved numerically by kinetic Monte Carlo algorithms [94, 95].

Even though noise in gene expression can be measured directly, the origin of these fluctuations is not always clear. Fluctuations could be directly due to the small number of proteins, as described in Eq. 4.11. However, it is also possible that the concentration of proteins is high, but the proteins are translated from a small number of mRNA molecules. Fluctuations in mRNA number then give rise indirectly to fluctuations in protein number. Currently, it is hard to measure small concentrations of mRNA and protein within single cells reliably. As a consequence, these questions are often addressed by modeling.

To get more insight into the source of noise in gene expression, a more complex model of gene expression is needed that takes into account both transcription and translation:



where  $M$  and  $P$  indicate mRNA and proteins,  $k_M$  and  $k_P$  are the mRNA and protein production rates and  $\gamma_M$  and  $\gamma_P$  are the mRNA and protein decay rates. The reaction in Eq. 4.12 describes the production and decay of mRNA molecules, analogous to the reaction in Eq. 4.6. The reactions in Eqs. 4.13 and 4.14 describe the production of proteins from the mRNA and their subsequent decay. Because protein production depends on the presence of mRNA, fluctuations in mRNA number give rise to additional fluctuations in protein number.

It was shown that in steady state the noise  $\eta_M$  in mRNA number and  $\eta_P$  in protein number is given by [96]:

$$\eta_M^2 = \frac{1}{\langle M \rangle}, \quad (4.15)$$

$$\eta_P^2 = \frac{1}{\langle P \rangle} + \frac{1}{1 + \phi} \frac{b}{\langle P \rangle}, \quad (4.16)$$

where  $\phi = \gamma_M/\gamma_P$  is the ratio of lifetimes of mRNA and protein and  $b = k_P/\gamma_M$  is the average number of proteins translated from one mRNA molecule. As mRNA molecules usually have a lifetime of minutes and proteins a lifetime of around an hour,  $\phi$  is small. The noise in mRNA number is again Poissonian. The noise in protein number is given by two terms: the first term is similar to the noise in mRNA number and corresponds to the intrinsic noise due to protein production. The second term depends on the mRNA dynamics and represents the extrinsic noise due to fluctuations in mRNA copy number.

The protein noise is mainly determined by  $b$ , the mean number of proteins produced from one mRNA. When  $b$  is large, the production of a mRNA is followed by a rapid burst of protein production. Because of the long lifetime of proteins, the fluctuations take a long time to decay. In this way the rapid fluctuations in mRNA number give rise to long-lived fluctuations in protein number. This type of fluctuations is a typical example of *burst noise*, well-known in electrical engineering.

A noise addition rule as in Eq. 4.16 can be formulated for a general network consisting of two components [97]. In this case the dynamics is described by the following reactions:

$$n_1 \xrightarrow{R_1^\pm(n_1)} n_1 \pm 1, \quad (4.17)$$

$$n_2 \xrightarrow{R_2^\pm(n_1, n_2)} n_2 \pm 1, \quad (4.18)$$

where  $n_1$  and  $n_2$  are the number of copies of the two components. The reaction rates  $R_1^\pm$  depend on  $n_1$  and the rates  $R_2^\pm$  on both  $n_1$  and  $n_2$  in arbitrary ways. In this case, the noise in  $n_2$  is given by:

$$\eta_2^2 = \frac{1}{\langle n_2 \rangle H_{22}} + \eta_1^2 \frac{H_{21}^2}{H_{22}^2} \frac{H_{22}/\tau_2}{H_{11}/\tau_1 + H_{22}/\tau_2}, \quad (4.19)$$

where  $H_{ij} = \partial \ln(R_i^-/R_i^+)/\partial \ln(n_j)$  is the logarithmic gain and  $\tau_i$  is the average lifetime of component  $i$ . Due to its generality, this expression can explain noise levels in proteins observed in a large number of different experiments [97] and also in other biochemical networks.

## 4.5 Molecular noise as a source of variation

As shown above, two living organisms that share all their genetic information will not behave in exactly the same way due to fluctuations on the molecular level. Ultimately, this is the reason why identical twins have completely different fingerprints and why cloned calico cats do not have identical fur patterns. In some cases, however, molecular noise can be a source of *epigenetic* variation – variation in the behavior of otherwise identical cells that is not encoded on the DNA but can be inherited by offspring.

For example, it is known that some bacteria exploit molecular noise to adapt to different conditions in the environment. These bacteria regulate genes by a mechanism called *phase variation* [98]. Here, a small fraction of a population of bacteria express certain genes that are not expressed in the rest of the population. This is not due to mutations in the DNA: when the minority population is isolated and allowed to regrow, the resulting population will again be divided into the same two fractions showing the same differences in gene expression.

A particular example of this is flagellar phase variation in *Salmonella enterica*, a bacterium responsible for food poisoning. Bacteria use long filaments called flagella to move and in a population of *S. enterica* the majority will express one type of flagellum whereas a minority expresses the other type. The immune system recognizes disease-causing bacteria by their external parts such as flagella. Presumably,

the bacterium switches between different types of flagella because the immune system attacks the majority flagellar type, but forgets about the minority expressing flagellar type. Similarly, *E. coli* shows phase variation in the expression of external appendages called type 1 fimbriae. These fimbriae are used to invade host tissues in the urinary tract and phase variation ensures that only a small fraction of the population invades the host, again evading discovery by the immune system. In most cases, the switch is completely stochastic, occurring at a rate of  $10^{-5}$  per generation. Often, phase variation occurs by the inversion of a large strand of DNA on the chromosome, from one direction in which transcription is possible, to another where transcription is inhibited. Although the mechanism of inversion is not understood in detail, the stochasticity is likely a consequence of fluctuations in the binding of the DNA inversion proteins.

Phase variation has been studied in single cells in the context of *bacterial persistence* [99]: when a population of bacteria is subjected to antibiotics, the majority of the population will die quickly, but a minority of the population dies much more slowly, if at all. Persistence is not due to genetically acquired antibiotic resistance, because the population will show the same response to antibiotics when regrown only from persister cells. It was observed in experiments that some cells in the population are slow-growing. Upon addition of antibiotics, these bacteria will survive whereas all fast-growing bacteria will die quickly. After removal of antibiotics a fraction of the persisters will switch to become fast-growing non-persisters that are again sensitive to antibiotics. Although the mechanism is not understood at the molecular level, the behavior of these bacteria was well described by assuming stochastic transitions between persister and non-persister cells.

In this way, the entire population is well adapted to fluctuations in the concentration of antibiotics in the environment. In the absence of antibiotics most cells will grow rapidly, so that the population will expand. At the same time, the bacteria always keep a small population of very slow growing bacteria as an insurance against the sudden appearance of antibiotics. The idea that random variation in behavior can be advantageous in the presence of random fluctuations in the environment is well known in ecology and economy and is known as *bet-hedging*. On the other hand, rather than randomly switching to different states, the bacterium could also just monitor its environment and respond to that directly as described in Section 4.2.1. Why would bacteria prefer the stochastic approach over the responsive approach? In the first case, for instance, a certain fraction of the population might be in the state that is not advantageous in the current environment. A responsive mechanism, on the other hand, must be actively maintained by expressing the relevant proteins, at the expense of energy that might be more useful for other purposes.

It was shown theoretically that the optimal mechanism depends on the cost of

responsive sensing and the time scale of the fluctuations in the environment [100]. In this model, the environment switches between different states stochastically. Bacteria can choose between different types of behavior, of which only one is optimal for the current state of the environment. It follows that if the fluctuations in the environment are fast, it is best for the survival of the population to use a responsive mechanism even if the costs of maintaining it are very high. On the other hand, when the fluctuations in the environment are slow it is more efficient to use stochastic switching: it is relatively expensive to maintain the sensory machinery of a responsive mechanism if the fluctuations occur very infrequently. Furthermore, it can be shown that for stochastic switching, the optimal rates of switching from one behavior to the other are the rates at which the environment fluctuates, even though the switching of the bacteria is completely uncorrelated to the fluctuations in the environment.

## 4.6 Noise and robustness in genetic networks

The proper functioning of biochemical networks in the cell can potentially be affected by molecular noise. An example was already mentioned in Section 4.3.2, where the repressilator network showed irregular oscillations mainly because of fluctuations induced by cell division. However, networks that occur naturally in the cell are often adapted to be insensitive to fluctuations within the cell.

For instance, the cyanobacterium *Synechococcus Elongatus* shows a very stable circadian rhythm in the expression level of all its genes. Circadian rhythms are oscillations with a period of approximately 24 hours that regulate the day-and-night cycle in many higher organisms, including humans. For a long time, bacteria were considered too simple to exhibit circadian oscillations. Cyanobacteria, however, are photosynthetic bacteria which use a circadian clock to switch off gene expression during the night. By inserting a bioluminescent protein in the genome, it was shown that in single cells of *S. elongatus* these oscillations are indeed noisy [101]. However, the noise is mainly in the amplitude of the oscillations. Even when the amplitude varied strongly between daughter cells at the moment of cell division, the period and the phase of the oscillation remained virtually unchanged in the offspring. Measurements indicated that the resulting oscillations have a correlation time of several months, even though the bacteria divide every 23 hours. This stability is in dramatic contrast to the performance of the repressilator.

A network that is insensitive to molecular noise is said to be *robust* against fluctuations. In the case of the circadian oscillations in *S. elongatus* the actual mechanism for robustness is still unknown. This is an important question, as it was shown re-

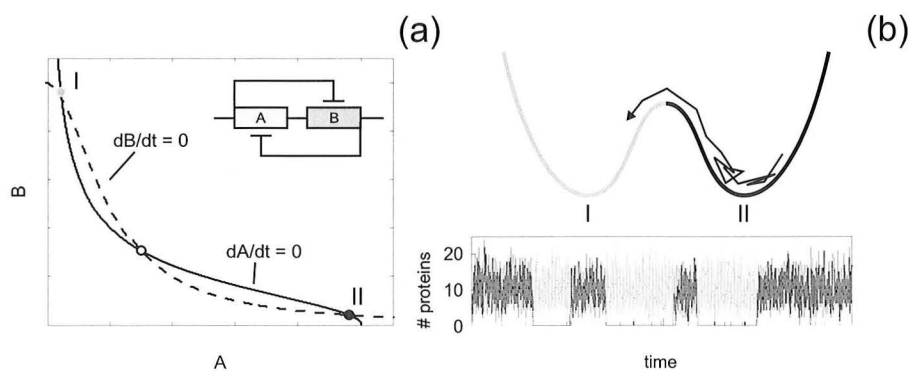


**Figure 4.8:** The genetic toggle switch. (a) Phase portrait and the nullclines  $dA/dt = 0$  (solid line) and  $dB/dt = 0$  (dashed line) in the bistable state. Steady states occur at the intersections of nullclines. There is one unstable steady state (white circle), a stable steady state at low A concentration (grey circle) and another stable steady state at low B concentration (black circle). (Inset) Schematic representation of the genetic toggle switch. (b) Toggle switch in the presence of fluctuations. The number of proteins A (black line) and B (gray line) in time obtained by stochastic simulation of the system in (a). The system flips stochastically between the A dominated and the B dominated state. The transitions are similar to those of a particle diffusing in a landscape with two potential wells.

cently that these oscillations can be reconstituted in the test tube by just three *S. elongatus* proteins, called KaiA, KaiB and KaiC, in the presence of ATP [102]. In this case, a 22 hour cycle in the binding of phosphate groups to KaiC is observed and this phosphorylation cycle is likely connected to the oscillations in gene expression observed in the cell. In other cases, however, it is known directly how the design of the network is connected to robustness against noise. For instance, it was shown experimentally that a gene that represses its own production shows much less noise in protein production than a single gene that has no feedback, when both genes are expressed at the same level on average [103].

The period of the circadian rhythm in *S. elongatus* is also surprisingly insensitive to variations in the temperature of the environment. This is a feature of all circadian clocks, known as *temperature compensation*. This is an example of a different type of robustness, namely against variation in parameters. Many biochemical networks show such robustness. For instance, it was shown that biochemical models of pattern formation in the early fruit fly embryo are remarkably resistant to large variations in the rate constants of the underlying chemical reactions, as long as the topology of the network remains unchanged [104]. In the rest of this section, I will focus on robustness against fluctuations in simple genetic switches.

A simple genetic switch is the *toggle switch*, consisting of two genes  $A$  and  $B$ , that mutually repress each other. Like the  $\lambda$  switch described in Section 4.2.2, this system has two stable steady states: state I, in which the concentration of  $A$  is high and  $B$  is repressed, and state II in which the situation is reversed. The dynamics of the protein concentrations  $A$  and  $B$  is described by the following dimensionless model that can be derived from the biochemical rate equations [105]:

$$\frac{dA}{dt} = \frac{\alpha_1}{1 + B^n} - A, \quad (4.20)$$

$$\frac{dB}{dt} = \frac{\alpha_2}{1 + A^m} - B, \quad (4.21)$$

where  $\alpha_1$  and  $\alpha_2$  are the expression rates of  $A$  and  $B$  in the absence of their repressor and the terms  $(1 + B^n)^{-1}$  and  $(1 + A^m)^{-1}$  describe the fraction of time the operator sites are free of  $A$  and  $B$ , respectively. The degree of cooperativity of repressor binding is given by  $n$  and  $m$ : if  $A$  binds to the DNA as a dimer,  $n = 2$ . For  $n, m > 1$  and appropriate values of  $\alpha_1$  and  $\alpha_2$ , these equations become *bistable* as shown in Fig. 4.8(a). Depending on the initial conditions, the system ends up in one of the stable states. When  $\alpha_1$  or  $\alpha_2$  change – for instance due to the effect of another transcription factor – one of the stable steady states can lose its stability and the system can become *monostable*.

However, in the presence of molecular noise the stable steady states of the toggle switch are not perfectly stable and the system can flip stochastically between state I and state II. Such transitions are shown in Fig. 4.8(b). A transition occurs, for instance, when, due to a fluctuation, enough of the repressed protein is expressed to switch off production of the active gene. Before a successful transition occurs, there are often several abortive attempts during which the concentration of the repressed gene is relatively high. The situation is similar to that of a particle diffusing in an energy landscape with two potential wells. Due to thermal fluctuations, the particle can get to the top of the energy barrier and escape from one well to the other, as indicated schematically in Fig. 4.8(b).

Such stochastic transitions in bistable transcriptional networks have also been seen in experiments. A synthetic toggle switch with a GFP protein fused to one of the two genes showed a bimodal fluorescence distribution in the bistable state [107]. The lac utilization network discussed in Section 4.2.1 shows bistable behavior [106]. This is because lactose induces expression of LacY, which in turn stimulates further lactose uptake. Such positive feedback makes bistability possible. Bistable behavior is monitored in single cells by inserting a plasmid with a GFP protein fused to the lac promoter, so that GFP is expressed when the *lac* genes are induced. The LacI repressor is inactivated by adding thio-methylgalactoside (TMG), a non-metabolizable



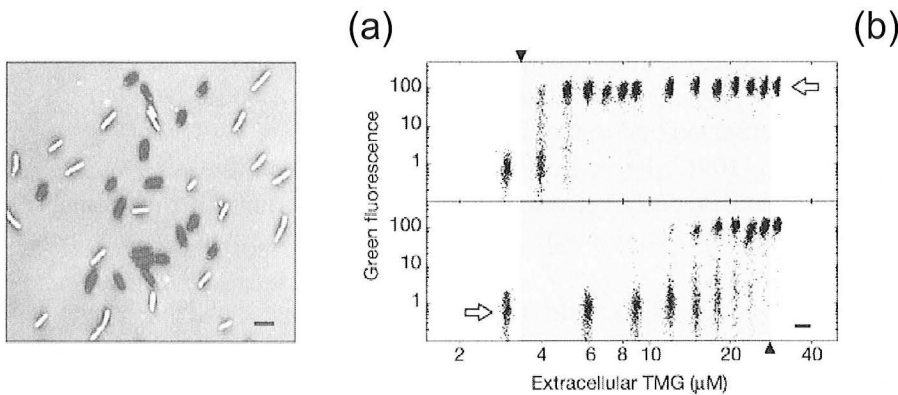


**Figure 4.9:** Bistability in the *lac* operon. (a) In the bistable state at  $18 \mu\text{M}$  thio-methylgalactoside (TMG), single cells of *E. coli* show bimodal distributions of *lac* expression as measured by GFP fluorescence (dark gray). (b) Distribution of fluorescence in a population of cells. For increasing concentrations of TMG, the system undergoes a bifurcation from a monostable to a bistable state and back. The bistable region is indicated in grey. Close to the bifurcation, the population shows a bimodal distribution of fluorescence. The system also shows hysteretic behavior: when the TMG concentration is reduced (upper panel) the switch occurs at a different concentration than when the TMG concentration is increased (lower panel). Figure adapted from [106].

lactose analogue. For intermediate concentrations of TMG the *lac* expression levels are found to be bistable.

Figure 4.9(a) shows that in the bistable region the GFP fluorescence is strongly bimodal, indicating that stochastic transitions occur between the two stable states at a rate faster than the timescale of the experiment. In Fig. 4.9(b) the distribution of GFP fluorescence is shown for cells that are initially uninduced or fully induced. From the figure it is clear that stochastic switching only occurs close to the boundary between the bistable and the monostable state. The system is also hysteretic: the switch between the uninduced state and the fully induced state occurs at a different position depending on whether the TMG concentration is increased or decreased. Such hysteric behavior is typical for bistable systems. These observations make it clear that the behavior of bistable switches is affected by molecular noise in the cell.

It is not clear yet whether bistability in the *lac* system has a specific function or whether bistability occurs in the natural system, where lactose rather than TMG is taken up. However, many genetic switches that are known to be essential are extremely stable. For instance, the switches that determine which cell type a cell in the developing embryo will develop into are so stable that they never accidentally

backtrack on their decision. Another example is the  $\lambda$  switch discussed in Section 4.2.2. The  $\lambda$  switch is remarkably reliable: in the absence of the SOS response it stays in the lysogenic state almost indefinitely. For bacteria without the RecA protein, it is estimated that the spontaneous switching rate is less than  $10^{-7}$  per cell per generation [108]. This rate is lower than the mutation rate of DNA, so that the switch flips spontaneously because of mutation rather than fluctuations. What is different in the architecture of the  $\lambda$  switches that it is so robust against molecular noise?

It was shown recently that the stability of genetic toggle switches increases dramatically when the genes for  $A$  and  $B$  have an overlapping promoter region [109]. In such an *exclusive switch*,  $A$  and  $B$  are transcribed in diverging directions. The  $\lambda$  switch is an example of an exclusive switch, as indicated in Fig. 4.4. The crucial difference in comparison to the general switch described in Eqs. 4.20 and 4.21 is that, since  $A$  and  $B$  share the same operator site, they cannot be bound to the operator site at the same time. The reason why such a switch is more stable than the general toggle switch is that it requires two rare events rather than one in order to flip: not only does the system need to produce a large number of the repressed protein, the operator should also be free of the other repressor long enough for the repressed protein to bind. Simulations show that as a consequence, the exclusive switch can be orders of magnitude more stable than the general toggle switch. This example shows how one can construct switches that are robust against fluctuations, but much work remains to be done to fully understand the robustness of switches such as the  $\lambda$  switch.

## 4.7 Spatial fluctuations

Even though molecular noise has received a lot of attention in the recent literature, most effort has gone into understanding *temporal fluctuations* caused by the random chemical kinetics within the cell. Implicitly, these studies assume that the cell behaves like a *well-stirred reactor*, so that all the reaction rates depend only on the average concentration within the cell and diffusion is ignored. However, another potential source of noise are *spatial fluctuations* due to the fact that the macromolecules in the cell move around by diffusion. In signaling networks, such as the chemotaxis system of *E. coli*, signals are probably transferred from one part of the cell to the other by diffusion [110, 111]. As these signaling molecules occur in small concentrations – in the order of  $10^2 - 10^3$  per cell – fluctuations due to the random nature of diffusion might be important. Spatial fluctuations could also play a role in gene expression, because transcription factors and macromolecules such as RNA

polymerase find the correct binding site on the DNA by diffusion through the cell. Unfortunately, it is not yet possible to observe experimentally the diffusive motion of single proteins in the cell. At the same time, there is a lack of appropriate techniques for studying spatial fluctuations by theory or simulation. As a consequence, the influence of diffusion on fluctuations in gene expression is largely unknown.

The diffusion coefficient of proteins in the cytoplasm of the cell has been measured to be in the order of  $1 \mu\text{m}^2\text{s}^{-1}$  [110]. As the volume of bacterial cells is on the order of  $1 \mu\text{m}^3$ , this means that a protein diffuses from one end in the cell in about 1 s. As transcription and translation occur on the time scales of minutes, this might suggest that spatial fluctuations play only a minor role in gene expression.

However, recent work on pole-to-pole oscillations of different proteins in bacteria has shown that spatial fluctuations are potentially important for systems that operate on a time scale of minutes or hours. Currently, the best studied are the MinCDE oscillations in *E. coli* [112–114]. The Min system specifies the mid-cell position for the division machinery, so that division results in two equally-sized daughter cells. The proteins MinC, MinD and MinE are found to oscillate from one pole to the other, where they bind to the membrane. MinC bound to the membrane inhibits the assembly of the division apparatus, thus ensuring that division occurs away from the cell poles. The oscillations occur on a time scale of minutes and the oscillation mechanism depends on diffusion to transport the proteins from one pole to the other. As the Min proteins occur only in 1000-2000 copies in the cell, spatial fluctuations are important.

Stochastic models of MinCDE oscillations that incorporate the diffusion of individual proteins show that this is indeed the case [115]. Surprisingly, spatial fluctuations seem to be beneficial rather than harmful, as for small copy numbers pole-to-pole oscillations can occur in a part of parameter space where the corresponding macroscopic model yields no oscillations. In the macroscopic model, Min oscillations are a Turing instability, occurring when a homogeneous distribution of Min proteins becomes unstable. Spatial fluctuations serve to further destabilize the homogeneous state, leading to oscillations even when for large copy numbers the homogeneous state is stable. Similar oscillations have been seen for the Spo0J/Soj proteins in the bacterium *Bacillus subtilis*, where the Soj protein relocates in an oscillatory fashion from one chromosome to the other during cell division. In this case, however, the relocation dynamics is highly stochastic due to the spatial fluctuations of the Soj protein [116].

The importance of spatial fluctuations for noise in gene expression can be estimated theoretically in the following way [117, 118]: for a promoter that binds a transcription factor, the rate of gene expression depends on the local concentration  $c$  of the transcription factor. It can be shown that if the transcription factors

have diffusion constant  $D$  and average concentration  $\bar{c}$ , the fluctuations in the local concentration are:

$$\frac{\sigma_c}{\bar{c}} = \frac{1}{\sqrt{Da\bar{c}\tau}}, \quad (4.22)$$

where  $\sigma_c$  is the standard deviation,  $a$  is the dimension of the binding site on the DNA and  $\tau$  is the time over which the occupancy is averaged by the process of gene expression. The term  $\sqrt{Da\bar{c}\tau}$  describes the spatial fluctuations and can be easily understood in a qualitative way. The number of transcription factors measured by the promoter is of order  $N \sim ca^3$  with a standard deviation  $\sigma_N \sim \sqrt{N}$ . After a time  $\tau_D \sim a^2/D$  the transcription factors around the promoter are replaced by diffusion. Thus, if the promoter measures the concentration over a time  $\tau$ , it makes  $\tau/\tau_D$  independent measurements, decreasing the standard deviation by a factor  $\sqrt{\tau/\tau_D}$ . Consequently, the fractional accuracy in measuring the local concentration of transcription factors is  $\sigma_c/\bar{c} = \sigma_N/N \sim 1/\sqrt{Da\bar{c}\tau}$ .

In bacteria, the concentration of transcription factors can be as low as 10-100 copies in a volume of  $1 \mu\text{m}^3$ . The averaging time  $\tau$  is given by the lifetime of the mRNA transcript and is of the order of 1 min. As promoter sites have a linear dimension of  $a \sim 3\text{nm}$  and the diffusion constant is of order  $D \sim 1\mu\text{m}^2\text{s}^{-1}$ , a lower bound for the fluctuations in the promoter occupancy is:

$$\frac{\sigma_c}{\bar{c}} = 20 - 60\%, \quad (4.23)$$

Such fluctuations in promoter occupancy give rise to fluctuations in gene expression. Even though it is not clear to what extent these results apply to more realistic models of gene expression, this indicates that spatial fluctuations could also be important in gene expression.

In this part of my thesis, I study the importance of spatial fluctuations by simulation in realistic models of gene expression. Currently, none of the existing techniques for simulating reaction-diffusion systems on the level of single particles is appropriate for studying gene expression: because gene expression takes place on a time scale of minutes and hours, conventional Brownian Dynamics techniques are too slow. On the other hand, techniques such as those in Refs. [115, 116] that solve the reaction-diffusion master equation numerically, have a limited spatial resolution. We have developed an algorithm, called Green's Function Reaction Dynamics (GFRD), that uses Green's functions for the diffusion equation to propagate the system efficiently from one reaction to another in an event-driven way. This algorithm is particularly efficient for low concentrations of the reactants, as is often the case in transcriptional regulatory networks.

In Chapter 5, I describe the algorithm and apply it to a simple model of gene expression. In Chapter 6, I use GFRD to study the effect of the diffusive motion of repressor molecules on the noise in mRNA and protein number in the case of a repressed gene, using a realistic model of gene expression. We will show that spatial fluctuations drastically enhance the noise in gene expression. For a fixed level of repression, the noise due to diffusion can be minimized by increasing the number of repressors or by decreasing the rate at which RNA polymerase initiates transcription. We also show that the effect of spatial fluctuations can be well described by a two-step kinetic scheme, where diffusion of the repressor towards the operator site and the subsequent association reaction are treated separately.



---

## Chapter 5

# Green's-function reaction dynamics

J.S. van Zon and P.R. ten Wolde,  
*Phys. Rev. Lett.* 94, 128103 (2005)

J.S. van Zon and P.R. ten Wolde,  
*J. Chem. Phys.* 123, 234910 (2005)

## 5.1 Introduction

Organisms can be viewed as information processing machines. Even relatively simple organisms, such as the bacterium *Escherichia coli*, can perform fairly complex computations as was shown in more detail in Chapter 4. Such functions arise from the collective properties of molecules that chemically and physically interact with one another. For this reason, computer simulations are a natural tool to elucidate the design principles that allow organisms to process information. However, the conventional numerical techniques are of limited use for this purpose, because they either ignore the molecular nature of the reactants or assume that the system is well stirred. We have developed a numerical technique, called Green's-function reaction dynamics (GFRD), that describes biochemical networks at the particle level and in both time and space. GFRD is an event-driven algorithm that uses Green's functions to combine in one step the propagation of the particles in space with the reactions between them. The event-driven nature of the algorithm makes the scheme particularly useful for problems in which the events are distributed over a wide range of length and time scales. Biochemical networks are an important example: GFRD takes small steps when the particles are close to one another, while it takes large jumps in time and space when the particles are far apart from one another. In the living cell, this is often the case, because the concentrations of the reactants are usually remarkably low. GFRD is thus highly suited for studying biochemical networks. However, the scheme is generic and the scope of GFRD is thus wider than biochemical networks. GFRD can be applied to a wide range of reaction-diffusion problems, including those in population dynamics, evolution and condensed-matter physics.

Table 5.1 gives an overview of the commonly used techniques for analyzing biochemical networks. The conventional approach is to write down the macroscopic rate equations and to solve the corresponding differential equations numerically. In this method, the evolution of the network is deterministic. It is implicitly assumed that the concentrations are large and that fluctuations can be neglected. However, in the living cell the concentrations are often very low, i. e. in the nanomolar to micromolar range. As a result, biochemical networks can be highly stochastic [88, 119].

The effect of fluctuations is often included by adding a noise term to the macroscopic rate equations [93]. However, at low concentrations, this approach is bound



| Description     |                                    | Accounts for spatial extent of network | Incorporates fluctuations   |
|-----------------|------------------------------------|--|-----------------------------|
| Continuum       | Ordinary differential equations    | No                                     | No                          |
|                 | Stochastic differential equations  | No                                     | Only at high concentrations |
| Master equation | Reaction diffusion equations       | Yes                                    | No                          |
|                 | Chemical master equation 0-d       | No                                     | Yes                         |
|                 | Reaction-diffusion master equation | Yes                                    | Yes                         |
| particle-based  | Brownian dynamics                  | Yes                                    | Yes                         |
|                 | GFRD                               | Yes                                    | Yes                         |

**Table 5.1:** Overview of the commonly used techniques and the newly developed technique, called Green’s-function reaction dynamics (GFRD), to simulate biochemical networks. GFRD takes both the discrete nature and the spatial distribution of the reactants into account.

to fail, as demonstrated by Togashi and Kaneko [120] and Shnerb and coworkers [121]. Here, the dynamics of simple reaction networks is shown to be qualitatively different from both the macroscopic rate equations and the chemical Langevin equations when the reactants are present in 10-100 copies in the reaction container. At such low concentrations, the discrete nature of the reactants has to be taken into account. In this case, the system is often described by a chemical master equation, as was discussed in Section 4.4. Currently, two techniques exist that are consistent with the (zero-dimensional) chemical master equation [122, 123]. As was explained in more detail in Section 4.4, the chemical master equation relies on the assumption that there are many non-reactive collisions to stir the system between the reactive collisions. In effect, it is implicitly assumed that at each instant the particles are uniformly distributed in space. This is a serious limitation. First of all, fluctuations of the components in space can be a major source of noise in biochemical networks as we will shown in in Section 5.3.2 and in Chapter 6. Moreover, signals often have to be transmitted from one place to the other by the diffusive motion of “messenger” molecules; their concentrations can be non-uniform, and more importantly, their low mobility can limit the response time of the network. In addition, many biochemical networks, such as those in embryonic development or in the immune response, involve a complex spatial (re)organization of the reactants. In all these cases, it is of crucial importance to describe the network in time and space.

A number of techniques have been developed that take into account the spatial distribution of the components and the stochastic character of the reactions between them [124–127]; these techniques are based upon the reaction-diffusion master equation [128, 129]. Two recent publications apply these techniques to biochemical networks [126, 127]. The key ingredient of these techniques is to divide the reaction

volume into a finite number of subvolumes; particles can react within a subvolume, but also diffuse from one subvolume to the next. Importantly, it is assumed that within each subvolume the particles are well-mixed. The techniques thus rely on the existence of a length and time scale on which the system is spatially uniform. In contrast, GFRD describes a biochemical network at the particle level. GFRD thus allows for a much better spatial and temporal resolution than techniques based upon the reaction-diffusion master equation.

In order to set up a particle-based algorithm, it would seem natural to develop a technique based upon Brownian dynamics. When particles move around by Brownian motion, their displacement after a certain time is given by a Gaussian distribution with a width depending on the time and the diffusion constant (See for instance Section 5.2.1 and Eq. 5.5). In Brownian dynamics algorithms, particles are propagated during a fixed time step by drawing a displacement from this distribution. When two particles overlap after the propagation step, the particles are allowed to react with each other with a probability depending on the reaction rate. If no reaction occurs, new positions are generated. Recently, Andrews and Bray have developed such a technique for simulating biochemical networks [130]. However, while Brownian Dynamics is correct, it is also inefficient, because at low concentrations particles often diffuse over large distances before reacting with other particles.

GFRD, on the other hand, exploits the exact solution of the Smoluchowski equation to concatenate the propagation of the particles in space with the reactions between them. GFRD thus alleviates the need to propagate the particles toward each other to let them react: even when the reactants are far apart from one another, GFRD can immediately jump to the next chemical reaction event. This event-driven nature makes the GFRD algorithm highly powerful, especially when the concentrations of the components are low.

In the next section, we describe the GFRD technique in detail. In the subsequent section, we apply GFRD to a bi-molecular reaction and to a simple model of gene expression. We explain why spatial fluctuations of the components can be a major source of noise in biochemical networks and show that the importance of spatial fluctuations increases for smaller diffusion constants. The calculations also reveal that GFRD is highly efficient under biologically relevant conditions. Our findings suggest that GFRD brings simulating biochemical networks at the particle level and in time and space within reach.

## 5.2 Overview of the algorithm

Two approaches seem to be potentially useful for simulating biochemical networks at the particle level and in time and space. The first is to let the particles undergo a random walk on a lattice and to let reaction partners react with a certain probability when they happen to meet each other. This technique has a number of limitations, the most important of which are that the physical dimensions of the particles and the interactions between them cannot conveniently be described.

Brownian dynamics is a more appealing technique. This is a stochastic dynamics scheme, in which the particles are propagated in space according to the overdamped limit of the Langevin equation. In Brownian dynamics, the solvent is considered implicitly; only the solute particles are considered explicitly. The forces experienced by these particles contain two parts: a conservative part, which arises from the interactions with the other solute particles, and a random part. The latter is the dynamical remnant of the solvent—the solutes are thought to experience random forces by collisions with particles from the solvent. Via the fluctuation-dissipation theorem and the Einstein relation, the random forces are related to the diffusion constant of the particles. To be more explicit, the equations of motion for the solute particles are given by:

$$\dot{\mathbf{r}}_s = \frac{D_s}{k_B T} (\mathbf{F}_s + \delta\mathbf{F}_s). \quad (5.1)$$

Here,  $\mathbf{r}_s$  denotes the position of solute particle  $s$ ,  $D_s$  is the diffusion constant of solute particle  $s$ ,  $k_B T$  is Boltzmann's constant times temperature,  $\mathbf{F}_s$  is the force exerted by the other solute particles, and  $\delta\mathbf{F}_s$  is the random force that arises from the interactions with the solvent.

Brownian Dynamics has a number of advantages over lattice-based techniques: the particles move in continuum space; it naturally allows for particles of different sizes and shapes; the interactions between particles—the potential of mean force—can easily be described; excluded volume effects are taken into account naturally; and a different diffusion constant can be assigned to each type of particles.

In principle, chemical reactions can be implemented into the Brownian Dynamics scheme [130]: the particles are propagated according to Eq. 5.1 and when two reaction partners happen to meet each other, they can react with a probability that is consistent with the rate constant. However, the major drawback of such a scheme is that very small time steps are needed in order to resolve the collision events. This makes brute-force Brownian Dynamics a very inefficient scheme to simulate biochemical networks.

The main idea of GFRD is to combine in one step the propagation of the particles

in space with the reactions between them. To see how this can be accomplished, one should realize that Brownian Dynamics is, in effect, a *numerical* procedure for solving the Smoluchowski equation [131]. Moreover, for a pair of particles, that not only move diffusively, but also can react according to  $A + B \rightarrow C + D + \dots$ , the Smoluchowski equation can be solved *analytically* using Green's functions. The Green's function for the pair of particles  $A$  and  $B$ ,  $p(\mathbf{r}, t | \mathbf{r}_0, t_0)$ , yields the probability that the inter-particle vector  $\mathbf{r}_0$  at time  $t_0$  becomes  $\mathbf{r}$  at a later time  $t$ . The essence of GFRD is to exploit this exact solution for a pair of particles to set up an event-driven algorithm. This allows GFRD to make large jumps in time when the particles are far apart from each other. In biochemical networks this is often the case as the reactant concentrations are usually low. GFRD is therefore ideally suited for biochemical networks, although it could clearly be used to study other reaction-diffusion problems as well.

We now describe the scheme in more detail. First, we will introduce in Section 5.2.1 the Green's functions and related quantities we use in the GFRD algorithm. In Section 5.2.2 We use these functions to set up an algorithm to simulate two particles that move by diffusion and react with each other. We will show in Section 5.2.3 how one can extend this algorithm to an arbitrary number of particles by breaking down the  $N$  particle problem in that of single particles and pairs of particles. Finally, we derive the Green's function needed for the applications presented in Section 5.3.

### 5.2.1 Green's functions

First, we consider the propagation of a *single* particle. We assume that the particle is spherical in shape and moves by free diffusion with a diffusion constant  $D$ . In this case, the diffusive motion of the particle is described by the Einstein diffusion equation:

$$\partial_t p_1(\mathbf{r}, t | \mathbf{r}_0, t_0) = D \nabla^2 p_1(\mathbf{r}, t | \mathbf{r}_0, t_0). \quad (5.2)$$

Here,  $p_1(\mathbf{r}, t | \mathbf{r}_0, t_0)$  is the probability that the particle is at position  $\mathbf{r}$  at time  $t$ , given that it was at  $\mathbf{r}_0$  at time  $t_0$ . This diffusion equation can be solved for the following initial condition and boundary condition:

$$p_1(\mathbf{r}, t_0 | \mathbf{r}_0, t_0) = \delta(\mathbf{r} - \mathbf{r}_0), \quad (5.3)$$

$$p_1(|\mathbf{r}| \rightarrow \infty, t | \mathbf{r}_0, t_0) = 0, \quad (5.4)$$

The solution is given by the well-known expression:

$$p_1(\mathbf{r}, t | \mathbf{r}_0, t_0) = \frac{1}{[4\pi D(t - t_0)]^{3/2}} \exp\left[-\frac{|\mathbf{r} - \mathbf{r}_0|^2}{4D(t - t_0)}\right]. \quad (5.5)$$

The solution  $p_1(\mathbf{r}, t | \mathbf{r}_0, t_0)$  subject to the initial condition in Eq. 5.3 is known as a *Green's function*. Provided that it can be found analytically, the Green's function is highly useful as it contains all the information of the system described by corresponding differential equation and boundary conditions. For instance, it has the property that the time evolution of a system with initial conditions  $\phi(\mathbf{r}_0, t_0)$  can be completely expressed in the Green's function  $p_1(\mathbf{r}, t | \mathbf{r}_0, t_0)$  as:

$$\phi(\mathbf{r}, t) = \int d\mathbf{r}_0 \phi(\mathbf{r}_0, t_0) p_1(\mathbf{r}, t | \mathbf{r}_0, t_0). \quad (5.6)$$

It is useful to consider the case in which the particle does not only move by diffusion, but also can decay according to the reaction:



with a decay rate  $k_d$ . We assume that, if the reaction occurs, it happens *instantaneously*. This means that the reaction can be decoupled from the diffusive motion of the particle. If the reaction is a Poisson process with  $k_d dt$  being the probability that a reaction occurs in an infinitesimal time interval  $dt$ , then the probability that the *next* reaction occurs between  $t$  and  $t + dt$  is given by:

$$q_d(t|t_0)dt = k_d \exp[-k_d(t - t_0)] dt. \quad (5.8)$$

In Section 5.2.2, we will use the single particle Green's function  $p_1(\mathbf{r}, t | \mathbf{r}_0, t_0)$  and the probability distribution  $q_d(t|t_0)$  to set up an event-driven algorithm.

The next step is to consider *one pair* of particles  $A$  and  $B$  that move around by diffusion and can react irreversibly according to:



We again assume that the particles  $A$  and  $B$  are spherical in shape. The diffusion constants for particle  $A$  and  $B$  are  $D_A$  and  $D_B$ , respectively. Furthermore, we assume that the particles react with an intrinsic rate constant  $k_a$  when they have approached each other within the reaction distance  $\sigma = (d_A + d_B)/2$ , where  $d_A$  and  $d_B$  are the diameters of particles  $A$  and  $B$ , respectively. In addition, the particles interact with each other via a potential  $U(\mathbf{r})$ , where  $\mathbf{r} = \mathbf{r}_B - \mathbf{r}_A$ . The force acting on particle B is thus given by  $-\nabla_B U(\mathbf{r}) = \mathbf{F}(\mathbf{r})$ , while the force acting on particle A is given by  $-\mathbf{F}(\mathbf{r})$ .

We aim to derive the pair Green's function  $p_2(\mathbf{r}_A, \mathbf{r}_B, t | \mathbf{r}_{A0}, \mathbf{r}_{B0}, t_0)$ , which gives the probability that the particles  $A$  and  $B$  are at positions  $\mathbf{r}_A$  and  $\mathbf{r}_B$  at time  $t$ , given that they were at  $\mathbf{r}_{A0}$  and  $\mathbf{r}_{B0}$  at time  $t_0$ , respectively. This distribution function satisfies for  $|\mathbf{r}| \geq \sigma$  the following Smoluchowski equation [131]:

$$\begin{aligned} \partial_t p_2(\mathbf{r}_A, \mathbf{r}_B, t | \mathbf{r}_{A0}, \mathbf{r}_{B0}, t_0) &= [D_A \nabla_A^2 + D_B \nabla_B^2 \\ &\quad - D_B \beta \nabla_B \cdot \mathbf{F}(\mathbf{r}) + D_A \beta \nabla_A \cdot \mathbf{F}(\mathbf{r})] \\ &\quad \times p_2(\mathbf{r}_A, \mathbf{r}_B, t | \mathbf{r}_{A0}, \mathbf{r}_{B0}, t_0). \end{aligned} \quad (5.10)$$

It will be convenient to make the coordinate transformation:

$$\mathbf{R} = \sqrt{D_B/D_A} \mathbf{r}_A + \sqrt{D_A/D_B} \mathbf{r}_B, \quad (5.11)$$

$$\mathbf{r} = \mathbf{r}_B - \mathbf{r}_A, \quad (5.12)$$

The differential operators in Eq. 5.10 can be expressed in  $\mathbf{R}$  and  $\mathbf{r}$  by the chain rule:

$$\nabla_A = \nabla_{\mathbf{R}} \cdot (\nabla_A \cdot \mathbf{R}) + \nabla_{\mathbf{r}} \cdot (\nabla_A \cdot \mathbf{r}) \quad (5.13)$$

$$= \sqrt{D_B/D_A} \nabla_{\mathbf{R}} - \nabla_{\mathbf{r}}. \quad (5.14)$$

Similarly;

$$\nabla_B = \sqrt{D_A/D_B} \nabla_{\mathbf{R}} + \nabla_{\mathbf{r}}. \quad (5.15)$$

For the divergences  $\nabla_{\mathbf{R}}^2$  and  $\nabla_{\mathbf{r}}^2$  one finds:

$$D_A \nabla_A^2 = D_B \nabla_{\mathbf{R}}^2 + D_A \nabla_{\mathbf{r}}^2 - \sqrt{D_A D_B} \nabla_{\mathbf{R}} \cdot \nabla_{\mathbf{r}}, \quad (5.16)$$

$$D_B \nabla_B^2 = D_A \nabla_{\mathbf{R}}^2 + D_B \nabla_{\mathbf{r}}^2 + \sqrt{D_A D_B} \nabla_{\mathbf{R}} \cdot \nabla_{\mathbf{r}}. \quad (5.17)$$

Using Eqs. 5.14, 5.15, 5.16 and 5.17, one can rewrite Eq. 5.10 as:

$$\begin{aligned} \partial_t p_2(\mathbf{R}, \mathbf{r}, t | \mathbf{R}_0, \mathbf{r}_0, t_0) &= (D_A + D_B) [\nabla_{\mathbf{R}}^2 + \nabla_{\mathbf{r}} \cdot (\nabla_{\mathbf{r}} - \beta \mathbf{F}(\mathbf{r}))] \\ &\quad \times p_2(\mathbf{R}, \mathbf{r}, t | \mathbf{R}_0, \mathbf{r}_0, t_0). \end{aligned} \quad (5.18)$$

It is seen that Eq. 5.18 describes two independent random processes—free diffusion in the coordinate  $\mathbf{R}$  and diffusion with a drift in the coordinate  $\mathbf{r}$ . This means that the distribution function  $p_2(\mathbf{r}_A, \mathbf{r}_B, t | \mathbf{r}_{A0}, \mathbf{r}_{B0}, t_0)$  can be factorized as

$p_2^{\mathbf{R}}(\mathbf{R}, t|\mathbf{R}_0, t_0)p_2^{\mathbf{r}}(\mathbf{r}, t|\mathbf{r}_0, t_0)$  and that the above equation can be written as one Smoluchowski equation for the coordinate  $\mathbf{R}$  and one for the coordinate  $\mathbf{r}$ :

$$\partial_t p_2^{\mathbf{R}}(\mathbf{R}, t|\mathbf{R}_0, t_0) = (D_A + D_B)\nabla_{\mathbf{R}}^2 \times p_2^{\mathbf{R}}(\mathbf{R}, t|\mathbf{R}_0, t_0), \quad (5.19)$$

$$\partial_t p_2^{\mathbf{r}}(\mathbf{r}, t|\mathbf{r}_0, t_0) = (D_A + D_B)\nabla_{\mathbf{r}} \cdot (\nabla_{\mathbf{r}} - \beta\mathbf{F}(\mathbf{r})) \times p_2^{\mathbf{r}}(\mathbf{r}, t|\mathbf{r}_0, t_0) \quad (5.20)$$

Equation 5.19 describes the free diffusive motion of the coordinate  $\mathbf{R}$ . The solution of that equation, for the initial condition  $p_2^{\mathbf{R}}(\mathbf{R}, t_0|\mathbf{R}_0, t_0) = \delta(\mathbf{R} - \mathbf{R}_0)$  and boundary condition  $p_2^{\mathbf{R}}(|\mathbf{R}| \rightarrow \infty, t|\mathbf{R}_0, t_0) = 0$ , is:

$$p_2^{\mathbf{R}}(\mathbf{R}, t|\mathbf{R}_0, t_0) = \frac{1}{[4\pi(D_A + D_B)(t - t_0)]^{3/2}} \exp\left[-\frac{|\mathbf{R} - \mathbf{R}_0|^2}{4(D_A + D_B)(t - t_0)}\right], \quad (5.21)$$

similar to Eq. 5.5 for a single particle, but with a different effective diffusion constant.

The non-trivial solution is that of the Smoluchowski equation for the inter-particle vector  $\mathbf{r}$ . This solution also has to take into account the reactions between  $A$  and  $B$ . The reaction can be incorporated as a boundary condition on the solution of the Smoluchowski equation. To be more explicit, the initial condition and boundary conditions for the coordinate  $\mathbf{r}$  are given by:

$$p_2^{\mathbf{r}}(\mathbf{r}, t_0|\mathbf{r}_0, t_0) = \delta(\mathbf{r} - \mathbf{r}_0), \quad (5.22)$$

$$p_2^{\mathbf{r}}(|\mathbf{r}| \rightarrow \infty, t|\mathbf{r}_0, t_0) = 0, \quad (5.23)$$

$$\begin{aligned} -j(\sigma, t|\mathbf{r}_0, t_0) &\equiv 4\pi\sigma^2 D \left( \frac{\partial}{\partial r} - \mathbf{F}(\mathbf{r}) \right) \times p_2^{\mathbf{r}}(\mathbf{r}, t|\mathbf{r}_0, t_0)|_{|\mathbf{r}|=\sigma}, \\ &= k_a p_2^{\mathbf{r}}(|\mathbf{r}| = \sigma, t|\mathbf{r}_0, t_0), \end{aligned} \quad (5.24)$$

where  $\partial/\partial_r$  denotes a derivative with respect to the inter-particle separation  $r$ . The reaction enters the problem as a third boundary condition at particle contact,  $|\mathbf{r}| = \sigma$ . Here  $j(\sigma, t|\mathbf{r}_0, t_0)$  is the outward radial flux of probability  $p_2^{\mathbf{r}}(\mathbf{r}, t|\mathbf{r}_0, t_0)$  through the ‘‘contact’’ surface of area  $4\pi\sigma^2$ . The boundary condition, also known as a *radiation* boundary condition [132, 133], states that this radial flux of probability equals the intrinsic rate constant times the probability that the particles  $A$  and  $B$  are in contact. In the limit  $k_a \rightarrow \infty$ , the radiation boundary condition reduces to an *absorbing* boundary condition  $p_2^{\mathbf{r}}(|\mathbf{r}| = \sigma, t|\mathbf{r}_0, t_0) = 0$ , while in the limit  $k_a \rightarrow 0$  the radiation boundary condition reduces to a *reflecting* boundary condition  $j(\sigma, t|\mathbf{r}_0, t_0) = 0$ .

The pair Green's function  $p_2^{\mathbf{r}}(\mathbf{r}, t | \mathbf{r}_0, t_0)$  is derived in Section 5.2.5 for the case in which  $\mathbf{F}(\mathbf{r}) = \mathbf{0}$  for  $|\mathbf{r}| > \sigma$ ; for cases in which  $\mathbf{F}(\mathbf{r}) \neq \mathbf{0}$  for  $|\mathbf{r}| > \sigma$ , the Green's functions could be obtained numerically. Here, we will discuss some useful quantities that can be derived from the Green's function. The first quantity of interest is the probability that a pair of particles, initially separated by  $\mathbf{r}_0$ , survives and does not recombine by time  $t$ . This so-called *survival* probability is given by:

$$S_a(t | \mathbf{r}_0, t_0) = \int_{|\mathbf{r}| > \sigma} d\mathbf{r} p_2^{\mathbf{r}}(\mathbf{r}, t | \mathbf{r}_0, t_0). \quad (5.25)$$

Clearly,  $S_a(t_0 | \mathbf{r}_0, t_0) = 1$  for  $|\mathbf{r}_0| > \sigma$ . The survival probability decreases in time, due to the reaction between particle  $A$  and  $B$ . Consequently, the rate of change of the survival probability at time  $t$  is related to the probability that particle  $A$  and  $B$  will have their reaction at time  $t$ . Thus, the second quantity of interest one can derive from the Green's function is the reaction rate  $q_a(t | \mathbf{r}_0, t_0)$ , which is defined as the probability per unit time that a pair, initially separated by  $\mathbf{r}_0$ , reacts at time  $t$ . It is related to the survival probability by:

$$q_a(t | \mathbf{r}_0, t_0) \equiv -\frac{\partial S_a(t | \mathbf{r}_0, t_0)}{\partial t}. \quad (5.26)$$

Since the reactions are assumed to occur only at contact, the reaction rate is also given by the flux at contact:

$$q_a(t | \mathbf{r}_0, t_0) = -j(\sigma, t | \mathbf{r}_0, t_0). \quad (5.27)$$

The above equation can also be obtained from Eq. 5.20 and Eq. 5.25 and by using the fact that the flux at  $|\mathbf{r}| \rightarrow \infty$  vanishes.

For a pair of particles  $A$  and  $B$  that react with each other *reversibly*, the irreversible reaction rate  $q_a(t | \mathbf{r}_0, t_0)$  can be interpreted as the probability that a pair of particles, initially separated by  $\mathbf{r}_0$  at time  $t_0$ , will have a next reaction at time  $t$ . This is used to set up the GFRD event-driven algorithm, which we will describe in the next section.

## 5.2.2 Two-particle algorithm

Using the single particle Green's functions in Eq. 5.5 and the pair Green's function in Eqs. 5.19 and 5.20 together with the reaction rates in Eqs. 5.8 and 5.26, it is possible to set up an event-driven algorithm to simulate two particles that move around by diffusion and can react with one another.

For the two-particle algorithm, we consider a single particle of type  $A$  that can react with a single particle of type  $B$  according to the following scheme:





with association rate  $k_a$  and dissociation rate  $k_d$ . We will simulate the system from a time  $t_0 = 0$  to time  $T$ . As a function of time, the system will flip-flop between the associated state  $C$  and the dissociated state  $A+B$ . The GFRD event-driven algorithm to propagate this system consists of iterating the following steps:

- (1) If the system is in the dissociated state  $A + B$ , then draw a next association time  $t$  according to  $q_a(t|\mathbf{r}_0, t_0)$ , where  $t_0$  is the current time in the simulation. (Eq. 5.26).
  - (a) If  $t \geq T$ , then the two particles will not react within the simulation time. New positions for  $A$  and  $B$  at time  $T$  are obtained from  $p_2^{\mathbf{R}}(\mathbf{R}, T|\mathbf{R}_0, t_0)$  (Eq. 5.21) and  $p_2^{\mathbf{r}}(\mathbf{r}, T|\mathbf{r}_0, t_0)$  (Eq. 5.34) with  $\mathbf{R}$  and  $\mathbf{r}$  as given by Eqs. 5.11 and 5.12.
  - (b) If  $t < T$ , then the next reaction will occur within the simulation time. Particles  $A$  and  $B$  are removed and a new position for particle  $C$  at time  $t$  is obtained from  $p_2^{\mathbf{R}}(\mathbf{R}, t|\mathbf{R}_0, t_0)$  (Eq. 5.21). The time is incremented, so that  $t_0 = t$ .
- (2) If the system is in the associated state  $C$ , then draw a next dissociation time from  $q_d(t|t_0)$  (Eq. 5.8).
  - (a) If  $t \geq T$ , then particle  $C$  will not have decayed within the simulation time  $T$ . A new position for particle  $C$ ,  $\mathbf{r}_C$ , at time  $T$  is obtained from  $p_1(\mathbf{r}_C, T|\mathbf{r}_{C0}, t_0)$  (Eq. 5.5)
  - (b) If  $t < T$ , the next reaction will occur within the simulation time. Particle  $C$  is removed and particles  $A$  and  $B$  are placed at time  $t$  adjacent to each other at positions around  $\mathbf{r}_C$  as obtained from  $p_1(\mathbf{r}_C, t|\mathbf{r}_{C0}, t_0)$  (Eq. 5.5). Specifically, the positions of particles  $A$  and  $B$  are given by  $\mathbf{R} = \mathbf{r}_C$  and  $\mathbf{r} = \sigma(\sin \theta \cos \phi, \sin \theta \sin \phi, \cos \theta)$ , with  $\theta$  and  $\phi$  chosen randomly.

The above algorithm propagates the system in one step from one reaction to the other. The time step  $\Delta t$  between consecutive reactions is obtained from the rate equations  $q_a(t|t_0)$  and  $q_d(t|t_0)$ . The simulation time  $T$  effectively imposes a maximum timestep  $\Delta t_{\max} = T - t_0$  on the algorithm.

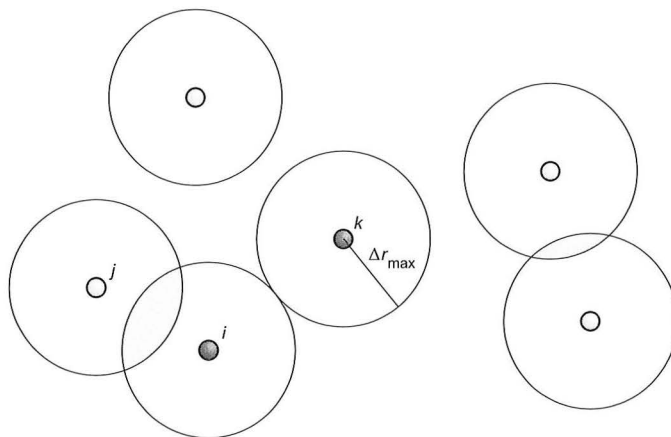


**Figure 5.1:** Determination of the maximum time step,  $\Delta t_{\max}$ . The maximum size of the time step is set by the requirement that each particle can interact with at most one other particle during that time step; each particle  $i$  can thus travel a distance of at most  $\Delta r_{\max,i}$  during a time step, as indicated by the circles. We have used the operational criterion  $\Delta r_{\max,i} = H \sqrt{6D_i \Delta t_{\max,i}}$ , with  $D_i$  being the diffusion constant of particle  $i$ . A value of  $H = 3$  was found to yield a good conservation of the correct steady-state distribution. In this example, each particle is assumed to have the same diffusion constant; the time step is limited by the constraint that particles  $i$  and  $k$  should not interact as particle  $i$  can already interact with particle  $j$ . Note that with this maximum time step the many-body problem of propagating the  $N$  particles is reduced to that of propagating single particles and pairs of particles.

### 5.2.3 Many-particle algorithm

The two-particle algorithm in Section 5.2.2 cannot be extended directly to include  $N$  particles. The reason for this is that it would require the  $N$  particle Green's function  $p_N(\{\mathbf{r}_i\}, t | \{\mathbf{r}_{0,i}\}, t_0)$ , which is intractable. However, it is possible to break down the  $N$  particle problem into single particles and pairs of particles by imposing a maximum time step  $\Delta t_{\max}$ .

Let us imagine a configuration of reactants as shown in Fig. 5.1. The circles indicate the distance the particles can travel in a time step  $\Delta t$ . For a particle that moves by free diffusion with a diffusion constant  $D$ , that distance scales as  $\langle |\Delta \mathbf{r}|^2 \rangle \sim D \Delta t$ . In principle, in a finite time particles can travel an arbitrarily large distance

by diffusion. In practice, however, the probability of such a large excursion is very small. We assume that within a time step  $\Delta t$  particles cannot diffuse further than a distance  $\Delta r_{\max} = H\sqrt{(6D\Delta t)}$ . For  $H = 3$ , for instance, 98.6% of the particles satisfy this criterion.

In Fig. 5.1, intersecting circles represent particles that may meet within the time step  $\Delta t$ . Isolated particles and pairs of interacting particles can be propagated analytically using Green's functions, as we was discussed in Section 5.2.1. Clearly, the larger the time step, the larger the circles and the greater the probability that reaction partners meet and react with each other. However, we cannot make the time step arbitrarily large: if a given particle can collide with more than one other particle during a time step, then propagating the particles becomes a many-body problem that we can not solve analytically. The size of a time step is thus limited by the requirement that each particle can interact with at most one other particle during that time step. In the representation of Fig. 5.1, this means that a circle can overlap with at most one other circle. This constraint sets an upper limit on the magnitude of a time step in our algorithm; we will call it  $\Delta t_{\max}$ . However, provided that we consider times  $\Delta t$  smaller than  $\Delta t_{\max}$  and limit displacements to  $\Delta r_{\max}$ , the problem can be reduced to that of propagating single particles and pairs of particles. For this situation an event-driven GFRD algorithm can be set up analogous to the two-particle algorithm in Section 5.2.2. The many particle algorithm then consists of the following steps:

- (1) Determine the maximum time step  $\Delta t_{\max}$ . The maximum time step is determined by the condition that only single particles or pairs of particles have to be considered (see Fig. 5.1). For each particle  $i$ , we determine the maximum time step  $\Delta t_{\max,i}$ , such that it can interact with at most one other particle. If all particles have the same diffusion constant  $D$ , this maximum time step is determined by  $r_{\text{SNN},i}$ , the distance to the second-nearest neighbor, as:

$$\Delta t_{\max,i} = \frac{(r_{\text{SNN},i} - 2\sigma)^2}{6DH^2}, \quad (5.29)$$

where  $\sigma = (d_A + d_B)/2$  is the reaction distance of the pair of particles. The maximum global time step is then given by:

$$\Delta t_{\max} = \min(\{\Delta t_{\max,i}\}). \quad (5.30)$$

In order to determine  $\Delta t_{\max,i}$  for particle  $i$ , we assume that during that step the particle can travel at most a distance  $\Delta r_{\max,i} = H\sqrt{6D_i\Delta t}$ , where  $D_i$  is

the diffusion constant of particle  $i$ . We find that  $H = 3$  suffices to preserve the correct steady-state distribution.

- (2) Determine the next reaction and next reaction time. We first construct a list of possible reactions  $\{R_\nu\}$ . Single particles can only undergo a dissociation or decay reaction. For pairs, both particles can undergo a dissociation or decay reaction, but in addition two particles can also associate. With each reaction  $R_\nu$ , we associate a survival probability function  $S_\nu(t - t_0)$  and a next-reaction distribution function  $q_\nu(t - t_0)$ ; the two are related via  $q_\nu(t - t_0) = -\partial S_\nu(t - t_0)/\partial t$ . For the association reactions,  $q_\nu(t - t_0) = q_a(t|\mathbf{r}_0, t_0)$  as given by Eq. 5.26 and  $S_\nu(t - t_0) = S_a(t|\mathbf{r}_0, t_0)$  as given by Eq. 5.25. For dissociation or decay reactions,  $q_\nu(t - t_0) = q_d(t|t_0) = k_d \exp(-k_d(t - t_0))$  and  $S_\nu(t - t_0) = \exp(-k_d(t - t_0))$ . For each reaction, we draw a tentative time step from the next-reaction distribution function  $q_\nu(t - t_0)$ .

From the list of tentative reactions, we choose as the actual next reaction the one that occurs first, *provided* that this reaction occurs within the maximum time step  $\Delta t_{\max}$ . Accordingly, the system will be propagated through a time  $\Delta t$  as given by:

$$\Delta t = \min(\{\Delta t_\nu\}, \Delta t_{\max}). \quad (5.31)$$

Note that if there is no tentative reaction for which the tentative next reaction time  $\Delta t_\nu < \Delta t_{\max}$ , then no reaction will occur within the time step.

- (3) Propagate particles. Single particles are propagated according to  $p_1(\mathbf{r}, t|\mathbf{r}_0, t_0)$  in Eq. 5.5; if a particle decays, then the products are placed next to each other at positions centered around  $\mathbf{r}$ . For each pair of particles, the following two substeps are executed: 1) a new position for the coordinate  $\mathbf{R}$  is obtained from Eq. 5.21; 2) if the pair has not reacted, a new inter-particle vector  $\mathbf{r}$  is obtained from  $p_2^r(\mathbf{r}, t|\mathbf{r}_0, t_0)$  in Eq. 5.34; else, if the pair has reacted, the products are placed adjacent to each other at positions around  $\mathbf{R}$ . If the algorithm generates a tentative displacement larger than the maximum displacement  $\Delta r_{\max, i}$ , we discard the result and draw a new displacement
- (4) Update particles. Update identities of particles according to the executed reaction. Delete or add particles created or destroyed in that reaction.

In the many-particle algorithm, the particles are propagated from one reaction to another, provided that a reaction occurs within the maximum time step  $\Delta t_{\max}$ . For all single particles and pairs of particles, with the exception of the single particle

or the pairs of particles undergoing a reaction, new positions at the end of each time step are generated from the Green's functions.

### 5.2.4 Boundary conditions

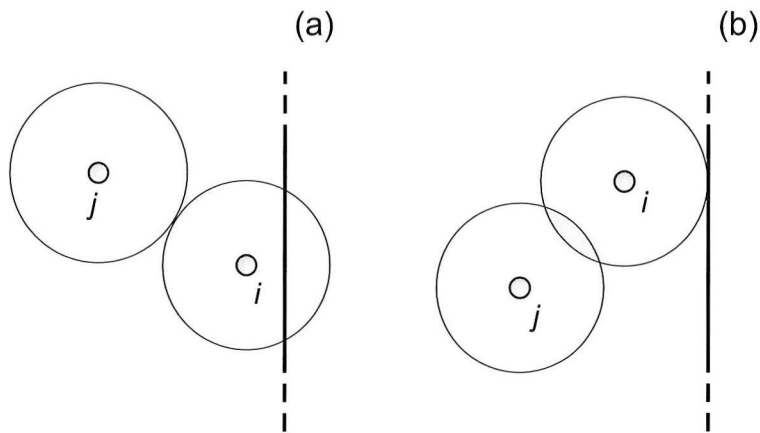
Boundaries can be naturally implemented in GFRD: as, in general, no analytical solution exists for a *pair* of particles in the presence of a boundary, we introduce the further requirement that during a time step a particle can only interact with either the wall of the container or with another particle, but not with both. The first case is shown schematically in Fig. 5.2(a) for a reflecting boundary. Here, particle  $j$  is propagated by free diffusion and particle  $i$  according to the Green's function for a particle in the presence of a reflecting boundary. In the case shown in Fig. 5.2(b), the position of both particles is chosen from the irreversible Green's function and because of the limit on the time step no position outside of the container will be generated. For the case of a rectangular container with reflecting boundary conditions, a new position is easily obtained, as we will discuss now. First, we treat the simple case of a particle near a reflecting plane.

Figure 5.3(a) shows how to generate a new position  $\mathbf{x}$  for a particle that is confined to a half-space by a reflecting boundary. First, for a particle initially located at  $\mathbf{x}_0$ , the Green's function  $p_b(\mathbf{x}, t|\mathbf{x}_0)$  for a particle in the presence of the reflecting boundary in Fig. 5.3(a) is given by:

$$p_b(\mathbf{x}, t|\mathbf{x}_0) = p_{\text{free}}(\mathbf{x}, t|\mathbf{x}_0) + p_{\text{free}}(\mathbf{x}, t|\mathbf{x}_1), \quad (5.32)$$

where  $p_{\text{free}}(\mathbf{x}, t|\mathbf{x}_0)$  and  $p_{\text{free}}(\mathbf{x}, t|\mathbf{x}_1)$  are the Green's functions for free diffusion in Eq. 5.5, for the particle at  $\mathbf{x}_0$  and for a mirror particle placed at  $\mathbf{x}_1$ , on the opposite side of the boundary. Because of symmetry, the fluxes of the two particles cancel on the boundary between I and II. As a consequence, the Green's function in Eq. 5.32 obeys the proper reflecting boundary conditions.

The fact that the Green's function  $p_b(\mathbf{x}, t|\mathbf{x}_0)$  can be expressed according to Eq. 5.32 implies a simple procedure for generating a new position  $\mathbf{x}$  for a particle initially located at  $\mathbf{x}_0$  and confined to a half-space. We draw a tentative new position  $\mathbf{x}'$  according to  $p_{\text{free}}(\mathbf{x}', t|\mathbf{x}_0)$ . If  $\mathbf{x}'$  lies outside of the half-space, in region II, we obtain a final position  $\mathbf{x}$  within region I by reflecting the displacement through the boundary, as shown in Fig. 5.3(a). It can be seen from Fig. 5.3(a) that, due to the symmetry of the problem, the probability of generating a final position  $\mathbf{x}$  using this reflection procedure is equal to  $p_{\text{free}}(\mathbf{x}, t|\mathbf{x}_1)$ . As a consequence, the resulting probability distribution  $p_b(\mathbf{x}, t|\mathbf{x}_0)$  is given by Eq. 5.32 and obeys the reflecting boundary conditions.



**Figure 5.2:** Maximum time step in the presence of a reflecting boundary (solid thick line). Now, the maximum time step is chosen such that a single particle  $i$  either reacts only with the boundary (a) or only with another particle  $j$  (b). In the case of (a) both particles are propagated by free diffusion or free diffusion in the presence of a reflecting boundary. In the case of (b) the pair Green's function is used.

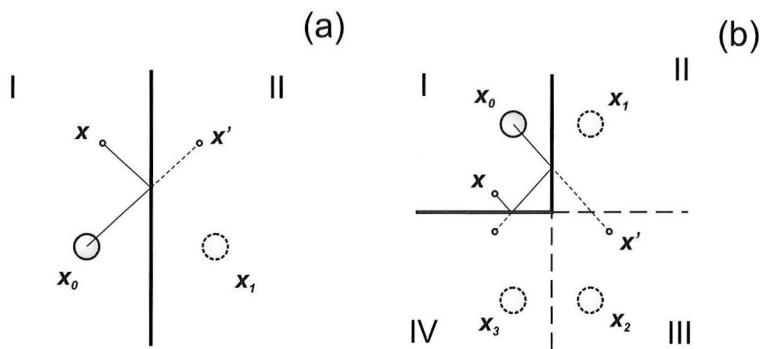


**Figure 5.3:** Drawing a new position for a particle that can interact with a reflecting boundary. (a) Particle confined to a half-space. A tentative new position  $x'$  is drawn from the Green's function for free diffusion,  $p_{\text{free}}(x', t|x_0)$ . If  $x'$  lies outside of region I, a final position  $x$  within region I is generated by reflection through the boundary. The dashed particle is a mirror particle located at  $x_1$ . (b) Particle confined to a quadrant. If a tentative position  $x'$  is drawn in quadrant II or IV, the procedure in (a) is followed. If a tentative position is drawn in quadrant II, a final position  $x$  is generated by reflection through both the vertical and the horizontal boundary. Mirror particles at  $x_1$ ,  $x_2$  and  $x_3$  are shown as dashed particles.

This procedure can be extended to a particle confined to a quadrant of the plane, as indicated in Fig. 5.3(b). In this case, the Green's function  $p_b(\mathbf{x}, t|\mathbf{x}_0)$  can be expressed as:

$$p_b(\mathbf{x}, t|\mathbf{x}_0) = \sum_i p_{\text{free}}(\mathbf{x}, t|\mathbf{x}_i), \quad (5.33)$$

with mirror particles at  $\mathbf{x}_1$ ,  $\mathbf{x}_2$  and  $\mathbf{x}_3$  as shown in Fig. 5.3(b). The flux due to the particles at  $\mathbf{x}_1$  and  $\mathbf{x}_2$  is balanced by the flux of the particles at  $\mathbf{x}_0$  and  $\mathbf{x}_3$  on the boundary between quadrant I and II. A similar argument holds for the boundary between quadrant I and IV, so that  $p_b(\mathbf{x}, t|\mathbf{x}_0)$  in Eq. 5.33 obeys the proper reflecting boundary conditions. We can extend the sampling procedure outlined above to the case of a particle confined to a quadrant as follows. We again generate a tentative new position  $\mathbf{x}'$  according to  $p_{\text{free}}(\mathbf{x}', t|\mathbf{x}_0)$ . If this tentative position is generated in quadrant II or IV, a final position  $\mathbf{x}$  within the container is generated by the procedure outlined in Fig. 5.3(a). When a tentative position  $\mathbf{x}'$  is generated in quadrant III, as shown in Fig. 5.3(b), a final position  $\mathbf{x}$  within the container is obtained by reflection through both the vertical and the horizontal boundary. When  $\mathbf{x}'$  lies in quadrant III, the probability of obtaining the final position  $\mathbf{x}$  in quadrant I using this procedure is given by  $p_{\text{free}}(\mathbf{x}', t|\mathbf{x}_2)$ . Similarly, when  $\mathbf{x}'$  is in quadrant II and IV, the probability of generating a  $\mathbf{x}$  in quadrant I is given by  $p_{\text{free}}(\mathbf{x}', t|\mathbf{x}_1)$  and  $p_{\text{free}}(\mathbf{x}', t|\mathbf{x}_3)$ , respectively. As a consequence, the resulting probability distribution  $p_b(\mathbf{x}, t|\mathbf{x}_0)$  obtained using this procedure is given by Eq. 5.33 and yields the correct reflecting boundary conditions.

This procedure can be extended to rectangular boxes, by taking into account more mirror charges. However, unless the density of reactants is very low the time step will be too small for particles to diffuse between parallel boundaries of the container. In this case, the problem reduces to that of a particle confined to a quadrant, as discussed above. Obtaining a final position within the container by reflections is only justified when the Green's function with reflecting boundary conditions can be written in terms of mirror particles. As a consequence, it is not directly applicable to more complicated boundaries such as cylinders or spheres. In this case, Green's functions can be obtained analytically for particles in the presence of reflecting cylindrical or spherical boundaries [132]. Arbitrarily-shaped containers can be constructed from planes, spheres, cylinders or other building blocks by restricting the maximum time step so that a particle can only interact with one of these elements at the same time.

### 5.2.5 Green's function for $U(\mathbf{r}) = 0$

In the absence of a long-range interaction,  $U(\mathbf{r}) = 0$ , we can analytically obtain the Green's function  $p_2^r(\mathbf{r}, t | \mathbf{r}_0, t_0)$  for a pair of particles  $A$  and  $B$  that move by free diffusion, but, upon contact, can react irreversibly with a rate constant  $k_a$ . In this case, the differential equation in Eq. 5.20 reduces to the Einstein diffusion equation and one can exploiting the analogy between the diffusion of particles and the conduction of heat in solids. The corresponding Green's function for the conduction of heat in solids is derived in Ref. [132] and is given by:

$$p_2^r(r, \theta, \phi, t | r_0) = \frac{1}{4\pi\sqrt{rr_0}} \sum_{n=0}^{\infty} \left[ (2n+1)P_n(\cos\theta) \right. \quad (5.34)$$

$$\left. \times \int_0^{\infty} e^{-Du^2t} F_{n+1/2}(ur) F_{n+1/2}(ur_0) u du \right], \quad (5.35)$$

where:

$$F_{\nu}(ur) = \frac{(2\sigma k_a + 1)U_{\nu}(ur) - 2u\sigma V_{\nu}(ur)}{[(R_{1,\nu})^2 + (R_{2,\nu})^2]^{1/2}}, \quad (5.36)$$

and:

$$U_{\nu}(ur) = J_{\nu}(ur)Y_{\nu}(u\sigma) - Y_{\nu}(ur)J_{\nu}(u\sigma), \quad (5.37)$$

$$V_{\nu}(ur) = J_{\nu}(ur)Y'_{\nu}(u\sigma) - Y_{\nu}(ur)J'_{\nu}(u\sigma), \quad (5.38)$$

$$R_{1,\nu} = (2\sigma k_a + 1)J_{\nu}(u\sigma) - 2u\sigma J'_{\nu}(u\sigma), \quad (5.39)$$

$$R_{2,\nu} = (2\sigma k_a + 1)Y_{\nu}(u\sigma) - 2u\sigma Y'_{\nu}(u\sigma). \quad (5.40)$$

In the above equations,  $P_n$  is the  $n$ th Legendre polynomial,  $J_n$  and  $Y_n$  are the  $n$ th Bessel function of the first and the second kind with derivatives  $J'_n$  and  $Y'_n$ . The total diffusion constant of the two particles  $A$  and  $B$  is given by  $D = D_A + D_B$  and the reaction distance by  $\sigma = (d_A + d_B)/2$ , where  $d_A$  and  $d_B$  are the diameters of the particles  $A$  and  $B$ , respectively. Here and below, we take  $t_0 = 0$ . The Green's function can be expressed in a more compact notation by:

$$p_2^r(r, \theta, \phi, t | r_0) = \sum_{n=0}^{\infty} C_n P_n(\cos\theta) R_n(r, t | r_0). \quad (5.41)$$

The probability  $f(r | r_0, t)$  of finding the particles separated by a distance between  $r$  and  $r + dr$  at time  $t$ , when they were at a distance  $r_0$  initially, is given by:



$$f(r|r_0, t) = \int r^2 dr \int \sin \theta d\theta \int d\phi p_2^*(r, \theta, \phi, t|r_0) \quad (5.42)$$

$$= 2\pi \sum_{n=0}^{\infty} C_n Q_n(\pi) r^2 R_n(r, t|r_0), \quad (5.43)$$

with

$$Q_n(\theta) = \int_0^\theta \sin \theta P_n(\cos \theta) d\theta. \quad (5.44)$$

The conditional probability  $g(\theta|r, r_0, t)$  that two particles are at an angle between  $\theta$  and  $\theta + d\theta$  with respect to the original direction  $\mathbf{r}_0 = \mathbf{r}_B - \mathbf{r}_A$ , given that they are separated by a distance  $r$  at time  $t$ , is:

$$g(\theta|r, r_0, t) = 2\pi \sum_{n=0}^{\infty} C_n Q'_n(\theta) r^2 R_n(r, t). \quad (5.45)$$

The survival probability  $S(t|r_0)$  is given by:

$$S(t|r_0) = \int_\sigma^\infty f(r|r_0, t) dr. \quad (5.46)$$

The above integral is complicated but it follows from the properties of the diffusion equation that it must be identical to the irreversible survival probability for the spherically symmetric case that only depends on  $r$ . For spherical symmetry, the survival probability can be more easily calculated and is given by [134, 135]:

$$S_{\text{irr}}(t|r_0) = 1 - \frac{\sigma}{r_0} \frac{k_a}{k_a + k_D} \left[ \operatorname{erfc}\left(\frac{r_0 - \sigma}{\sqrt{4Dt}}\right) - W\left(\frac{r_0 - \sigma}{\sqrt{4Dt}}, \alpha_{\text{irr}} \sqrt{t}\right) \right], \quad (5.47)$$

where  $k_D = 4\pi\sigma D$ ,  $\alpha_{\text{irr}} = (1 + k_a/k_D)\sqrt{D}/\sigma$  and  $W(a, b) = \exp(2ab + b^2)\operatorname{erfc}(a + b)$ .

Prior to the simulations, we construct a look-up table for the integrand of  $q_a(t|r_0)$  and look-up tables for the integrands of  $f(r|r_0, t)$  and  $g(\theta|r, r_0, t)$ ; essentially, the latter look-up tables are one large four-dimensional look-up table for the Green's function  $p_2^*(r, \theta, \phi, t|r_0)$ . During the simulations, the look-up table for  $q_a(t|r_0)$  allows us to efficiently obtain the next reaction time. Similarly, the other look-up tables make it possible to efficiently determine a new position for the reaction partners (in case they have not reacted): we first draw a  $r$  from the distribution  $f(r|r_0, t)$ ; next we draw  $\theta$  from the distribution  $g(\theta|r, r_0, t)$  and finally we choose  $\phi$  uniformly distributed between 0 and  $2\pi$ . Precisely how we do this, is outlined in Section 5.2.6.

When numerically calculating the Green's function, we sum contributions up to  $n = n_{\max}$ , the number of terms needed for the sum in Eqs. 5.34, 5.41, 5.43, and 5.45 to converge. However, for small  $t$  the convergence is very slow and many terms need to be taken into account. In order to reduce  $n_{\max}$ , we exploit the fact that for small  $t$ , the probability that the two particles will interact with each other, is relatively small. In other words, for small  $t$  the full solution  $p_2^{\mathbf{r}}(\mathbf{r}, t|\mathbf{r}_0)$  is dominated by free diffusion. We can use this observation to reduce  $n_{\max}$  by writing the Green's function as  $p_2^{\mathbf{r}}(\mathbf{r}, t|\mathbf{r}_0) = p_{\text{free}}(\mathbf{r}, t|\mathbf{r}_0) + p_{\text{corr}}(\mathbf{r}, t|\mathbf{r}_0)$ , where  $p_{\text{free}}$  is the solution for free diffusion and  $p_{\text{corr}}$  is a correction term that takes into account the reacting boundary at  $r = \sigma$ . The free diffusion term in Eq. 5.5 is expressed in polar coordinates as:

$$p_{\text{free}}(r, \theta, \phi, t|r_0) = \frac{1}{[4\pi Dt]^{3/2}} \exp\left[-\frac{r^2 + r_0^2 - 2rr_0 \cos \theta}{4Dt}\right]. \quad (5.48)$$

Using the fact that  $p_{\text{free}}(r, \theta, \phi, t|r_0)$  can also be written [132] as:

$$\begin{aligned} p_{\text{free}}(r, \theta, \phi, t|r_0) &= \frac{1}{4\pi\sqrt{rr_0}} \sum_{n=0}^{n_{\max}} \left[ (2n+1)P_n(\cos \theta) \right. \\ &\quad \times \int_0^\infty e^{-Du^2t} J_{n+1/2}(ur) J_{n+1/2}(ur_0) u \, du, \end{aligned} \quad (5.49)$$

we find by comparison with Eq. 5.34 that  $p_{\text{corr}}$  can be expressed as:

$$\begin{aligned} p_{\text{corr}}(r, \theta, \phi, t|r_0) &= -\frac{1}{4\pi\sqrt{rr_0}} \sum_{n=0}^{n_{\max}} \left[ (2n+1)P_n(\cos \theta) \right. \\ &\quad \times \int_0^\infty e^{-Du^2t} \frac{R_1}{R_1^2 + R_2^2} (R_1 F_1 + R_2 F_2) u \, du, \end{aligned} \quad (5.50)$$

where

$$R_1 = (2\sigma k_a + 1)J_{n+1/2}(u\sigma) - 2u\sigma J'_{n+1/2}(u\sigma), \quad (5.51)$$

$$R_2 = (2\sigma k_a + 1)Y_{n+1/2}(u\sigma) - 2u\sigma Y'_{n+1/2}(u\sigma), \quad (5.52)$$

$$F_1 = J_{n+1/2}(ur)J_{n+1/2}(ur_0) - Y_{n+1/2}(ur)Y_{n+1/2}(ur_0), \quad (5.53)$$

$$F_2 = J_{n+1/2}(ur)Y_{n+1/2}(ur_0) + J_{n+1/2}(ur_0)Y_{n+1/2}(ur). \quad (5.54)$$

As the correction term  $p_{\text{corr}}(r, \theta, \phi, t|r_0)$  is usually small for small  $t$ ,  $n_{\max}$ , the number of terms that needs to be included in order to accurately compute the functions  $f(r, |r_0, t)$  and  $g(\theta|r, r_0, t)$ , is strongly reduced. For both very short times and  $r_0 \sim \sigma$ ,

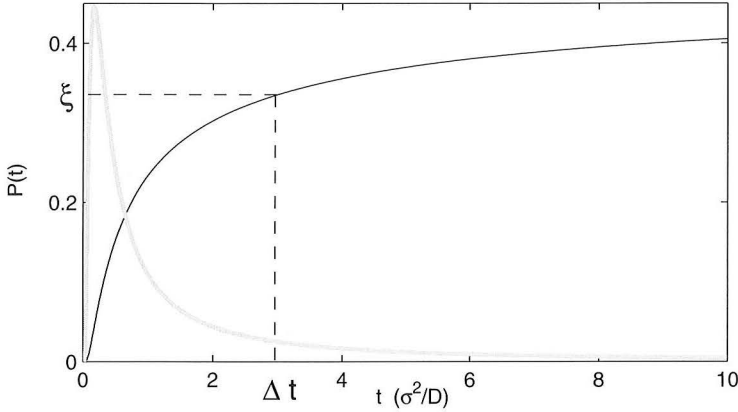


**Figure 5.4:** Drawing a random number according to probability of next reaction  $q_a(t|r_0)$  for a pair of particles initially separated by  $r_0$  (grey line). The cumulative distribution function is given by  $1 - S(t|r_0)$  (black line), where  $S(t|r_0)$  is the irreversible survival probability in Eq. 5.47. A random number  $\xi$  is generated, uniformly distributed between  $0 < \xi < 1$ . The corresponding next-reaction time  $\Delta t$  is given by  $1 - S(\Delta t|r_0) = \xi$ . Here,  $r_0 = 2\sigma$ ,  $D = 1$  and  $k_a = 1 \cdot 10^3$ .

the correction term in Eq. 5.50 still converges very slowly. In this case, a brute-force Brownian dynamics scheme could be used. In the applications in Section 5.3 and Chapter 6, however, this was not necessary.

### 5.2.6 Drawing random numbers from an arbitrary distribution

In the GFRD algorithm, we frequently have to draw a random number  $x$  according to a probability distribution  $p(x)$ . This can be done by constructing the cumulative probability distribution [136]:

$$P(x) = \int_0^x p(x') dx'. \quad (5.55)$$

We draw a random number  $\xi$ , uniformly distributed in the interval  $0 < \xi < 1$ . The value of  $x$  is determined such that  $P(x) = \xi$ , as indicated in Fig. 5.4. A random number  $x$  is generated between  $x$  and  $x + dx$  if a random number  $\xi$  is generated in the interval  $P(x) \leq \xi < P(x + dx)$ . The probability for drawing  $\xi$  in this interval is given by  $P(x + dx) - P(x) = P'(x)dx = p(x)dx$ , so that this procedure yields the correct distribution  $p(x)$ .

In Fig. 5.4, we show as an example the procedure for drawing a next-reaction time  $\Delta t$  from the distribution of next-reaction times  $q(t|r_0)$  for a pair of particles

initially separated by a distance  $r_0$ . For each association reaction  $R_\nu$ , we generate a random number  $\xi_\nu$ , uniformly distributed in the interval  $0 < \xi_\nu < 1$ . The corresponding next-reaction time  $\Delta t_\nu$  is given by:

$$\xi_\nu = \int_0^{\Delta t_\nu} q_\nu(t') dt' = 1 - S_\nu(\Delta t_\nu). \quad (5.56)$$

where the last step follows from the definition of the reaction rate in Eq. 5.26. In general, for association reactions  $S_\nu(\infty) \neq 0$ : for two particles, that can diffuse and react subject to the boundary condition Eq. 5.23, there is a finite probability that they *never* react; this is related to the well-known fact that in 3D a random walker, that starts at the origin, can “escape” and never return to the origin. If  $\xi_\nu > (1 - S_\nu(\infty))$ , then the reaction  $R_\nu$  does not occur and it is dropped from the list of possible reactions.

When using look-up tables we use a similar procedure. When drawing a next-reaction time  $\Delta t$ , for instance, we first construct the cumulative distribution function  $Q(t_i|r_0) = 1 - S(t_i|r_0)$  from the look-up table  $Q(t_i|r_{0,j})$  by linear interpolation:

$$Q(t_i|r_0) = Q(t_i|r_{0,j}) + \frac{r_0 - r_{0,j}}{r_{0,j+1} - r_{0,j}} [Q(t_i|r_{0,j+1}) - Q(t_i|r_{0,j})], \quad (5.57)$$

where  $t_i$  and  $r_{0,j}$  indicate the entries in the table and  $j$  is such that  $r_{0,j} \leq r_0 < r_{0,j+1}$ . We then generate a random number  $\xi$ , uniformly distributed between  $0 < \xi < 1$  and obtain the next-reaction time  $\Delta t$  after linear interpolation:

$$\Delta t = t_i + \frac{\xi - Q(t_i|r_0)}{Q(t_{i+1}|r_0) - Q(t_i|r_0)} (t_{i+1} - t_i), \quad (5.58)$$

where  $i$  is such that  $Q(t_i|r_0) \leq \xi < Q(t_{i+1}|r_0)$ . In a similar fashion, we draw  $r$  from  $f(r|r_0, t)$  in Eq. 5.43 and  $\theta$  from  $g(\theta|r, r_0, t)$  in Eq. 5.45.

## 5.3 Results

This section is organized as follows: first we study a simple bimolecular reaction to show that GFRD accurately reproduces analytical results. Then we turn our attention to a very simple model of gene expression as a typical example of a system that is well handled by the GFRD technique. We specifically focus on the levels of noise in protein concentrations and find dramatic differences between GFRD and results from the well-stirred chemical master equation, which ignores spatial fluctuations. Finally, we compare the performance of GFRD to a conventional Brownian Dynamics algorithm.

### 5.3.1 Bi-molecular reaction

To test the validity of our approach, we study the reversible bimolecular reaction:



As a first test of GFRD, we focus on an *isolated* pair of particles  $A$  and  $B$  that are in an open system. We use a setup in which particle  $A$ , with diameter  $\sigma$ , is placed at the origin and held fixed during the simulation. The second particle  $B$ , also with diameter  $\sigma$ , is initially placed at random in a spherical shell of radius  $r_0$  centered around particle  $A$ . We then propagate particle  $B$  for a time  $t_{\text{sim}}$ . During this time, particle  $B$  can diffuse freely with a diffusion constant  $D$  and it can associate with particle  $A$  with a rate constant  $k_a$  and dissociate from it with a rate constant  $k_d$ . Typically, particle  $B$  will associate with and dissociate from  $A$  a (large) number of times during the simulation. We repeat this whole procedure many times. This allows us to calculate the reversible distribution function  $p_{\text{rev}}(r, t|r_0, t_0)$ , which gives the probability that the two particles  $A$  and  $B$ , separated by a distance  $r_0$  at time  $t_0$ , are a distance  $r$  apart at a later time  $t$ . This numerical result can be compared to the analytical solution derived by Kim and Shin for the *reversible* reaction shown in Eq. 5.59 [135].

If the next reaction time were larger than the simulation time,  $t_{\text{sim}}$ , then we could in principle directly propagate the particles through  $t_{\text{sim}}$ . However, this would not provide a stringent test of our algorithm. At each step, we therefore choose a maximum time step  $\Delta t_{\text{max}}$  at random from the interval  $[10^{-4}\tau, t_{\text{sim}}]$ , where  $\tau = \sigma^2/D$  is the unit of time. This could be interpreted as mimicking the constraint on the maximum time step arising from the presence of other particles.

Figure 5.5 shows excellent agreement for  $p_{\text{rev}}(r, t|r_0, t_0)$  between theory and simulation for  $r_0 = \sigma$ . We find similar agreement between theory and simulation for other initial distances  $r_0$  and for other values of the diffusion constant  $D$  and reaction rates  $k_a$  and  $k_d$ . It should be realized that because the particles are initially placed at contact, many reactions can occur during the time  $t_{\text{sim}}$ . Moreover, because we divide the simulation time into smaller intervals, we must propagate the particles many times, using the Green's function for an extensive range of  $r$ ,  $(t - t_0)$  and  $r_0$ . Thus, at least for the case of an isolated pair of particles, this procedure provides a thorough test of our algorithm.

Next, we want to study a more complex system in which a single particle of type  $A$  is held fixed at the center of a spherical container of radius  $R$  and is surrounded by  $N_B$  particles of type  $B$ . Particle  $A$  can again react with a particle  $B$  to form the product  $C$  according to the scheme in Eq. 5.59; particle  $C$ , like particle  $A$ , does not

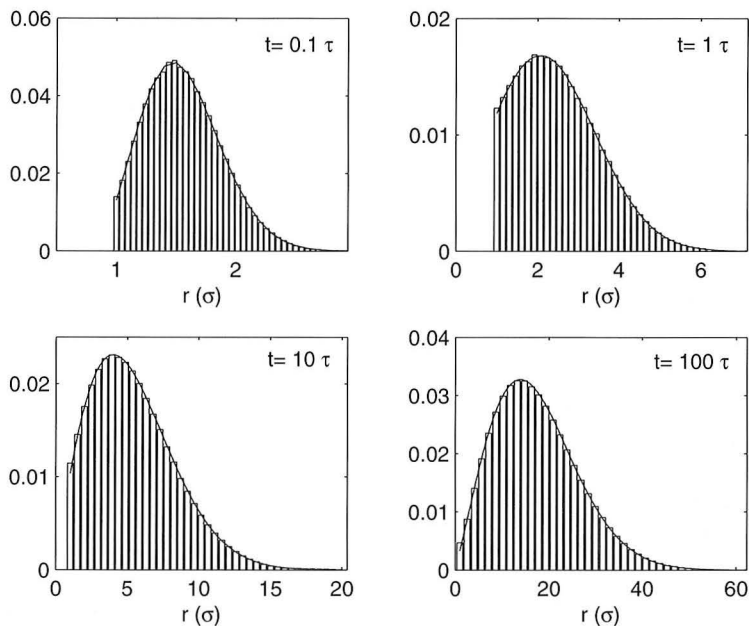


**Figure 5.5:** The distribution  $p_{\text{rev}}(r, t | \sigma, t_0 = 0)$  for  $t = 0.1\tau, 1\tau, 10\tau$  and  $100\tau$ . For  $r < \sigma$ , the distribution  $p_{\text{rev}}(r, t | \sigma, t_0) = 0$  due to the hard sphere repulsion between the particles. The bars denote the simulation results and the solid lines denote the analytical solutions of Kim and Shin [135]. Note that the particles are initially placed at contact ( $r_0 = \sigma$ ). The forward rate constant  $k_a = 1000 \text{ molecule}^{-1} \sigma^3 \tau^{-1}$  and the backward rate constant is  $k_d = 1\tau^{-1}$ . The unit of time  $\tau = \sigma^2/D$ .

diffuse. Particles  $B$  and  $C$  do not react, although they are not allowed to overlap with each other. The excluded volume interactions between a pair of two  $B$  particles and between a pair of a  $B$  and a  $C$  particle is taken into account by using reflecting boundary conditions, i.e. by setting  $k_a = 0$  in Eq. 5.24. We note that the requirement that the  $B$  and  $C$  particles are not allowed to overlap, may impose a constraint on the maximum size of the time step,  $\Delta t_{\text{max}}$ .

As the  $B$  particles diffuse through the container, they will come into contact with the fixed particle  $A$ . When in contact, the particles  $A$  and  $B$  can enter the bound state  $C$  with forward rate  $k_a$ . When in the bound state, other  $B$  particles approaching the fixed  $C$  particle cannot react with it. Only after dissociation into the unbound state  $A + B$ , occurring at rate  $k_d$ , can another reaction occur. On average, there will be a probability  $p_{\text{bound}}$  of finding the  $A$  particle bound to the  $B$  particle. In steady state, we have that:

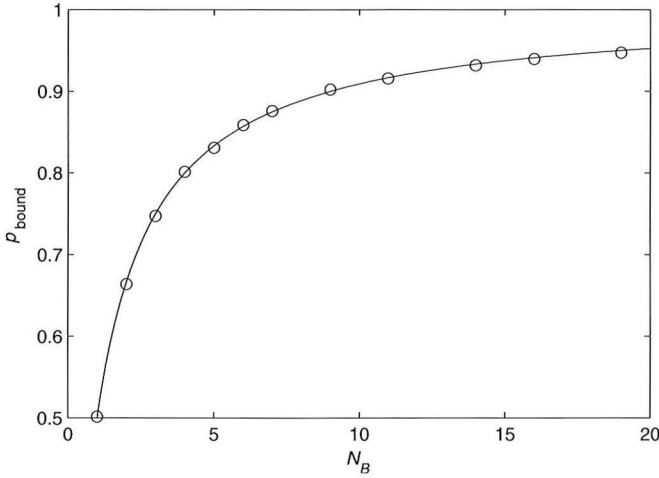


**Figure 5.6:** The probability  $p_{\text{bound}}$  that the  $A$  particle is bound to a  $B$  particle as a function of the total number of  $B$  particles for the reaction scheme shown in Eq. 5.59. The symbols indicate the simulation results, while the solid line denotes the mean-field prediction (Eq. 5.61 with  $g_{AB}(\sigma) = 1$ ). The radius of the container is  $R = 200\sigma$  and the equilibrium constant is chosen such that it is equal to the interaction volume  $V$ . The error bars in the simulation results are smaller than the size of the symbols.

$$k_a g_{AB}(\sigma)[A][B]_T = k_d[C], \quad (5.60)$$

where  $g_{AB}(r)$  is the radial distribution function for the pair of particles  $A$  and  $B$ ,  $[B]_T = N_B/V$  is the total concentration of  $B$  molecules and  $[A] + [C] = 1/V$  is the total concentration of  $A$  molecules. The probability to find a  $A$  particle in the bound state is  $V[C]$ , so that  $p_{\text{bound}}$  is given by:

$$p_{\text{bound}} = \frac{KN_B}{V + KN_B}, \quad (5.61)$$

where  $V$  is the volume available for the  $B$  particles,  $N_B$  is the total number of  $B$  particles and

$$K = g_{AB}(\sigma)k_a/k_d \quad (5.62)$$

is the equilibrium constant.

The radial distribution function  $g_{AB}(r)$  describes the spatial correlations arising from the interactions between the particles [137]. It is conceivable that in this system the excluded volume interactions between the particles induce spatial correlations. These correlations could affect the density of  $B$  particles that are in contact

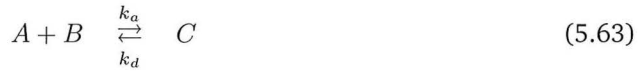
with the  $A$  particle and thereby the probability that the  $A$  particle is bound to a  $B$  particle. In Eq. 5.62, the distribution function at contact,  $g_{AB}(\sigma)$ , thus describes the effect of the spatial correlations on the equilibrium constant. However, the concentrations that we consider here are very low and the spatial correlations are thus expected to be small. Indeed, the simulations reveal that  $g_{AB}(r) \approx 1$  for all distances  $r > \sigma$ . If  $g_{AB}(\sigma) = 1$ , then Eqs. 5.61 and 5.62 reduce to the well-known mean-field results that can straightforwardly be obtained by solving the macroscopic rate equations in steady-state. In Fig. 5.6, we compare the simulation results to the mean-field prediction for  $p_{\text{bound}}$ . We find excellent agreement.

In conclusion, we have shown that our algorithm provides an accurate way of simulating particles that can move by diffusion and react according to monomolecular and bimolecular reactions. As more complicated reactions, such as trimolecular reactions, can, in general, be decomposed into these elementary reactions, we are now in a position to simulate more complex systems.

### 5.3.2 Simple model of gene expression

In this section we present results for a model of gene expression. It should be stressed that the model is highly simplified. The purpose here is to show the power of our approach. Nevertheless, we find interesting effects due to the spatial fluctuations of the components that could be of relevance for more realistic systems.

The reaction network consists of the following reactions:



In Eqs. 5.63–5.65,  $A$  represents a promoter region on the DNA and  $B$  a RNA polymerase molecule that moves by free diffusion and can bind with a forward rate  $k_a$  to the promoter site to form the RNAP-DNA complex  $C$ . This complex can dissociate with a rate constant  $k_d$ . Alternatively, it can produce a protein  $P$  at a production rate  $k_{\text{prod}}$ . Proteins degrade with a decay rate  $k_{\text{dec}}$ . Note that, in this model, when a protein is produced the RNAP dissociates from the DNA.

In the simulations, we fix the promoter site, i.e. the  $A$  particle, in the center of a spherical container of radius  $R$ . The volume of the container is  $V = 1\mu\text{m}^3$ , which is comparable to that of the *Escherichia coli* cell. The promoter site is surrounded by  $N_B = 18$  RNAP molecules, corresponding to the concentration of free RNAP of 30 nM as found in the living cell [138]. The RNAP molecules move with



a diffusion constant  $D = 1\mu\text{m}^2\text{s}^{-1}$ , which is comparable to that of similarly sized proteins [110]. We assume that, at contact, the RNAP can associate with the promoter site at a rate as determined by the Maxwell-Boltzmann velocity distribution. This leads to  $k_a = \pi\sigma^2\langle v_{AB} \rangle = 3 \cdot 10^9\text{M}^{-1}\text{s}^{-1}$ , where  $v_{AB}$  is the relative velocity of the particles  $A$  and  $B$ . We note that this estimate is equal to the rate of collisions between hard spheres in the low density limit [137, 139]. We could arrive at an alternative estimate for  $k_a$  using the diffusion constant and a molecular “jump” distance  $\lambda$ . This would lead to  $k_a = 4\pi\sigma^2D/\lambda$ . Both estimates give similar results for the value of  $k_a$ . The dissociation rate is chosen such that the equilibrium constant  $K = k_a/k_d$  equals the one reported in [138], yielding  $k_d = 21.5\text{s}^{-1}$ . We assume that the diameters of the promoter site and the RNAP molecules are equal and given by  $\sigma = 5\text{nm}$ .

Here, we only simulate the promoter site and the RNAP molecules explicitly in space. The proteins are assumed to be uniformly distributed in space. Moreover, we reduce both the degradation and the production of protein molecules to single-step Poisson processes. This a strong simplification—in order to produce a protein, DNA is first transcribed into mRNA, and the mRNA is then translated into proteins; moreover, both processes consist of a large number of steps [140]. Nevertheless, this model allows us to demonstrate the power and the flexibility of our algorithm. In particular, the production and decay reactions can simply be added to our list of possible reactions,  $\{R_\nu\}$  (see Section 5.2.3). The next-reaction distribution function for the production reaction is given by  $q_{\text{prod}}(t) = k_{\text{prod}}N_C \exp(-k_{\text{prod}}N_C t)$ , where  $N_C = 0$  if the RNAP is unbound and  $N_C = 1$  if it is bound to the DNA, while the propensity function for the degradation reaction is given by  $q_{\text{decay}}(t) = k_{\text{decay}}N_P \exp(-k_{\text{decay}}N_P t)$ . In this way, the spatially-resolved GFRD scheme can naturally be combined with kinetic Monte Carlo schemes, such as the Gillespie algorithm [122], that are based upon the well-stirred chemical master equation.

Since we are interested in the importance of spatial fluctuations in gene expression, it is natural to compare the GFRD results to those obtained using the zero-dimensional chemical master equation. The latter approach does take into account the discrete nature of the reactants and the stochastic character of their interactions, but it treats the spatial fluctuations in a mean-field manner: at each instant, it is implicitly assumed that the particles are uniformly distributed in space. This approach is justified if there are many non-reactive collisions to stir the system in between the reactive collisions. However, the RNAP is present in low copy numbers, and, upon contact, it rapidly associates with the promoter site on the DNA. As a consequence, this reaction is diffusion-limited. As we show below, this can have important implications for the noise in gene expression.

We can calculate the noise in protein number from the well-stirred master equa-

tion using the method of moment generating functions [93]. In what follows,  $a$ ,  $c$  and  $p$  denote the number of molecules  $A$ ,  $C$  and  $P$ , respectively. The master equation for the time evolution of the distribution function  $P(c, p, t)$  is given by:

$$\begin{aligned} \partial_t P(c, p, t) = & k_a N_B (2 - c) P(c - 1, p, t) + k_d (c + 1) P(c + 1, p, t) \\ & k_{\text{prod}} (c + 1) P(c + 1, p - 1, t) + k_{\text{dec}} (p + 1) P(c, p + 1, t) \\ & - [k_a N_B (1 - c) + (k_d + k_{\text{prod}})c + k_{\text{dec}}p] P(c, p, t) \end{aligned} \quad (5.66)$$

where we used that  $a + c = 1$ . We can calculate the mean and standard deviations in  $c$  and  $p$  by expressing the steady-state solution to Eq. 5.66 in terms of the generating function  $F(x, y)$ , given by:

$$F(x, y) = \sum_{c,p} x^c y^p P(c, p, t). \quad (5.67)$$

We can calculate the moments of  $c$  from the generating function using the following relations:

$$\partial_x F(x, y) \Big|_{x,y=1} = \langle c \rangle \quad (5.68)$$

$$\partial_x^2 F(x, y) \Big|_{x,y=1} = \langle c(c - 1) \rangle \quad (5.69)$$

$$\partial_x \partial_y F(x, y) \Big|_{x,y=1} = \langle cp \rangle \quad (5.70)$$

The moments for  $p$  can be obtained in similar fashion. In steady state, Eq. 5.66 can be expressed in generating functions  $F(x, y)$  as follows:

$$k_a N_B u F = [(k_a N_B + k_d + k_{\text{prod}})u + k_a N_B u^2 - k_{\text{prod}}v] \partial_u F + k_{\text{dec}} v \partial_v F, \quad (5.71)$$

where  $F = F(u, v)$  and where we defined  $u = x - 1$  and  $v = y - 1$ . To obtain Eq. 5.71, we multiplied both sides of Eq. 5.66 with  $x^c y^p$  and summed over  $c$  and  $p$ . Furthermore, we used the relation:

$$\sum_{c,p} x^c y^p (c + 1) P(c + 1, p, t) = \partial_x \sum_{c,p} x^{c+1} y^p P(c + 1, p, t) = \partial_x F(x, y) \quad (5.72)$$

and similar relations for the other terms in Eq. 5.66. We can now obtain the moments by expanding  $F(x, y)$  around  $x = 1$  and  $y = 1$  to second order, or:

$$F(u, v) = 1 + X_1 u + X_2 v + \frac{1}{2} X_{11} u^2 + \frac{1}{2} X_{22} v^2 + X_{12} uv \quad (5.73)$$

Using the relations in Eqs. 5.68–5.70, we can relate the moments with the coefficients of the expansion in Eq. 5.73 as  $X_1 = \langle c \rangle$ ,  $X_2 = \langle p \rangle$ ,  $X_{11} = \langle c(c-1) \rangle$ ,  $X_{22} = \langle p(p-1) \rangle$  and  $X_{12} = \langle cp \rangle$ . Inserting Eq. 5.73 into Eq. 5.71 and comparing the prefactors of the different powers of  $u$  and  $v$  up to second order, yields the following relations:

$$(k_a N_B + k_d + k_{\text{prod}})X_1 = k_a N_B \quad (5.74)$$

$$k_{\text{dec}}X_2 = k_{\text{prod}}X_1 \quad (5.75)$$

$$X_{11} = 0 \quad (5.76)$$

$$(k_a N_B + k_d + k_{\text{prod}} + k_{\text{dec}})X_{12} = k_f N_B X_2 \quad (5.77)$$

$$k_{\text{dec}}X_{22} = k_{\text{prod}}X_{12} \quad (5.78)$$

The average number of  $C$  and  $P$  molecules can be calculated from Eqs. 5.74 and 5.75 and is given by:

$$\overline{N_C} = \frac{K_1}{1 + K_1}, \quad (5.79)$$

$$\overline{N_P} = \frac{K_2 K_1}{1 + K_1}, \quad (5.80)$$

where  $K_1 = k_a N_B / (k_d + k_{\text{prod}})$  and  $K_2 = k_{\text{prod}} / k_{\text{dec}}$  and  $N_B$  is the total number of  $B$  molecules.

In Fig. 5.7 we show the mean number of proteins  $\overline{N_P}$  as a function of the protein production rate  $k_{\text{prod}}$ , while keeping the decay rate fixed at  $k_{\text{decay}} = 0.04\text{s}^{-1}$ . As the concentration of RNAP that is not bound to the DNA is low, spatial correlations are expected to be negligible and  $g_{AB}(r) \approx 1$ . The simulation results for the average number of proteins,  $\overline{N_P}$ , should therefore follow the mean-field predictions in Eqs. 5.79 and 5.80. Fig. 5.7 shows that this is indeed the case. However, in contrast to the mean-field analysis, the GFRD simulations allow us to quantify the effect of the *spatial fluctuations* of the RNAP molecules on the *noise* in the protein synthesis.

We can quantify the magnitude of the noise in protein production by computing the following quantity [138]:

$$\eta_P^2 = \frac{\overline{N_P^2(t)} - \overline{N_P}^2}{\overline{N_P}^2}. \quad (5.81)$$

In the following analysis we have changed the degradation rate such that the average number of proteins,  $\overline{N_P}$ , is constant. This allows us to focus on the effect of

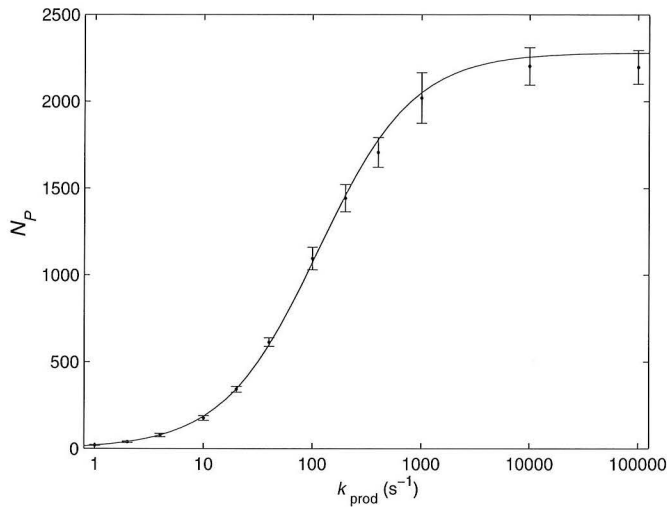


**Figure 5.7:** The mean protein number  $\overline{N}_P$  as a function of the protein production rate  $k_{\text{prod}}$  as obtained from the GFRD simulations for the reaction scheme shown in Eqs. 5.63 – 5.65. The solid line denotes the mean-field prediction given by Eq. 5.80.

spatial fluctuations on the noise in protein production—we thus eliminate the fairly trivial changes in the noise due to changes in the average number of proteins.

We can calculate the noise from the chemical master equation using Eqs. 5.76–5.78. It is given by:

$$\eta_C^2 = \frac{1}{\overline{N}_C} - 1, \quad (5.82)$$

$$\eta_P^2 = \frac{1}{\overline{N}_P} - \frac{k_{\text{dec}}}{k_a N_B + k_d + k_{\text{prod}} + k_{\text{dec}}}. \quad (5.83)$$

In the simulations, we change the decay rate to keep the average number of proteins fixed as we vary the production rate. The decay rate is then given by  $k_{\text{dec}} = (k_{\text{prod}}/\overline{N}_P)K_1/(1 + K_1)$  and the noise in  $P$  as function of  $k_{\text{prod}}$  is:

$$\eta_P^2 = \frac{1}{\overline{N}_P} - \frac{k_{\text{prod}}k_a N_B}{k_{\text{prod}}k_a N_B + \overline{N}_P(k_a N_B + k_d + k_{\text{prod}})^2}. \quad (5.84)$$

The first term on the right describes the result that would have been obtained if gene expression were a simple linear birth-and-death process. The second term reflects the fact that in order to produce a protein, it is necessary, albeit not sufficient, for

a RNAP molecule to bind to the promoter site. This term, and thus the noise in gene expression, goes through a minimum at  $k_{\text{prod}} = k_a N_B + k_d$  and vanishes for both small and large  $k_{\text{prod}}$ . In these regimes, gene expression reduces to a simple linear birth-and-death process. In the limit of small  $k_{\text{prod}}$ , the production of the protein is the rate limiting step. The RNAP molecule will associate to and dissociate from the promoter site a large number of times, before it actually induces gene expression. The former process is thus in equilibrium on the time scale of gene expression. Hence, the birth term is given by  $k_{\text{birth}} = p_{\text{bound}} k_{\text{prod}}$ , with  $p_{\text{bound}}$  being the probability that a RNAP molecule is bound to the promoter (see Eq. 5.61); the death term is given by  $k_{\text{death}} = k_{\text{decay}}$ . In the limit of large  $k_{\text{prod}}$ , the binding of a RNAP molecule to the promoter site is the rate limiting step: as soon as a RNAP molecule is bound to the promoter, a protein will be produced. This means that the birth term is given by  $k_{\text{birth}} = k_a (1 - p_{\text{bound}}) [B]$ ; the death term is again  $k_{\text{death}} = k_{\text{decay}}$ . For a linear birth-and-death process, the noise is determined by the average number of proteins,  $\eta_P = 1/\sqrt{\overline{N_P}}$  [93]. As we have set the decay rate  $k_{\text{decay}}$  such that  $\overline{N_P}$  is constant, the noise in gene expression must be the same in the limiting regimes of small and large  $k_{\text{prod}}$ , in which gene expression reduces to a birth-and-death process.

Figure 5.8 shows the noise in the protein concentration as a function of the synthesis rate for  $\overline{N_P} = 1000$ . The GFRD results are compared to those obtained using the chemical master equation. It is seen that for small  $k_{\text{prod}}$  both approaches yield identical results. In this regime, protein synthesis is the rate-limiting step. Indeed, on the time scale of gene expression the RNAP molecules have sufficient time to become well mixed in the cell. As a result, the effects of diffusion are negligible and the noise reduces to the expected value for a linear birth-and-death process.

However, for  $k_{\text{prod}} \gtrsim 1\text{s}^{-1}$ , spatial fluctuations can have a drastic effect on the noise in gene expression. In this regime, the noise of the spatially-resolved model is larger than that of the “well-stirred reactor” model. In fact, Fig. 5.8 shows that it grows fairly rapidly with increasing  $k_{\text{prod}}$ . The tracks of the number of proteins as a function of time in Fig. 5.9 elucidate the origin of the increased noise. For low production rate, these fluctuations are small and featureless. For increasing  $k_{\text{prod}}$ , however, protein production increasingly occurs in “bursts”, where a short period of rapid protein production is followed by a longer period of pure protein decay. These bursts lead to large fluctuations in the protein concentration.

The burst-like behavior is due to a very broad distribution of arrival times of RNAP molecules at the promoter, much broader than the corresponding Poisson distribution for the system without spatial fluctuations. This is illustrated in Fig. 5.10, which shows the distribution of rebind times. The rebind time is defined as the time between the last dissociation event of a RNAP molecule and the next association

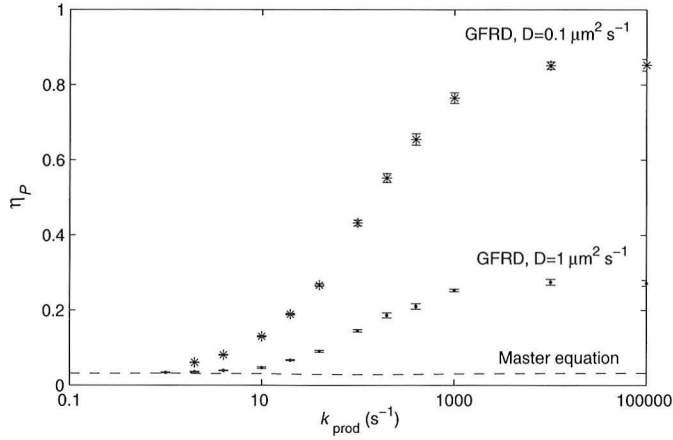


**Figure 5.8:** The noise in protein level  $\eta_P$  as a function of protein production rate  $k_{\text{prod}}$  for the reaction scheme shown in Eqs. 5.63 – 5.65. Compared are the results obtained by GFRD with a diffusion constant of  $D = 1 \mu\text{m}^2 \text{s}^{-1}$  (·) and  $D = 0.1 \mu\text{m}^2 \text{s}^{-1}$  (\*) and the result using the chemical master equation (dashed line). The mean number of proteins was held constant at  $\overline{N}_P = 1000$  by changing the degradation rate  $k_{\text{decay}}$  of the protein.

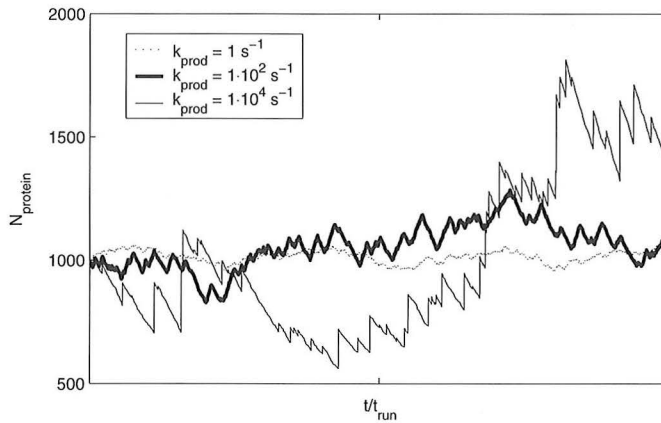


**Figure 5.9:** Tracks of protein levels in time for different protein production rates  $k_{\text{prod}}$ . Time is renormalized such that each separate track consists of the same number of production and degradation events. As  $k_{\text{prod}}$  becomes larger, the fluctuations in protein number increase. At the same time, protein production starts to occur in “bursts”, where a brief period of protein production is followed by a longer period of protein degradation. These bursts are caused by the broad distribution of DNA-rebind times of the RNA polymerase (see also Fig. 5.10).

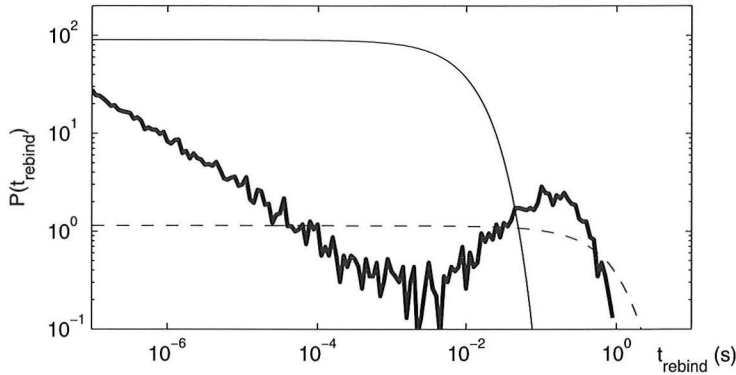


**Figure 5.10:** The distribution of rebind times for the spatially-resolved model and the well-stirred model. The rebind time is defined as the time between the last dissociation event and the subsequent binding of a RNA polymerase to the DNA. The distribution of the spatially-resolved model (thick solid line) is bimodal, with a strong narrow peak for very short times and a broad peak for larger times. Two rebind-time distributions are shown for the well-stirred model: one given by  $k_a[\text{RNAP}] \exp(-k_a[\text{RNAP}] t_{\text{rebind}})$  (thin solid line) and the other by  $k_{\text{on}}[\text{RNAP}] \exp(-k_{\text{on}}[\text{RNAP}] t_{\text{rebind}})$  (thin dashed line), where  $k_{\text{on}}$  is given by the diffusion limited reaction rate  $4\pi\sigma D$ . Note that the GFRD results are bracketed by the two distributions of the well-stirred model, consistent with the idea that in the spatially-resolved model there are many rebinding events at short times due to RNAPs that have just dissociated from the DNA and thus rebind to the DNA with the intrinsic rate constant  $k_a$ , but also rebinding events at much longer times corresponding to RNAP molecules that have to find the operator from ‘scratch’ and hence bind the DNA at a rate  $k_{\text{on}}$ , which is limited by diffusion.

event of any RNAP molecule to the DNA. Interestingly, the rebind-time distribution of the spatially-resolved model is bimodal, with a narrow peak for very short times and a broader peak for long times. This is in contrast to the rebind-time distribution of the well-stirred model, in which the rebind times are distributed exponentially. Note that we have plotted two rebind-time distributions for the well-stirred model: one assuming that the rebind rate is given by the intrinsic association rate  $k_a$  and one assuming it is given by the diffusion limited rate  $4\pi\sigma D$ , which takes into account the time it takes for the RNA polymerase to find the DNA-binding site by diffusion.

In Fig. 5.10, the first peak of the GFRD results is due to the fact that when the RNA polymerase dissociates from the DNA, it is placed at contact with the binding site on the DNA. As a consequence, the RNA polymerase can rebind to the DNA very quickly. On the other hand, there is a small chance that even when placed at contact the RNA polymerase diffuses away and ‘escapes’ from the operator site. In this case, it takes much longer time for this or, more likely, another RNA polymerase

to find the binding site on the DNA. This is reflected by the broad peak for larger rebind times. Importantly, for large  $k_{\text{prod}}$ , each of the rapid rebindings of the RNA polymerase leads to the creation of a protein, causing the observed burst in protein production. After a series of rebindings, the RNA polymerase eventually diffuses away from the binding site and protein degradation occurs, until another RNAP binds and a new series of protein synthesis reactions starts. Fig. 5.10 also shows that the rebind-time distribution of the spatially-resolved model is bracketed between the two distributions of the well-stirred model discussed above; this is consistent with the idea that in the spatially-resolved model, the rebinding events take place at both very short time scales and rather long time scales. In Section 6.5, we will address this problem analytically.

Fig. 5.8 shows that for very large production rates, the noise ultimately reaches a plateau value. At these high values of  $k_{\text{prod}}$  the promoter site becomes an “absorbing” boundary for the RNAP molecules. Fig. 5.8 also reveals that the height of the plateau increases as the diffusion constant  $D$  becomes smaller. This is not surprising, because the importance of spatial fluctuations is expected to be larger for smaller diffusion constants. However, it does clearly show that in order to determine the significance of spatial fluctuations in gene expression, it is of interest to establish the value of the diffusion constant of the RNA polymerase experimentally.

This model of gene expression is obviously highly simplified, as our aim here is to present a new particle-based technique to simulate biochemical networks. We assume that the RNAP molecules move by simple diffusion, while it has been suggested that proteins find their target sites on the DNA via a combination of free diffusion in the cytoplasm, sliding along the DNA, and hopping from one DNA segment to the next [141]. As mentioned above, we also ignore the production of mRNA as an intermediate step in protein synthesis; the production of mRNA provides an extra source of noise and, together with translation, makes the noise in the protein synthesis step non-Poissonian [140]. More important for the phenomena described here, we ignore the fact that it takes time (20-40s) to make the transcript—we thus neglect the time delay between the binding of a RNAP molecule to the DNA and its release from the DNA; secondly, we do not take into account that, after transcription, the RNAP dissociates from the DNA at a certain distance away from its original binding site. The probability of rebinding within a short time decreases rapidly with increasing distance from the binding site. However, we find in Chapter 6 that such spatial fluctuations are significant in the case of transcription factors. Nevertheless, the results presented here show that spatial fluctuations could be a major source of noise in gene expression. Lastly, we point out that the increased noise due to the serial rebinding of signaling molecules to ‘detection’ molecules is expected to play a role not only in gene regulatory networks, but also in signal transduction networks



such as those in bacterial chemotaxis [142] and in the immune response [143].

### 5.3.3 Performance

The essence of the GFRD scheme is to exploit the analytical solution of the time when the particles are far apart from each other. This allows GFRD to make large jumps in time when the particles are far apart from each other. This suggests that the efficiency of GFRD depends upon the density of the system. Here, we briefly discuss the computational efficiency of GFRD.

The GFRD algorithm can be divided in two parts. In the first part, the maximum time step is determined and the particles are divided into single particles and pairs of particles. This step is relatively fast and scales with the number of particles  $N$  as  $N^2$ . This dependence on  $N$  can be reduced by the use of a neighbor list or a cell list [144]; provided that updating the list is not rate limiting, a neighbor list or cell list allows the overall CPU time of the first step of the algorithm to scale linearly with  $N$ .

In the second part of the algorithm, the particles are propagated according to the Green's functions. Since only single particles or pairs of particles are propagated, the CPU time for this step scales linearly with the number of particles. However, this step is rather slow due to the relatively complicated procedure for propagating the pairs of particles: the CPU time to propagate a pair of particles through one time step is about a factor ten higher in GFRD than in brute-force Brownian dynamics; indeed, propagating the pairs of particles is the rate limiting step in the GFRD algorithm. Importantly, the cost of propagating a pair of particles does not depend upon the size of the time step. This means that GFRD becomes more efficient as the average maximum time step increases. The size of the maximum time step is determined by the average distance to the second-nearest neighbor. This distance scales with the density of the system, not with the total number of particles that constitute the system. In contrast, for brute-force Brownian dynamics, the size of the timestep is determined rather by the diameter of the particles, as overlap between two particles has to be accurately resolved. Thus, a good test for the performance of GFRD is the dependence of the distribution of propagation times on the density of the system.

In Figure 5.11 we show the distribution of propagation times  $\Delta t$  for the bimolecular reaction described in Section 5.3.1 as a function of density. For  $N_B = 18$  ( $[B] = 30$  nM), the value used in the above model of gene expression, the distribution has a maximum at  $\Delta t = 1 \cdot 10^{-4}$ s. As expected, the propagation times become smaller if the density increases. For  $[B] = 1\mu\text{M}$ , the peak in the distribution shifts to  $\Delta t = 1 \cdot 10^{-6}$ s.

In biochemical networks, the concentrations of the components can be very low.

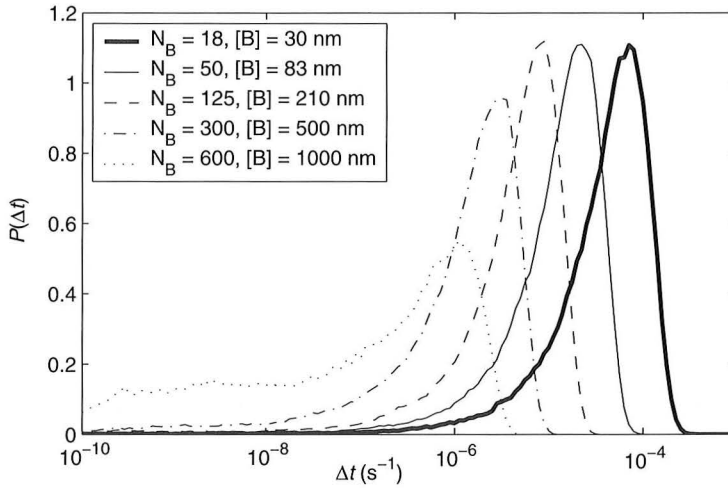


**Figure 5.11:** The distribution of propagation times  $\Delta t$  for a system consisting of a single particle  $A$  in the center of a spherical box of volume  $V = 1\mu\text{m}^3$ , surrounded by  $N_B$  particles  $B$ ; the particles  $A$  and  $B$  can react according to a bimolecular reaction scheme (see Eq. 5.59). In the GFRD simulations, we use a lower cut-off for the propagation time,  $2.5 \cdot 10^{-10}\text{s}$ , which corresponds to the time step used in a brute-force Brownian Dynamics simulation.

In gene networks, for example, the concentrations of the gene regulatory proteins are often in the nanomolar regime. In signal transduction networks, the concentrations of the components may also be fairly low, i.e. in the micromolar range. The analysis presented here suggests that with GFRD it should be possible to reach time steps of at least  $10^{-6} - 10^{-4}\text{s}$  for such networks. In contrast, in a brute-force Brownian Dynamics simulation, we cannot use a time step larger than  $10^{-10} - 10^{-9}\text{s}$  ( $10^{-5} - 10^{-4}\sigma^2/D$ ) in order to preserve the correct distribution (as, for instance, defined by the requirement that the analytical solution for the Green's function  $p_{\text{rev}}(\mathbf{r}, t|\mathbf{r}_0, t_0)$  as shown in Fig. 5.5 can be accurately reproduced). Hence, even though the CPU time required to execute one step is a factor ten larger in GFRD than in Brownian Dynamics, the overall speed of GFRD is two to five orders of magnitude higher than that of conventional particle-based schemes for simulating biochemical networks in time and space.

## 5.4 Discussion and conclusions

The GFRD algorithm is not the first algorithm that uses Green's functions to simulate chemical reactions. However, GFRD differs in two fundamental ways from the algorithms in Refs. [145–147]. The latter algorithms were designed to simulate only a single reversible reaction [145–147]. In contrast, the main idea of GFRD is that by choosing a maximum time step, it is possible to decompose a network of events into elementary events that occur *independently* from each other and for which Green's functions can be derived (see Fig. 5.1). This decomposition is the key ingredient of GFRD that makes it possible to simulate a whole network of chemical reactions, and not just a single chemical reaction. Secondly, GFRD is event-driven, while the schemes of Refs. [145–147] are not. This has two important advantages. First of all, even when the reaction partners are far apart from each other, GFRD can immediately jump to the next reaction event; this cannot be accomplished by methods that use a fixed time step and reaction zone for executing the reactions [145–147]—in these methods, the reaction partners first have to be propagated toward each other using increasingly smaller time steps, before they can react within the reaction zone [145–147]. Secondly, and more importantly, the event-driven nature allows GFRD the simulation of arbitrary complex networks: reactions with multiple products and branching pathways—where a component can undergo a number of competing reactions (see for instance Eqs. 5.63 and 5.64)—can be handled, because only single and binary Green's functions are needed to propagate the system till the next event. In contrast, schemes that use a fixed time step for the reactions [145–147] would require intractable *many-body* Green's functions, involving both reactants *and* products, to simulate these networks.

In the GFRD algorithm discussed here, we restrict ourselves to  $U(r) = 0$  for  $|r| > \sigma$ . If, however,  $U(r) \neq 0$  for  $|r| > \sigma$ , then the range of the interaction plays an important role in determining the maximum time step. Instead of requiring that no more than two particles might collide and react in a single time step, one must now require that no more than two particles might come within each other's range of interaction during one time step. This means that the *range* of  $U(r)$  takes the place of the diameter  $\sigma$  in determining the maximum time step in the algorithm outlined in 5.2.3. Nevertheless, it can happen that this requirement cannot be satisfied and that a configuration arises in which more than two particles are within the range of the interaction potential. In this case, it is (practically) impossible to factorize the Green's function and brute-force Brownian Dynamics should be used to propagate these particles. We note, however, that the range of the interaction potential is usually quite short as compared to the diameter of the particles. Even potentially long-ranged electrostatic interactions, for instance, are typically screened in the liv-

ing cell. Indeed, the range of protein-protein interactions and protein-DNA interactions is typically less than 20% of the diameter of the particles (see Ref. [148] and references therein). This means that in most cases GFRD can be applied straightforwardly.

We also comment here on our approximation that molecules are spherically symmetric objects. In nature, proteins often have complicated non-spherical shapes. Moreover, protein-protein interactions can occur through specific patches on the surfaces of the proteins. In these cases, the reaction rates do not only depend upon the distance (as in our present algorithm), but also on the relative orientation of the particles. In principle, this orientation dependence could be incorporated into GFRD by solving a diffusion equation that also includes the orientation of the particles. It should be noted, however, that due to rotational diffusion the relative orientation between particles does not persist on the time scale to diffuse towards a distant reaction partner. This means that the relative orientation of the particles can be integrated out and that the problem can be reduced to that described by the current GFRD algorithm. In this case, the particle diameters correspond to the average interaction diameters and the rate constants correspond to effective reaction rates, i.e. rates averaged over the different reaction rates corresponding to the different relative orientations of the particles. In this context we also point out that the experimentally measured quantities are usually the average reaction rates. However, when experimental data becomes available that shows that the orientations of the particles are important, then it is indeed of interest to upgrade the current GFRD algorithm by including the particle orientations.

Finally, we remark that the assumption that particles move by (free) diffusion is not essential. An event-driven algorithm of this type could also be set up for particles that move by other mechanisms than diffusion, such as active transport. In the simplest case, active transport could be modeled as diffusion with a drift term. If necessary, the required Green's functions could be obtained numerically.

In conclusion, we have developed a new technique, called Green's-function reaction dynamics, to simulate biochemical networks at the particle level and in both time and space. The main idea of the technique is to choose a maximum time step such that only single particles or pairs of particles have to be considered. For these particles, the Smoluchowski equation can be solved analytically using Green's functions. The analytical solution can then be used to set up an event-driven algorithm, quite analogous to the kinetic Monte Carlo schemes as originally developed by Bortz, Kalos and Lebowitz [94] to simulate Ising spin systems and by Gillespie to numerically solve the chemical master equation [122]. We would like to stress, however, that in contrast to the widely used "Gillespie" algorithm, our technique makes it possible to simulate biochemical networks at the particle level and in both time and

*space.*

The analysis presented in Section 5.3.3 shows that GFRD is highly efficient. This should make it possible to simulate biochemical networks at much larger length and time scales than hitherto possible. In addition, we believe that the scheme has the potential to be even more efficient. In the current scheme, we use a global maximum time step that pertains to all the particles in the system. It seems natural, however, to assign to each particle an individual maximum time step. In such a scheme, each particle would have its own individual clock. This approach would make it possible to devote most computational effort to those particles that interact frequently; the particles that are initially far from other particles are only updated once the time has come when they have a reasonable chance to interact. A second possible improvement would be to exploit the low concentration of the components in another way. In the current scheme, we explicitly take into account excluded volume interactions. In fact, this often imposes a limit on the maximum time step. If the concentrations are low, however, we would expect the excluded volume effects to be negligible for the behavior of the network. In Chapter 6, we will show how these observations can be incorporated into the algorithm to even further enhance the performance of Green's Function Reaction Dynamics.



---

## **Chapter 6**

# **Spatial fluctuations of transcription factors**

J.S. van Zon, M. Morelli and P.R. ten Wolde,  
*to be submitted*

## 6.1 Introduction

As was discussed in more detail in Chapter 4, cells process information from the outside and regulate their internal state by means of proteins and DNA. Because these molecules often occur in small numbers in living cells, stochastic fluctuations in the components must often be taken into account when describing these systems. These fluctuations are especially significant in gene expression, where transcription factors can often occur in copy numbers as low as tens of molecules per cell and it is an important question how the cell can still perform reliably in the presence of such fluctuations [75, 88, 90–92].

Noise in gene expression results not only from a noisy environment but is also due to the inherently stochastic dynamics of the molecules involved in gene expression [90]. The stochastic dynamics that leads to this intrinsic noise has two origins. First, the reactions between molecules are of a probabilistic nature. Second, molecules move through the cell by diffusion or, in the case of eukaryotic cells, by either diffusion or active transport. Diffusion is a stochastic process and could potentially contribute to the noise in gene expression. Because it is difficult to experimentally probe the spatial dynamics of single molecules in the cell, it is currently unknown to what extent noise in gene expression is affected by spatial fluctuations of the components.

Fluctuations in gene expression are often studied analytically or by computer simulation, using the zero-dimensional chemical master equation [93, 122]. This approach takes into account the stochastic reaction kinetics of the molecules involved, but ignores their diffusive motion. It assumes that the cell is a ‘well-stirred reactor’, where the reaction rates only depend on the global concentrations of the reactants involved and does not take into account the spatial positions of the particles in the cell. In Chapter 5, several simulation techniques have been discussed that model the effect of diffusion, but it was shown that they are either too slow to accurately model the dynamics on the long timescales relevant to gene expression or describe the system in a coarse-grained way, i.e. on the level of local concentrations rather than single particles [124–127].

In Chapter 5 we introduced a simulation technique, called Green’s-function reaction dynamics (GFRD), that allows us to simulate reaction-diffusion systems on long timescales and for individual particles. In this chapter, we use this technique to study the effect of the spatial fluctuations due to diffusion on a simple system



in gene expression: a single gene under the control of a repressor  $R$ . We find that for this system the intrinsic noise is dominated by the diffusive motion of the repressor molecules. We also show how a cell could minimize the effect of the spatial fluctuations, either by tuning the open complex formation rate or by changing the number of repressors and their affinity for the binding site on the DNA. Finally, we show that even though spatial fluctuations can dramatically enhance the noise in gene expression, its effect can be described by a zero-dimensional chemical master equation, provided that the reaction rates for repressor binding and unbinding are appropriately renormalized.

## 6.2 Model and simulation

Several publications have discussed the effect of fluctuations in the binding of transcription factors to the operator site [118, 149–153]. Most of these models are relatively simple, ignoring, for instance, production of mRNA [150–152]. Moreover all these studies, with the exception of Ref. [118], ignore the role of the spatial fluctuations of the transcription factors. Here, we study transcription in a more detailed way, taking into account production of both mRNA and proteins, open complex formation and operator clearance. Furthermore, we explicitly model the diffusive motion of the repressor molecules.

Most repressors bind to a binding site that (partially) overlaps the RNA polymerase (RNAP) binding site, preventing RNAP from binding to the promoter region and thereby switching off gene expression. In the absence of a repressor on the operator site, RNAP can initiate transcription and translation, ultimately resulting in the production of a protein. We model this by the following reaction network:



Equations 6.1 and 6.2 describe the competition between the binding of the repressor  $R$  and the RNAP molecules  $Rp$  to the operator site  $O$ . In our simulation we fix the binding site  $O$  in the center of a container with volume  $V = 1\mu\text{m}^3$ , comparable to the volume of a single *Escherichia coli* cell. The operator site  $O$  is surrounded by  $N_R$

repressor molecules  $R$ , that diffuse with diffusion constant  $D = 1\mu\text{m}^2\text{s}^{-1}$ , as has been reported for proteins of a similar size [110]. We simulate both the operator site and the repressor molecules as spherical particles with diameter  $\sigma = 10\text{nm}$ . The intrinsic forward rate  $k_{\text{fR}} = 6 \cdot 10^9\text{M}^{-1}\text{s}^{-1}$  for the repressor particles  $R$  at contact is estimated from the Maxwell-Boltzmann distribution, as was done in Chapter 5. The backward rate  $k_{\text{bR}}$  depends on the interaction between the DNA binding site of the repressor and the operator site on the DNA and varies greatly between different operons, with stronger repressors having a lower  $k_{\text{bR}}$ . In our simulations, we vary  $k_{\text{bR}}$  between  $1 - 0.01\text{ s}^{-1}$ . The concentration of RNAP is much higher than that of the repressor. Because of this we treat the RNAP as distributed homogeneously within the cell and we do not take diffusion of RNAP into account explicitly. Instead, RNAP associates with the operator site  $O$  with a diffusion-limited rate  $k_{\text{fRp}} = 4\pi\sigma D[\text{Rp}]$ . In our simulations, the concentration of free RNAP is  $[\text{Rp}] = 0.5\mu\text{M}$  [154], leading to a forward rate  $k_{\text{fRp}} = 38\text{s}^{-1}$ . Finally, the backward rate  $k_{\text{bRp}} = 0.5$  is determined such that  $K_{\text{eq}} = 4\pi\sigma D/k_{\text{bRp}} = 1.4 \cdot 10^9\text{M}^{-1}$  [155].

Transcription initiation is described by Eqs. 6.3 and 6.4. Before productive synthesis of RNA occurs, first the RNAP in the RNAP-promoter complex  $ORp$  unwinds approximately one turn of the promoter DNA to form the open complex  $ORp^*$ . The open complex formation rate  $k_{\text{OC}}$  has been measured to be on the order of  $0.3 - 3\text{s}^{-1}$  [156]. As some experiments find open complex formation to be only weakly reversible [156], we approximate this step as an irreversible reaction. After open complex formation, RNAP must first escape the promoter region before another RNAP or repressor can bind. Since elongation occurs at a rate of  $50 - 100$  nucleotides  $\text{s}^{-1}$  and between  $30 - 60$  nucleotides must be cleared by RNAP before the promoter is accessible, a waiting time of  $t_{\text{clear}} = 1\text{s}$  is required before another binding can occur. Since promoter clearance consists of many individual elongation events that obey Poisson statistics individually, we model the step as a fixed time delay  $t_{\text{clear}}$ , not as a Poisson process with rate  $1/t_{\text{clear}}$ .

Equations 6.5-6.9 describe the dynamics of mRNA and protein numbers. After clearing the promoter region, RNAP starts elongation of the transcript  $T$ . As for clearance, the elongation step is modeled with a fixed time delay  $t_{\text{elon}} = 30\text{s}$ , corresponding to a  $1500\text{ Bp}$  gene. When a mRNA  $M$  is formed, it can degrade with a rate  $k_{\text{dm}}$ . Here, the mRNA degradation rate is determined by the average mRNA concentration in the unrepresed state and is of the order  $0.01\text{s}^{-1}$ . Furthermore, a mRNA molecule can form a mRNA-ribosome complex  $MT$  and start translation. We assume that  $b = 5$  proteins are produced on average from a single mRNA molecule, so that the start of translation occurs at a rate  $k_{\text{ribo}} = b k_{\text{dm}}$ . Again, after a fixed time delay  $t_{\text{trans}} = 30\text{s}$  a protein  $P$  is produced. The mRNA is available for ribosome binding immediately after the start of translation. Due to the delay in protein production,

$M$  can be degraded while the mRNA-ribosome complex  $MT$  is still present, so that  $M$  represents the mRNA leader region rather than the entire mRNA molecule. Finally, the protein  $P$  degrades at a rate  $k_{dp}$ , which depends on the average protein concentration and is of order  $1 \cdot 10^{-4} s^{-1}$ . Most proteins are long-lived and the concentration of proteins mainly decreases by dilution due to cell division. The decay rate used here corresponds to dilution with a cell cycle time of around 1h.

We simulate the above reaction network using Green's-function reaction dynamics (GFRD). Only the operator site  $O$  and the repressor particles  $R$  are simulated in space. All other reactions are assumed to occur homogeneously within the cell and are simulated according to the well-stirred model [95] or with fixed time delays for reaction steps involving elongation. A few modifications with respect to the algorithm described in Chapter 5 are implemented to improve simulation speed. First, we neglect excluded volume interactions between repressor particles mutually, as the concentration of repressor is very low. This means that the only potential reaction pairs we consider are operator-repressor pairs. Secondly, we use periodic boundary conditions instead of a reflecting boundary, which leads to a larger average time step. As the operator site  $O$  is both small compared to the volume of the cell and is far removed from the cell boundary, this has no effect on the dynamics of the system. Finally, as the repressor backward rate  $k_{bR}$  is rather small, the operator site can be occupied by a repressor for a time long compared to the average simulation time step. If the repressor is bound to the operator site longer than a time  $L^2/6D$ , where  $L$  is the length of the sides of our container, the other repressor molecules diffuse on average from one side of the box to the other. Consequently, when the repressor eventually dissociates from the operator site, the other repressor molecules have lost all memory of their positions at the time of repressor binding. Here, when a repressor will dissociate after a time longer than  $L^2/6D$  we do not propagate the other repressors with GFRD, but we only update the master equation and fixed delay reactions. We update the positions of the free repressors at the moment that the operator site becomes accessible again, by assigning each free repressor molecule a random position in the container; the dissociated repressor is put at contact with the operator site. We see no noticeable difference between this scheme and results obtained by the full GFRD algorithm described in Chapter 5.

For the reaction network in Eqs. 6.1-6.9, the steady state concentrations are given by:

$$K_1[O] = [ORp], \quad (6.10)$$

$$K_2[O][R] = [OR], \quad (6.11)$$

$$K_3[ORp] = [ORp^*], \quad (6.12)$$

$$K_4[M] = [ORp], \quad (6.13)$$

$$K_5[P] = [M], \quad (6.14)$$

where  $K_1 = k_{\text{frp}}/(k_{bRp} + k_{\text{OC}})$ ,  $K_2 = k_{\text{fr}}/k_{bR}$ ,  $K_3 = k_{\text{OC}}t_{\text{clear}}$ ,  $K_4 = k_{\text{OC}}/k_{\text{dm}}$  and  $K_5 = k_{\text{ribo}}/k_{\text{dp}}$  are equilibrium constants. Because we consider here a single operator site surrounded by  $N_R$  repressors, we have the conservation relations:

$$[O] + [ORp] + [ORp^*] + [OR] = 1/V, \quad (6.15)$$

$$[R] + [OR] = N_R/V, \quad (6.16)$$

where  $V$  is the total volume available for the repressors. Using Eqs. 6.10 – 6.12 together with Eqs. 6.15 and 6.16, we find for  $N_{ORp} = V[ORp]$ , the average occupancy of the operator site by RNAP, and  $N_{OR} = V[OR]$ , the average occupancy of the operator site by the repressor, that:

$$K_1[1 - (1 + K_3)N_{ORp} - N_{OR}] - N_{ORp} = 0 \quad (6.17)$$

$$\frac{K_2}{V}[1 - (1 + K_3)N_{ORp} - N_{OR}]N_R - N_{OR} = 0, \quad (6.18)$$

Solving Eqs. 6.17 and 6.18 and using Eqs. 6.13 and 6.14, we find that the average mRNA number  $N_M$  and average protein number  $N_P$  is given by:

$$N_M = \frac{K_4 K_1 V}{K_2 N_R + V(1 + K_1(1 + K_3))}, \quad (6.19)$$

$$N_P = K_5 N_M. \quad (6.20)$$

We vary the free parameters in the reaction network described in Eqs. 6.1-6.9 in the following way: first, we choose the concentration of mRNA and protein in the absence of repressor molecules. In this case, tuning of the concentrations is most straightforward by adjustment of the mRNA and protein decay rates  $k_{\text{dm}}$  and  $k_{\text{dp}}$ . In our simulation we fix the mRNA and protein numbers in the unrepresed state at  $N_M = 50$  and  $N_P = 2 \cdot 10^5$ . The mRNA and protein decay rates then follow straightforwardly from Eqs. 6.19 and 6.20.

Next, we determine by what factor these concentrations should decrease in the repressed state. This can be done by changing the number of repressors  $N_R$  and the repressor backward rate  $k_{bR}$ . We define the repression level  $f$  as the transcription initiation rate in the absence of repressors divided by the initiation rate in the repressed state [157]. According to this definition, the concentration of mRNA and proteins in the repressed state is a fraction  $f$  of the concentration in the unrepressed state. This means that:

$$K_2 N_R + V(1 + K_1(1 + K_3)) = \frac{V(1 + K_1(1 + K_3))}{f}, \quad (6.21)$$

leading to:

$$\frac{N_R}{k_{bR}} = \frac{1 - f}{f} \frac{V(1 + K_1(1 + K_3))}{k_{fR}}. \quad (6.22)$$

Thus, a fixed repression level  $f$  does not specify a unique combination of  $N_R$  and  $k_{bR}$ : increasing the number of repressors twofold, while also increasing the repressor backward rate by the same factor, gives the same repression level. This means that the cell can control mRNA and protein levels in the repressed state either by having a large number of repressors that stay on the DNA for a short time or by having a small number of repressors, possibly even one, that stay on the DNA for a long time. Even though it is conceivable that the latter is preferable for economic reasons, there is no difference between the two extremes in terms of the average gene expression. In our simulation we vary  $N_R$  and  $k_{bR}$ , but use a fixed repression level  $f = 0.01$ . Consequently, in the repressed state on average  $N_{\text{mRNA}} = 0.5$  and  $N_P = 200$ .

### 6.3 Simulation results: dynamics and noise

To study the effect of spatial fluctuations on the repression of genes, we simulate the reaction network described in Eqs. 6.1-6.9 both by GFRD, thus explicitly taking into account the diffusive motion of the repressor particles, and according to the well-stirred model, where the repressor particles are assumed to be homogeneously distributed in space and the dynamics depends only on the concentration of repressor. In Fig. 6.1 we show the behavior of mRNA and protein numbers for a system with open complex formation rate  $k_{OC} = 30s^{-1}$  and with varying numbers of repressors  $N_R$ . We keep the repression factor fixed at  $f = 0.01$  so that with increasing  $N_R$  the repressor backward rate  $k_{bR}$  is also increased, i. e. repressor particles are bound to the DNA for a shorter time.

It is clear from Fig. 6.1 that there is a dramatic difference between the behavior of mRNA and protein numbers between the GFRD simulation and the well-stirred

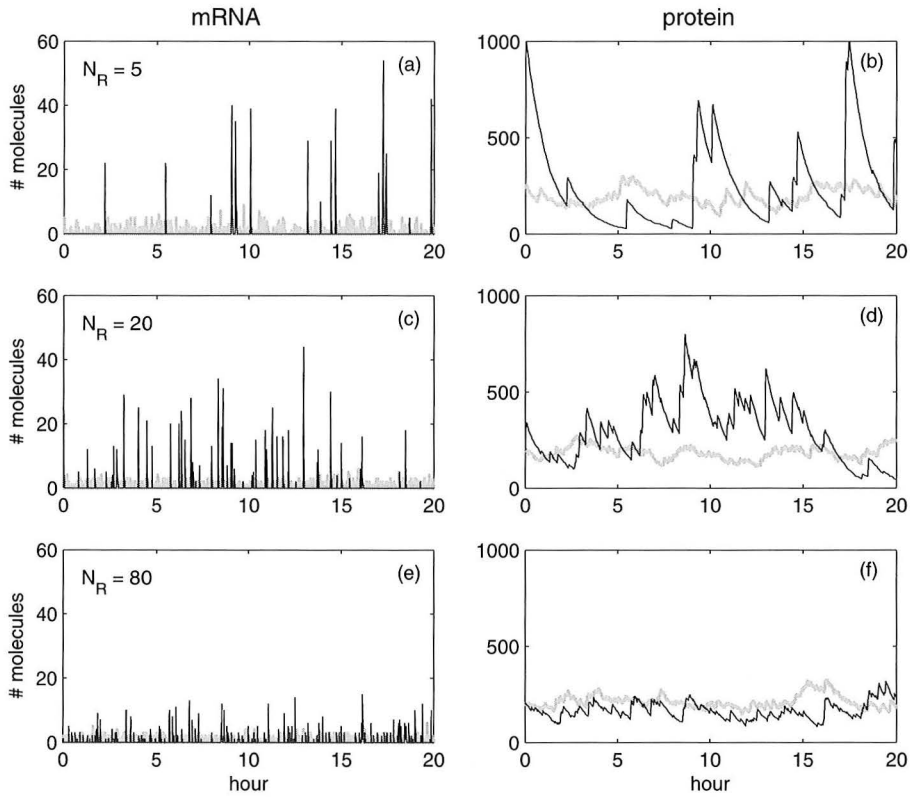


**Figure 6.1:** Dynamics of mRNA and protein numbers in the repressed state for different number of repressors  $N_R$ . The number of mRNA and protein molecules is shown for simulations with GFRD (black line) and according to the master equation (gray line). In the GFRD simulation, diffusion of repressor particles is explicitly included. (a) and (b)  $N_R = 5$ . (c) and (d)  $N_R = 20$ . (e) and (f)  $N_R = 80$ . In general, there is a dramatic difference in dynamics due to the spatial fluctuations of the repressor molecules. This difference becomes more pronounced as the number of repressors decreases. However, we find that in all cases  $\langle N_M \rangle = 0.5$  and  $\langle N_P \rangle = 200$ , on average.

model. When spatial fluctuations of the repressor molecules are included, mRNA is no longer produced in a continuous fashion, but instead in sharp, discontinuous bursts during which the mRNA level can reach levels comparing to those of the unrepressed state. These bursts in mRNA production consequently lead to peaks in protein number. As the protein decay rate is much lower than that of mRNA, these peaks are followed by periods of exponential decay over the course of hours. Due to these fluctuations, protein numbers often reach levels of around 5 – 10% of the protein levels in the unrepressed state. In contrast, in the absence of repressor diffusion, the fluctuations around the average protein number are much lower. For both cases, however, the average behavior is identical: even though the dynamics is very different, we always find that on average  $\langle N_{\text{mRNA}} \rangle = 0.5$  and  $\langle N_P \rangle = 200$ . Also, in all cases the fluctuations in mRNA number are larger than those in protein number. This means that the translation step functions as a low-pass filter to the repressor signal.

When we increase the number of repressors  $N_R$  and change  $k_{\text{bR}}$  in such a way that the repression level  $f$  remains constant, we find that both for GFRD and the well-stirred model the fluctuations in mRNA and protein number decrease. In the absence of spatial fluctuations this effect is minor, but for GFRD this decrease is sharp: for large number of repressors, the burst in mRNA become both weaker and more frequent. This in turn leads to smaller peaks and shorter periods of exponential decay in protein numbers. In fact, as  $N_R$  is increased both approaches converge to the same behavior. At around  $N_R \approx 100$ , the dynamics of the protein number is similar for the well-stirred model and the spatially resolved model. The same happens for mRNA number when  $N_R \approx 500$ .

In Fig. 6.2, we quantify the noise in mRNA and protein number, defined as in Eq. 5.84, while we change the number of repressors  $N_R$ . As we keep the amount of repression fixed at  $f = 0.01$ , we simultaneously vary the backward rate  $k_{\text{bR}}$  according to Eq. 6.22. When all parameters are the same, the noise for the GFRD simulation, including the diffusive motion of the repressors, is always larger than the noise for the well-stirred model, where the diffusive motion is ignored. In both cases, the noise decreases when the number of repressors is increased and the repressor backward rate becomes larger. This is consistent with the mRNA and protein tracks shown in Fig. 6.1. We also investigated the effect of changing the open complex formation rate  $k_{\text{OC}}$ . In nature, this rate can be tuned by changing the base pair composition of the promoter region on the DNA. When we change  $k_{\text{OC}}$ , we change the mRNA decay rate  $k_{\text{dm}}$  so that the average mRNA and protein concentration remain unchanged. We find that when  $k_{\text{OC}}$  is lowered, the fluctuations in mRNA and protein levels are sharply reduced. When  $k_{\text{OC}}$  is much larger than the RNAP backward rate  $k_{\text{bRp}} = 0.5\text{s}^{-1}$ , almost every RNAP binding to the promoter DNA will

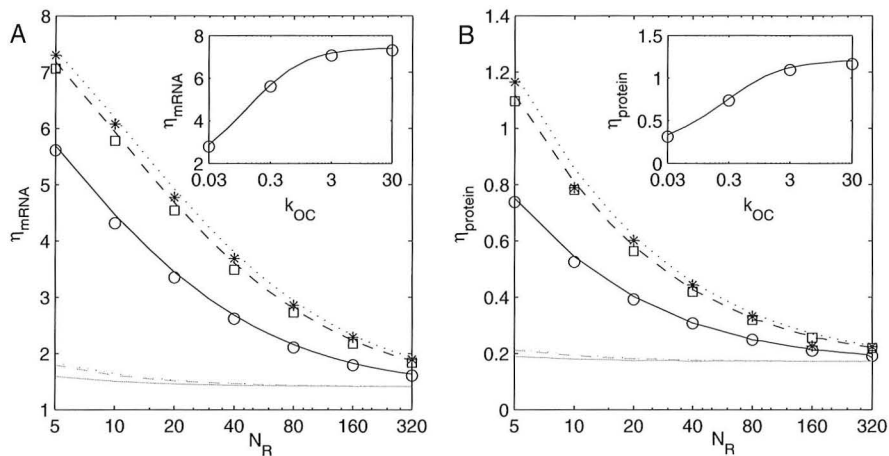


**Figure 6.2:** Noise in (a) mRNA number and (b) protein number as a function of the number of repressors  $N_R$  and for constant repression factor  $f = 0.01$ . Data obtained by GFRD simulation is shown for  $k_{\text{OC}} = 0.3(\circ)$ ,  $3(\square)$  and  $30(*)\text{s}^{-1}$ . Noise levels for the well-stirred model are shown as grey lines and those for the well-stirred model with reaction rates renormalized according to Eqs. 6.35 and 6.36 are shown as black lines, both for  $k_{\text{OC}} = 0.3$  (solid lines),  $3$  (dashed lines) and  $30$  (dotted lines)  $\text{s}^{-1}$ . Only when the reaction rates are properly renormalized does the noise agree well with the simulations that include the effect of diffusion. (Insets) Noise levels as a function of  $k_{\text{OC}}$ . Symbols indicate results for GFRD and lines are results for the chemical master equation with renormalized reaction rates.

result in transcription of a mRNA. For  $k_{\text{OC}}$  smaller than  $k_{\text{bRp}}$ , RNAP binding will lead to transcription only infrequently. As a consequence, the operator filters out part of the fluctuations in RNAP binding due to the diffusive motion of the repressor particles, leading to the decrease in noise observed in Fig. 6.2. This shows that the open complex formation rate plays a considerable role in controlling noise in gene expression.

## 6.4 Simulations results: operator binding

To understand how the diffusive motion of repressor molecules leads to increased fluctuations in mRNA and protein numbers, it is useful to look in some detail at the dynamics of repressor-DNA binding. In Fig. 6.3(a), we show the *OR* bias for both GFRD and the well-stirred model. The *OR* bias is a moving time average over  $OR(t)$  with a  $50\text{s}$  time window and should be interpreted as the fraction of time the



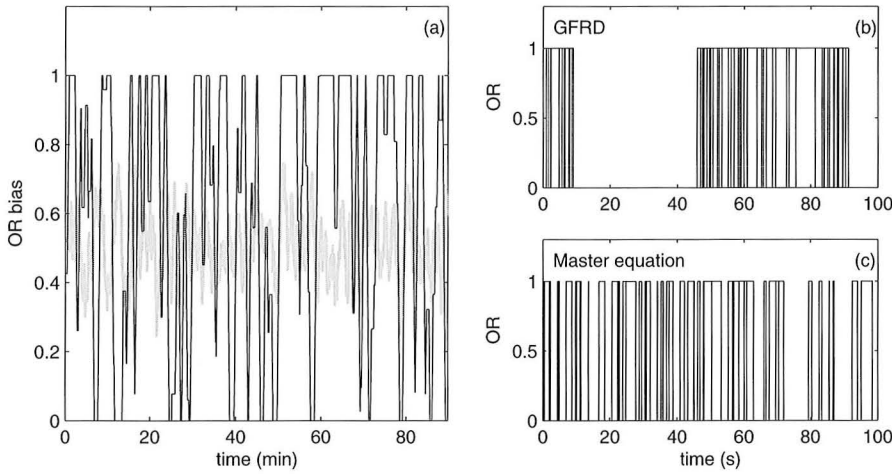


**Figure 6.3:** Dynamics of repressor binding for a repression factor of  $f = 0.5$  and  $N_R = 5$ . (a) The  $OR$ -bias for GFRD (black line) and the well-stirred model (gray line). The  $OR$ -bias is defined as the fraction of time a repressor is bound to the operator site in the last 50 seconds. When the diffusive motion of repressor molecules is included (black line), the  $OR$ -bias switches between periods where repressors are continuously bound to or absent from the DNA for long times. (b) and (c) Time trace of the occupancy of the operator site by repressor molecules. When  $OR = 1$  a repressor is bound to the operator site and  $OR = 0$  indicates either a free operator site or one with RNAP bound. For the GFRD simulations, an initial binding is followed by several rapid rebindings, whereas for the well-stirred model binding and rebinding is much more unstructured. Note that here, for reasons of clarity,  $f = 0.5$  instead of  $f = 0.01$  as used in the text and Figs. 6.1 and 6.2.

operator site was bound by repressor particles over the last 50 seconds. The results we show here are for  $N_R = 5$  repressors and a repression factor  $f = 0.5$ . At this repression factor,  $k_{bR}$  is such that the repressor molecules are bound to the operator only fifty percent of the time, making it easier to visualize the operator dynamics than in the case of  $f = 0.01$  as used above.

The  $OR$  bias for the well-stirred model fluctuates around the average value  $\langle OR \rangle = 0.5$ , indicating that on the timescale of 50s several binding and unbinding events occur, in agreement with  $k_{bR} = 1.26s^{-1}$  for  $f = 0.5$ . On the other hand, when including spatial fluctuations, the  $OR$  bias switches between periods in which repressors are bound to the DNA continuously and periods in which the repressors are virtually absent, both on timescales much longer than the 50s time window. How is it possible that repressors are bound to the operator site for times much longer than the timescale set by the dissociation rate from the DNA? The answer to that

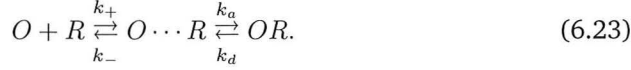
question can be found in Figs. 6.3(b) and (c), where a time trace is shown of the operator occupancy by the repressor for both GFRD and the well-stirred model. The time trace for the simulation of the well-stirred model in Fig. 6.3(c) shows a familiar picture: binding and dissociation of the repressor from the operator occurs irregularly, the time between events given by Poisson distributions. The time trace for GFRD in Fig. 6.3(b) looks rather different. Here, in general a dissociation event is followed by a rebinding very rapidly. Only occasionally does a dissociation result in the operator being unbound by repressors for a longer time. When this happens, repressors stay away from the operator for a time much longer than the typical time separating binding events in Fig. 6.3(c). These series of rapid rebindings followed by periods of prolonged absence from the operator result in the aberrant *OR* bias shown in Fig. 6.3(a).

The occurrence of rapid rebindings is intimately related to the nature of diffusion. When diffusion and the positions of the reactants are ignored all dynamics is based only on the average concentration of the reactants. As a consequence, when in this approach a repressor dissociates from the operator site, the probability of rebinding depends only on the concentration of repressor in the cell. On the level of actual positions of the reactants, this amounts to placing the repressor at a random position in the container. The situation is very different for the GFRD approach, where the positions of the reactants are taken into account. After a dissociation from the operator site, the repressor particle is placed at contact with the operator site. Because of the close proximity of the repressor to its binding site, it has a high probability of rapidly rebinding to and only a small probability of diffusing away from the binding site. At the same time, when the repressor eventually diffuses away from the operator site, the probability that the same, or more likely, another repressor diffuses to and binds the operator site is much smaller than the probability of binding in the well-stirred model, as will be shown quantitatively in Section 6.5. This results in the behavior observed in Fig. 6.3(b).

It can now be understood that the bursts in mRNA production correspond to the prolonged absence of repressor from the operator site compared to the well-stirred model. Especially for low repressor concentrations, these periods of absence can be long enough that the concentration of mRNA reaches values comparable to those in the unrepresed state for brief periods of time. When a repressor binds to the operator site, due to the rapid rebindings it will remain bound effectively for a time much longer than the mRNA lifetime, leading to long periods where mRNA is absent in the cell. This shows that for small numbers of repressors spatial fluctuations and not stochastic chemical kinetics are the dominant contribution to the noise in mRNA and protein numbers in the repressed state.

## 6.5 Two-step kinetic scheme

In this section we investigate to what extent the effect of diffusion on the repressor dynamics can be modeled by the two-step kinetic scheme [158, 159]:



The first step in Eq. 6.23 describes the diffusion of repressor to the operator site resulting in the encounter complex  $O \cdots R$ , with the rates  $k_+$  and  $k_-$  depending on the diffusion coefficient  $D$  and the size of the particles. The next step describes the subsequent binding of repressor to the DNA. The rates  $k_+$ ,  $k_-$ ,  $k_a$  and  $k_d$  are related to the microscopic rates defined in Eq. 6.1, which can be seen as follows. If we assume that the encounter complex is in steady state, we have:

$$[O \cdots R] = \frac{k_+}{k_- + k_a} [O][R] + \frac{k_d}{k_- + k_a} [OR]. \quad (6.24)$$

For the time evolution of  $[OR]$  we can now write:

$$\begin{aligned} [\dot{OR}] &= k_a [O \cdots R] - k_d [OR] \\ &= \frac{k_+ k_a}{k_- + k_a} [O][R] + \frac{k_a k_d - k_d (k_- + k_a)}{k_- + k_a} [OR] \\ &= k'_{fR} [O][R] - k'_{bR} [OR] \end{aligned} \quad (6.25)$$

mapping the two-step kinetic scheme can onto the reaction in Eq. 6.1, but with effective rate constants defined by [158]:

$$k'_{fR} = \frac{k_+ k_a}{k_- + k_a} \quad (6.26)$$

$$k'_{bR} = \frac{k_- k_d}{k_- + k_a} \quad (6.27)$$

The two-step kinetic scheme should yield the same average concentrations as the scheme in Eq. 6.1, so that for the equilibrium constant one has:

$$\frac{k'_{fR}}{k'_{bR}} = \frac{k_{fR}}{k_{bR}}, \quad (6.28)$$

where  $k_{fR}$  and  $k_{bR}$  are the microscopic reaction rates defined in Eq. 6.1.

It is possible to express the effective rate constants  $k'_{fR}$  and  $k'_{bR}$  in terms of the microscopic rate constants. For the setup used here, where a single operator  $O$

is surrounded by a homogeneous distribution of repressor R, the rate  $k_+$  follows from the solution of the steady state diffusion equation with a reactive boundary condition with rate  $k = k_a$  at contact [131, 159] and is given by the diffusion-limited reaction rate  $k_D = 4\pi\sigma D$ . The rates  $k_-$  and  $k_a$  depend on the exact definition of the encounter complex  $O \cdots R$ . It is natural to identify the rate  $k_d$  with the intrinsic dissociation rate  $k_{bR}$ , thus  $k_d = k_{bR}$ . From these expressions for  $k_+$  and  $k_d$  and the restriction on the equilibrium constant in Eq. 6.28 one finds:

$$\frac{k_a}{k_-} = \frac{k_{fR}}{k_D}. \quad (6.29)$$

Inserting this result into Eqs. 6.26 and 6.27, yields:

$$k'_{fR} = \frac{k_D k_{fR}}{k_D + k_{fR}} \quad (6.30)$$

$$k'_{bR} = \frac{k_D k_{bR}}{k_D + k_{fR}} \quad (6.31)$$

These renormalized rate constants have a clear interpretation. For the effective forward rate in Eq. 6.30 it follows, for instance, that:

$$\frac{1}{k'_{fR}} = \frac{1}{k_D} + \frac{1}{k_{fR}} \quad (6.32)$$

or that, on average, the time required for repressor binding is given by the time needed to diffuse towards the operator plus the time for a reaction to occur when the repressor is in contact with the operator site [159]. The effective backward rate has a similar interpretation. The probability that after dissociation the repressor diffuses away from the operator site and never returns is given by  $S_{\text{irr}}(t \rightarrow \infty | r_0 = \sigma)$ , where  $S_{\text{irr}}(t, r_0)$  is the irreversible survival probability in Eq. 5.47 and  $\sigma$  is the reaction distance. It follows from Eq. 5.47, that:

$$\lim_{t \rightarrow \infty} S_{\text{irr}}(t | r_0 = \sigma) = \frac{k_D}{k_{fR} + k_D} \quad (6.33)$$

so that the expression for  $k'_{bR}$  can be written as:

$$k'_{bR} = k_{bR} S_{\text{irr}}(t \rightarrow \infty | r_0 = \sigma), \quad (6.34)$$

or that the effective dissociation rate is the microscopic dissociation rate multiplied by the probability that after dissociation the repressor escapes from the operator site [159].

For diffusion limited reactions, such as the reaction considered here, we have that  $k_{fR} \gg k_D$  and Eqs. 6.30 and 6.31 reduce to:

$$k'_{fR} = k_D, \quad (6.35)$$

$$k'_{bR} = k_D k_{bR} / k_{fR}. \quad (6.36)$$

In Fig. 6.2, we compare the noise profiles for the GFRD algorithm with those obtained by a simulation of the master equation, where instead of the microscopic rates  $k_{fR}$  and  $k_{fB}$  we use the renormalized rates from Eqs. 6.35 and 6.36. Surprisingly, we find complete agreement. One of the main reasons why this is unexpected, is that for the master equation the time between events is Poisson-distributed, whereas after a dissociation the time to the next rebinding is distributed according to a power-law distribution when diffusion is taken into account [135].

How is it possible that this power-law behavior is not at all of influence on the noise profile? This is because the average rebinding time is much smaller than any of the other relevant timescales in the network. Specifically, rebinding times are so short that the probability that a RNAP will bind before a rebinding is negligible. As a consequence, the transcription network is not at all influenced by the brief period the operator site is accessible before a rebinding occurs: for the transcription machinery the series of consecutive rebindings is perceived as a single event. Power-law distributions are only expected for rebinding times. When a repressor diffuses in from the bulk towards the operator site the distribution of arrival times is expected to be Poissonian, because in the bulk the repressors are distributed homogeneously at a fixed concentration.

It is possible to reinterpret the effective rate constants in Eq. 6.35 and 6.36 in the language of rapid rebindings. The probability  $P$  that a rebind will occur after a dissociation from the DNA is given by:

$$P = 1 - S_{\text{irr}}(t \rightarrow \infty | r_0 = \sigma), \quad (6.37)$$

where again  $S_{\text{irr}}(t | r_0 = \sigma)$  is the irreversible survival probability in Eq. 5.47 evaluated at particle contact. The probability that  $n$  consecutive rebindings occur before the repressor diffuses away from the operator site is then given by:

$$P_n = (1 - S_\infty)^n S_\infty, \quad (6.38)$$

where we defined  $S_t = S_{\text{irr}}(t | r_0 = \sigma)$ . From this follows that the average number of rebindings is given by:

$$\begin{aligned}
 N_{RB} &= \sum_{n=0}^{\infty} n(1 - S_{\infty})^n S_{\infty} \\
 &= (1 - S_{\infty})/S_{\infty}.
 \end{aligned} \tag{6.39}$$

Using the expression in Eq. 6.33, we find that:

$$N_{RB} = \frac{k_{fR}}{k_D} \tag{6.40}$$

Combining this with Eqs. 6.35 and 6.36, we get:

$$k'_{fR} = k_{fR}/N_{RB}, \tag{6.41}$$

$$k'_{bR} = k_{bR}/N_{RB}. \tag{6.42}$$

In words; after an initial binding the repressor spends  $N_{RB}$  times longer on the DNA than expected on the basis of the microscopic backward rate, as it rebinds on average  $N_{RB}$  times. Because the average occupancy should not change, the forward rate should be renormalized in the same way. In conclusion, the effects of diffusion are properly included in the chemical master equation of the well-stirred model when the reaction rates are renormalized by the average number of rebindings.

## 6.6 Discussion

The large fluctuations due to diffusion of the repressor molecules have a significant implication for the functioning of the repressor network. For some applications it might be crucial that the protein number is not only low on average, but remains low all the time. For instance, if the protein  $P$  itself functions as a transcription factor, it might by accident induce the expression of another gene when it is present in large enough numbers due to a fluctuation. Thus, when diffusion is taken into account not all combinations of repressor number  $N_R$  and repressor backward rate  $k_{bR}$  that obey Eq. 6.22 are equivalent. If in the repressed state the fluctuations in protein number should be small, the cell should increase the number of repressors and decrease the binding affinity to the operator site, so that repressors stay bound to the DNA only briefly.

The rapid rebindings observed in our simulations are a general phenomenon. Whenever the association of a molecule to a binding site occurs close to the place where it dissociates, these rebindings might occur. To what extent can these rebindings always be taken into account by renormalizing the reaction rates according to

Eqs. 6.35 and 6.36? In the current problem, this is possible because the time between dissociation and a subsequent rapid rebinding is very short compared to the time it takes RNAP to bind to the operator site on average. For the diffusion constant used here, a rebinding typically occurs on a timescale of  $10^{-8} - 10^{-6}$  s. As a consequence, RNAP virtually never binds to the operator when the repressor is still close to the binding site.

We find that the same holds for more general cases. For instance, we simulated a system in which repression occurred in a cooperative way. In this case the repressor backward rate is smaller when two repressors are bound to the operator than when a single repressor is bound. We found that again the fluctuations were well described by a well-stirred model with properly renormalized reaction rates. In this case, when one of the repressors dissociates, the time to a subsequent rebinding is short enough that the probability for the other repressor to dissociate in the mean time is negligible for reasonable values of cooperativity. When we do not consider repressors, but instead look at activators, we find that diffusion of the activators leads to enhancement of noise in protein level through a similar mechanism. Finally, the short timescale on which these rebindings occur may make it difficult to observe these rebindings experimentally and reaction rates measured biochemically will probably already be corrected according to Eqs. 6.35 and 6.36.

However, similar rebinding dynamics has been observed in the case of restriction enzymes, such as EcoRV. Restriction enzymes cleave specific sites on the DNA and it is thought that restriction enzymes find the correct binding site on the DNA by *facilitated diffusion*: a combination of free 3D diffusion and 1D sliding along the DNA [160]. Recently, it was shown that restriction enzymes translocate along the DNA predominantly through multiple cycles of dissociation-rebinding reactions, where the restriction enzyme, after dissociating from its initial site on the DNA, moves by 3D diffusion before rebinding to a new site on the *same* segment of the DNA [161, 162]. These dissociation-rebinding cycles are similar to the rebinding reactions observed in our simulations. For EcoRV, it has been estimated that after an initial association 10-100 rebindings occur before the restriction enzyme escapes to the bulk solution [162], in good agreement with the average number of rebindings calculated in Section 6.5.

In this chapter, we focus on a single operator site surrounded by repressor molecules. In this case, we find that the dynamics is well described by a master equation. This means that, apart from the renormalization in Eqs. 6.35 and 6.36, the spatial extension of our system effectively plays no role in determining the noise. We expect that this no longer holds when the number of binding sites is increased. In this case, the noise between binding sites that are close together in the cell might show correlations. This could for instance be important for ligand binding in bacterial

chemotaxis, where the receptor are thought to occur in dense clusters [163, 164]. It has also been shown recently in bacteria that coregulated genes tend to lie closer to each other on the DNA, suggesting that spatial relations might also be important in this case [165].

## 6.7 Conclusion

We have shown here by simulation that at least in the case of gene repression spatial fluctuations due to diffusion of repressor are an important contribution to the intrinsic noise of the system. Here, diffusion contributes to the noise by means of rapid rebindings: when the repressor dissociates from the operator site, it is so close to the binding site that it has a high probability of binding again after a very short time, on the order of  $10^{-8} - 10^{-6}$  s. As a consequence of these rebindings, we find that in the repressed state the production of mRNA can occur in sharp bursts, leading to fluctuations in the protein number that can be as large as 10% of the protein concentration in the unrepressed state. The rapid rebindings due to diffusion are a general phenomenon and not restricted to transcription networks alone.

Our simulation also suggests several ways in which the cell could minimize the effect of these fluctuations. We find that for the same level of repression, it is advantageous to have a large number of repressors that stay on the DNA for a short time rather than having few repressors that stay on the DNA for a long time. We also find that the amount of noise in mRNA and protein number is reduced by decreasing the rate of open complex formation by the RNA polymerase. Thus, the latter process functions as a 'low-pass filter', filtering out the rapid fluctuations due to repressor binding.

Finally, we find that the effect of spatial fluctuations and rapid rebindings can be well described by a two-step kinetic scheme, where formation of an encounter complex by diffusion and the subsequent association reaction are treated separately. As a consequence, the spatial fluctuations are well approximated by a chemical master equation, where the association and dissociation reactions are corrected for the average number of rapid rebindings.



---

# Bibliography

- [1] R. A. Bagnold. *The Physics of Blown Sand and Desert Dunes*. Methuen, London, 1941.
- [2] R. A. Bagnold. *Sand, Wind and War: Memoires of a Desert Explorer*. University of Arizona Press, Tucson, Arizona, 1991.
- [3] H. M. Jaeger, S. R. Nagel, and R. P. Behringer. Granular solids, liquids, and gases. *Reviews of Modern Physics*, 68(4):1259–1273, 1996.
- [4] C. H. Liu, S. R. Nagel, D. A. Schecter, S. N. Coppersmith, S. Majumdar, O. Narayan, and T. A. Witten. Force fluctuations in bead packs. *Science*, 269(5223):513–515, 1995.
- [5] D. A. Head, A. V. Tkachenko, and T. A. Witten. Robust propagation direction of stresses in a minimal granular packing. *European Physical Journal E*, 6(1):99–105, 2001.
- [6] T. S. Majmudar and R. P. Behringer. Contact force measurements and stress-induced anisotropy in granular materials. *Nature*, 435(7045):1079–1082, 2005.
- [7] M. E. Cates, J. P. Wittmer, J. P. Bouchaud, and P. Claudin. Jamming, force chains, and fragile matter. *Physical Review Letters*, 81(9):1841–1844, 1998.
- [8] A. J. Liu and S. R. Nagel. Nonlinear dynamics - jamming is not just cool any more. *Nature*, 396(6706):21–22, 1998.
- [9] C. S. O'Hern, L. E. Silbert, A. J. Liu, and S. R. Nagel. Jamming at zero temperature and zero applied stress: The epitome of disorder. *Physical Review E*, 68(1):011306, 2003.
- [10] V. Trappe, V. Prasad, L. Cipelletti, P. N. Segre, and D. A. Weitz. Jamming phase diagram for attractive particles. *Nature*, 411(6839):772–775, 2001.

- [11] D. Howell, R. P. Behringer, and C. Veje. Stress fluctuations in a 2d granular couette experiment: A continuous transition. *Physical Review Letters*, 82(26):5241–5244, 1999.
- [12] J. B. Knight, H. M. Jaeger, and S. R. Nagel. Vibration-induced size separation in granular media - the convection connection. *Physical Review Letters*, 70(24):3728–3731, 1993.
- [13] J. C. Williams. Segregation of particulate materials - review. *Powder Technology*, 15(2):245–251, 1976.
- [14] A. Rosato, K. J. Strandburg, F. Prinz, and R. H. Swendsen. Why the brazil nuts are on top - size segregation of particulate matter by shaking. *Physical Review Letters*, 58(10):1038–1040, 1987.
- [15] M. A. Kessler and B. T. Werner. Self-organization of sorted patterned ground. *Science*, 299(5605):380–383, 2003.
- [16] T. Shinbrot and F. J. Muzzio. Reverse buoyancy in shaken granular beds. *Physical Review Letters*, 81(20):4365–4368, 1998.
- [17] R. Ramirez, D. Risso, and P. Cordero. Thermal convection in fluidized granular systems. *Physical Review Letters*, 85(6):1230–1233, 2000.
- [18] M. Faraday. On the forms and states of fluids on vibrating elastic surfaces. *Philosophical Transactions of the Royal Society of London*, 121:319–340, 1831.
- [19] F. Melo, P. B. Umbanhowar, and H. L. Swinney. Hexagons, kinks, and disorder in oscillated granular layers. *Physical Review Letters*, 75(21):3838–3841, 1995.
- [20] P. B. Umbanhowar, F. Melo, and H. L. Swinney. Localized excitations in a vertically vibrated granular layer. *Nature*, 382(6594):793–796, 1996.
- [21] O. Lioubashevski, Y. Hamiel, A. Agnon, Z. Reches, and J. Fineberg. Oscillons and propagating solitary waves in a vertically vibrated colloidal suspension. *Physical Review Letters*, 83(16):3190–3193, 1999.
- [22] B. Andreotti, P. Claudin, and S. Douady. Selection of dune shapes and velocities - part 2: A two-dimensional modelling. *European Physical Journal B*, 28(3):341–352, 2002.
- [23] V. Schwammle and H. J. Herrmann. Geomorphology: Solitary wave behaviour of sand dunes - colliding dunes appear to traverse through one another and emerge unscathed. *Nature*, 426(6967):619–620, 2003.

- 
- [24] F. Reif. *Fundamentals of Statistical and Thermal Physics*. McGraw-Hill, New York, 1965.
- [25] A. Donev, I. Cisse, D. Sachs, E. Variano, F. H. Stillinger, R. Connelly, S. Torquato, and P. M. Chaikin. Improving the density of jammed disordered packings using ellipsoids. *Science*, 303(5660):990–993, 2004.
- [26] I. Goldhirsch and G. Zanetti. Clustering instability in dissipative gases. *Physical Review Letters*, 70(11):1619–1622, 1993.
- [27] S. McNamara and W. R. Young. Inelastic collapse in 2 dimensions. *Physical Review E*, 50(1):R28–R31, 1994.
- [28] T. Zhou and L. P. Kadanoff. Inelastic collapse of three particles. *Physical Review E*, 54(1):623–628, 1996.
- [29] S. Luding and S. McNamara. How to handle the inelastic collapse of a dissipative hard-sphere gas with the tc model. *Granular Matter*, 113, 1998.
- [30] D. Goldman, M. D. Shattuck, C. Bizon, W. D. McCormick, J. B. Swift, and H. L. Swinney. Absence of inelastic collapse in a realistic three ball model. *Physical Review E*, 57(4):4831–4833, 1998.
- [31] H. King, R. White, I. Maxwell, and N. Menon. Inelastic impact of a sphere on a massive plane: nonmonotonic velocity-dependence of the restitution coefficient. 2002. E-print cond-mat/0209490.
- [32] Y. S. Du, H. Li, and L. P. Kadanoff. Breakdown of hydrodynamics in a one-dimensional system of inelastic particles. *Physical Review Letters*, 74(8):1268–1271, 1995.
- [33] K. van der Weele, D. van der Meer, and D. Lohse. Clustering in een granulair gas. *Nederlands Tijdschrift voor de Natuurkunde*, 68:22–25, 2002.
- [34] K. van der Weele, D. van der Meer, M. Versluis, and D. Lohse. Hysteretic clustering in granular gas. *Europhysics Letters*, 53(3):328–334, 2001.
- [35] D. R. M. Williams and F. C. MacKintosh. Driven granular media in one dimension: Correlations and equation of state. *Physical Review E*, 54(1):R9–R12, 1996.
- [36] D. L. Blair and A. Kudrolli. Velocity correlations in dense granular gases. *Physical Review E*, 6405(5):050301, 2001.

- [37] G. D'Anna, P. Mayor, A. Barrat, V. Loreto, and F. Nori. Observing brownian motion in vibration-fluidized granular matter. *Nature*, 424(6951):909–912, 2003.
- [38] A. Puglisi, A. Baldassarri, and V. Loreto. Fluctuation-dissipation relations in driven granular gases. *Physical Review E*, 66(6):061305, 2002.
- [39] K. Feitosa and N. Menon. Breakdown of energy equipartition in a 2d binary vibrated granular gas. *Physical Review Letters*, 88(19):198301, 2002.
- [40] A. Barrat, V. Loreto, and A. Puglisi. Temperature probes in binary granular gases. *Physica a-Statistical Mechanics and Its Applications*, 334(3-4):513–523, 2004.
- [41] F. Rouyer and N. Menon. Velocity fluctuations in a homogeneous 2d granular gas in steady state. *Physical Review Letters*, 85(17):3676–3679, 2000.
- [42] A. Puglisi, V. Loreto, U. M. B. Marconi, A. Petri, and A. Vulpiani. Clustering and non-gaussian behavior in granular matter. *Physical Review Letters*, 81(18):3848–3851, 1998.
- [43] S. McNamara and W. R. Young. Dynamics of a freely evolving, two-dimensional granular medium. *Physical Review E*, 53(5):5089–5100, 1996.
- [44] A. Kudrolli, M. Wolpert, and J. P. Gollub. Cluster formation due to collisions in granular material. *Physical Review Letters*, 78(7):1383–1386, 1997.
- [45] A. Kudrolli and J. Henry. Non-gaussian velocity distributions in excited granular matter in the absence of clustering. *Physical Review E*, 62(2):R1489–R1492, 2000.
- [46] J. S. Olafsen and J. S. Urbach. Clustering, order, and collapse in a driven granular monolayer. *Physical Review Letters*, 81(20):4369–4372, 1998.
- [47] W. Losert, D. G. W. Cooper, J. Delour, A. Kudrolli, and J. P. Gollub. Velocity statistics in excited granular media. *Chaos*, 9(3):682–690, 1999.
- [48] J. S. Olafsen and J. S. Urbach. Velocity distributions and density fluctuations in a granular gas. *Physical Review E*, 60(3):R2468–R2471, 1999.
- [49] A. Prevost, D. A. Egolf, and J. S. Urbach. Forcing and velocity correlations in a vibrated granular monolayer. *Physical Review Letters*, 89(8):084301, 2002.
- [50] G. W. Baxter and J. S. Olafsen. Kinetics - gaussian statistics in granular gases. *Nature*, 425(6959):680–680, 2003.

- 
- [51] S. J. Moon, M. D. Shattuck, and J. B. Swift. Velocity distributions and correlations in homogeneously heated granular media. *Physical Review E*, 6403(3):031303, 2001.
- [52] A. Barrat, T. Biben, Z. Racz, E. Trizac, and E. van Wijland. On the velocity distributions of the one-dimensional inelastic gas. *Journal of Physics a-Mathematical and General*, 35(3):463–480, 2002.
- [53] A. Barrat and E. Trizac. Random inelasticity and velocity fluctuations in a driven granular gas. *European Physical Journal E*, 11(1):99–104, 2003.
- [54] T.P.C. van Noije and M.H. Ernst. Velocity distributions in homogeneous granular fluids: the free and the heated case. *Granular Matter*, 1:57–64, 1998.
- [55] M. H. Ernst and R. Brito. Driven inelastic maxwell models with high energy tails. *Physical Review E*, 65(4):040301, 2002.
- [56] I. S. Aranson and J. S. Olafsen. Velocity fluctuations in electrostatically driven granular media. *Physical Review E*, 66(6):061302, 2002.
- [57] J. J. Brey and M. J. Ruiz-Montero. Velocity distribution of fluidized granular gases in the presence of gravity. *Physical Review E*, 67(2):021307, 2003.
- [58] A. Barrat and E. Trizac. Molecular dynamics simulations of vibrated granular gases. *Physical Review E*, 66(5):051303, 2002.
- [59] D. Paolotti, C. Cattuto, U. M. B. Marconi, and A. Puglisi. Dynamical properties of vibrofluidized granular mixtures. *Granular Matter*, 5(2):75–83, 2003.
- [60] O. Herbst, P. Muller, M. Otto, and A. Zippelius. Local equation of state and velocity distributions of a driven granular gas. *Physical Review E*, 70(5):051313, 2004.
- [61] S. Ulam. On the operations of pair production, transmutations and generalized random walks. *Advances in Applied Mathematics*, 1:7–21, 1980.
- [62] M. H. Ernst and R. Brito. Asymptotic solutions of the nonlinear boltzmann equation for dissipative systems. In T. Poeschel and N. Brilliantov, editors, *Granular Gas Dynamics*. Springer-Verlag, Berlin, 2003.
- [63] J. Bougie, S. J. Moon, J. B. Swift, and H. L. Swinney. Shocks in vertically oscillated granular layers. *Physical Review E*, 66(5):051301, 2002.
- [64] S. J. Moon, J. B. Swift, and H. L. Swinney. Steady-state velocity distributions of an oscillated granular gas. *Physical Review E*, 69(1):011301, 2004.

- [65] C. Bizon, M. D. Shattuck, J. B. Swift, W. D. McCormick, and H. L. Swinney. Patterns in 3d vertically oscillated granular layers: Simulation and experiment. *Physical Review Letters*, 80(1):57–60, 1998.
- [66] J. C. Crocker and D. G. Grier. Methods of digital video microscopy for colloidal studies. *Journal of Colloid and Interface Science*, 179(1):298–310, 1996.
- [67] S. Warr, J. M. Huntley, and G. T. H. Jacques. Fluidization of a 2-dimensional granular system - experimental-study and scaling behavior. *Physical Review E*, 52(5):5583–5595, 1995.
- [68] D. I. Goldman, M. D. Shattuck, S. J. Moon, J. B. Swift, and H. L. Swinney. Lattice dynamics and melting of a nonequilibrium pattern. *Physical Review Letters*, 90(10):104302, 2003.
- [69] A. van Leeuwenhoek. Letter no. 26[18] october 9th 1676. In *The Collected Letters of Antoni van Leeuwenhoek*. Swets and Zeitlinger, Amsterdam, 1952.
- [70] E. G. Ruestow. *The Microscope in the Dutch Republic*. Cambridge University Press, Cambridge, 1996.
- [71] A. van Leeuwenhoek. Letter no. 75[39] september 17th 1683. In *The Collected Letters of Antoni van Leeuwenhoek*. Swets and Zeitlinger, Amsterdam, 1952.
- [72] R. Hooke. *Philosophical Experiments and Observations of the Late Eminent Dr. Robert Hooke*. Frank Cass, London, 1726.
- [73] E. Schrödinger. *What is Life?* Cambridge University Press, Cambridge, 1944.
- [74] L. H. Hartwell, J. J. Hopfield, S. Leibler, and A. W. Murray. From molecular to modular cell biology. *Nature*, 402(6761):C47–C52, 1999.
- [75] J. M. Raser and E. K. O’Shea. Noise in gene expression: Origins, consequences, and control. *Science*, 309(5743):2010–2013, 2005.
- [76] D. Voet and J. G. Voet. *Biochemistry*. John Wiley and Sons, New York, 1995.
- [77] M. Ptashne and A. Gann. *Genes and Signals*. Cold Spring Harbor Laboratory Press, New York, 2002.
- [78] D. A. Padgett, J. F. Sheridan, J. Dorne, G. G. Berntson, J. Candelora, and R. Glaser. Social stress and the reactivation of latent herpes simplex virus type 1. *Proceedings of the National Academy of Sciences of the United States of America*, 95(20):12070–12070, 1998.

- 
- [79] S. L. Spruance. Pathogenesis of herpes-simplex labialis - experimental induction of lesions with uv-light. *Journal of Clinical Microbiology*, 22(3):366–368, 1985.
- [80] M. Ptashne. *A Genetic Switch: Phage Lambda and Higher Organisms*. Cell Press and Blackwell Science Publishing, Cambridge, Massachusetts, 1992.
- [81] A. L. Barabasi and Z. N. Oltvai. Network biology: Understanding the cell's functional organization. *Nature Reviews Genetics*, 5(2):101–U15, 2004.
- [82] P. Erdős and A. Rényi. On the evolution of random graphs. *Bulletin of the International Statistical Institute*, 38(4):343–347, 1960.
- [83] D. J. Watts and S. H. Strogatz. Collective dynamics of 'small-world' networks. *Nature*, 393(6684):440–442, 1998.
- [84] M. E. J. Newman. Fast algorithm for detecting community structure in networks. *Physical Review E*, 69:066133, 2004.
- [85] N. Kashtan and U. Alon. Spontaneous evolution of modularity and network motifs. *Proceedings of the National Academy of Sciences of the United States of America*, 102(39):13773–13778, 2005.
- [86] S. S. Shen-Orr, R. Milo, S. Mangan, and U. Alon. Network motifs in the transcriptional regulation network of *Escherichia coli*. *Nature Genetics*, 31(1):64–68, 2002.
- [87] R. Milo, S. Shen-Orr, S. Itzkovitz, N. Kashtan, D. Chklovskii, and U. Alon. Network motifs: Simple building blocks of complex networks. *Science*, 298(5594):824–827, 2002.
- [88] M. B. Elowitz and S. Leibler. A synthetic oscillatory network of transcriptional regulators. *Nature*, 403(6767):335–338, 2000.
- [89] R. Y. Tsien. The green fluorescent protein. *Annual Review of Biochemistry*, 67:509–544, 1998.
- [90] M. B. Elowitz, A. J. Levine, E. D. Siggia, and P. S. Swain. Stochastic gene expression in a single cell. *Science*, 297(5584):1183–1186, 2002.
- [91] N. Rosenfeld, J. W. Young, U. Alon, P. S. Swain, and M. B. Elowitz. Gene regulation at the single-cell level. *Science*, 307(5717):1962–1965, 2005.
- [92] J. M. Pedraza and A. van Oudenaarden. Noise propagation in gene networks. *Science*, 307(5717):1965–1969, 2005.

- [93] N. G. van Kampen. *Stochastic Processes in Physics and Chemistry*. North-Holland, Amsterdam, 1992.
- [94] A. B. Bortz, M. H. Kalos, and J. L. Lebowitz. New algorithm for monte-carlo simulation of ising spin systems. *Journal of Computational Physics*, 17(1):10–18, 1975.
- [95] D. T. Gillespie. Exact stochastic simulation of coupled chemical reactions. *Journal of Chemical Physics*, 81:2340–2361, 1977.
- [96] E. M. Ozbudak, M. Thattai, I. Kurtser, A. D. Grossman, and A. van Oudenaarden. Regulation of noise in the expression of a single gene. *Nature Genetics*, 31(1):69–73, 2002.
- [97] J. Paulson. Summing up the noise in gene networks. *Nature*, 427(6973):415–418, 2004.
- [98] I. R. Henderson, P. Owen, and J. P. Nataro. Molecular switches - the on and off of bacterial phase variation. *Molecular Microbiology*, 33(5):919–932, 1999.
- [99] N. Q. Balaban, J. Merrin, R. Chait, L. Kowalik, and S. Leibler. Bacterial persistence as a phenotypic switch. *Science*, 305(5690):1622–1625, 2004.
- [100] E. Kussell, R. Kishony, N. Q. Balaban, and S. Leibler. Bacterial persistence: A model of survival in changing environments. *Genetics*, 169(4):1807–1814, 2005.
- [101] I. Mihalcescu, W. H. Hsing, and S. Leibler. Resilient circadian oscillator revealed in individual cyanobacteria. *Nature*, 430(6995):81–85, 2004.
- [102] M. Nakajima, K. Imai, H. Ito, T. Nishiwaki, Y. Murayama, H. Iwasaki, T. Oyarna, and T. Kondo. Reconstitution of circadian oscillation of cyanobacterial kaic phosphorylation in vitro. *Science*, 308(5720):414–415, 2005.
- [103] A. Becskei and L. Serrano. Engineering stability in gene networks by autoregulation. *Nature*, 405(6786):590–593, 2000.
- [104] G. von Dassow, E. Meir, E. M. Munro, and G. M. Odell. The segment polarity network is a robust development module. *Nature*, 406(6792):188–192, 2000.
- [105] J. L. Cherry and F. R. Adler. How to make a biological switch. *Journal of Theoretical Biology*, 203(2):117–133, 2000.



- 
- [106] E. M. Ozbudak, M. Thattai, H. N. Lim, B. I. Shraiman, and A. van Oudenaarden. Multistability in the lactose utilization network of *Escherichia coli*. *Nature*, 427(6976):737–740, 2004.
- [107] T. S. Gardner, C. R. Cantor, and J. J. Collins. Construction of a genetic toggle switch in *Escherichia coli*. *Nature*, 403(6767):339–342, 2000.
- [108] E. Aurell and K. Sneppen. Epigenetics as a first exit problem. *Physical Review Letters*, 88(4):048101, 2002.
- [109] P. B. Warren and P. R. ten Wolde. Enhancement of the stability of genetic switches by overlapping upstream regulatory domains. *Physical Review Letters*, 92(12):128101, 2004.
- [110] M. B. Elowitz, M. G. Surette, P. E. Wolf, J. B. Stock, and S. Leibler. Protein mobility in the cytoplasm of *Escherichia coli*. *Journal of Bacteriology*, 181(1):197–203, 1999.
- [111] T. T. Le, S. Harlepp, C. C. Guet, K. Dittmar, T. Emonet, T. Pan, and P. Cluzel. Real-time RNA profiling within a single bacterium. *Proceedings of the National Academy of Sciences of the United States of America*, 102(26):9160–9164, 2005.
- [112] M. Howard, A. D. Rutenberg, and S. de Vet. Dynamic compartmentalization of bacteria: Accurate division in *e-coli*. *Physical Review Letters*, 87(27):278102, 2001.
- [113] K. Kruse. A dynamic model for determining the middle of *Escherichia coli*. *Biophysical Journal*, 82(2):618–627, 2002.
- [114] K. C. Huang, Y. Meir, and N. S. Wingreen. Dynamic structures in *Escherichia coli*: Spontaneous formation of MinE rings and MinD polar zones. *Proceedings of the National Academy of Sciences of the United States of America*, 100(22):12724–12728, 2003.
- [115] M. Howard and A. D. Rutenberg. Pattern formation inside bacteria: Fluctuations due to the low copy number of proteins. *Physical Review Letters*, 90(12):128102, 2003.
- [116] K. Dubrovinski and M. Howard. Stochastic model for Soj relocation dynamics in *Bacillus subtilis*. *Proceedings of the National Academy of Sciences of the United States of America*, 102(28):9808–9813, 2005.

- [117] H. C. Berg and E. M. Purcell. Physics of chemoreception. *Biophysical Journal*, 20(2):193–219, 1977.
- [118] W. Bialek and S. Setayeshgar. Physical limits to biochemical signaling. *Proceedings of the National Academy of Sciences of the United States of America*, 102(29):10040–10045, 2005.
- [119] H. H. McAdams and A. Arkin. Stochastic mechanisms in gene expression. *Proceedings of the National Academy of Sciences of the United States of America*, 94(3):814–819, 1997.
- [120] Y. Togashi and K. Kaneko. Transitions induced by the discreteness of molecules in a small autocatalytic system. *Physical Review Letters*, 86(11):2459–2462, 2001.
- [121] N. M. Shnerb, Y. Louzoun, E. Bettelheim, and S. Solomon. The importance of being discrete: Life always wins on the surface. *Proceedings of the National Academy of Sciences of the United States of America*, 97(19):10322–10324, 2000.
- [122] D. T. Gillespie. General method for numerically simulating stochastic time evolution of coupled chemical-reactions. *Journal of Computational Physics*, 22:403, 1976.
- [123] C. J. Morton-Firth and D. Bray. Predicting temporal fluctuations in an intracellular signalling pathway. *Journal of Theoretical Biology*, 192(1):117–128, 1998.
- [124] M. Malek-Mansour and J. Houard. New approximation scheme for the study of fluctuations in nonuniform non-equilibrium systems. *Physics Letters A*, 70(5-6):366–368, 1979.
- [125] P. Hanusse and A. Blanche. A Monte-Carlo method for large reaction-diffusion systems. *Journal of Chemical Physics*, 74(11):6148–6153, 1981.
- [126] J. Elf and M. Ehrenberg. Spontaneous separation of bi-stable biochemical systems into spatial domains of opposite phases. *Systems Biology*, 2:230–236, 2004.
- [127] M. Ander, P. Beltrao, B. D. Ventura, J. Ferkinghoff-Borg, M. Foglierini, A. Kaplan, C. Lemerle, I. Tomas-Oliveira, and L. Serrano. Smartcell, a framework to simulate cellular processes that combines stochastic approximation with diffusion and localisation: analysis of simple networks. *Systems Biology*, 1:129–138, 2004.

- [128] C. W. Gardiner. *Handbook of Stochastic Methods*. Springer-Verlag, Berlin, 1985.
- [129] F. Baras and M. M. Mansour. Microscopic simulation of chemical instabilities. *Advances in Chemical Physics*, 100:393, 1997.
- [130] S. S. Andrews and D. Bray. Stochastic simulation of chemical reactions with spatial resolution and single molecule detail. *Physical Biology*, 1(3):137–151, 2004.
- [131] M. Smoluchowski. Versuch einer mathematischen theorie der koagulationkinetik losungen. *Zeitschrift fr Physikalische Chemie*, 92:129–168, 1917.
- [132] H. S. Carslaw and J. C. Jaeger. *Conduction of Heat in Solids*. Oxford University Press, New York, 1959.
- [133] N. Agmon and A. Szabo. Theory of reversible diffusion-influenced reactions. *Journal of Chemical Physics*, 92(9):5270–5284, 1990.
- [134] S. A. Rice. *Diffusion Limited Reactions*. Elsevier Science, New York, 1985.
- [135] H. Kim and K. J. Shin. Exact solution of the reversible diffusion-influenced reaction for an isolated pair in three dimensions. *Physical Review Letters*, 82(7):1578–1581, 1999.
- [136] W. H. Press, S. A. Teukolsky, W. T. Vetterling, and B. P. Flannery, editors. *Numerical Recipes in C*. Cambridge University Press, Cambridge, 1992.
- [137] J.-P. Hansen and I. R. McDonald. *Theory of Simple Liquids*. Academic, San Diego, 1986.
- [138] P. S. Swain, M. B. Elowitz, and E. D. Siggia. Intrinsic and extrinsic contributions to stochasticity in gene expression. *Proceedings of the National Academy of Sciences of the United States of America*, 99(20):12795–12800, 2002.
- [139] H. X. Zhou and A. Szabo. Comparison between molecular-dynamics simulations and the smoluchowski theory of reactions in a hard-sphere liquid. *Journal of Chemical Physics*, 95(8):5948–5952, 1991.
- [140] P. B. Warren and P. R. ten Wolde. Chemical models of genetic toggle switches. *Journal of Physical Chemistry B*, 109(14):6812–6823, 2005.
- [141] O. G. Berg, R. B. Winter, and P. H. Vonhippel. Diffusion-driven mechanisms of protein translocation on nucleic-acids .1. models and theory. *Biochemistry*, 20(24):6929–6948, 1981.

- [142] S. S. Andrews. Serial rebinding of ligands to clustered receptors as exemplified by bacterial chemotaxis. *Physical Biology*, 2:111–122, 2005.
- [143] S. Valitutti, S. Muller, M. Cella, E. Padovan, and A. Lanzavecchia. Serial triggering of many t-cell receptors by a few peptide-mhc complexes. *Nature*, 375(6527):148–151, 1995.
- [144] D. Frenkel and B. Smit. *Understanding Molecular Simulation, From Algorithms to Applications*. Academic, San Diego, 1996.
- [145] A. L. Edelstein and N. Agmon. Brownian dynamics simulations of reversible-reactions in one-dimension. *Journal of Chemical Physics*, 99(7):5396–5404, 1993.
- [146] H. Kim, M. Yang, and K. J. Shin. Dynamic correlation effect in reversible diffusion-influenced reactions: Brownian dynamics simulation in three dimensions. *Journal of Chemical Physics*, 111(3):1068–1075, 1999.
- [147] A. V. Popov and N. Agmon. Three-dimensional simulations of reversible bimolecular reactions: The simple target problem. *Journal of Chemical Physics*, 115(19):8921–8932, 2001.
- [148] M. G. Noro, N. Kern, and D. Frenkel. The role of long-range forces in the phase behavior of colloids and proteins. *Europhysics Letters*, 48(3):332–338, 1999.
- [149] M. S. Ko. A stochastic model for gene induction. *J Theor Biol*, 153(2):181–94, 1991.
- [150] T. B. Kepler and T. C. Elston. Stochasticity in transcriptional regulation: Origins, consequences, and mathematical representations. *Biophysical Journal*, 81(6):3116–3136, 2001.
- [151] R. Karmakar and I. Bose. Graded and binary responses in stochastic gene expression. *Physical Biology*, 1:197–205, 2004.
- [152] J. R. Pirone and T. C. Elston. Fluctuations in transcription factor binding can explain the graded and binary responses observed in inducible gene expression. *Journal of Theoretical Biology*, 226(1):111–121, 2004.
- [153] M. L. Simpson, C. D. Cox, and G. S. Sayler. Frequency domain chemical langevin analysis of stochasticity in gene transcriptional regulation. *Journal of Theoretical Biology*, 229(3):383–394, 2004.

- 
- [154] H. Bremer, P. Dennis, and M. Ehrenberg. Free RNA polymerase and modeling global transcription in *Escherichia coli*. *Biochimie*, 85(6):597–609, 2003.
- [155] M. R. McClure. A biochemical analysis of the effect of RNA polymerase concentration on the in vivo control of RNA chain initiation frequency. In D. L. F. Lennon, F. W. Stratman, and R. N. Zahlten, editors, *Biochemistry of Metabolic Processes*, pages 207–217. Elsevier, New York, 1983.
- [156] A. Revyakin, R. H. Ebright, and T. R. Strick. Promoter unwinding and promoter clearance by RNA polymerase: Detection by single-molecule DNA nanomanipulation. *Proceedings of the National Academy of Sciences of the United States of America*, 101(14):4776–4780, 2004.
- [157] J. M. G. Vilar and S. Leibler. DNA looping and physical constraints on transcription regulation. *Journal of Molecular Biology*, 331(5):981–989, 2003.
- [158] M. Eigen. Diffusion control in biochemical reactions. In S. L. Mintz and S. M. Widemeyer, editors, *Quantum Statistical Mechanics in the Natural Sciences*, pages 37–61. Plenum Press, New York, 1974.
- [159] D. Shoup and A. Szabo. Role of diffusion in ligand-binding to macromolecules and cell-bound receptors. *Biophysical Journal*, 40(1):33–39, 1982.
- [160] P. H. Von Hippel and O. G. Berg. Facilitated target location in biological systems. *Journal of Biological Chemistry*, 264(2):675–678, 1989.
- [161] N. P. Stanford, M. D. Szczelkun, J. F. Marko, and S. E. Halford. One- and three-dimensional pathways for proteins to reach specific DNA sites. *Embo Journal*, 19(23):6546–6557, 2000.
- [162] D. M. Gowers, G. G. Wilson, and S. E. Halford. Measurement of the contributions of 1d and 3d pathways to the translocation of a protein along DNA. *Proceedings of the National Academy of Sciences of the United States of America*, 102(44):15883–15888, 2005.
- [163] J. R. Maddock and L. Shapiro. Polar location of the chemoreceptor complex in the *Escherichia-Coli* cell. *Science*, 259(5102):1717–1723, 1993.
- [164] D. Bray, M. D. Levin, and C. J. Morton-Firth. Receptor clustering as a cellular mechanism to control sensitivity. *Nature*, 393(6680):85–88, 1998.
- [165] P. B. Warren and P. R. ten Wolde. Statistical analysis of the spatial distribution of operons in the transcriptional regulation network of *Escherichia coli*. *Journal of Molecular Biology*, 342(5):1379–1390, 2004.

*Bibliography*

---

---

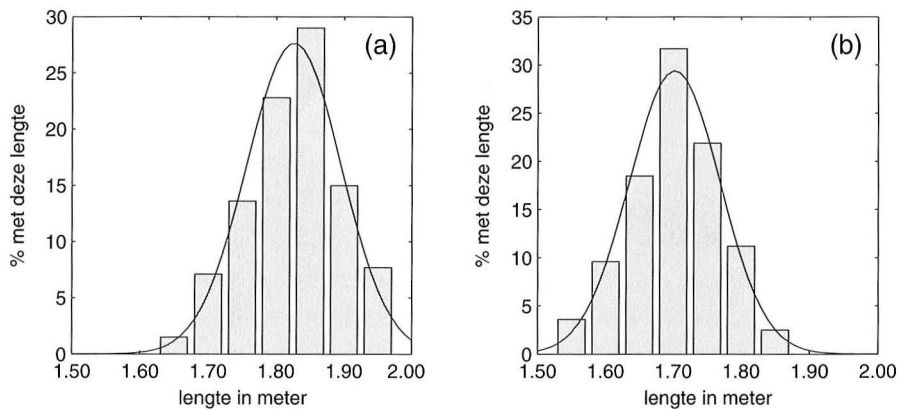
# Samenvatting

De titel van mijn proefschrift luidt, in het Nederlands: “Stochastische dynamica in zand en cellen.” Hieronder zal ik proberen uit te leggen wat “stochastische dynamica” precies is en waarom ik het heb bestudeerd in zulke verschillende systemen als zand en cellen.

## Stochastische dynamica

In 2004 was volgens het Centraal Bureau voor de Statistiek de lengte van de gemiddelde Nederlandse man en vrouw respectievelijk 1 meter 82 en 1 meter 68. Echter, iedereen die door een drukke winkelstraat loopt ziet meteen dat mensen in het algemeen bijhoorlijk verschillende lichaamslengte hebben. Op het eerste gezicht lijkt het dus of we over lichaamslengte eigenlijk geen voorspellingen kunnen doen. Toch blijkt dat als we tellen hoeveel mensen een bepaalde lengte hebben, die lengteverdeling een vast patroon laat zien. Als voorbeeld is in Figuur S.1(a) en (b) de lengteverdeling te zien van Nederlandse mannen en vrouwen tussen de 20 en 34 jaar oud. In allebei de gevallen hebben de meeste mensen een lengte in de buurt van het gemiddelde. Er is echter ook altijd een klein aantal mensen met een lengte die daar veel van afwijkt. De vorm van zulke verdelingen wordt goed beschreven door de zogenaamde *Gaussische verdeling*, zoals ook te zien is in Figuur S.1(a) en (b).

Het blijkt dat veel schijnbaar onvoorspelbare processen toch goed met precies zo'n Gaussische verdeling kunnen worden beschreven. Als je bijvoorbeeld een muntje een groot aantal keer opgooit, volgt het aantal keren dat je kop krijgt ook een Gaussische verdeling. De Gaussische verdeling heeft twee belangrijke eigenschappen. Als eerste heb je de plek van de piek van de verdeling, het gemiddelde. De andere eigenschap is hoe breed de verdeling is. Hoe breder de verdeling, des te groter de afwijking van het gemiddelde die je kan vinden. Het is bijvoorbeeld voorstelbaar dat bij andere dieren de spreiding in lichaamslengte groter of kleiner is dan bij mensen. Een grootte zoals lichaamslengte, die willekeurig varieert van

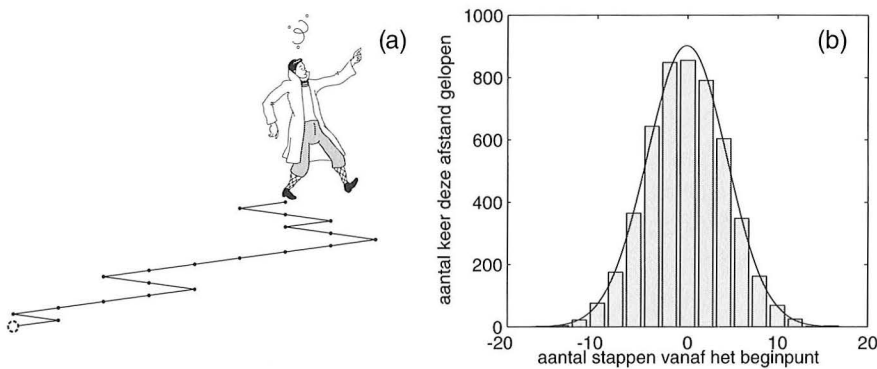


**Figuur 5.1:** De Gaussische verdeling. De verdeling van lichaamslengten van (a) 1017 mannen en (b) 987 vrouwen tussen de 20 en 34 jaar. De verdeling van lichaamslengten wordt goed beschreven met een zogenaamde Gaussische verdeling die als een zwarte lijn in beide figuren is weergegeven. Gebaseerd op informatie uit het Statistisch Jaarboek 2004 van het Centraal Bureau voor de Statistiek.

persoon tot persoon, wordt ook wel een *stochastische* grootte genoemd, naar het Griekse werkwoord voor “raden”.

Gaussische verdelingen komen ook in de natuurkunde regelmatig voor, bijvoorbeeld in de beschrijving van gassen. Een kleine hoeveelheid gas, zoals bijvoorbeeld de lucht in een opgeblazen ballon, bestaat al uit ontelbaar veel gasmolekulen die allemaal wanordelijk door elkaar heen bewegen en met elkaar botsen. Het is ondoenlijk voor ieder gasmolekuul uit te rekenen hoe het precies beweegt en dus lijkt het onmogelijk om de eigenschappen van het gas in de ballon uit te rekenen uit het gedrag van de molekulen waaruit het gas bestaat. Maar eerder bleek dat we iets over de lengte van een grote groep mensen kunnen zeggen, terwijl we lengte van één enkel persoon niet kunnen voorspellen. Zo kunnen we op dezelfde manier iets zeggen over het gedrag van de ontelbaar veel molekulen in een gas, zelfs als we niet precies kunnen voorspellen wat een enkel gasmolekuul precies doet. We kunnen bijvoorbeeld kijken naar de verschillende snelheden van de molekulen in een gas. Het blijkt dat deze snelheidsverdeling precies een Gaussische verdeling volgt: verreweg de meeste molekulen bewegen relatief rustig, maar een kleine fractie vliegt met veel hogere snelheid rond. Net als bij alle Gaussische verdelingen, wordt ook deze alleen bepaald door de gemiddelde snelheid en de spreiding van de verdeling. Als het gas als geheel niet stroomt, is de gemiddelde snelheid nul. De spreiding van snelheden kunnen we heel makkelijk meten: dat is namelijk wat wij als temperatuur voelen.





**Figuur S.2:** De dronkenmanswandeling. (a) Een voorbeeld van een dronkenmanswandeling van 20 stappen. Het beginpunt is aangegeven door de gestreepte cirkel. De zwarte punten geven de opeenvolgende stappen aan. Het eindpunt is op zeven stappen rechts van het beginpunt. (b) De verdeling van eindpunten na 5000 dronkenmanswandelingen van 20 stappen. De meeste wandelingen komen vlak bij het beginpunt uit.

In een koud gas bewegen de molekulen willekeurig maar niet zo snel, in een heet gas heel hard. Als een gas koud genoeg is bewegen de molekulen zo langzaam dat ze aan elkaar gaan klonteren en een vloeistof, zoals water, kunnen vormen.

Een ander voorbeeld uit de natuurkunde is dat van de zogenaamde *dronkenmanswandeling*, zoals afgebeeld in Figuur S.2(a). Wanneer een dronkenlap 's avonds vanuit het café naar huis loopt, nemen we aan dat hij zo dronken is dat ieder volgende stap even vaak naar links gaat als naar rechts. De route die hij dan loopt is volkomen willekeurig en er zijn allerlei interessante vragen over te stellen. Waar kan hij bijvoorbeeld allemaal uitkomen na honderd van die willekeurige stappen gezet te hebben? En hoeveel stappen moet hij op deze manier zetten om een redelijke kans te hebben uit te komen bij zijn huis aan het einde van de straat? De verdeling van afgelegde afstand na twintig willekeurige stappen is afgebeeld in Figuur S.2(b). Ook in dit geval volgt de afgelegde afstand een Gaussische verdeling. De gemiddelde afgelegde afstand is nul. Dit komt doordat een stap naar links even waarschijnlijk is als een stap naar rechts. De breedte van de verdeling geeft aan hoe ver van het beginpunt je uit kan komen. De spreiding blijkt maar langzaam toe te nemen met het aantal afgelegde stappen. Als de afstand van het café naar huis te groot wordt, is een dronkenmanswandeling dus een uiterst inefficiënte manier om thuis te komen.

Terwijl maar weinig cafégangers er zo aan toe zijn dat ze op de bovenstaande manier naar huis moeten komen, komen dergelijke dronkenmanswandelingen vaak voor in de natuurkunde. Een voorbeeld dat ook voor dit proefschrift van groot

belang is, is de zogenaamde *Brownse beweging*. In 1828 observeerde de Britse botanicus Robert Brown onder de microscoop dat in water drijvend stuifmeel eenzelfde soort willekeurige dronkenmanswandeling ondergaat. Dacht Brown in eerste instantie te maken te hebben met iets levends, later nam hij dezelfde willekeurige beweging waar met stofkorreltjes en (bizar genoeg) met stukjes van de egyptische Sfinx. In 1905 verklaarde Einstein deze Brownse beweging door te realiseren dat de stuifmeeldeeltjes zo klein zijn, dat zij door willekeurige botsingen met de omringende watermolekulen heen en weer geslingerd worden. Door het gedrag van zulke deeltjes in water te bestuderen is het dus mogelijk om iets te leren over het gedrag van molekulen, die verder voor ons niet direct zichtbaar zijn. Om die reden vormden metingen aan de Brownse beweging in het begin van de vorige eeuw dan ook één van de eerste overtuigende bewijzen voor het daadwerkelijk bestaan van molekulen en atomen.

De positie van een stofdeeltje in water varieert dus op een willekeurige wijze in de tijd. Dit soort gedrag wordt in het algemeen aangeduid als *stochastische dynamica*. Net als in het geval van lichaamslengte, geldt ook hier dat we misschien niet het gedrag van een enkel stofdeeltje in water kunnen voorspellen, maar dat we wel iets kunnen zeggen over het gedrag van een groot aantal deeltjes. Op die manier vormt de dronkenmanswandeling een verklaring voor *diffusie*, het verschijnsel dat bijvoorbeeld een druppel inkt in water zich langzaam uitspreidt, zelfs als we zorgen dat er geen enkele stroming in het water is. Ieder inktdeeltje afzonderlijk ondergaat dan een onvoorspelbare dronkenmanswandeling. Maar alle inktdeeltjes bij elkaar leveren een kleurprofiel dat we wel goed kunnen voorspellen. De tak van de natuurkunde die zich bezig houdt met het beschrijven van het gedrag van grote aantallen deeltjes die zich afzonderlijk willekeurig gedragen wordt de *statistische fysica* genoemd. De statistische fysica is onmisbaar gebleken om de eigenschappen van alledaagse materie, zoals vaste stoffen, vloeistoffen en gassen, uit het gedrag van atomen en molekulen te begrijpen. In dit proefschrift hebben we de technieken van de statistische fysica toegepast om het gedrag van korrelvormige materialen, zoals zand, en dat van levende cellen, zoals bacteriën, beter te begrijpen. Waarom we dat hebben gedaan en wat we daar van hebben geleerd, zal ik nu proberen uit te leggen.

## Stochastische dynamica in zand

Iedereen die wel eens op het strand met zand gespeeld heeft, weet dat zand zowel de eigenschappen van een vaste stof als van een vloeistof heeft. Als je van zand een zandkasteel bouwt, maak je gebruik van de eerste eigenschap. Maar als

zand in beweging wordt gebracht, bijvoorbeeld door de zwaartekracht of door het te schudden, kan het zich als een vloeistof gedragen. Als je langs de helling van een duin loopt, bijvoorbeeld, “stroomt” het zand vaak als een kleine lawine naar beneden. Deze eigenschappen zijn niet uniek voor zand, maar gelden in het algemeen voor alle korrelvormige of *granulaire* materialen zoals graan, rijst, poeders of sneeuw. De overgang tussen de vaste en de ‘vloeibare’ toestand van granulaire materialen kun je op een handige manier gebruiken, bijvoorbeeld door graan uit een silo te laten stromen en het zo naar een andere plek te transporteren. Het kan echter ook op een gevaarlijke manier plaatsvinden, bijvoorbeeld in het geval van sneeuw- of modderlawines. Vreemd genoeg begrijpen we dit soort schijnbaar alledaagse dingen lang niet altijd en kunnen we soms voor rare verrassingen komen te staan. Een voorbeeld: in de industriële verwerking van poeders, worden twee poeders vaak met elkaar gemengd door ze door elkaar te schudden. Het blijkt dat als de twee poeders bijvoorbeeld te veel verschillen wat korrelgrootte betreft, dit juist het tegenovergestelde resultaat levert: de twee poeders ontmengen zich en raken op grootte gesorteerd. Het is pas sinds de laatste jaren dat we dit soort gedrag beter begrijpen. Meer voorbeelden van verrassend gedrag van zand en andere granulaire materialen zijn beschreven in Hoofdstuk 1.

Eén van de uitdagingen die we tegenkomen wanneer we granulaire materialen proberen te begrijpen, is dat het aantal korrels vaak zo groot is, dat we niet het gedrag van iedere korrel afzonderlijk kunnen volgen. Maar net zoals we in de statistische fysica niet het gedrag van ieder individueel molecuul hoeven te kennen om de eigenschappen van een vloeistof of een gas uit te kunnen rekenen, zo kunnen we dezelfde techniek ook op granulaire materialen toepassen. In dat geval kunnen we een granulaire ‘vloeistof’, zoals zand stromend langs een duinhelling, misschien beschrijven als een gewone vloeistof, maar dan niet met molekulen maar met korrels als bouwstenen. Toch is er een groot verschil tussen stromende granulaire materialen en vloeistoffen: granulaire materialen zijn *dissipatief*. Wat betekent dit precies? Als twee korrels in een granulaire materiaal met elkaar botsen, raken ze wat bewegingsenergie kwijt: de korrels hebben ze na de botsing minder snelheid dan daarvoor. De missende bewegingsenergie is tijdens de botsing *gedissipeerd*, oftewel weggelekt in de vorm van wrijvingswarmte. Dat dissipatie in granulaire materialen heel belangrijk is, blijkt uit het volgende simpele experiment (waarvan je de experimentele opstelling na afloop kunt opeten). Neem een M&M en laat dat boven een tafelblad vallen. De M&M zal een aantal keer stuiteren en uiteindelijk op de tafel tot rust komen. Herhaal hetzelfde experiment maar nu met een zakje M&Ms. Het zakje M&Ms stuitert nauwelijks en komt vrijwel meteen tot rust. Waar komt dit enorme verschil tussen het gedrag van één enkele M&M en een groot aantal M&Ms vandaan? Dat is het resultaat van de vele botsingen tussen de M&Ms in het zakje,

waarbij alle bewegingsenergie van de M&Ms weglekt. Het is om precies dezelfde reden dat in de constructie van bunkers vaak zandzakken worden gebruikt. Zandzakken houden kogels en bomscherven heel efficiënt tegen omdat in de botsingen tussen de zandkorrels de bewegingsenergie van de projectielen razendsnel wordt gedissipeerd.

Het resultaat van deze dissipatieve botsingen is dat een granulaair materiaal de hele tijd in beweging gehouden moet worden om het zich als een vloeistof te laten gedragen. Zonder energietoevoer, bijvoorbeeld door te schudden, komen de korrels meteen op een hoopje tot rust. Heel anders is het gedrag van gewone vloeistoffen en gassen. Als molekulen met elkaar botsen raken zij geen bewegingsenergie kwijt. Het gevolg is dat de molekulen in een vloeistof en een gas altijd in beweging blijven (zoals we hebben gezien in de discussie over de Brownse beweging). Het feit dat voor gewone vloeistoffen energie behouden is maakt het relatief makkelijk om aan de willekeurige beweging van de molekulen te rekenen. Voor granulaire materialen kunnen wij zulke vereenvoudigingen helaas niet gebruiken. Dat maakt het rekenen aan granulaire materialen meteen heel spannend: systemen, zoals granulaire materialen, waaraan energie toegevoerd moet worden om ze aan de gang te houden, staan bekend als *niet-evenwicht systemen*. In ons dagelijks leven komen we dergelijke systemen veel tegen. Ons lichaam in het bijzonder en levende cellen in het algemeen zijn typische voorbeelden van zulke systemen. De hoop is dat we door het bestuderen van relatief eenvoudige granulaire materialen misschien meer te weten komen over hoe we zulke niet-evenwichts systemen in het algemeen kunnen beschrijven.

Wij doen dat door te kijken naar zogenaamde *granulaire gassen*. Een granulaair gas is bijvoorbeeld te maken door een aantal kogeltjes in een doos te doen en dan de doos hard te schudden. Een voorbeeld van een granulaair gas van zulke kogeltjes is afgebeeld op pagina 67. Net zoals in een gas de dichtheid van molekulen veel lager is dan in een vloeistof, zo is een granulaair gas een granulaire vloeistof met een hele lage dichtheid. Doordat in een granulaair gas de korrels niet zo dicht op elkaar zitten als in een granulaire vloeistof is het gedrag van een granulaair gas veel simpeler en dus hopelijk makkelijker te begrijpen. We zijn geïnteresseerd in de verschillen tussen een granulaair gas en een gewoon gas dat uit molekulen bestaat. Eerder zagen we al dat het voor gewone gassen nuttig is om naar de snelheidsverdeling van de molekulen te kijken. Het blijkt nu dat de snelheidsverdeling die wordt gemeten voor de korrels in een granulaair gas niet de Gaussische verdeling volgt, maar een duidelijk andere vorm heeft. Omdat de Gaussische verdeling zo algemeen voorkomt en niet afhangt van het precieze systeem - het beschrijft immers niet alleen het gedrag van gassen, maar ook lichaamslengtes en nog veel meer - is dit een heel fundamenteel verschil tussen gewone gassen en dissipatieve granulaire gassen en willen we graag snappen waar dat verschil vandaan komt.

Helaas leveren de verschillende experimenten, berekeningen en computersimulaties geen heldere resultaten op. Het is duidelijk dat Gaussische snelheidsverdelingen in granulaire gassen alleen in speciale gevallen voorkomen. Verder vindt men veel verschillende snelheidsverdelingen, afhankelijk van de experimentele opstelling, van het soort en het aantal korrels en van de dichtheid van de granulaire gassen. In Hoofdstuk 2 hebben wij de snelheidsverdeling onderzocht met computersimulaties. We hebben ontdekt dat we, in ieder geval in onze simulatie, al die verschillende snelheidsverdelingen kunnen verklaren met behulp van maar twee parameters, één die de hoeveelheid dissipatie in botsing tussen de korrels beschrijft en één die beschrijft hoe energie aan het systeem wordt toegevoerd. De laatste parameter verschilt van experiment tot experiment en we denken dat we hiermee iets van de tegenstrijdige resultaten uit de experimentele literatuur kunnen verklaren. In Hoofdstuk 3 beschrijf ik de resultaten van experimenten die ik heb gedaan tijdens een bezoek aan de University of Texas in Austin. Veel experimenten aan granulaire gassen zijn uitgevoerd aan zogenaamde twee-dimensionele gassen. Hierbij worden metalen kogeltjes opgesloten tussen twee doorzichtige zijwanden en op en neer geschud. Op deze manier kan de beweging van de kogeltjes met behulp van een camera worden gevolgd. Wij hebben ontdekt dat in zo'n soort experiment de snelheidsverdeling erg kan worden beïnvloed door wrijving tussen de kogeltjes en de zijwanden. Dit betekent dat de resultaten van eerdere experimenten waarschijnlijk niet betrouwbaar zijn.

## Stochastische dynamica in cellen

De kleinste levende organismen zijn bacteriën. De bacterie *Escherichia coli*, een vaste bewoner van ons darmstelsel, is ongeveer  $1 \mu\text{m}$ , ofwel één miljoenste meter, lang. Er passen ongeveer een half miljoen van zulke bacteriën in de punt aan het eind van deze zin. Het is een misvatting te denken dat zulke kleine organismen ook erg simpel zijn. In tegendeel, hoe beter men bacteriën bestudeert, des te meer men erachter komt dat zij in veel gevallen niet onderdoen voor de grote, ingewikkelde cellen waar onder andere de mens uit bestaat. bacteriën meten bijvoorbeeld voortdurend de toestand van zichzelf en de omgeving en passen op basis daarvan hun gedrag aan. Zo verteert *E. coli* alleen de suikerachtige stof lactose als zijn favoriete suiker, glucose, niet aanwezig is. De meeste bacteriën zwemmen of kruipen in de richting van een voedselbron en weg van schadelijke stoffen. Andere bacteriën, zoals die van de soort *Vibrio* waar onder andere ook de cholera bacterie onder valt, communiceren met hun soortgenoten en besluiten, als ze vinden dat ze met genoeg zijn, met zijn allen licht te geven of de cellen van een andere organisme aan te vallen. Door alle

ontwikkelingen in de biologie van de afgelopen jaren is het mogelijk te begrijpen hoe levende cellen dit soort beslissingen nemen. Het blijkt dat bacteriën informatie verwerken en beslissingen nemen met behulp van netwerken van molekulen die met elkaar reageren, zogenaamde *biochemische netwerken*. Die netwerken vertonen grote gelijkenis met de elektronische circuits die we bijvoorbeeld in CD-spelers vinden. De schakelaars, versterkers en filters die we in CD-spelers vinden, zien we ook terug in biochemische netwerken, waarbij de rol van elektrische stroompjes, transistors en weerstanden is overgenomen door molekulen zoals DNA en eiwitten. Omdat deze netwerken doorgaans uit veel molekulen bestaan die op ingewikkelde manieren met elkaar reageren, is het vaak moeilijk het gedrag van zulke netwerken te begrijpen, zelfs als men al veel weet van de molekulen waar ze uit bestaan. Om die reden onderzoekt men deze netwerken het meest in de reëlf simpele bacteriën in plaats van in ingewikkelder cellen.

Eén van de redenen waarom natuurkundigen geïnteresseerd zijn in bacteriën en andere cellen is omdat zij zo klein zijn dat hun wereld volledig wordt gedomineerd door de willekeurige fluctuaties die ook verantwoordelijk zijn voor de Brownse beweging. De manier waarop bacteriën een voedselbron zoeken is bijvoorbeeld volledig aangepast aan het feit dat zij niet in een rechte lijn kunnen zwemmen omdat zij door de Brownse beweging van hun omgeving voortdurend van hun koers gestoten worden. Maar ook het binnenwerk van de bacterie wordt in belangrijke mate door deze fluctuaties aangetast. De molekulen die samen een biochemisch netwerk vormen reageren met elkaar door middel van botsingen die, net als voor gassen, op een willekeurige manier plaatsvinden. Bovendien bewegen deze molekulen in het binnenste van de bacterie door middel van de Brownse beweging. Voordat zij met elkaar kunnen reageren moeten deze molekulen elkaar dus eerst ontmoeten via de willekeurige dronkenmanswandeling die hierboven is beschreven. In experimenten aan de bacterie *E. coli* is inderdaad gemeten dat om deze redenen de productie van bepaalde eiwitten in de cel op willekeurige wijze in de tijd varieert. Een belangrijke vraag is hoe een bacterie nog steeds betrouwbaar kan werken als zijn mechaniek zich voor een deel willekeurig gedraagt. Hoe voorkomt een bacterie bijvoorbeeld dat hij door zulke fluctuaties een verkeerde keus maakt? Dit is ook een belangrijke vraag in elektronische signaalverwerking, waar men ruis in het signaal te lijf gaat met filters en andere oplossingen. Ook voor sommige biochemische netwerken blijkt dat zij door de evolutie zo zijn ingericht dat ze relatief ongevoelig zijn voor deze fluctuaties, ook wel *moleculaire ruis* genoemd. Dergelijke moleculaire ruis is ook van belang in de ingewikkelder cellen waar mensen uit bestaan. Door moleculaire fluctuaties tijdens de ontwikkeling van het menselijk embryo hebben één-eiige tweelingen bijvoorbeeld totaal verschillende vingerafdrukken, ondanks het feit dat ze precies hetzelfde erfelijk materiaal bezitten.

Omdat experimenten aan fluctuaties in levende cellen nog lastig zijn, worden ze vaak aangevuld met wiskundige modellen en computersimulaties. Een probleem daarbij is dat diffusie van molekulen in de cel in berekeningen moeilijk mee is te nemen en dat de bestaande simulatietechnieken voor diffusie óf te langzaam zijn voor deze biologische problemen óf onnauwkeurig. Daarom nemen de meeste berekeningen en simulaties als versimpeling aan dat de inhoud van een cel “goed gemengd” is, zodat het niet nodig is de exacte locatie van de molekulen in de cel te weten en dus diffusie geen rol speelt. Wij zijn hier om twee redenen niet tevreden mee: als eerste weten we dat sommige molekulen door middel van de Brownse beweging een signaal van één kant van een cel naar de andere doorgeven. Ten tweede kunnen de fluctuaties ten gevolge van de Brownse beweging die de molekulen ondergaan bijdragen aan de totale fluctuaties in de cel. Beide gevallen kunnen dus met de huidige simulatietechnieken niet goed onderzocht worden. In Hoofdstuk 5 beschrijven we een nieuwe simulatietechniek waarmee dat wel kan. Het voordeel van deze techniek is, dat door op een slimme manier gebruik te maken van onze kennis over de Brownse beweging, we in staat zijn om heel efficiënt de reacties en Brownse beweging van een groot aantal molekulen te volgen. In een eerste toepassing van onze techniek, proberen we in Hoofdstuk 6 te bepalen in hoeverre de fluctuaties van de Brownse beweging bijdragen aan de totale fluctuaties in de cel. Voor een eiwit waarvan de productie wordt gecontroleerd door een ander eiwit, vinden we dat de fluctuaties in het aantal geproduceerde eiwitten in sommige situaties grotendeels het gevolg is van de Brownse beweging van het controlerend eiwit. Verder hebben we een elegante manier gevonden om die extra fluctuaties zo te beschrijven dat hiervoor ook een veel simpeler techniek, die een “goed gemengde” cel veronderstelt, kan worden gebruikt.





---

# Dankwoord

Geen onderdeel van het proefschrift zo doorwrocht als het dankwoord! Om het één en ander voor mijzelf makkelijker te maken, heb ik voorgenomen mij te beperken tot alleen die mensen, die op directe wijze hebben bijgedragen aan het werk dat in dit proefschrift verzameld is. Al die mensen die er voor zorgden dat ik de afgelopen vier jaar geregeld gedwongen was mijn wetenschappelijke arbeid te onderbreken voor het hebben van een leuke tijd zullen dus helaas mijn dank op andere wijze tegemoet moeten zien.

Als eerste wil ik Fred, mijn promotor, bedanken. Ik heb toentertijd mijn afstudeeronderzoek met een paar maanden uitgesteld in afwachting van jouw komst naar de VU en ik kan niet zeggen dat ik daar ooit spijt van heb gehad. Toen jij mij in het begin een keer hoorde zeggen dat ik “voor Fred” werkte, corrigeerde jij dat het “samen met Fred” moest zijn. Zo heb ik het gedurende de hele verdere periode inderdaad ook ervaren. Verder heb ik altijd het gevoel gehad dat voor jou mijn persoonlijke ontwikkeling als natuurkundige altijd boven eventuele andere belangen ging en dat je altijd bereid was moeite te doen om je student in de wereld vooruit kon helpen. Ik wil je ook bedanken voor de grote vrijheid waarmee je mij eerst in jouw groep en later voor een groot deel ook in een andere groep hebt laten werken. Jouw stelling, dat theoretische natuurkunde bij uitstek geschikt is om verschillende soorten onderzoek naast elkaar te doen, heb ik met veel plezier ter harte genomen.

Natuurlijk wil ik ook Pieter Rein, mijn copromotor, bedanken. Toen ik nog zoekende was naar een leuke afwisseling voor mijn werk aan granulaire gassen, begon jij aan de VU met het onderzoek naar biochemische netwerken waar ik met de jaren toch wel een beetje mijn hart aan verloren heb. Toen jij later definitief naar het Amolf verhuisde, ben ik je tenminste voor één ochtend in de week gevolgd. Behalve de stimulerende discussies tijdens en na de groupmeeting op de woensdag, verzag je me gedurende de rest van de week rijkelijk van steun via telefoon en e-mail. Het lijkt me duidelijk dat zonder jouw uitgebreide kennis van simulatietechnieken “onze” techniek nooit het stadium van de tekentafel ontstegen was. Als laatste wil

ik nog mijn bewondering uitspreken voor je intellectuele uithoudingsvermogen. Ik herinner me nog in het bijzonder een bijeenkomst waar wij na uren met van uitputting geknakte lichamen in onze stoelen hingen en jij nog onvermoeibaar onzichtbare vergelijkingen op het whiteboard schreef met een pen waar geen druppel inkt meer in zat.

Promotoren en copromotoren komen doorgaans met een groep en in beide gevallen heb ik het daar naar mijn mening bijzonder mee getroffen. Als eerste zijn er de twee Complexe Systemen groepen aan de VU. Naast al die tijd tijdens de lunch en de thee die ik eigenlijk aan de wetenschap had moeten besteden, waren de vele gedeelde zomerscholen, werkbesprekingen en horeca-bezoeken ook altijd erg nuttig en leuk. In de experimentele groep ben ik voor een theoreticus die geen espresso lust altijd welwillend ontvangen. In het bijzonder wil ik de volgende mensen bedanken: David, die in ruil voor een enkele vraag over Nederland altijd bereid was de kieren-de gaten in mijn kennis van de biologie te dichten en met wie ik ook met plezier aan onderzoek gewerkt heb. Bram en Joost, die er in sterke mate aan hebben bijgedragen dat ik nu wèl om negen uur op de VU ben. Tot verdriet van onze vriendinnen is het niet altijd duidelijk waar bij ons het werk ophoudt en de vriendschap begint. Dan is er ook nog de groep aan het Amolf. Ik heb mij altijd verheugd op mijn wekelijks uitje naar Watergraafsmeer en heb me daar (ondanks dat de receptionisten mij nooit vertrouwden) als relatieve buitenstaander altijd thuisgevoeld. Ik wil hier de volgende mensen bij naam noemen: Pim, met wie ik pas het afgelopen half jaar heb samengewerkt. Rosalind, met wie het altijd leuk en nuttig was om over wetenschap en andere dingen te praten. Ik ben nog steeds jaloers dat jij binnenkort wellicht wel in het lab mag staan! Marco, met wie ik onverhoopt veel heb samengewerkt. Liep ons onderzoek in eerste instantie parallel aan elkaar, het waren die duivelse tabellen die ons uiteindelijk tot een, wat mij betreft, prettige samenwerking brachten. Joost, Rosalind en David verdienen nog een extra woord van dank voor het lezen van en discussiëren over verschillende delen van dit proefschrift. Joost en Rutger tenslotte hebben het aangedurfd om als mijn paranimfen te fungeren.

I would also like to thank Dr. Harry Swinney for his hospitality during my stay in his group at the University of Texas at Austin. I had a very enjoyable time in Austin! I also want to thank Dan Goldman for his daily advise and Jennifer Kreft for her hard work during the writing (and rewriting) of our article.

Als laatste dien ik natuurlijk Una te bedanken. Op niemand heeft de last van de wetenschap zwaarder neergedrukt dan op jou! Met ijzeren geduld knik je altijd vriendelijk als ik 's avonds weer vertel over dat ene leuke experiment of die nieuwe bijzondere bacterie. De tol van het wetenschappelijk bedrijf op onze relatie is verschrikkelijk geweest: woonden wij vier jaar geleden nog in één en hetzelfde huis, daarna achtereenvolgens een straat uit elkaar en aan de andere kant van de stad,

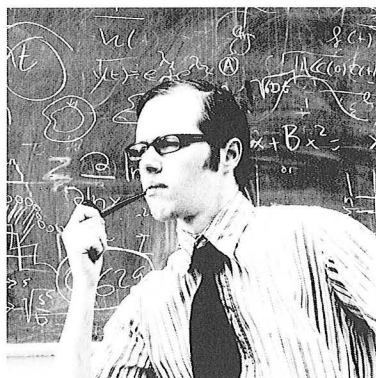
nu zullen wij omwille van de wetenschap in verschillende landen moeten wonen. Zal mijn tweede post-doc dan op een ander continent zijn en een eventuele vaste aanstelling in een laboratorium in een geostationaire baan om de aarde?



---

# Curriculum Vitae

Jeroen van Zon is geboren op 30 maart 1977 te Haarlem. Hij groeide op in Maarssenbroek en doorliep het Christelijk Gymnasium in Utrecht. In 1995 begon hij de studie natuur- en sterrenkunde aan de Vrije Universiteit Amsterdam. In 2002 studeerde hij in de groep Theoretical Soft Condensed Matter and Complex Systems van prof.dr F. C. MacKintosh *cum laude* af op een onderwerp in de statistische mechanica. In hetzelfde jaar startte hij zijn promotieonderzoek op het gebied van de statistische mechanica van granulaire materialen en van levende cellen, onder be-



geleiding van prof.dr. F. C. MacKintosh en dr. P. R. ten Wolde, de laatste verbonden aan het FOM Instituut voor Atoom- en Molekulfysica in Amsterdam. Dit proefschrift, getiteld “Stochastic Dynamics in Sand and Cells”, vormt de weerslag van vier jaar onderzoek, waarvan delen reeds zijn gepubliceerd in internationale vaktijdschriften. Behalve zuiver theoretisch onderzoek is hij ook betrokken geweest bij de uitvoering van enkele experimenten. Na zijn promotie zal hij als post-doctoraal onderzoeker verbonden zijn aan het Imperial College te Londen. Zijn hobby’s zijn: wetenschap, lezen en muziek luisteren.

